

IMPACT OF DFIG-BASED WIND FARMS ON GENERATOR DISTANCE PHASE BACKUP PROTECTION

A Thesis

Submitted to the College of Graduate Studies and Research

In Partial Fulfillment of the Requirements

For the Degree of Master of Science

In the Department of Electrical and Computer Engineering

University of Saskatchewan

Saskatoon, Saskatchewan

By

Yongzheng Zhang

PERMISSION TO USE

I agree that the Library, University of Saskatchewan, may make this thesis freely available for inspection. I further agree that permission for copying of this thesis for scholarly purpose may be granted by the professor or professors who supervised the thesis work recorded herein or, in their absence, by the Head of the Department or the Dean of the College in which the thesis work was done. It is understood that due recognition will be given to me and to the University of Saskatchewan in any use of the material in this thesis. Copying or publication or any other use of this thesis for financial gain without approval by the University of Saskatchewan and my written permission is prohibited.

Request for permission to copy or to make any other use of the material in this thesis in whole or part should be addressed to:

Head of the Department of Electrical and Computer Engineering
University of Saskatchewan
57 Campus Drive
Saskatoon, Saskatchewan S7N 5A9
Canada

ABSTRACT

Renewable energy technologies are clean sources of energy that have a lower environmental impact than conventional energy technologies. Among all the renewable energy sources, wind energy is clean and plentiful compared to nonrenewable energy sources like fossil fuels and cost-effective compared to other renewable energy sources such as nuclear. Therefore, the potential for wind energy is immense. Nowadays, wind farms are increasingly employed in power systems in order to meet the growing demand of energy as well as the growing environmental awareness. Grid integration of large capacity of wind energy requires, however, new approaches for system operation, control, dynamic enhancement and protection.

This thesis reports the results of digital time-domain simulation studies that are carried out to investigate the effect of Doubly-Fed Induction Generator (DFIG)-based wind farms on the performance of generator distance phase backup protection element (Relay (21)) in order to identify important issues that protection engineers need to consider when designing and setting a generator protection system. Such investigation is achieved through incorporating a large DFIG-based wind farm in a study system that inspired from an actual power system. The incorporation takes place under different Relay (21) zone settings. In this context, comparative studies between the relay performance with and without the presence of the DFIG-based wind farm during different faults are presented. The effects of fault location, fault type, generator loading, power flows in the transmission lines in conjunction with wind farm rating and location are also investigated.

For validation purposes, time-domain simulations are conducted on benchmark models using the ElectroMagnetic Transients program (EMTP-RV). The results of the investigations carried out in this thesis reveal that DFIG -based wind farm has an effect on the generator distance phase backup protection that leads to error in measured impedance by the generator distance phase backup protection element. This effect varies according to fault type, fault location, generator loading, power flows on transmission lines as well as DFIG-based wind farm rating and location.

ACKNOWLEDGEMENTS

Foremost, I would like to express my sincere gratitude to my supervisor Dr. Sherif O. Faried. His expertise, understanding, and patience, offered considerably help to my graduate study experience. I appreciate his vast knowledge and skill in many areas and his continuous support of my M.Sc study and related research.

I would also like to thank Dr. Mohamed Elsamahy for taking time out from his busy schedule to provide some rather helpful advices throughout my entire research. My appreciation also goes to Keaton A. Wheeler for the encouragement and inspiration he has offered.

Lastly, a very special thank goes out to my family and all my friends for their encouragement and support.

TABLE OF CONTENTS

PERMISSION TO USE	i
ABSTRACT	ii
ACKNOWLEDGEMENTS.....	iii
TABLE OF CONTENTS	iv
LIST OF FIGURES	vi
LIST OF TABLES	xiv
LIST OF SYMBOLS	xv
1. INTRODUCTION.....	1
1.1 Wind Energy.....	1
1.2 Wind Turbines	1
1.2.1 Doubly-fed induction generator wind turbine	2
1.3 Generator Distance Phase Backup Protection	2
1.3.1 Distance Relay Characteristics	3
1.3.2 Distance Relay Operation.....	5
1.4 Generator Capability Curve	5
1.5 Coordination between Relay (21) and GOEC.....	6
1.6 Research Objective and Scope of the Thesis	7
2. POWER SYSTEM MODELING FOR LARGE DISTURBANCE STUDIES.....	9
2.1 General	9
2.2 System under Study	9
2.3 Power System Modeling	10
2.3.1 Modeling of the synchronous machine	10
2.3.2 Modeling of the transmission line	13
2.3.3 Excitation system.....	16
2.3.4 Modeling of the transformer.....	17
2.3.5 Modeling of the DFIG Wind Turbine.....	17
2.3.6 Modeling of the two Large Systems	18
2.4 A Sample Case Study.....	18
2.5 Summary	27
3. IMPACT OF DFIG-BASED WIND FARMS ON GENERATOR DISTANCE PHASE BACKUP PROTECTION	28
3.1 Introduction	28
3.2 Setting of Generator Phase Backup Protection (Relay (21))	28
3.3 Setting Relay (21) According to 50% of the Generator Load Impedance at the Rated Power Factor Angle of the Generator.....	30
3.3.1 Performance of Relay (21) at 65% of the generator loading.....	30
3.3.2 Performance of Relay (21) at 75% of the generator loading.....	45
3.3.3 Performance of Relay (21) at 85% of the generator loading.....	58
3.3.4 Effect of the DFIG-based wind farm on Relay (21) measured impedance.....	69
3.3.4.1 Effect of the generator loading	70
3.3.4.2 Effect of the fault type	70
3.3.4.3 Effect of the fault Location.....	70
3.3.5 Effect of the transmission line power flows.....	72
3.3.6 Effect of the DFIG-based wind farm rating and location	80

3.4 Setting Relay (21) According to 67% of the Generator Load Impedance at the Rated Power Factor Angle of the Generator.....	87
3.5 Summary	87
4. SUMMARY AND CONCLUSIONS.....	88
4.1 Summary	88
4.2 Conclusion.....	88
REFERENCES	90
APPENDIX A.....	93
APPENDIX B.....	96
APPENDIX C.....	98

LIST OF FIGURES

Figure 1.1: Typical structure of a DFIG wind turbine.	2
Figure 1.2: Distance protection zones in the Z plane.	4
Figure 1.3: A mho distance relay characteristic.	4
Figure 1.4: Relay (21) employed as generator distance backup protection.	5
Figure 1.5: Generator capability curves for turbogenerators.	6
Figure 1.6: Transformation of a P-Q plot to an R-X plot.	7
Figure 2.1: System under study.	9
Figure 2.2: Modeling of the synchronous machine in the d-q reference frame.	11
Figure 2.3: A series capacitor-compensated transmission line.	14
Figure 2.4: Voltage phasor diagram.	14
Figure 2.5: Block diagram of the excitation system.	16
Figure 2.6: Schematic diagram of a DFIG wind turbine.	17
Figure 2.7: Load flow results of the bus voltages and real power flows of the system under study.	18
Figure 2.8: Transient time responses of generator real power output, generator speed, DFIG-based wind farm real power output, bus M voltage, real power flows in L ₁ and L ₂ during and after clearing a three-cycle three-phase fault at F ₁	19
Figure 2.9: Transient time responses of generator real power output, generator speed, DFIG-based wind farm real power output, bus M voltage, real power flows in L ₁ and L ₂ during and after clearing a three-cycle line-to-line fault at F ₁	21
Figure 2.10: Transient time responses of generator real power output, generator speed, DFIG-based wind farm real power output, bus M voltage, real power flows in L ₁ and L ₂ during a sustained three-phase fault at F ₁	23
Figure 2.11: Transient time responses of generator real power output, generator speed, DFIG-based wind farm real power output, bus M voltage, real power flows in L ₁ and L ₂ during a sustained line-to-line fault at F ₁	25
Figure 3.1: Apparent impedance measurement with system infeed currents.	28
Figure 3.2: Coordination between Relay (21) and the GOEC limit.	30
Figure 3.3: Load flow results of the bus voltages and real power flows of the system under 65% generator loading.	31
Figure 3.4: Relay (21) tripping signal, transient time responses of generator active and reactive powers, active and reactive power flows from Bus 1 to Bus M during a line-to-line fault at F ₁ (no wind farm in the system).	32
Figure 3.5: Relay (21) measured impedance trajectory and its tripping signal, transient time responses of generator active and reactive powers, active and reactive power flows from Bus 1 to Bus M, DFIG-based wind farm active and reactive powers during a line-to-line fault at F ₁	33
Figure 3.6: Relay (21) tripping signal, transient time responses of generator active and reactive powers, active and reactive power flows from Bus 1 to Bus M during a three-phase fault at F ₁ (no wind farm in the system).	35
Figure 3.7: Relay (21) measured impedance trajectory and its tripping signal, transient time responses of generator active and reactive powers, active and reactive power flows from Bus 1 to Bus M, DFIG-based wind farm active and reactive powers during a three-phase at F ₁	36

Figure 3.8: Transient time responses of generator active and reactive powers, active and reactive power flows from Bus 1 to Bus M during a line-to-line fault at F_2 (no wind farm in the system).....	39
Figure 3.9: Relay (21) measured impedance, transient time responses of generator active and reactive powers, active and reactive power flows from Bus 1 to Bus M, DFIG-based wind farm active and reactive powers during a line-to-line fault at F_2	40
Figure 3.10: Transient time responses of generator active and reactive powers, active and reactive power flows from Bus 1 to Bus M during a three-phase fault at F_2 (no wind farm in the system).....	42
Figure 3.11: Relay (21) measured impedance trajectory, transient time responses of generator active and reactive powers, active and reactive power flows from Bus 1 to Bus M, DFIG-based wind farm active and reactive powers during a three-phase at F_2	43
Figure 3.12: Relay (21) tripping signal, transient time responses of generator active and reactive powers, active and reactive power flows from Bus 1 to Bus M during a line-to-line fault at F_1 (no wind farm in the system).	46
Figure 3.13: Relay (21) measured impedance trajectory and its tripping signal, transient time responses of generator active and reactive powers, active and reactive power flows from Bus 1 to Bus M, DFIG-based wind farm active and reactive powers during a line-to-line fault at F_1	47
Figure 3.14: Relay (21) tripping signal, transient time responses of generator active and reactive powers, active and reactive power flows from Bus 1 to Bus M during a three-phase fault at F_1 (no wind farm in the system).	49
Figure 3.15: Relay (21) measured impedance trajectory and its tripping signal, transient time responses of generator active and reactive powers, active and reactive power flows from Bus 1 to Bus M, DFIG-based wind farm active and reactive powers during a three-phase at F_1	50
Figure 3.16: Transient time responses of generator active and reactive powers, active and reactive power flows from Bus 1 to Bus M during a line-to-line fault at F_2 (no wind farm in the system).....	52
Figure 3.17: Relay (21) measured impedance trajectory, transient time responses of generator active and reactive powers, active and reactive power flows from Bus 1 to Bus M, DFIG-based wind farm active and reactive powers during a line-to-line fault at F_2	53
Figure 3.18: Transient time responses of generator active and reactive powers, active and reactive power flows from Bus 1 to Bus M during a three-phase fault at F_2 (no wind farm in the system).....	55
Figure 3.19: Relay (21) measured impedance trajectory, transient time responses of generator active and reactive powers, active and reactive power flows from Bus 1 to Bus M, DFIG-based wind farm active and reactive powers during a three-phase at F_2	56
Figure 3.20: Relay (21) tripping signal, transient time responses of generator active and reactive powers, active and reactive power flows from Bus 1 to Bus M during a line-to-line fault at F_1 (no wind farm in the system).....	58
Figure 3.21: Relay (21) measured impedance trajectory and its tripping signal, transient time responses of generator active and reactive powers, active and reactive power flows from Bus 1 to Bus M, DFIG-based wind farm active and reactive powers during a line-to-line fault at F_1	59

Figure 3.22: Relay (21) tripping signal, transient time responses of generator active and reactive powers, active and reactive power flows from Bus 1 to Bus M during a three-phase fault at F_1 (no wind farm in the system).	61
Figure 3.23: Relay (21) measured impedance trajectory and its tripping signal, transient time responses of generator active and reactive powers, active and reactive power flows from Bus 1 to Bus M, DFIG-based wind farm active and reactive powers during a three-phase at F_1	62
Figure 3.24: Transient time responses of generator active and reactive powers, active and reactive power flows from Bus 1 to Bus M during a line-to-line fault at F_2 (no wind farm in the system).	64
Figure 3.25: Relay (21) measured impedance trajectory, transient time responses of generator active and reactive powers, active and reactive power flows from Bus 1 to Bus M, DFIG-based wind farm active and reactive powers during a line-to-line fault at F_2	65
Figure 3.26: Transient time responses of generator active and reactive powers, active and reactive power flows from Bus 1 to Bus M during a three-phase fault at F_2 (no wind farm in the system).	67
Figure 3.27: Relay (21) measured impedance trajectory, transient time responses of generator active and reactive powers, active and reactive power flows from Bus 1 to Bus M, DFIG-based wind farm active and reactive powers during a three-phase at F_2	68
Figure 3.28: <i>PEMI</i> for line-to-line faults at different generator loading levels.	71
Figure 3.29: <i>PEMI</i> for three-phase faults at different generator loading levels.	71
Figure 3.30: Load flow results of the bus voltages and real power flows of the system under 65% generator loading.	72
Figure 3.31: Relay (21) tripping signal, transient time responses of generator active and reactive powers, active and reactive power flows from Bus 1 to Bus M during a line-to-line fault at F_1 (no wind farm in the system).	73
Figure 3.32: Relay (21) measured impedance trajectory and its tripping signal, transient time responses of generator active and reactive powers, active and reactive power flows from Bus 1 to Bus M, DFIG-based wind farm active and reactive powers during a line-to-line fault at F_1	74
Figure 3.33: Relay (21) tripping signal, transient time responses of generator active and reactive powers, active and reactive power flows from Bus 1 to Bus M during a three-phase fault at F_1 (no wind farm in the system).	76
Figure 3.34: Relay (21) measured impedance trajectory and its tripping signal, transient time responses of generator active and reactive powers, active and reactive power flows from Bus 1 to Bus M, DFIG-based wind farm active and reactive powers during a three-phase at F_1	77
Figure 3.35: <i>PEMI</i> for line-to-line faults at different L_1 power flow conditions.	79
Figure 3.36: <i>PEMI</i> for three-phase faults at different L_1 power flow conditions.	79
Figure 3.37: Load flow results of the bus voltages and real power flows of the system under 65% generator loading.	80
Figure 3.38: Transient time responses of generator active and reactive powers, active and reactive power flows from Bus 1 to Bus K, during a line-to-line fault at F_2 (no wind farm in the system).	81

Figure 3.39: Relay (21) measured impedance, transient time responses of generator active and reactive powers, active and reactive power flows from Bus 1 to Bus K, DFIG-based wind farm active and reactive powers during a line-to-line fault at F_2	82
Figure 3.40: Transient time responses of generator active and reactive powers, active and reactive power flows from Bus 1 to Bus K, during a three-phase fault at F_2 (no wind farm in the system).	84
Figure 3.41: Relay (21) measured impedance trajectory, transient time responses of generator active and reactive powers, active and reactive power flows from Bus 1 to Bus K, DFIG-based wind farm active and reactive powers during a three-phase at F_2	85
Figure B.1: Equivalent circuit of the system under study.	96
Figure C.1: Transient time responses of generator active and reactive powers, active and reactive power flows from Bus 1 to Bus M during a line-to-line fault at F_3 (no wind farm in the system).	98
Figure C.2: Relay (21) measured impedance trajectory, transient time responses of generator active and reactive powers, active and reactive power flows from Bus 1 to Bus M, DFIG-based wind farm active and reactive powers during a line-to-line fault at F_3	99
Figure C.3: Transient time responses of generator active and reactive powers, active and reactive power flows from Bus 1 to Bus M during a three-phase fault at F_3 (no wind farm in the system).	100
Figure C.4: Relay (21) measured impedance trajectory, transient time responses of generator active and reactive powers, active and reactive power flows from Bus 1 to Bus M, DFIG-based wind farm active and reactive powers during a three-phase at F_3	101
Figure C.5: Transient time responses of generator active and reactive powers, active and reactive power flows from Bus 1 to Bus M during a line-to-line fault at F_3 (no wind farm in the system).	102
Figure C.6: Relay (21) measured impedance trajectory, transient time responses of generator active and reactive powers, active and reactive power flows from Bus 1 to Bus M, DFIG-based wind farm active and reactive powers during a line-to-line fault at F_3	103
Figure C.7: Transient time responses of generator active and reactive powers, active and reactive power flows from Bus 1 to Bus M during a three-phase fault at F_3 (no wind farm in the system).	104
Figure C.8: Relay (21) measured impedance trajectory, transient time responses of generator active and reactive powers, active and reactive power flows from Bus 1 to Bus M, DFIG-based wind farm active and reactive powers during a three-phase at F_3	105
Figure C.9: Transient time responses of generator active and reactive powers, active and reactive power flows from Bus 1 to Bus M during a line-to-line fault at F_3 (no wind farm in the system).	106
Figure C.10: Relay (21) measured impedance trajectory, transient time responses of generator active and reactive powers, active and reactive power flows from Bus 1 to Bus M, DFIG-based wind farm active and reactive powers during a line-to-line fault at F_3	107
Figure C.11: Transient time responses of generator active and reactive powers, active and reactive power flows from Bus 1 to Bus M during a three-phase fault at F_3 (no wind farm in the system).	108

Figure C.12: Relay (21) measured impedance trajectory, transient time responses of generator active and reactive powers, active and reactive power flows from Bus 1 to Bus M, DFIG-based wind farm active and reactive powers during a three-phase at F_3 ...	109
Figure C.13: Relay (21) tripping signal, transient time responses of generator active and reactive powers, active and reactive power flows from Bus 1 to Bus M during a line-to-line fault at F_1 (no wind farm in the system).....	110
Figure C.14: Relay (21) measured impedance trajectory and its tripping signal, transient time responses of generator active and reactive powers, active and reactive power flows from Bus 1 to Bus M, DFIG-based wind farm active and reactive powers during a line-to-line fault at F_1	111
Figure C.15: Relay (21) tripping signal, transient time responses of generator active and reactive powers, active and reactive power flows from Bus 1 to Bus M during a three-phase fault at F_1 (no wind farm in the system).....	112
Figure C.16: Relay (21) measured impedance trajectory and its tripping signal, transient time responses of generator active and reactive powers, active and reactive power flows from Bus 1 to Bus M, DFIG-based wind farm active and reactive powers during a three-phase at F_1	113
Figure C.17: Relay (21) tripping signal, transient time responses of generator active and reactive powers, active and reactive power flows from Bus 1 to Bus M during a line-to-line fault at F_1 (no wind farm in the system).....	114
Figure C.18: Relay (21) measured impedance trajectory and its tripping signal, transient time responses of generator active and reactive powers, active and reactive power flows from Bus 1 to Bus M, DFIG-based wind farm active and reactive powers during a line-to-line fault at F_1	115
Figure C.19: Relay (21) tripping signal, transient time responses of generator active and reactive powers, active and reactive power flows from Bus 1 to Bus M during a three-phase fault at F_1 (no wind farm in the system).....	116
Figure C.20: Relay (21) measured impedance trajectory and its tripping signal, transient time responses of generator active and reactive powers, active and reactive power flows from Bus 1 to Bus M, DFIG-based wind farm active and reactive powers during a three-phase at F_1	117
Figure C.21: Relay (21) tripping signal, transient time responses of generator active and reactive powers, active and reactive power flows from Bus 1 to Bus M during a line-to-line fault at F_1 (no wind farm in the system).....	118
Figure C.22: Relay (21) measured impedance trajectory and its tripping signal, transient time responses of generator active and reactive powers, active and reactive power flows from Bus 1 to Bus M, DFIG-based wind farm active and reactive powers during a line-to-line fault at F_1	119
Figure C.23: Relay (21) tripping signal, transient time responses of generator active and reactive powers, active and reactive power flows from Bus 1 to Bus M during a three-phase fault at F_1 (no wind farm in the system).....	120
Figure C.24: Relay (21) measured impedance trajectory and its tripping signal, transient time responses of generator active and reactive powers, active and reactive power flows from Bus 1 to Bus M, DFIG-based wind farm active and reactive powers during a three-phase at F_1	121

Figure C.25: Relay (21) tripping signal, transient time responses of generator active and reactive powers, active and reactive power flows from Bus 1 to Bus M during a line-to-line fault at F_2 (no wind farm in the system).	122
Figure C.26: Relay (21) measured impedance trajectory and its tripping signal, transient time responses of generator active and reactive powers, active and reactive power flows from Bus 1 to Bus M, DFIG-based wind farm active and reactive powers during a line-to-line fault at F_2	123
Figure C.27: Relay (21) tripping signal, transient time responses of generator active and reactive powers, active and reactive power flows from Bus 1 to Bus M during a three-phase fault at F_2 (no wind farm in the system).	124
Figure C.28: Relay (21) measured impedance trajectory and its tripping signal, transient time responses of generator active and reactive powers, active and reactive power flows from Bus 1 to Bus M, DFIG-based wind farm active and reactive powers during a three-phase at F_2	125
Figure C.29: Relay (21) tripping signal, Transient time responses of generator active and reactive powers, active and reactive power flows from Bus 1 to Bus M during a line-to-line fault at F_3 (no wind farm in the system).	126
Figure C.30: Relay (21) measured impedance trajectory and its tripping signal, transient time responses of generator active and reactive powers, active and reactive power flows from Bus 1 to Bus M, DFIG-based wind farm active and reactive powers during a line-to-line fault at F_3	127
Figure C.31: Relay (21) tripping signal, transient time responses of generator active and reactive powers, active and reactive power flows from Bus 1 to Bus M during a three-phase fault at F_3 (no wind farm in the system).	128
Figure C.32: Relay (21) measured impedance trajectory and its tripping signal, transient time responses of generator active and reactive powers, active and reactive power flows from Bus 1 to Bus M, DFIG-based wind farm active and reactive powers during a three-phase at F_3	129
Figure C.33: Relay (21) tripping signal, transient time responses of generator active and reactive powers, active and reactive power flows from Bus 1 to Bus M during a line-to-line fault at F_1 (no wind farm in the system).	130
Figure C.34: Relay (21) measured impedance trajectory and its tripping signal, transient time responses of generator active and reactive powers, active and reactive power flows from Bus 1 to Bus M, DFIG-based wind farm active and reactive powers during a line-to-line fault at F_1	131
Figure C.35: Relay (21) tripping signal, transient time responses of generator active and reactive powers, active and reactive power flows from Bus 1 to Bus M during a three-phase fault at F_1 (no wind farm in the system).	132
Figure C.36: Relay (21) measured impedance trajectory and its tripping signal, transient time responses of generator active and reactive powers, active and reactive power flows from Bus 1 to Bus M, DFIG-based wind farm active and reactive powers during a three-phase at F_1	133
Figure C.37: Relay (21) tripping signal, transient time responses of generator active and reactive powers, active and reactive power flows from Bus 1 to Bus M during a line-to-line fault at F_2 (no wind farm in the system).	134

Figure C.38: Relay (21) measured impedance trajectory and its tripping signal, transient time responses of generator active and reactive powers, active and reactive power flows from Bus 1 to Bus M, DFIG-based wind farm active and reactive powers during a line-to-line fault at F_2	135
Figure C.39: Relay (21) tripping signal, transient time responses of generator active and reactive powers, active and reactive power flows from Bus 1 to Bus M during a three-phase fault at F_2 (no wind farm in the system).	136
Figure C.40: Relay (21) measured impedance trajectory and its tripping signal, transient time responses of generator active and reactive powers, active and reactive power flows from Bus 1 to Bus M, DFIG-based wind farm active and reactive powers during a three-phase at F_2	137
Figure C.41: Relay (21) tripping signal, transient time responses of generator active and reactive powers, active and reactive power flows from Bus 1 to Bus M during a line-to-line fault at F_3 (no wind farm in the system).	138
Figure C.42: Relay (21) measured impedance trajectory and its tripping signal, transient time responses of generator active and reactive powers, active and reactive power flows from Bus 1 to Bus M, DFIG-based wind farm active and reactive powers during a line-to-line fault at F_3	139
Figure C.43: Relay (21) tripping signal, transient time responses of generator active and reactive powers, active and reactive power flows from Bus 1 to Bus M during a three-phase fault at F_3 (no wind farm in the system).	140
Figure C.44: Relay (21) measured impedance trajectory and its tripping signal, transient time responses of generator active and reactive powers, active and reactive power flows from Bus 1 to Bus M, DFIG-based wind farm active and reactive powers during a three-phase at F_3	141
Figure C.45: Relay (21) tripping signal, transient time responses of generator active and reactive powers, active and reactive power flows from Bus 1 to Bus M during a line-to-line fault at F_1 (no wind farm in the system).	142
Figure C.46: Relay (21) measured impedance trajectory and its tripping signal, transient time responses of generator active and reactive powers, active and reactive power flows from Bus 1 to Bus M, DFIG-based wind farm active and reactive powers during a line-to-line fault at F_1	143
Figure C.47: Relay (21) tripping signal, transient time responses of generator active and reactive powers, active and reactive power flows from Bus 1 to Bus M during a three-phase fault at F_1 (no wind farm in the system).	144
Figure C.48: Relay (21) measured impedance trajectory and its tripping signal, transient time responses of generator active and reactive powers, active and reactive power flows from Bus 1 to Bus M, DFIG-based wind farm active and reactive powers during a three-phase at F_1	145
Figure C.49: Relay (21) tripping signal, transient time responses of generator active and reactive powers, active and reactive power flows from Bus 1 to Bus M during a line-to-line fault at F_2 (no wind farm in the system).	146
Figure C.50: Relay (21) measured impedance trajectory and its tripping signal, transient time responses of generator active and reactive powers, active and reactive power flows from Bus 1 to Bus M, DFIG-based wind farm active and reactive powers during a line-to-line fault at F_2	147

Figure C.51: Relay (21) tripping signal, transient time responses of generator active and reactive powers, active and reactive power flows from Bus 1 to Bus M during a three-phase fault at F_2 (no wind farm in the system).	148
Figure C.52: Relay (21) measured impedance trajectory and its tripping signal, transient time responses of generator active and reactive powers, active and reactive power flows from Bus 1 to Bus M, DFIG-based wind farm active and reactive powers during a three-phase at F_2	149
Figure C.53: Relay (21) tripping signal, transient time responses of generator active and reactive powers, active and reactive power flows from Bus 1 to Bus M during a line-to-line fault at F_3 (no wind farm in the system).	150
Figure C.54: Relay (21) measured impedance trajectory and its tripping signal, transient time responses of generator active and reactive powers, active and reactive power flows from Bus 1 to Bus M, DFIG-based wind farm active and reactive powers during a line-to-line fault at F_3	151
Figure C.55: Relay (21) tripping signal, transient time responses of generator active and reactive powers, active and reactive power flows from Bus 1 to Bus M during a three-phase fault at F_3 (no wind farm in the system).	152
Figure C.56: Relay (21) measured impedance trajectory and its tripping signal, transient time responses of generator active and reactive powers, active and reactive power flows from Bus 1 to Bus M, DFIG-based wind farm active and reactive powers during a three-phase at F_3	153

LIST OF TABLES

Table 2.1: Wind Farm Composition.....	10
Table 3.1: Relay (21) settings based on the three criteria.	29
Table A.1: Synchronous generator data.	93
Table A.2: Transformer data.....	94
Table A.3: Wind farm parameters.....	94

LIST OF SYMBOLS

AC	Alternating Current
AVM	Average value model
BtB	Back to back
CT	Current transformer
d	Direct axis
DC	Direct current
DFIG	Double fed induction generator
e_d, e_q	d- and q- axis components of the stator voltage
E_f	Internal or rotor field excitation voltage
e_{fd}	Field voltage
G	Generator
GCC	Generator capability curve
GOEC	Generator steady-state overexcited capability limit
GSC	Grid side converter
HV	High-voltage
i_d, i_q	d- and q- axis components of the stator current
I_{Line1}, I_{Line2}	Line currents
L_{11d}	Self-inductance of the d-axis damper winding
L_{11q}, L_{22q}	Self-inductances of the q-axis damper winding
L_{ad}	d-axis magnetizing inductance
L_{aq}	q-axis magnetizing inductance
L_d, L_q	d- and q- axis components of the stator inductance
L_{ffd}	Self-inductance of the field winding

LV	Low-voltage
MTA	Relay (21) Maximum Torque Angle
MVA	Apparent power
MVAR	Reactive power
MW	Active power
P	Real power
$P_{bus1\ to\ M}$	Active power flows from Bus 1 to Bus M
P_{DFIG}	DFIG-based wind farm active power
$PEMI$	Percentage error in the measured impedance by Relay (21)
P_{gen}	Generator active power
PMSG	Permanent-magnet synchronous generator
PMW	Pulse-width modulated
Q	Reactive power
q	Quadrature axis
$Q_{bus1\ to\ M}$	Reactive power flows from Bus 1 to Bus M
Q_{DFIG}	DFIG-based wind farm reactive power
Q_{gen}	Generator reactive power
R_{1d}, R_{2d}	d-axis damper winding resistances
R_{1q}, R_{2q}	q-axis damper winding resistances
R ₂₁	Relay (21)
R_a	Armature resistance
R_c	Current transformation ratio
R_L	Resistance of the series capacitor compensated transmission line
RPF	Rated power factor

RPFA	Power factor angle
RSC	Rotor-Side Converter
R_v	Voltage transformation ratio
t	Time
T_{ELEC}	Electrical torque
T_{MECH}	Mechanical torque
V_b	Infinite-bus voltage
V_{bd}, V_{bq}	d- and q- axis components of infinite-bus voltage
V_C	Voltage across the capacitor of the series capacitor compensated transmission line
V_{Cd}, V_{Cq}	d- and q- axis components of voltage across the capacitor of the series capacitor compensated transmission line
V_L	Voltage across the inductance of the series capacitor compensated transmission line
V_{Ld}, V_{Lq}	d- and q- axis components of voltage across the inductance of the series capacitor compensated transmission line
V_R	Voltage across the resistance of the series capacitor compensated transmission line
V_{Rd}, V_{Rq}	d- and q- axis components of voltage across the resistance of the series capacitor compensated transmission line
VT	Voltage transformer
V_t	Generator terminal voltage
V_{td}, V_{tq}	d- and q- axis components of generator terminal voltage
WF	Wind farm
X_C	Series capacitor reactance

X_d	Generator direct-axis synchronous reactance
X_L	Inductive reactance of the series capacitor compensated transmission line
X_s	Generator stator reactance
Z_1	Zone 1
Z_2	Zone 2
Z_{21}	Relay (21) reach
Z_3	Zone 3
Z_{GCC}	Maximum setting of Relay (21) to keep the coordination with GOEC limit
Z_{max}	The maximum setting of Relay (21)
Z_N	Impedance measured by relay (21) without wind farm
Z_{sl}	Transmission line series impedance
Z_t	Transformer series impedance
Z_w	Impedance measured by relay (21) with wind farm
Ψ_{1d}	d-axis damper winding flux linkage
Ψ_{1q}, Ψ_{2q}	q-axis damper winding flux linkages
Ψ_d, Ψ_q	d- and q- axis components of the stator flux linkages
ω	Angular velocity
ω_0	Synchronous frequency (337 rad/sec)
θ_N	Angle of the impedance measured by relay (21) without wind farm
θ_w	Angle of the impedance measured by relay (21) with wind farm

1. INTRODUCTION

1.1 Wind Energy

Growth in energy demands in conjunction with the raising awareness of environmental impacts of traditional generation sources has resulted in increase of the integration of renewable energy resources with existing power systems. As a result, large scale wind farms are being adopted as green sources in transmission networks. With the rapid advancement in technology of power semiconductor switching devices, grid integration of large renewable energy sources is now achievable. As of the end of 2015, over 250,000 wind turbines are operating around the world, with a total capacity of 432,883 MW [1]. There are some large wind farms worldwide such as the 6000 MW Gansu wind farm in China, the 1500 MW Muppandal wind farm in India, and the 1320 MW Alta (Oak Creek-Mojave) wind farm in the United States [2].

1.2 Wind Turbines

Wind turbines generate electricity through an electrical generator driven by the power of wind [3]. Typical types of wind turbines are small scale (less than 10 kW output capacity), intermediate scale (10 to 250 kW output capacity) and large scale (250 kW and upper output capacity) [4]. As the increased amount of renewable energy sources and distributed generators employed into existing power systems, large scale wind power still lies in the future for many countries because if there are large amounts of intermittent energy sources in the system, new capacity with lower investment costs, such as wind power, will be favored [5].

For wind turbine application, there are basically two types of generators in use: fixed speed wind generator and variable speed wind generator [6]. Due to limitations like poor power quality and low efficiency, the further application of fixed speed induction generators is limited. Meanwhile, variable speed wind generators allows operating wind turbine at optimum tip speed ratio and, therefore, optimum power efficiency for wide range of wind speed [7]. As a result, variable speed wind generators are widely used nowadays. Most of the major wind turbine manufacturers are developing new megawatt scale wind turbines based on variable-speed operation with pitch control using either a permanent magnet synchronous generator (PMSG) or a doubly fed induction generator (DFIG) [8]. Furthermore, different kinds of power electronics devices might be attached to variable speed wind generators due to different control strategies.

1.2.1 Doubly-fed induction generator wind turbine

A typical structure of a doubly-fed induction generator (DFIG) wind turbine is shown in Figure 1.1 [9]. The stator of the induction machine is directly connected to the grid while the wound rotor windings are connected to the grid through both slip rings and indirect AC/DC-DC/AC converter system which controls the rotor as well as the grid currents.

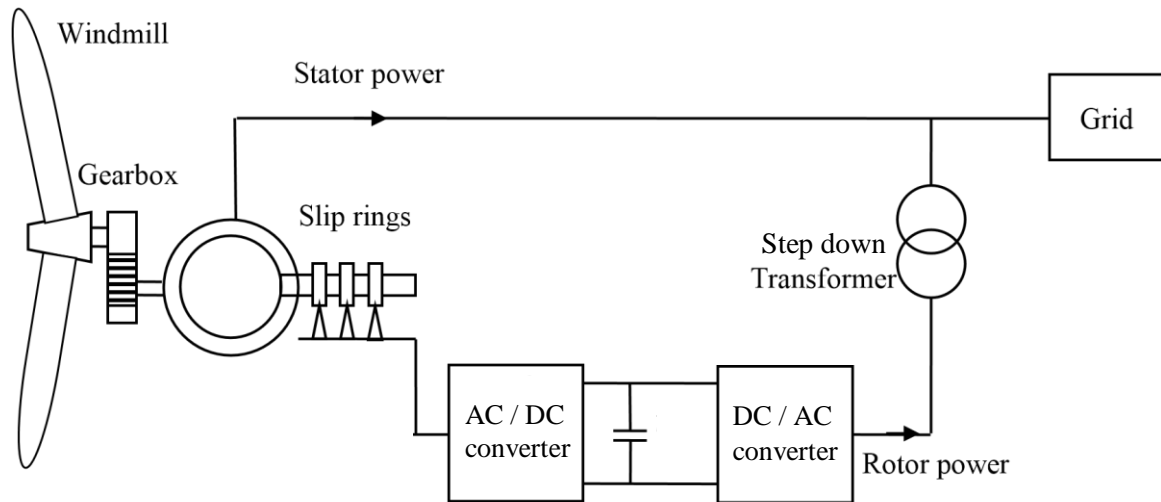


Figure 1.1: Typical structure of a DFIG wind turbine.

Depending on the rotational speed of its generator, a DFIG system can either deliver power through the stator and rotor to the grid or absorb power from the grid through the rotor. When operating above synchronous speed, power from the rotor travel through the converters and flows into the grid. And when operating below synchronous speed, power from the grid flows into the rotor through the converters [3].

Nowadays, the existence of wind farms in the power grid is posing new challenges to the power system protection systems. Examples of these protection systems are transmission line protection, bus bar protection, and generator protection [11]. This research focuses mainly on the generator distance phase backup protection.

1.3 Generator Distance Phase Backup Protection

Backup protection is defined as “protection that operates independently of specified components in the primary protective system” [10]. It may duplicate the primary protection, or may be intended to operate only if the primary protection fails or is temporarily out of service.

Typically there are two types of backup protection that might be chosen for a generator: backup of relays protecting the generator protection zone and backup of relays protecting external zones. Two types of relays are commonly used: a distance type of Relay (21) or a voltage restrained/voltage-controlled time-overcurrent Relay (51V). In such an application, the choice of the relay type is usually a function of the type of relaying used on the lines connected to the generator. In order to simplify zones coordination, the distance backup relay is used where distance relaying is used for line protection, while the overcurrent type of backup relay is used where overcurrent relaying is used for line protection [10].

1.3.1 Distance Relay Characteristics

Distance relay is a generic term covering those forms of protective relays in which the response to the input quantities is primarily a function of the electrical circuit distance between the relay location and the fault point. The distance relay operates on the principle of comparing the voltage and current to obtain a measure of the ratio between these quantities. The relationship between the observed voltage and current is measured to determine if the total impedance seen by the relay corresponds to a trip region of the complex R-X plane. The interaction between the measured voltage and current are displayed in the R-X plane as a circle that either goes through the origin or is offset from passing through the origin by a prescribed amount. The measured quantities literally compute the impedance seen from the relay to the fault, which constitutes a distance measurement [11].

Distance relay (21) (Relay (21)) is designed to adjust a maximum impedance seeing in order to form a threshold for tripping. These relay thresholds are often plotted in Z plane such as Figure 1.2 [12], as an example of a relay with three zones of protection, illustrating a circular characteristic passing through the origin, commonly known as a “mho” characteristic. Relay measurements that fall close to the origin and inside the specified threshold setting are identified as faults for which the relay should operate and vice versa. Normally, time delays are set to Relay (21) output tripping signals if the fault is determined in zone 2 or 3. This ensures the distance relay to act as backup protection for adjacent lines as well as allows primary line protective devices operate first. Protective zones of distance relays are usually divided into three as shown in Figure 1.2: zone 1 (Z_1) protects 85% of the line while zone 2 (Z_2) covers 150% of the line, and zone 3 (Z_3) covers 225% [13].

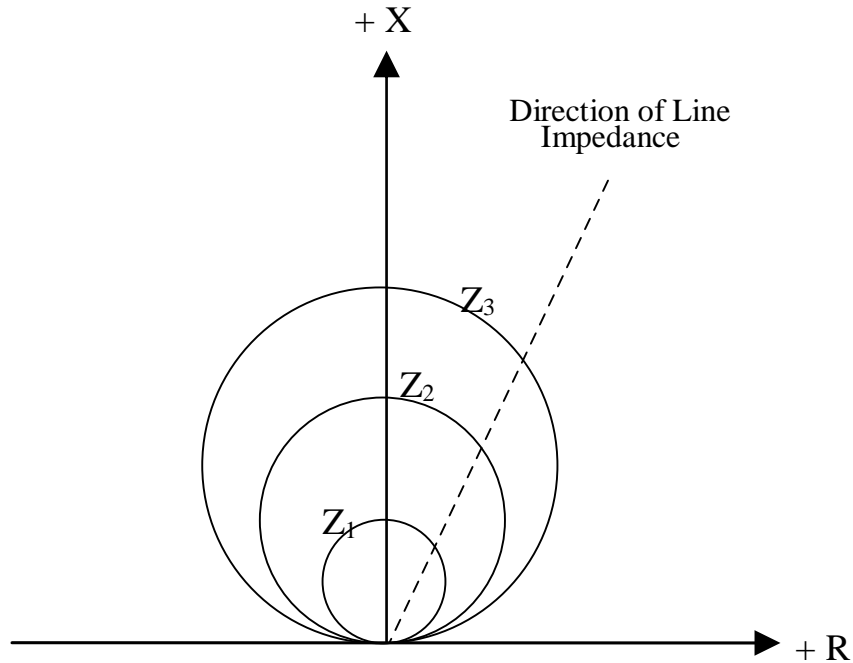


Figure 1.2: Distance protection zones in the Z plane.

One zone of Relay (21) with a mho characteristic, as shown in Figure 1.3, is commonly used for system distance phase backup protection. The origin of the plot in Figure 1.3 is defined by the location of the voltage transformer (VT). The angle between the R-axis and the line drawn through the center of the characteristic circle and the origin is the maximum torque angle (MTA) of the relay. The relay reach is the length of the vector drawn from the origin with an angle equal to the MTA to the circumference of the circle (OL, Figure 1.3). Furthermore, for Relay (21), both of the relay reach and the MTA are settable parameters [12].

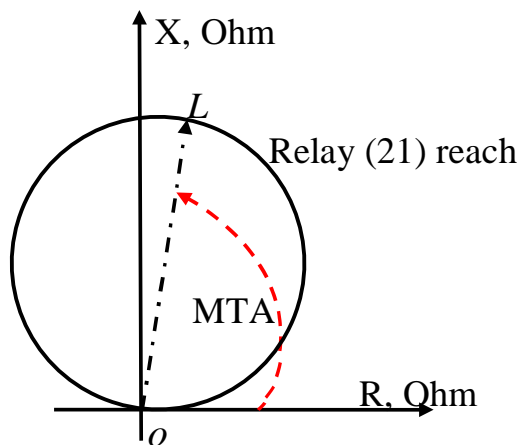


Figure 1.3: A mho distance relay characteristic.

1.3.2 Distance Relay Operation

The application of Relay (21) as generator distance phase backup protection is shown in Figure 1.4. When a fault is detected inside Relay (21) protective zone reach, Relay (21) would operate, outputting a tripping signal to isolate the generator from the fault. This protects the generator from any fault that failed to be cleared by other primary line protection elements such as circuit breakers.

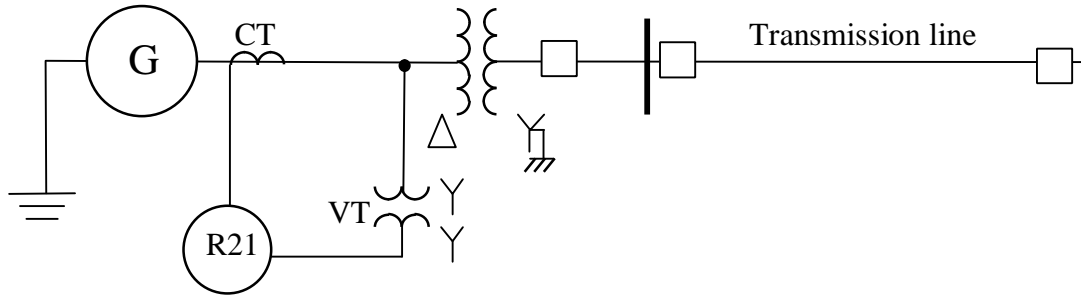


Figure 1.4: Relay (21) employed as generator distance backup protection.

1.4 Generator Capability Curve

A generator capability curve (GCC) is a plot of apparent power capability (MVA) at generator rated voltage using active and reactive power (MW and MVAR) as the two principle axis. A capability curve separates the region of safe operation (inside the curve) from the region of unsafe operation (outside the curve) [14]. The construction of a capability curve for the lagging region follows the guide provided in IEEE Std 67 [15]. The loading on generator should not exceed the generator rating as it may lead to overheating of stator. Generator operation should be away from steady state stability limit and generator field current should not exceed its limiting value as it may cause rotor heating. All these limitations provides performance curves which are important in practical applications [16].

The capability curve of a turbogenerator (cylindrical rotor synchronous machine), as shown in Figure 1.5, is a composite of three distinct limits (A-B, B-D and D-E). The upper boundary of the curve (A-B) is the rotor field thermal limit specified at a dc current rating. Given that the synchronous generator terminal voltage is one per unit, this boundary is often approximated by an arc with a center at a value equal to $1/X_s$ in per unit on the negative y axis (the MVAR axis) and a radius of E_f/X_d where E_f is the internal or rotor field excitation voltage. The right hand boundary (B-D) is the synchronous generator stator current limit. The center of the arc defining this limit is

the origin while the radius is one per unit. The lower boundary (D-E) is the end iron heating limit (heating in the end laminations of the stator core) which occurs during leading power factor, underexcited operating conditions. The boundary (A-C) represents the generator steady-state overexcited capability (GOEC) limit [12].

1.5 Coordination between Relay (21) and GOEC

Relay (21) has to operate within the GOEC limit with an adequate range for overload and stable power swings. Hence, it is necessary to coordinate the GOEC limit with Relay (21) characteristic so that both curves can be shown in one plot and taken into consideration when setting Relay (21). In order to coordinate the two curves, GOEC limit should be converted to an R-X plot. Figure 1.6 illustrates this conversion where the Relay (21) current transformer and the voltage transformer ratios (R_c/R_v) convert the primary ohms to the secondary side quantities that are set within the relay while the kV is the rated voltage of the generator and the MVA is the rated power of the generator [18], [19].

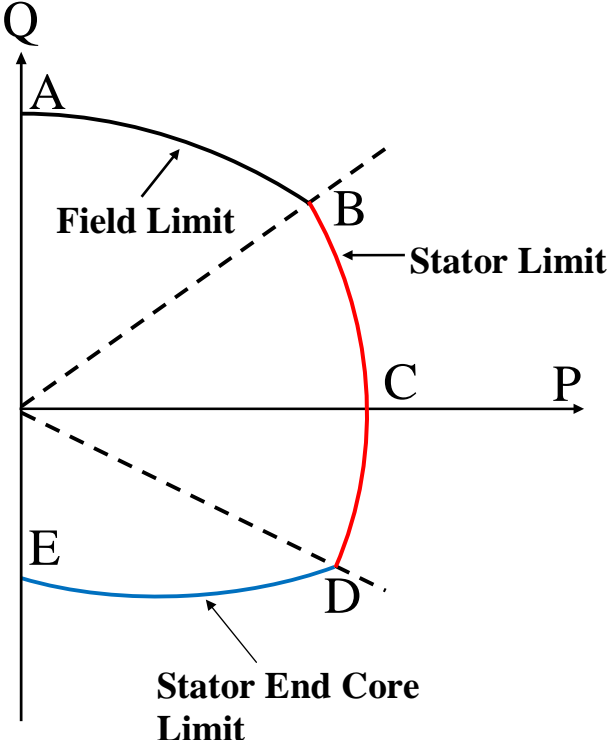


Figure 1.5: Generator capability curves for turbogenerators.

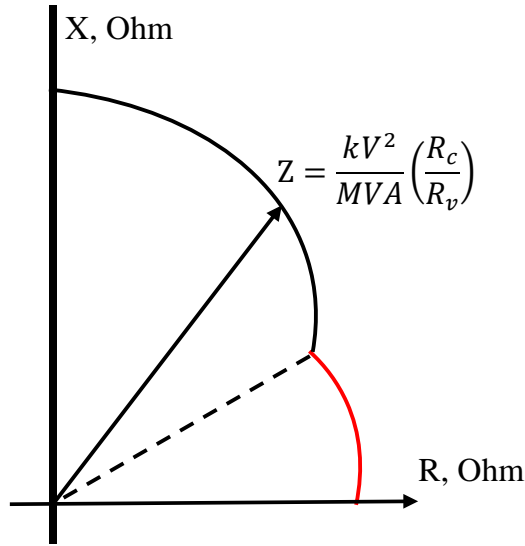


Figure 1.6: Transformation of a P-Q plot to an R-X plot.

1.6 Research Objective and Scope of the Thesis

An intensive effort to increase the participation of renewable sources in the fuel and energy balance has resulted in the growth of wind farms connected to the power system at both the distribution network (up to 66 kV) and the high-voltage (HV) transmission network (above 138 kV) [20]. Wind speed varies continuously throughout the day resulting in fluctuating wind farm output power. Because of the unpredictable variation of the wind speed, the transmitted power and relay side voltage and current (with respect to grid voltage and current) vary accordingly. Such variation of voltage and current due to the incorporation of wind energy into power system is posing new challenges to power system protections, such as generator distance phase backup protections, in which impedance criterion is used for operation decision making.

The impact of wind farms on transmission line protection has been recently investigated. Adaptive protection schemes for power systems with wind farms are proposed to mitigate the effect of the variations of the wind-farm power output on the relay reach setting [21]-[24]. The effect of DFIG-based wind farms on the low-voltage ride through on transmission line distance relay performance is studied in [25]. The results of these studies reveal that the reactive power absorbed by the DFIGs leads to protection miss-coordination of the distance relays [26]-[28].

Until now, no research has been reported on the impact of large wind farms on generator distance phase backup protection. The main objective of this research work is to investigate the impact of large DFIG-based wind farms tapped to the transmission system on the performance of

the generator phase backup protection (distance relay (21)). This is achieved through incorporating a large DFIG-based wind farm into a typical power system and examining Relay (21) performance during line-to-line and three-phase faults at different fault locations for different generator loadings, transmission line power flows, wind farm location and wind farm rating.

This thesis is organized into four chapters, a list of references section and three appendices. Chapter 1 introduces the fundamentals of wind energy, DFIG-based wind farm. Brief introductions to generator distance phase backup protection and generator capability curve are also presented as well as this objective of research.

In Chapter 2, the system under investigations conducted in this thesis is introduced along with the detailed dynamic models of its individual components. Besides, a sample case of study is presented at the end of this chapter.

Chapter 3 demonstrates the impact of DFIG-based wind farm on Relay (21). The effect of multiple DFIG-wind farms is also investigated.

Chapter 4 summarizes the research described in this thesis and presents some conclusions.

The data of the systems under investigations are given in Appendix A.

Relay setting calculations are presented in Appendix B.

Results for the case studies that are not reported in Chapters 3 are given in Appendix C.

2. POWER SYSTEM MODELING FOR LARGE DISTURBANCE STUDIES

2.1 General

In this chapter, the system used for the studies reported in this thesis is described and the mathematical models of its various components are presented. Digital time-domain simulations of a case study of the system during three-phase and line-to-line faults are presented at the end of this chapter.

2.2 System under Study

The system used in the investigations of this thesis is shown in Figure 2.1. It consists of a 700 MVA thermal generating station connected via a transformer to two large systems (S_1 and S_2) through two 500 kV transmission lines designated as L_1 and L_2 . A DFIG-based wind farm is tapped to L_1 at bus M. The composition, rating, operating wind speed and power output of the wind farm are given in Table 2.1 and the system data are given in Appendix A. Faults are assumed to occur on L_1 at F_1 , F_2 and F_3 at distances 100 km, 200 km and 300 km respectively from Bus M. Dynamic simulation studies on this test system are conducted using the EMTP/RV.

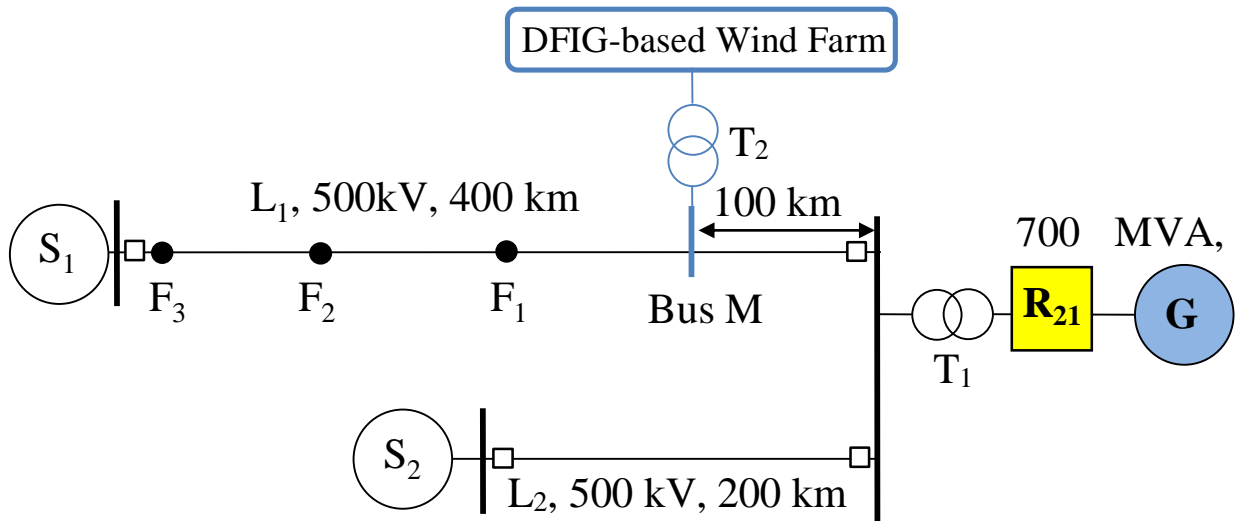


Figure 2.1: System under study.

Table 2.1: Wind Farm Composition.

Wind farm	Rating, operating speed and output power
DFIG	Aggregated model of 400×1.5 MW wind turbines, wind speed = 11.24 m/s, power ≈ 583 MW.

2.3 Power System Modeling

The nonlinear differential equations of the system under study are derived by developing individually the mathematical models which represent the various components of the system, namely the synchronous generator, the DFIG-based wind farm, the excitation system, the transmission line and the two large systems. Knowing the mutual interaction among these models, the whole system differential equations can be formed.

2.3.1 Modeling of the synchronous machine

In a conventional synchronous machine, the stator circuit consisting of a three-phase winding produces a sinusoidally space distributed magnetomotive force. The rotor of the machine carries the field (excitation) winding which is excited by a dc voltage. The electrical damping due to the eddy currents in the solid rotor and, if present, the damper winding is represented by three equivalent damper circuits; one on the direct axis (d-axis) and the other two on the quadrature axis (q-axis). The performance of the synchronous machine can be described by the equations given below in the d-q reference frame [29]. In these equations, the convention adopted for the signs of the voltages and currents are that v is the impressed voltage at the terminals and that the direction of positive current i corresponds to generation. The sign of the currents in the equivalent damper windings is taken positive when they flow in a direction similar to that of the positive field current as shown in Figure 2.2.

With time t expressed in seconds, the angular velocity ω expressed in rad/s ($\omega_0 = 377 \text{ rad/sec}$) and the other quantities expressed in per unit, the stator equations become:

$$e_d = \frac{1}{\omega_0} \frac{d\Psi_d}{dt} - \frac{\omega}{\omega_0} \Psi_q - R_a i_d \quad (2.1)$$

$$e_q = \frac{1}{\omega_0} \frac{d\Psi_q}{dt} + \frac{\omega}{\omega_0} \Psi_d - R_a i_q \quad (2.2)$$

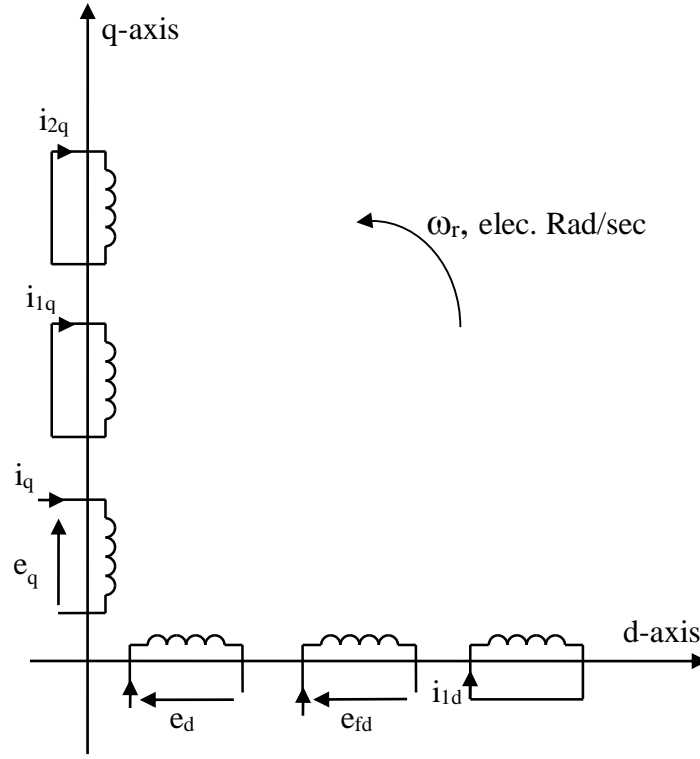


Figure 2.2: Modeling of the synchronous machine in the d-q reference frame.

The rotor equations:

$$e_{fd} = \frac{1}{\omega_0} \frac{d\Psi_{fd}}{dt} + R_{fd} i_{fd} \quad (2.3)$$

$$0 = \frac{1}{\omega_0} \frac{d\Psi_{1d}}{dt} + R_{1d} i_{1d} \quad (2.4)$$

$$0 = \frac{1}{\omega_0} \frac{d\Psi_{1q}}{dt} + R_{1q} i_{1q} \quad (2.5)$$

$$0 = \frac{1}{\omega_0} \frac{d\Psi_{2q}}{dt} + R_{2q} i_{2q} \quad (2.6)$$

The stator flux linkage equations:

$$\Psi_d = -L_d i_d + L_{ad} i_{fd} + L_{ad} i_{1d} \quad (2.7)$$

$$\Psi_q = -L_q i_q + L_{aq} i_{1q} + L_{aq} i_{2q} \quad (2.8)$$

The rotor flux linkage equations:

$$\Psi_{fd} = L_{ffd}i_{fd} + L_{ad}i_{1d} - L_{ad}i_d \quad (2.9)$$

$$\Psi_{1d} = L_{ad}i_{fd} + L_{11d}i_{1d} - L_{ad}i_d \quad (2.10)$$

$$\Psi_{1q} = L_{11q}i_{1q} + L_{aq}i_{2q} - L_{aq}i_q \quad (2.11)$$

$$\Psi_{2q} = L_{aq}i_{1q} + L_{22q}i_{2q} - L_{aq}i_q \quad (2.12)$$

The air-gap torque equation:

$$T_{ELEC} = \Psi_d i_q - \Psi_q i_d \quad (2.13)$$

The overall differential equations which describe the transient performance of the synchronous machine are given by the following matrix equation:

$$\left[\frac{dX_{syn}}{dt} \right] = [At_{syn}][X_{syn}] + [Bt_{syn}] \begin{bmatrix} V_{td} \\ V_{tq} \\ e_{fd} \end{bmatrix} \quad (2.14)$$

where

$$\begin{aligned} [X_{syn}] &= [i_d \quad i_q \quad i_{fd} \quad i_{1q} \quad i_{1d} \quad i_{2q}]^T \\ [At_{syn}] &= [L]^{-1}[Qt] \\ [Bt_{syn}] &= [L]^{-1}[Rt] \\ [L] &= \begin{bmatrix} -L_d & 0 & L_{ad} & 0 & L_{ad} & 0 \\ 0 & -L_q & 0 & L_{aq} & 0 & L_{aq} \\ -L_{ad} & 0 & L_{ffd} & 0 & L_{ad} & 0 \\ 0 & -L_{aq} & 0 & L_{11q} & 0 & L_{aq} \\ -L_{aq} & 0 & L_{ad} & 0 & L_{11d} & 0 \\ 0 & -L_{aq} & 0 & L_{aq} & 0 & L_{22q} \end{bmatrix} \end{aligned} \quad (2.15)$$

$$[Qt] = \begin{bmatrix} \omega_0 R_a & -\omega L_q & 0 & \omega L_{aq} & 0 & \omega L_{aq} \\ \omega L_d & \omega_0 R_a & -\omega L_{ad} & 0 & -\omega L_{ad} & 0 \\ 0 & 0 & -\omega_0 R_{fd} & 0 & 0 & 0 \\ 0 & 0 & 0 & -\omega_0 R_{1q} & 0 & 0 \\ 0 & 0 & 0 & 0 & -\omega_0 R_{1d} & 0 \\ 0 & 0 & 0 & 0 & 0 & -\omega_0 R_{2q} \end{bmatrix}$$

$$[Rt] = \begin{bmatrix} \omega_0 & 0 & 0 \\ 0 & \omega_0 & 0 \\ 0 & 0 & \omega_0 \\ 0 & 0 & 0 \\ 0 & 0 & 0 \\ 0 & 0 & 0 \end{bmatrix}$$

here, the superscript T means matrix transpose.

The synchronous machine swing equation can be written as:

$$\frac{2H}{\omega_o} \frac{d\omega}{dt} = T_{MECH} - T_{ELEC} \quad (2.16)$$

$$\frac{d\delta}{dt} = \omega - \omega_o \quad (2.17)$$

In the above two equations (2.16 and 2.17), ω is in radians per second, the inertia constant H is in seconds, and the load angle δ is in radians, ω_o is the synchronous frequency (377 rad/sec) and the mechanical and electrical torques T_{MECH} and T_{ELEC} are in per unit.

2.3.2 Modeling of the transmission line

A series capacitor-compensated transmission line may be represented by the RLC circuit shown in Figure 2.3 [30]. In the voltage phasor diagram shown in Figure 2.4, the rotor angle δ is the angle (in elec. rad) by which the q-axis leads the reference voltage V_b . The differential equations for the circuit elements, after applying Park's transformation [30], can be expressed in the d-q reference frame by the following matrix expressions.

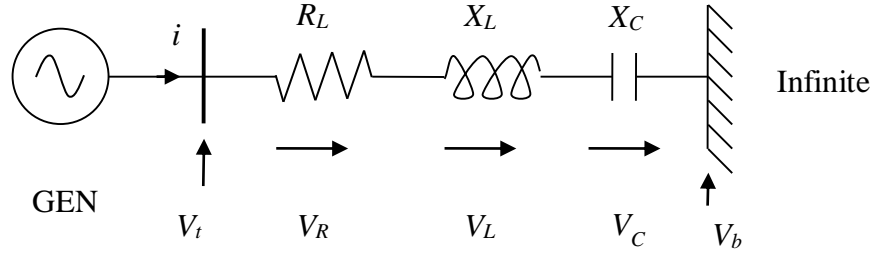


Figure 2.3: A series capacitor-compensated transmission line.

The voltage across the resistance:

$$\begin{bmatrix} V_{Rd} \\ V_{Rq} \end{bmatrix} = \begin{bmatrix} R_L & 0 \\ 0 & R_L \end{bmatrix} \begin{bmatrix} i_d \\ i_q \end{bmatrix} \quad (2.18)$$

The voltage across the inductance:

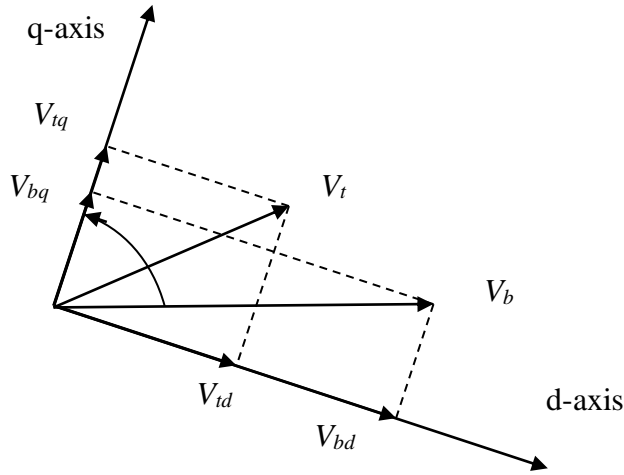


Figure 2.4: Voltage phasor diagram.

$$\begin{bmatrix} V_{Ld} \\ V_{Lq} \end{bmatrix} = \begin{bmatrix} 0 & -\frac{\omega}{\omega_0} X_L \\ \frac{\omega}{\omega_0} X_L & 0 \end{bmatrix} \begin{bmatrix} i_d \\ i_q \end{bmatrix} + \begin{bmatrix} \frac{X_L}{\omega_0} & 0 \\ 0 & \frac{X_L}{\omega_0} \end{bmatrix} \begin{bmatrix} \frac{di_d}{dt} \\ \frac{di_q}{dt} \end{bmatrix} \quad (2.19)$$

The voltage across the capacitor:

$$\begin{bmatrix} \frac{dV_{Cd}}{dt} \\ \frac{dV_{Cq}}{dt} \end{bmatrix} = \begin{bmatrix} \omega_0 X_C & 0 \\ 0 & \omega_0 X_C \end{bmatrix} \begin{bmatrix} i_d \\ i_q \end{bmatrix} + \begin{bmatrix} 0 & \omega \\ -\omega & 0 \end{bmatrix} \begin{bmatrix} V_{Cd} \\ V_{Cq} \end{bmatrix} \quad (2.20)$$

The overall equations of the transmission line can be written as

$$\begin{bmatrix} \frac{dV_{Cd}}{dt} \\ \frac{dV_{Cq}}{dt} \\ V_{id} \\ V_{iq} \end{bmatrix} = [Att] \begin{bmatrix} V_{Cd} \\ V_{Cq} \end{bmatrix} + [Rt1] \begin{bmatrix} \frac{di_d}{dt} \\ \frac{di_q}{dt} \end{bmatrix} + [Rt2] \begin{bmatrix} i_d \\ i_q \end{bmatrix} + [Btt][V_b] \quad (2.21)$$

where

$$\begin{aligned} [Att] &= \begin{bmatrix} 0 & \omega \\ -\omega & 0 \\ 1 & 0 \\ 0 & 1 \end{bmatrix} \\ [Rt1] &= \begin{bmatrix} 0 & 0 \\ 0 & 0 \\ \frac{X_L}{\omega_0} & 0 \\ 0 & \frac{X_L}{\omega_0} \end{bmatrix} \\ [Rt2] &= \begin{bmatrix} \omega_0 X_C & 0 \\ 0 & \omega_0 X_C \\ R_L & -\frac{\omega}{\omega_0} X_L \\ \frac{\omega}{\omega_0} X_L & R_L \end{bmatrix} \\ [Btt] &= \begin{bmatrix} 0 \\ 0 \\ \sin \delta \\ \cos \delta \end{bmatrix} \end{aligned} \quad (2.22)$$

It is worth noting here that if the transmission line is not series capacitive compensated, the capacitive reactance and the voltage across the capacitor are set to zero in Equations (2.20, 2.21 and 2.22).

2.3.3 Excitation system

The block diagram representation of the excitation system used in this study is shown in Figure 2.5, and the corresponding data are given in Appendix A [30].

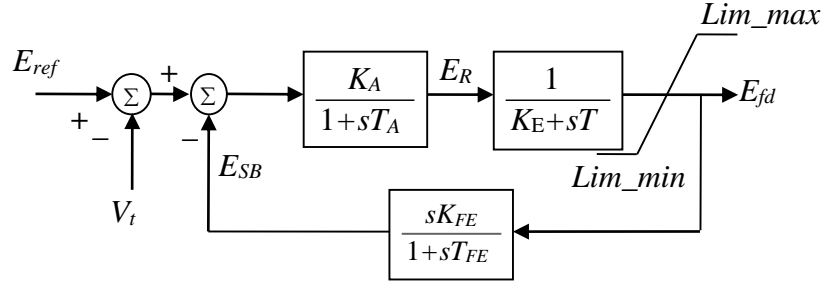


Figure 2.5: Block diagram of the excitation system.

Utilizing the relationship between the excitation system output voltage and the field voltage given by $E_{fd} = \frac{L_{ad}}{R_{fd}} e_{fd}$, the state-space equation of the excitation system can be derived from its block diagram and is given by

$$\left[\frac{dX_v}{dt} \right] = [At_v][X_v] + [Bt_v] \begin{bmatrix} V_t \\ E_{ref} \end{bmatrix} \quad (2.23)$$

where

$$[X_v] = [e_{fd} \quad E_R \quad E_{SB}]^T$$

$$[At_v] = \begin{bmatrix} -\frac{K_E}{T_E} & \frac{1}{T_E} \frac{R_{fd}}{L_{ad}} & 0 \\ 0 & -\frac{1}{T_A} & -\frac{K_A}{T_A} \\ -\frac{K_E K_F L_{ad}}{T_E T_F R_{fd}} & \frac{K_F}{T_F T_E} & -\frac{1}{T_F} \end{bmatrix} \quad (2.24)$$

$$[Bt_v] = \begin{bmatrix} 0 & 0 \\ -\frac{K_A}{T_A} & \frac{K_A}{T_A} \\ 0 & 0 \end{bmatrix}$$

2.3.4 Modeling of the transformer

The three-phase transformer is constructed by using three single-phase transformers connected in Delta (LV side)/Y grounded (HV side). The transformer leakage and magnetizing reactances as well as the winding resistances and core loss are represented in the model.

2.3.5 Modeling of the DFIG Wind Turbine

The basic configuration of a DFIG wind turbine is shown in Figure 2.6, where the stator of the induction machine is directly connected to the grid and the wound rotor is connected to the grid through a back-to-back (BtB) link. The BtB link consists of two, three-phase pulse-width modulated (PWM) VSCs (Rotor-Side Converter (RSC) and Grid-Side Converter (GSC)) coupled to a common dc bus. A line inductor and an ac filter are used at the GSC to improve power quality. A crowbar is used as a backup protection device. Details of DFIG wind turbines mathematical modeling and control are given in [31].

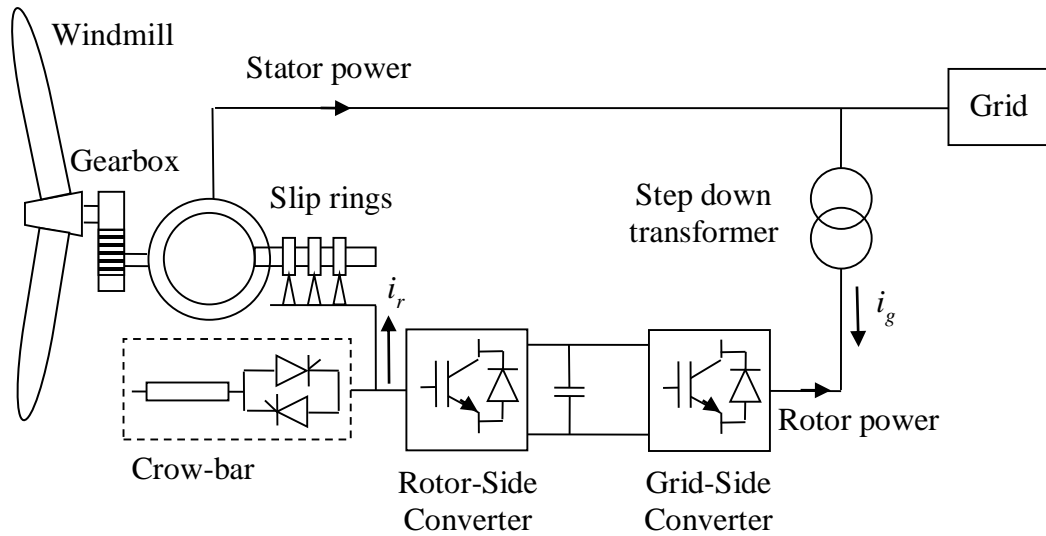


Figure 2.6: Schematic diagram of a DFIG wind turbine.

The aggregated model of 1.5 MW, 60 Hz DFIG wind turbines in [3] is used in this thesis. The model includes a pitch control to limit the maximum speed, a dc resistive chopper to limit the dc voltage and avoid the crowbar ignition during ac faults, a two-mass model to represent low frequency oscillations of the wind turbine drive system and over/under voltage protection. The DFIG converters are modeled with their average value models (AVMs) [32],[33].

2.3.6 Modeling of the two Large Systems

The two large systems, S_1 and S_2 are modeled by constant voltage source at the synchronous frequency behind a very small inductive reactance.

2.4 A Sample Case Study

In the studies conducted in this thesis, the ElectroMagnetic Transient Program (EMTP-RV) is used for modeling the various system components and producing the time-domain simulation results [34]. Due to the initialization process in the EMTP-RV, simulation results are displayed starting at time = 1.9 seconds. Moreover, faults are assumed to occur at $t = 2$ seconds.

Figure 2.7 shows the power flow results for the bus voltages and the line real power flows of the system under study. The transient time responses of the generator real power output and speed, the DFIG-based wind farm real power output, bus M voltage and the real power flows in the transmission lines during and after clearing three-cycle, three-phase and line-to-line faults at F_1 are shown respectively in Figures 2.8 and 2.9. Figures 2.10 and 2.11 show the same transient time responses for the cases of sustained three-phase and line-to-line faults at the same location. Such sustained faults are due to failures in the transmission line protection.

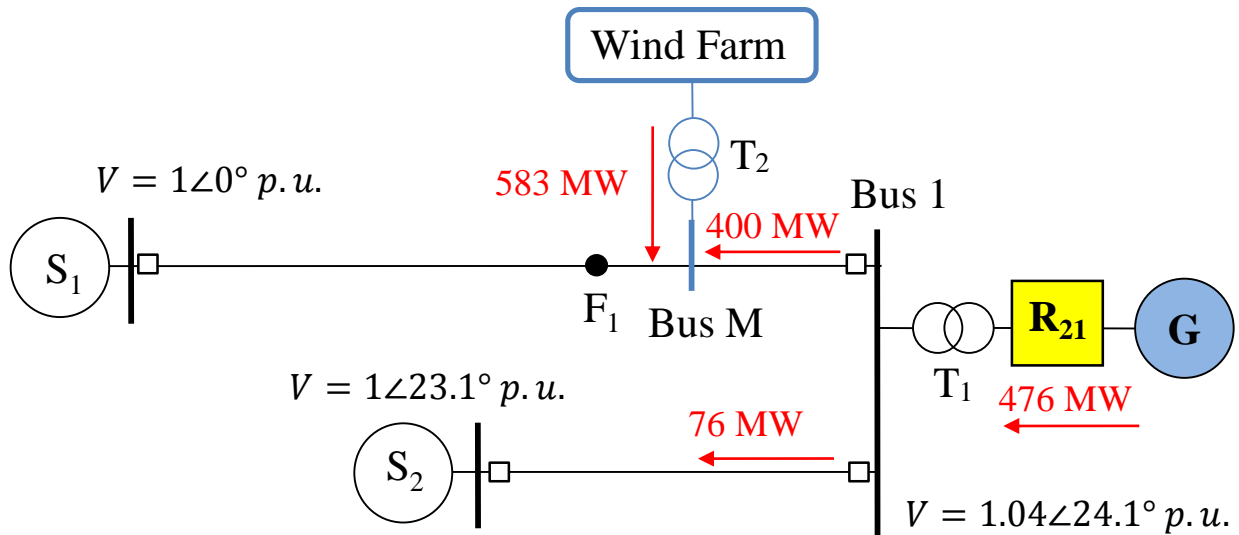


Figure 2.7: Load flow results of the bus voltages and real power flows of the system under study.

The following observations can be made from examining Figures 2.8 and 2.9 (successful fault clearings):

- The system is stable after fault clearing for both types of faults as the generator power and speed oscillate around their pre-fault steady-state values. The power flows on the transmission lines and the wind farm terminal voltage drop immediately at the instant of fault inception but recover after fault clearing.

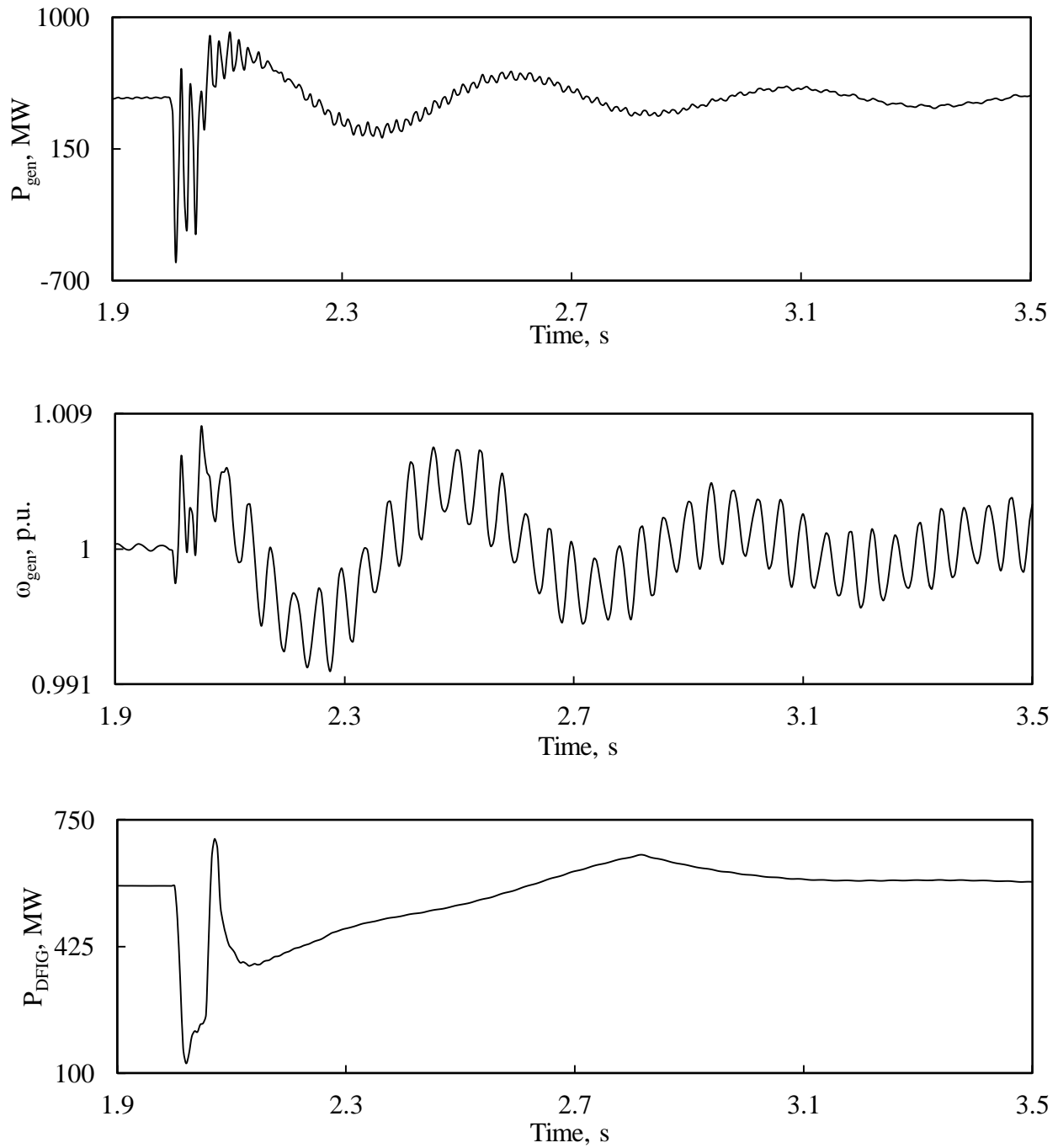


Figure 2.8: Transient time responses of generator real power output, generator speed, DFIG-based wind farm real power output, bus M voltage, real power flows in L_1 and L_2 during and after clearing a three-cycle three-phase fault at F_1 .

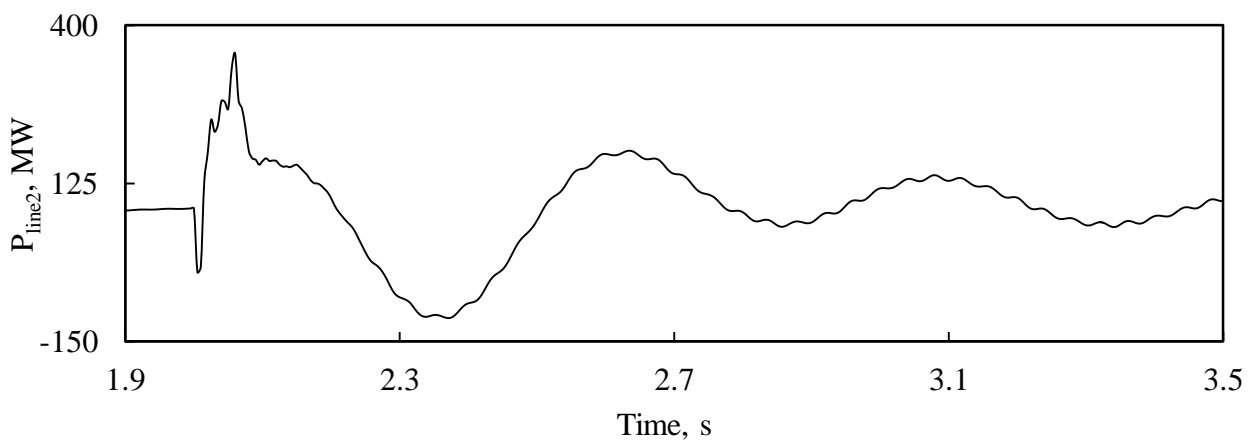
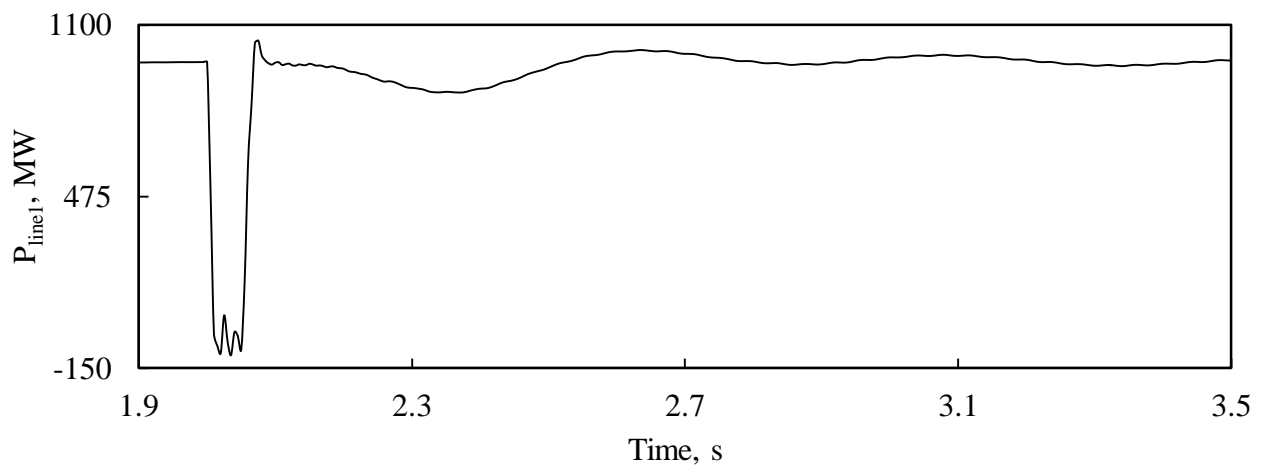
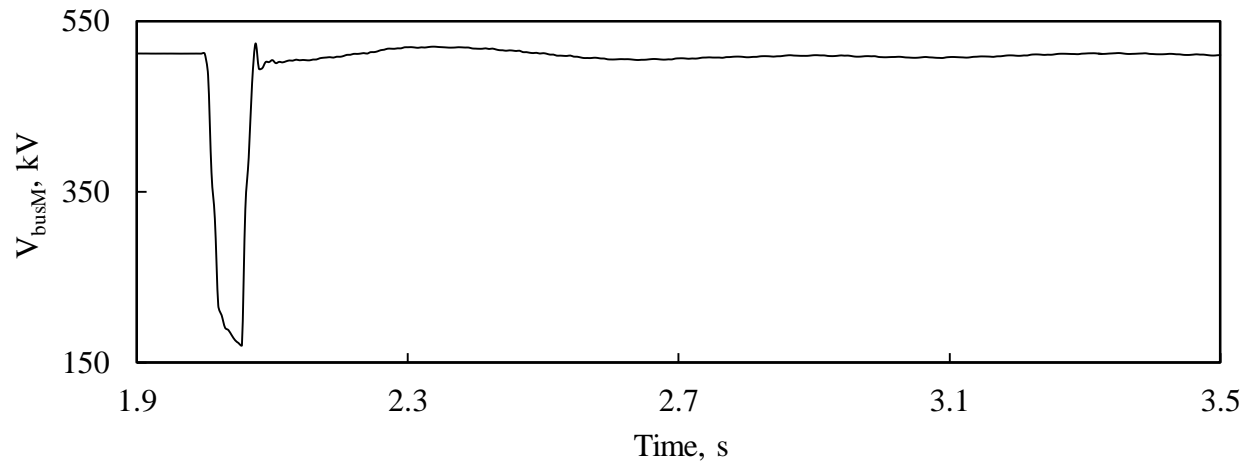


Figure 2.8: Continued.

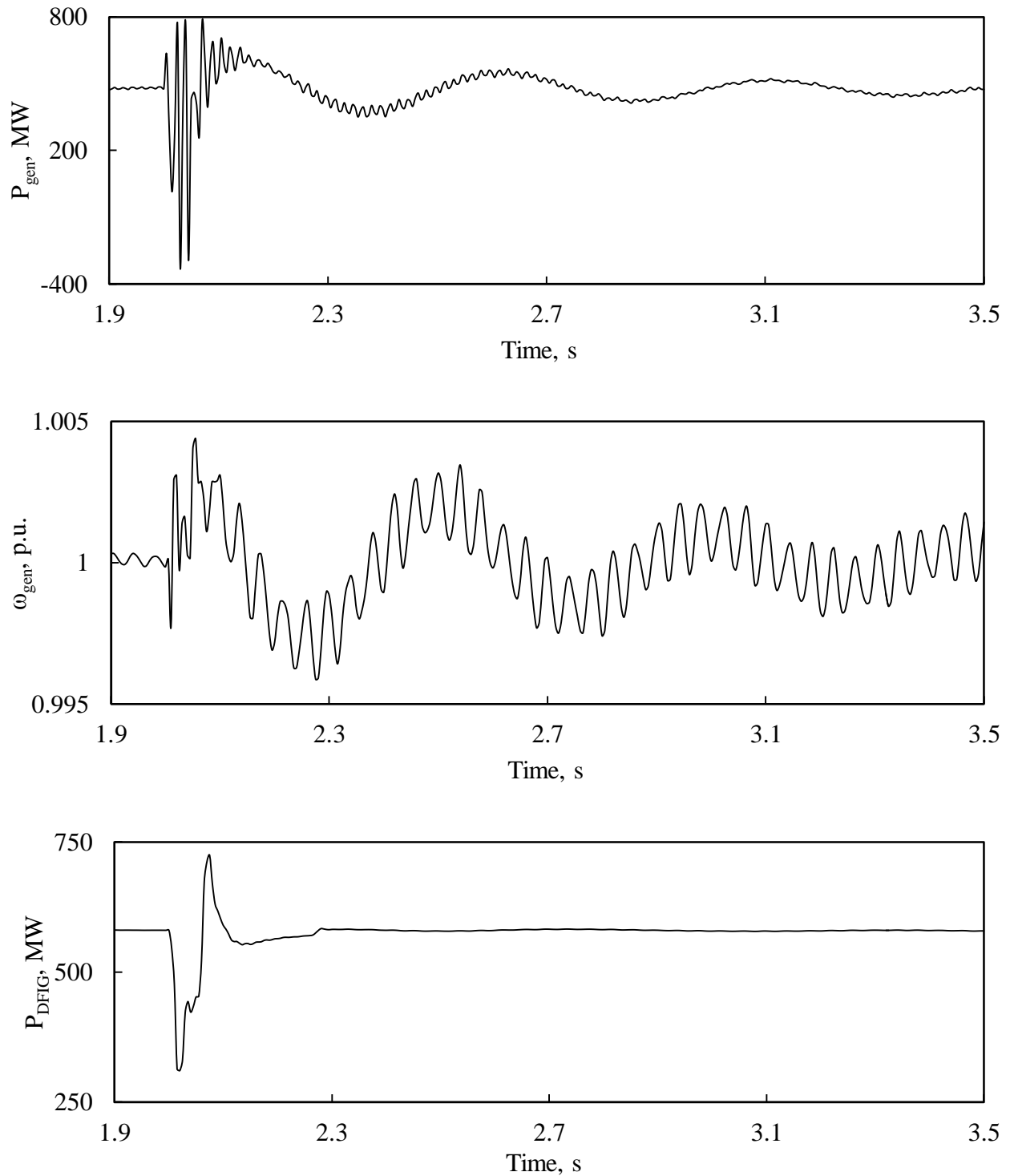


Figure 2.9: Transient time responses of generator real power output, generator speed, DFIG-based wind farm real power output, bus M voltage, real power flows in L_1 and L_2 during and after clearing a three-cycle line-to-line fault at F_1 .

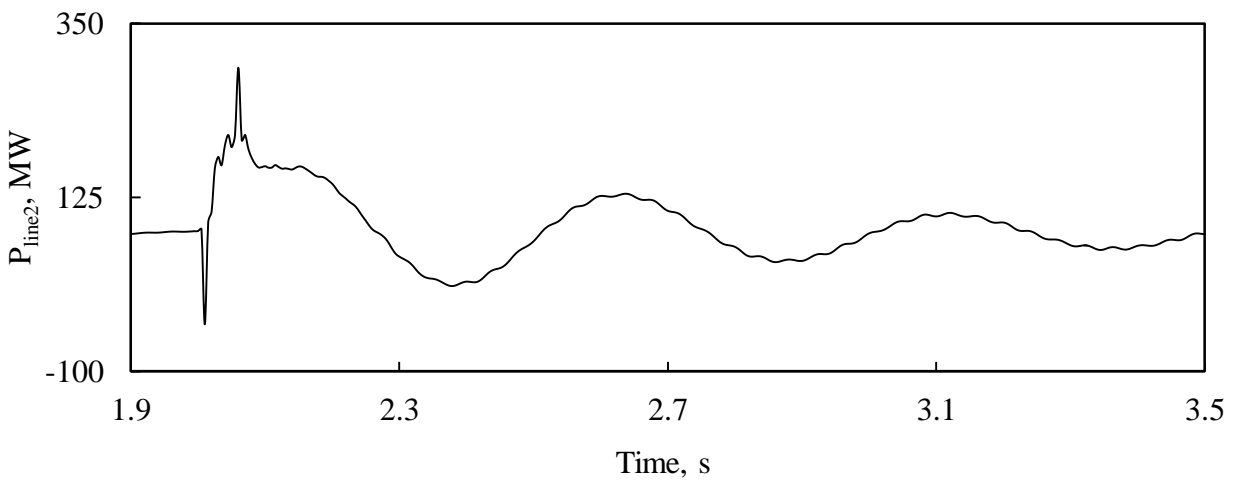
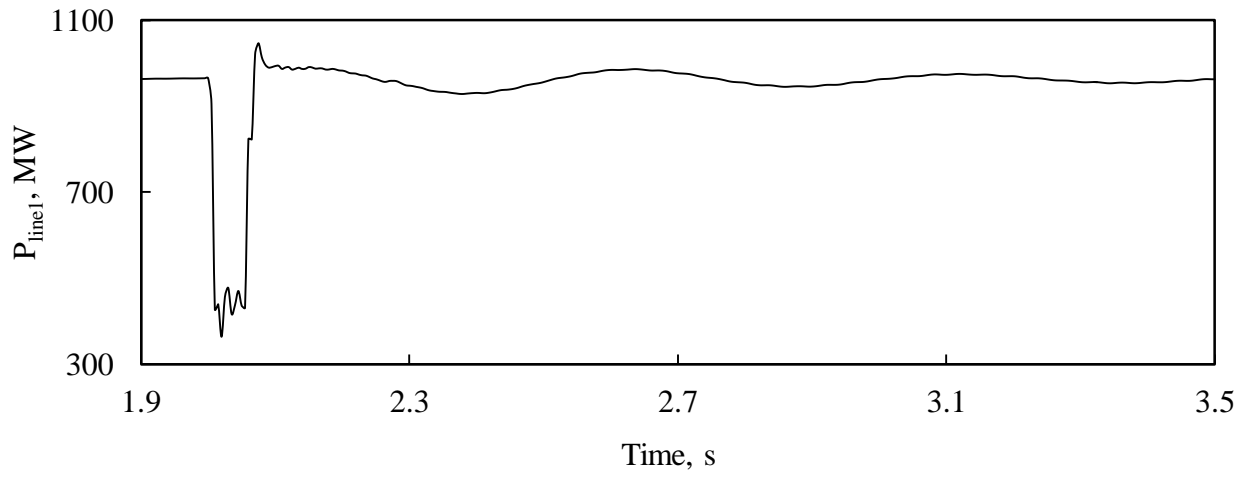
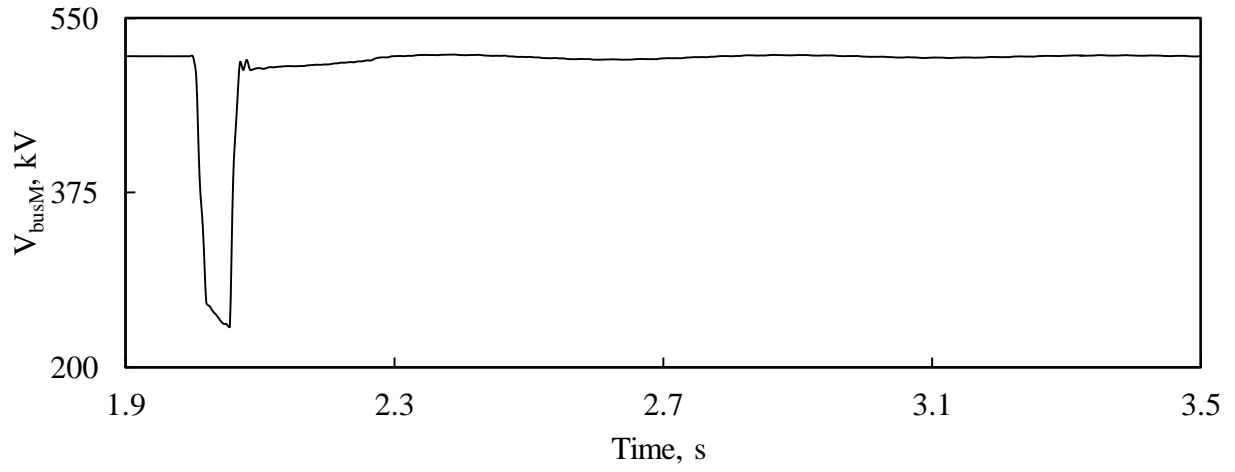


Figure 2.9: Continued.

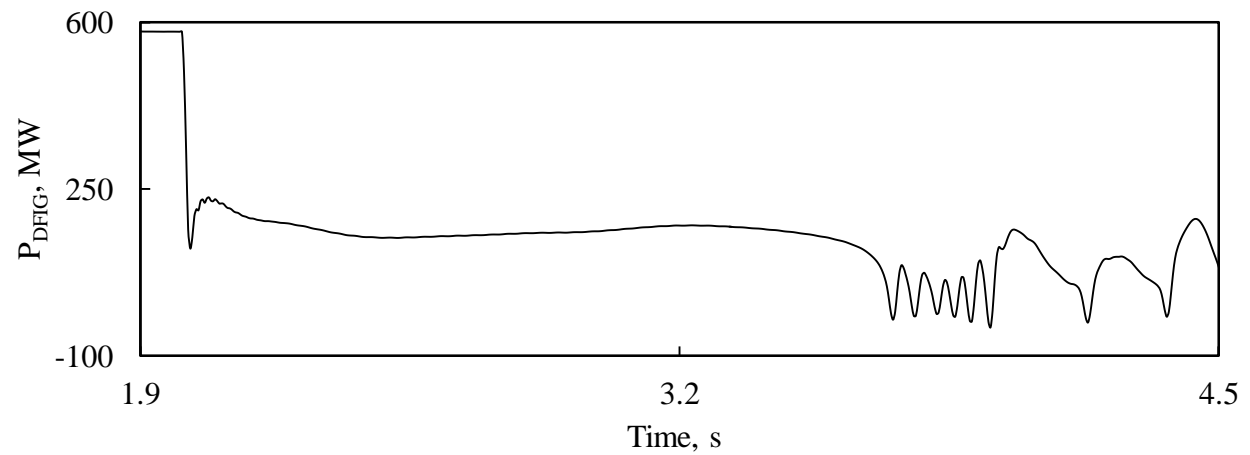
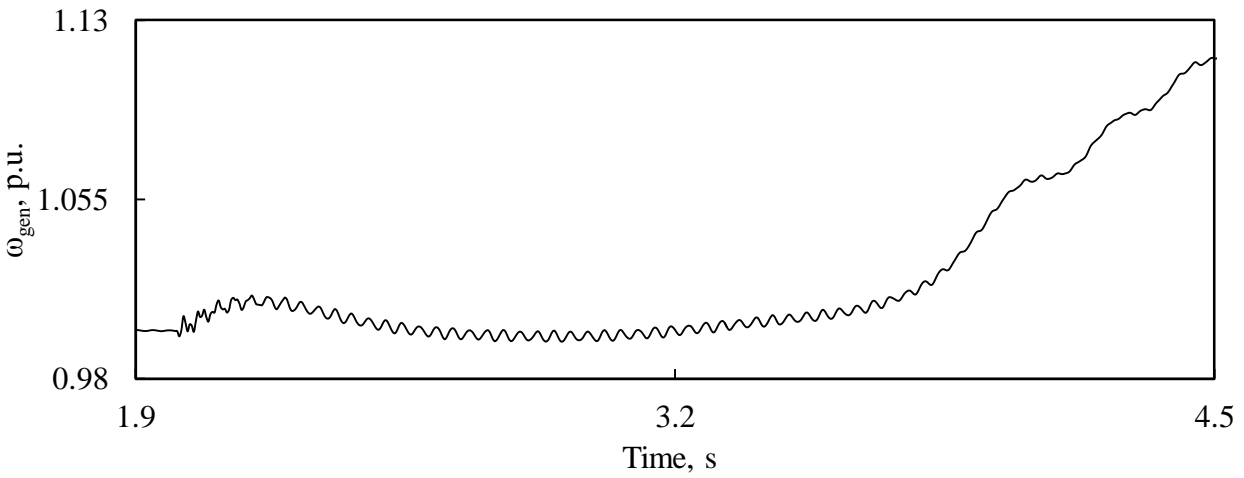
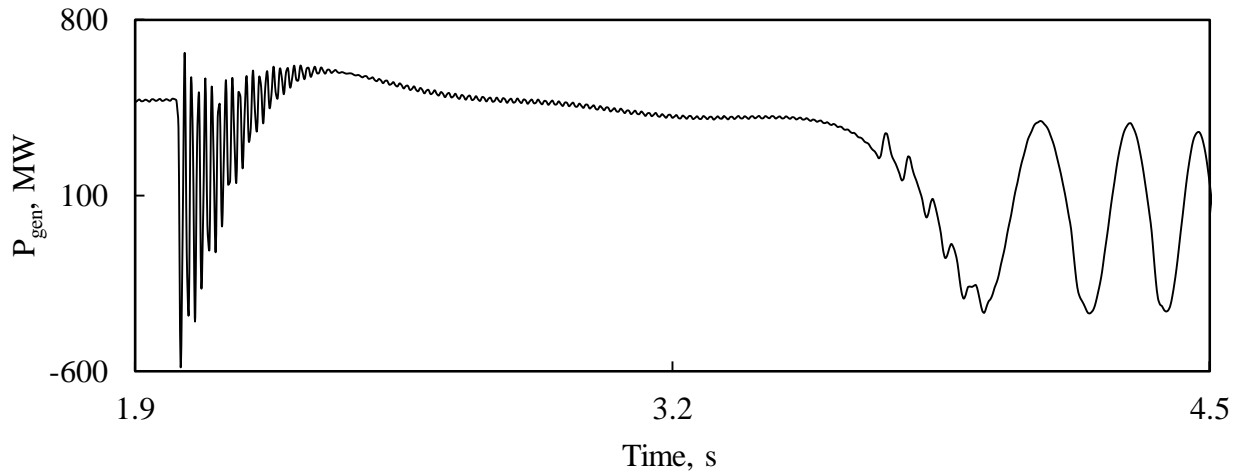


Figure 2.10: Transient time responses of generator real power output, generator speed, DFIG-based wind farm real power output, bus M voltage, real power flows in L_1 and L_2 during a sustained three-phase fault at F_1 .

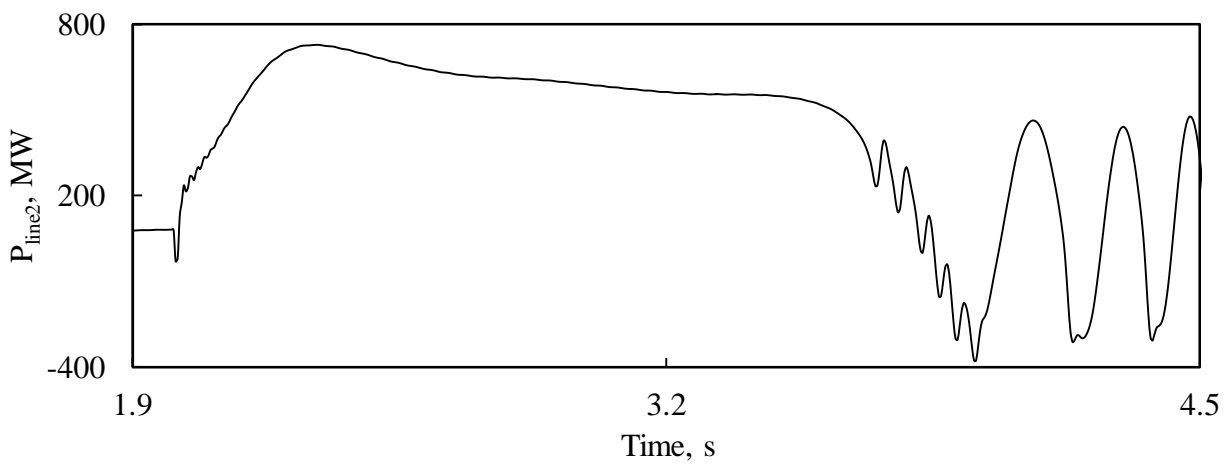
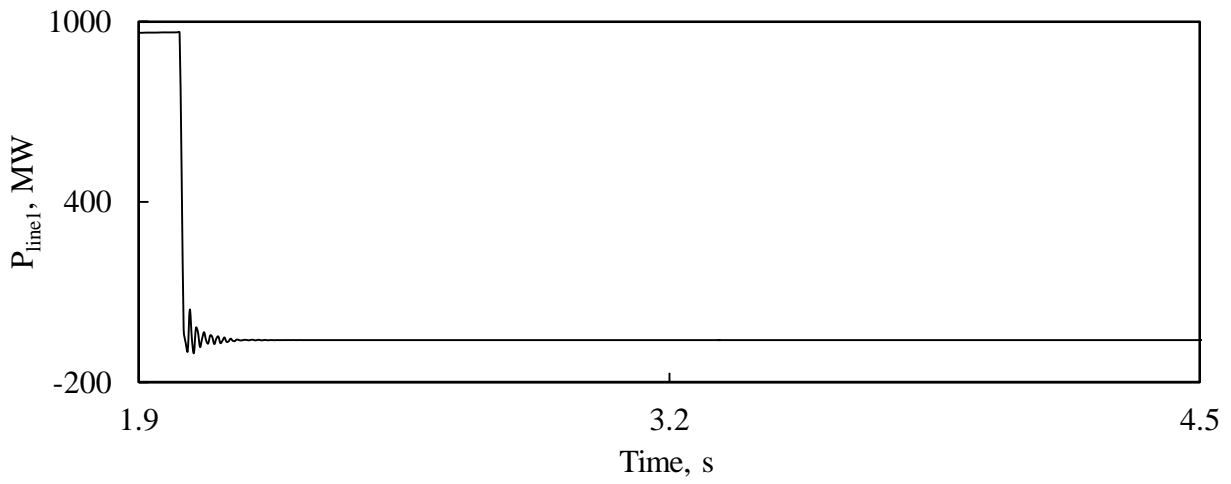
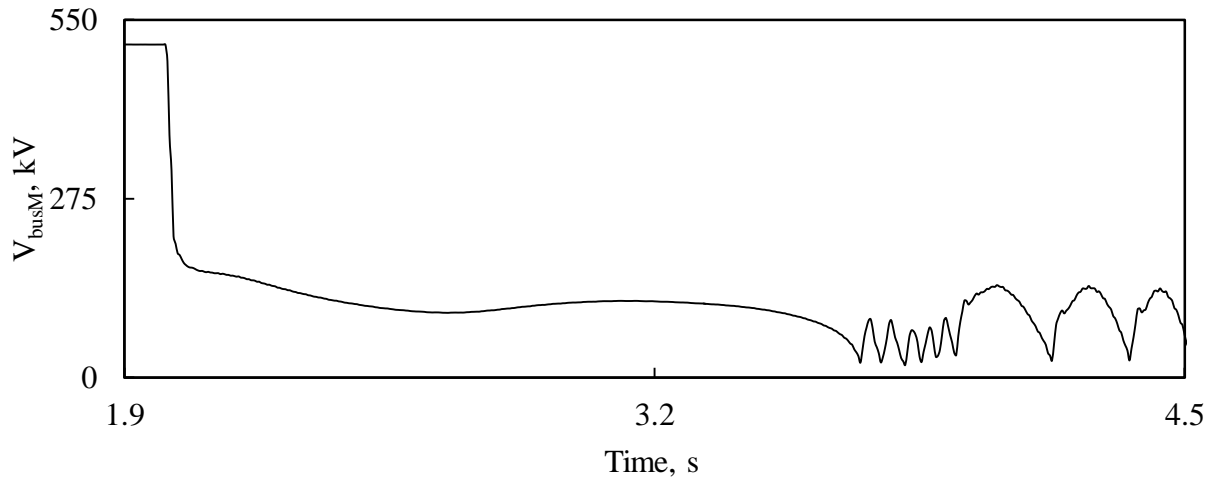


Figure 2.10: Continued.

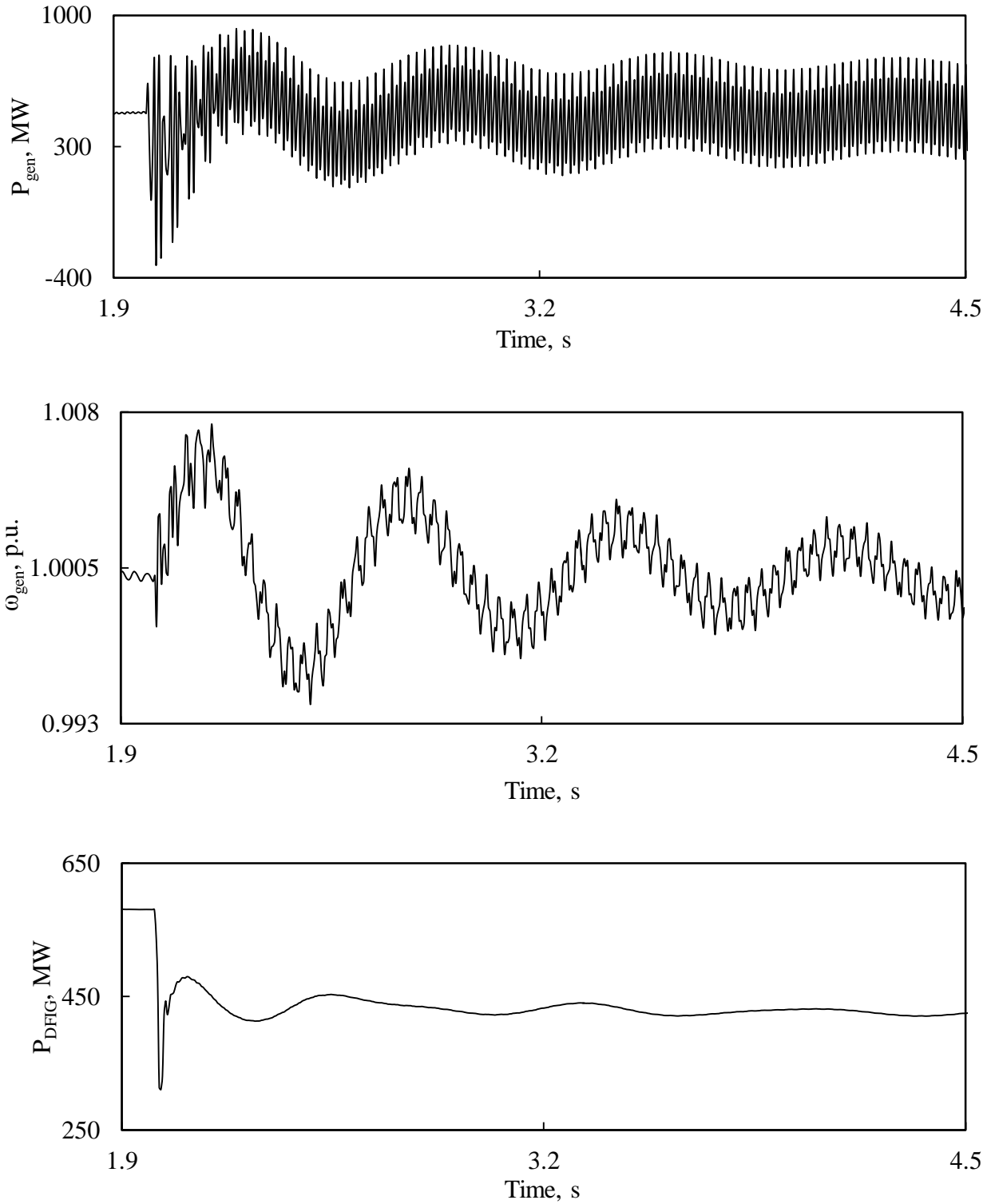


Figure 2.11: Transient time responses of generator real power output, generator speed, DFIG-based wind farm real power output, bus M voltage, real power flows in L_1 and L_2 during a sustained line-to-line fault at F_1 .

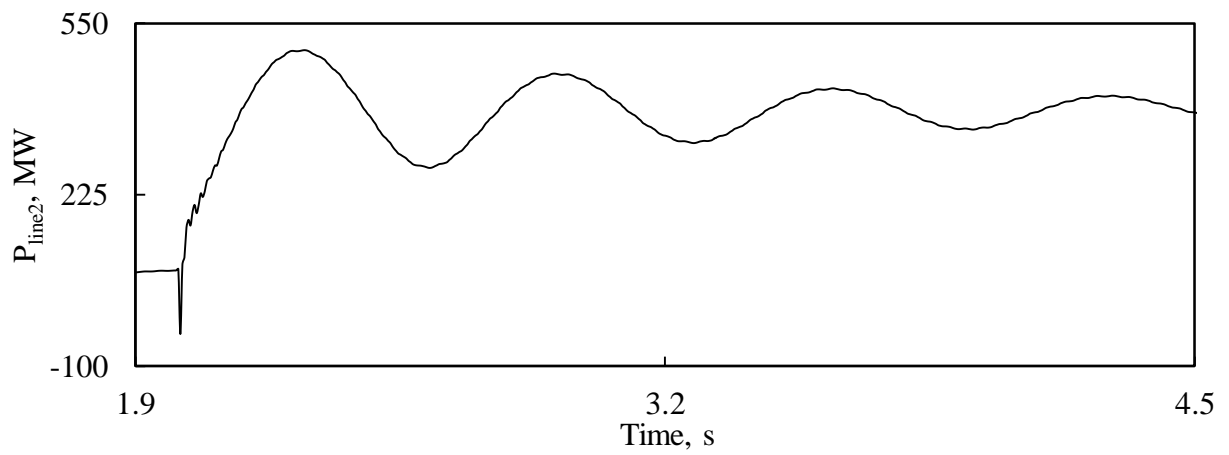
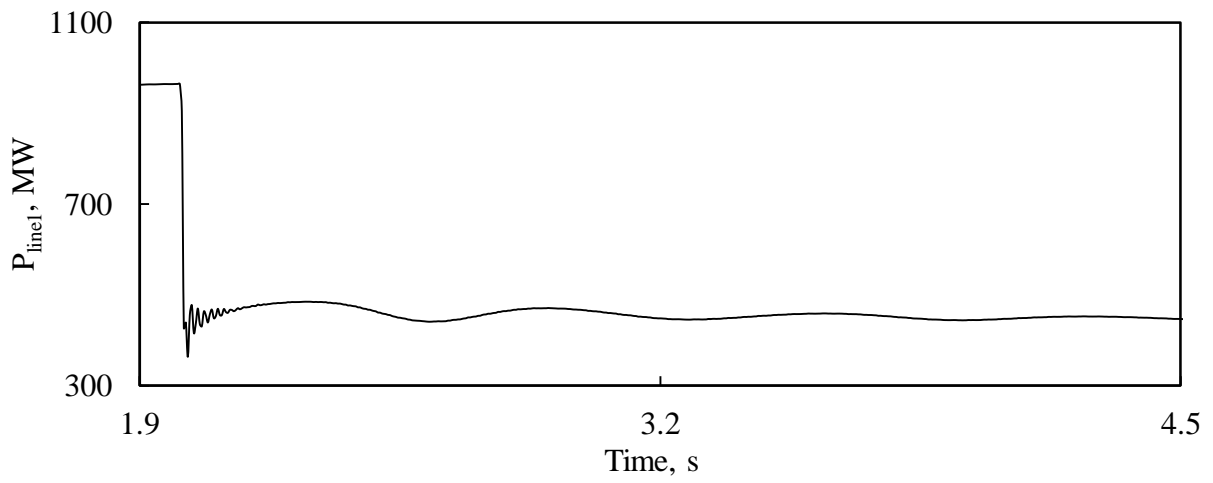
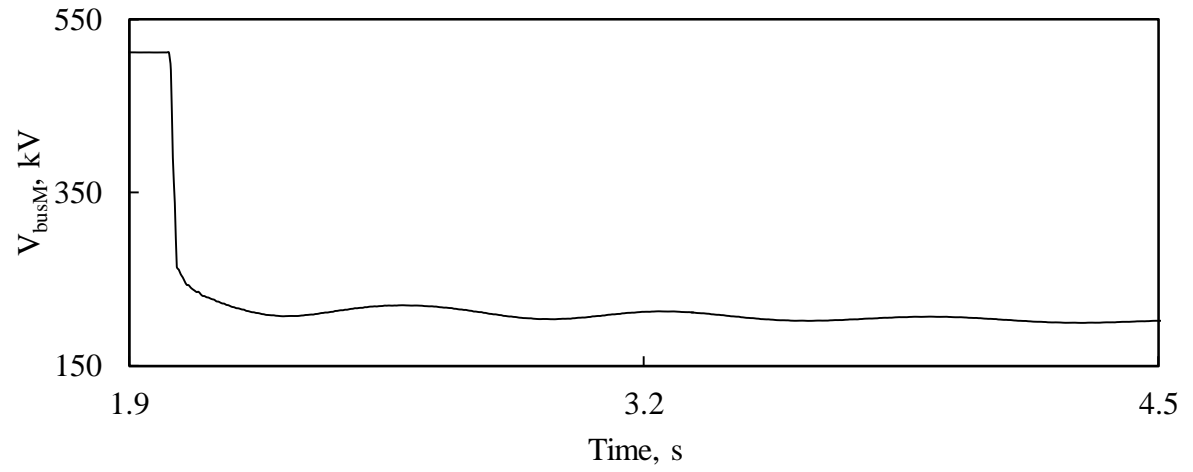


Figure 2.11: Continued.

The following observations can be made from examining Figures 2.10 and 2.11 (unsuccessful fault clearings):

- In the case of a three-phase fault, the system loses its stability as the generator speed is increasing and its real power exhibits a low frequency sustained oscillations.
- In the case of a line-to-line fault, the generator real power also exhibits sustained oscillations with a low frequency of 120 Hz.
- The system loses its stability as the generator speed is increasing and the real power exhibits sustained oscillations.

2.5 Summary

This chapter introduces the system used for the studies reported in this thesis and presents the mathematical models of its various components. A digital time-domain simulations of a case study of the system during three-phase and line-to-line faults is also presented and some observations are noted. As it has been shown in the study case that a failure in clearing a fault due to a malfunction in the transmission line relaying may result in system instability, a generator phase backup protection is a necessity.

3. IMPACT OF DFIG-BASED WIND FARMS ON GENERATOR DISTANCE PHASE BACKUP PROTECTION

3.1 Introduction

In this chapter, investigations are carried out to explore the effect of DFIG-based wind farms on the performance of generator phase backup protection (Relay (21)). In this context, comparative studies between the relay performance with and without the presence of the DFIG-based wind farm during line-to-line and three-phase faults are presented. The effects of fault location, generator loading and power flows on the transmission lines on the relay performance are also investigated in this chapter.

3.2 Setting of Generator Phase Backup Protection (Relay (21))

When a distance relay is employed to provide phase backup protection for transmission system faults, the effect of the system infeed current must be considered since the system infeed current increases the impedance of the faulted line seen by Relay (21). This increase happens because Relay (21) current and the faulted line current are not at the same value. The effect of the infeed current is incorporated in the power system of Figure 3.1.

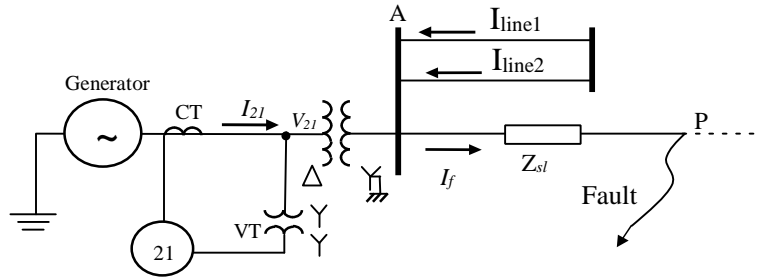


Figure 3.1: Apparent impedance measurement with system infeed currents.

With the infeed current, the voltage at the relay, V_{21} , during a three-phase fault at point P is:

$$V_{21} = Z_t I_{21} + Z_{st} I_f \quad (3.1)$$

where $Z_t = R_t + jX_t$, is the transformer series impedance (R_t = winding resistance, X_t = leakage reactance) and Z_{st} is the transmission line series impedance.

The impedance seen by the relay, Z_{21} is given by:

$$Z_{21} = \frac{V_{21}}{I_{21}} = \frac{X_t I_{21} + Z_{sl} I_f}{I_{21}} = X_t + Z_{sl} \frac{I_f}{I_{21}} \quad (3.2)$$

It can be observed that the “apparent impedance” of the line is determined by the ratio of the fault current to the relay current. Thus, this configuration apparent impedance would necessitate a much larger reach for Relay (21) to detect a fault than that calculated for a radial system with no system infeed current.

As a phase backup protection for generators, Relay (21) elements are usually set at the smallest of the following three criteria [35], [36]:

1. 120% of the longest line with system infeed currents.
2. 50% to 67% of the generator load impedance at the rated power factor angle (RPFA) of the generator.
3. 80% to 90% of the generator load impedance at the maximum torque angle (typically 85°).

Relay (21) settings based on these criteria are given in Table 3.1 and the detailed calculations are presented in Appendix B. A time delay of 1 second for the relay elements is considered in the investigations reported in this thesis to provide the proper coordination with the transmission line backup relays.

Table 3.1: Relay (21) settings based on the three criteria.

Criterion		Relay (21) setting
1	120% of the longest transmission line with system infeed	$Z_{21} = 18.9425 \Omega$
2	50% to 67% of the generator load impedance (Z_{load}) at the rated power factor angle (RPFA) of the generator.	50%, $Z_{21} = 12.518 \Omega$ 60%, $Z_{21} = 15.022 \Omega$ 67%, $Z_{21} = 16.7741 \Omega$
3	90% of the generator load impedance at the maximum torque angle (85°)	$Z_{21} = 17.918 \Omega$

Since the largest reach of Relay (21) should not exceed the GOEC limit, Figure 3.2 coordinates Relay (21) maximum reach and the GOEC limit. It can be observed that for this research, the maximum reach of Relay (21), namely Z_{max} , which is 90% of the generator load impedance at the maximum torque angle, is still inside the GOEC limit. Note that the smaller

circles, namely $Z_{21_50\%}$ and $Z_{21_67\%}$, are the actual relay settings used in Sections 3.3 and 3.4. It can be seen that both reaches are within the GOEC limit.

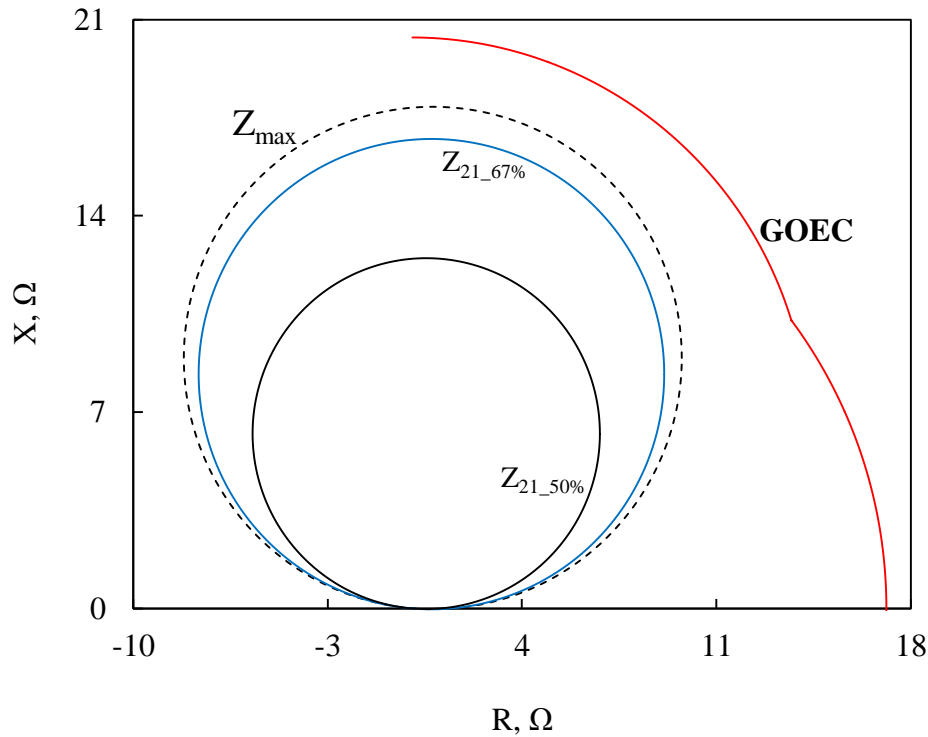


Figure 3.2: Coordination between Relay (21) and the GOEC limit.

3.3 Setting Relay (21) According to 50% of the Generator Load Impedance at the Rated Power Factor Angle of the Generator

As it can be seen from Table 3.1, Criterion 2 yields the smallest relay reach. Therefore, in the investigations conducted in this thesis, Relay (21) is set according to this criterion at 50% of the generator loading impedance at RPF of the generator which yields to $Z_{21} = 12.52 \Omega$ at $MTA = 85^\circ$. It is worth noting here that the effect of setting Relay (21) at another value within the 50% to 67% zone is discussed at the end of this chapter.

3.3.1 Performance of Relay (21) at 65% of the generator loading

At this loading, the generator delivers 364 MW and 273 MVAR to systems S_1 and S_2 . The bus voltages and real power flows under this operating condition are shown in Figure 3.3. As it can be seen from this figure, most of the generator real power output flows in L_1 .

Figure 3.4 illustrates Relay (21) tripping signal, transient time responses of the generator active and reactive powers as well as the active and reactive power flows from Bus 1 to Bus M

during a line-to-line fault at F_1 for the case of no wind farm in the system. Figure 3.5 depicts the same responses in addition to the measured impedance trajectories of Relay (21) for the case of a DFIG-based wind farm at Bus M. The corresponding responses for the case of a three-phase fault at F_1 are illustrated respectively in Figures 3.6 and 3.7.

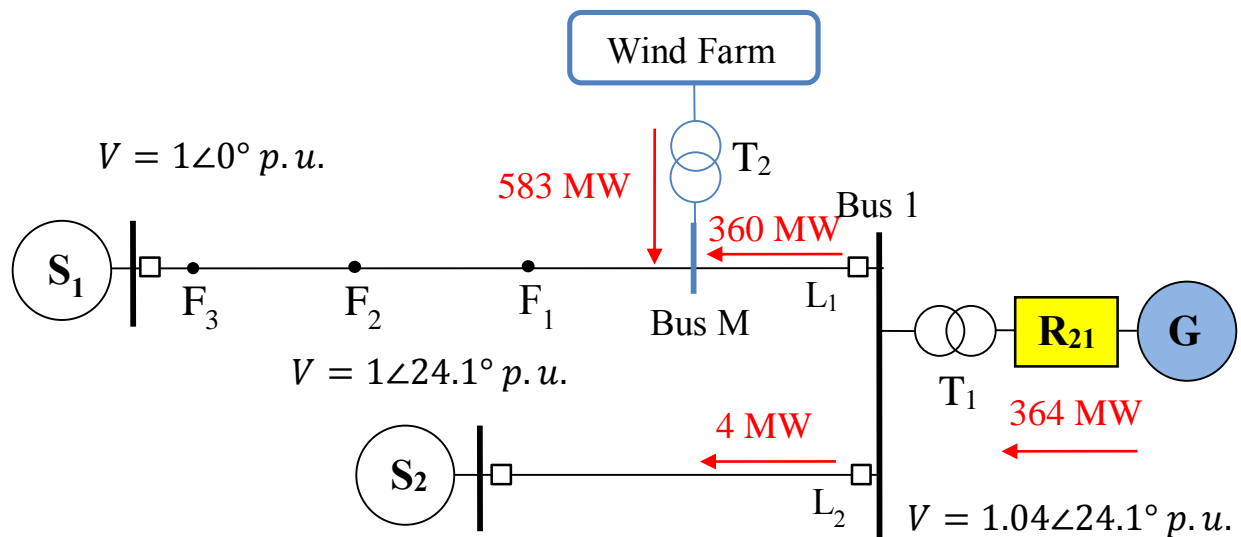


Figure 3.3: Load flow results of the bus voltages and real power flows of the system under 65% generator loading.

In response to the sudden system voltage drops caused by the high reactive power requirements due to the fault, the generator field current increases and results in an increase in the generator reactive power output (Q_{gen}) as shown in Figures 3.4 to 3.7. Regarding the DFIG-based wind farm, the occurrence of the fault activates the grid and rotor-side converters protection system which causes the crowbar to isolate the converters. As a result, the DFIG-based wind farm operates as an induction generator and starts to absorb a large amount of reactive power from the system (negative values of Q_{DFIG}) as shown in Figures 3.5 and 3.7.

The performance of Relay (21) during the two types of faults can be evaluated by examining its measured impedance trajectories depicted in Figures 3.5 and 3.7 in the absence and presence of the DFIG-based wind farm. It can be seen from these figures that these trajectories penetrate and stay inside the relay zone enough time to cause the relay to trip at $t = 3.015$ seconds. It can also be seen that the presence of the DFIG-based wind farm does not result in appreciable difference in Relay (21) performance in the cases of line-to-line and three-phase faults at F_1 .

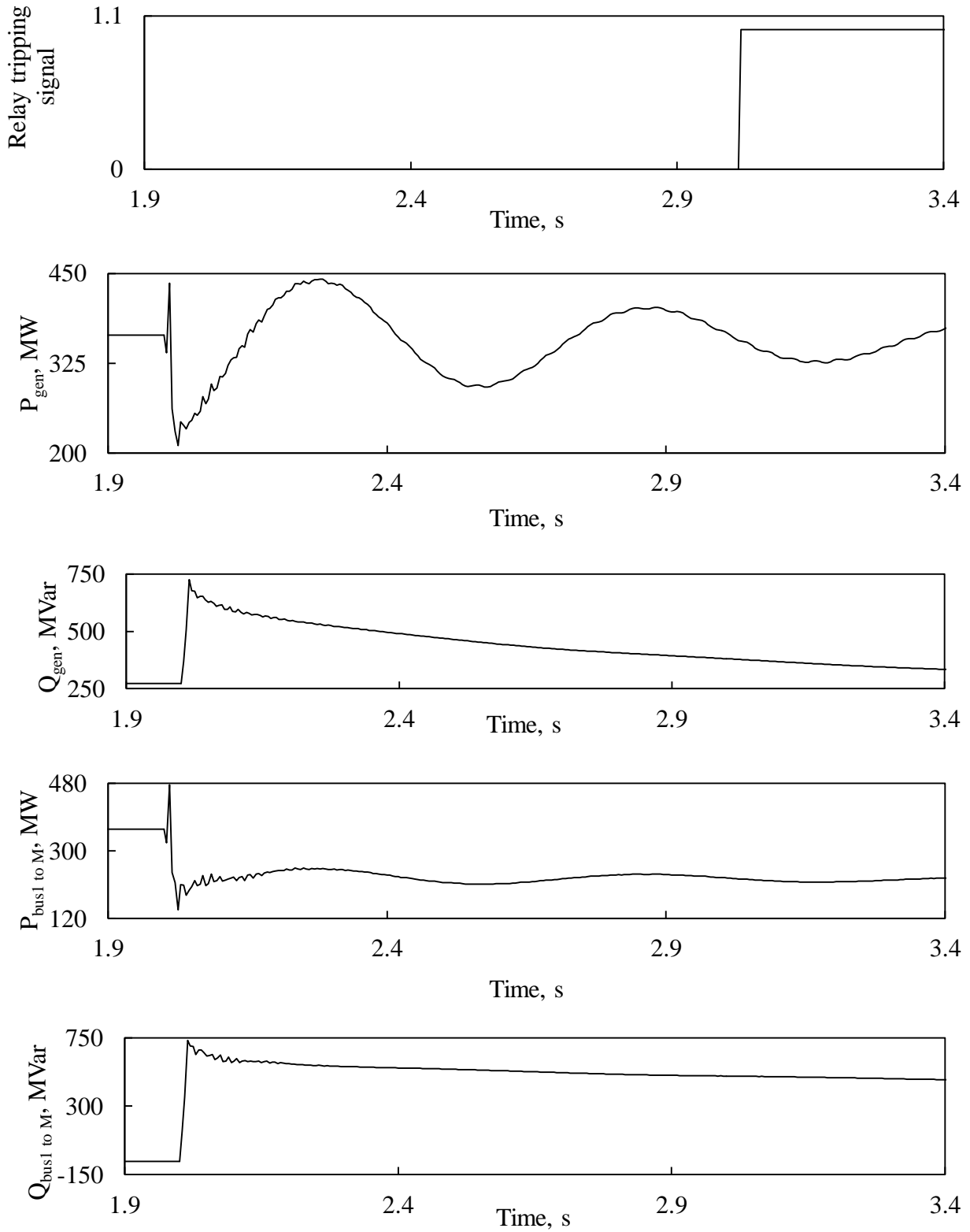


Figure 3.4: Relay (21) tripping signal, transient time responses of generator active and reactive powers, active and reactive power flows from Bus 1 to Bus M during a line-to-line fault at F_1 (no wind farm in the system).

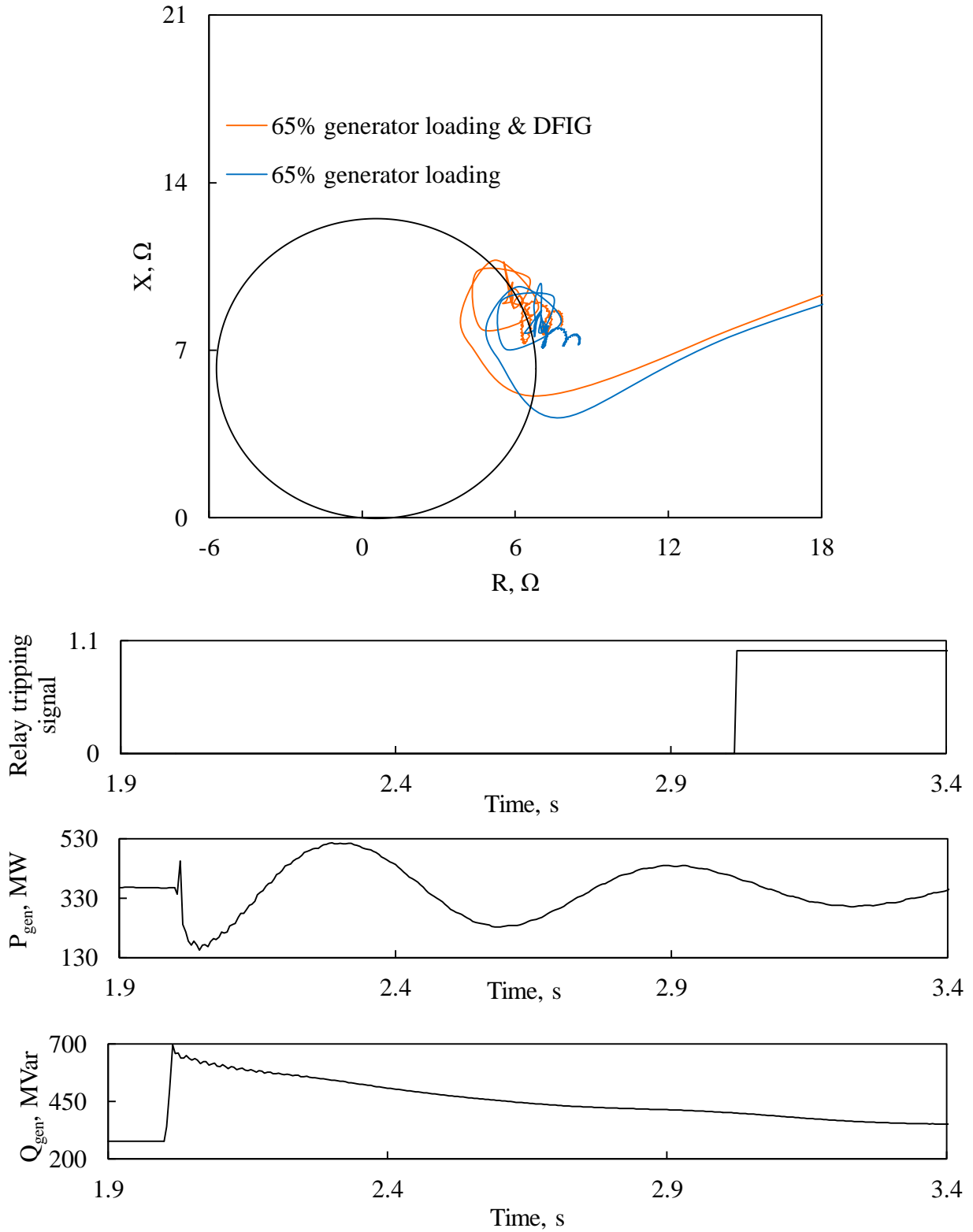


Figure 3.5: Relay (21) measured impedance trajectory and its tripping signal, transient time responses of generator active and reactive powers, active and reactive power flows from Bus 1 to Bus M, DFIG-based wind farm active and reactive powers during a line-to-line fault at F_1 .

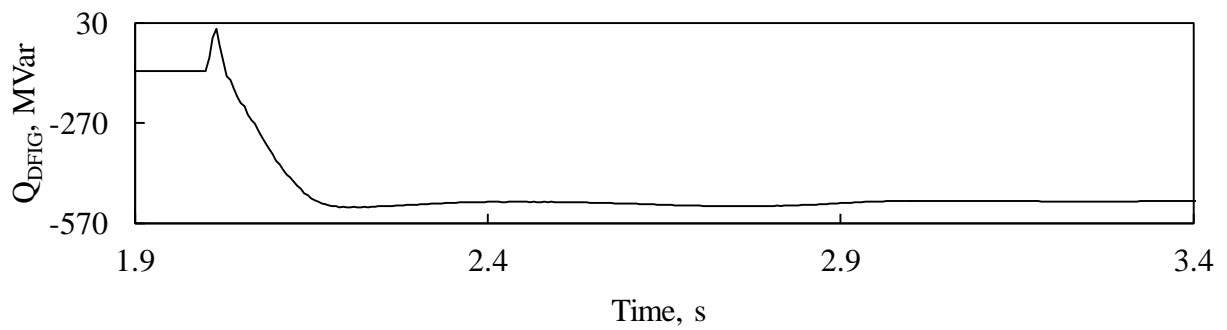
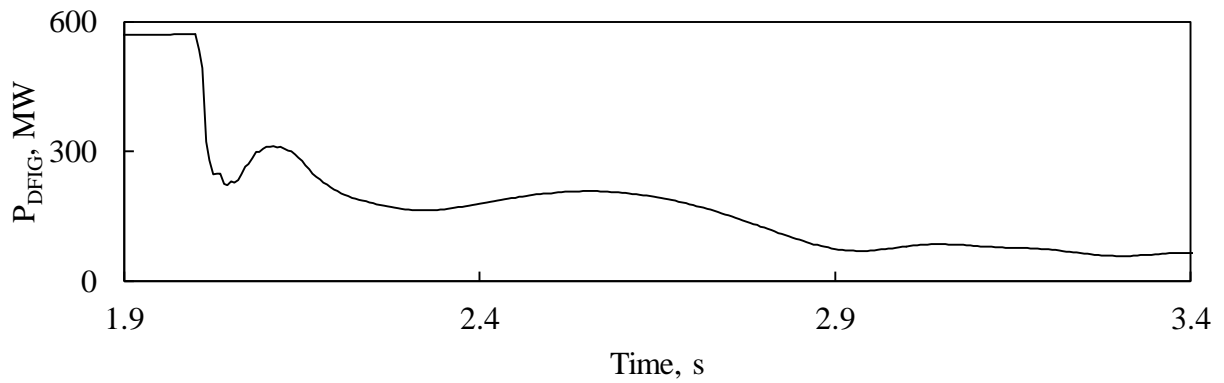
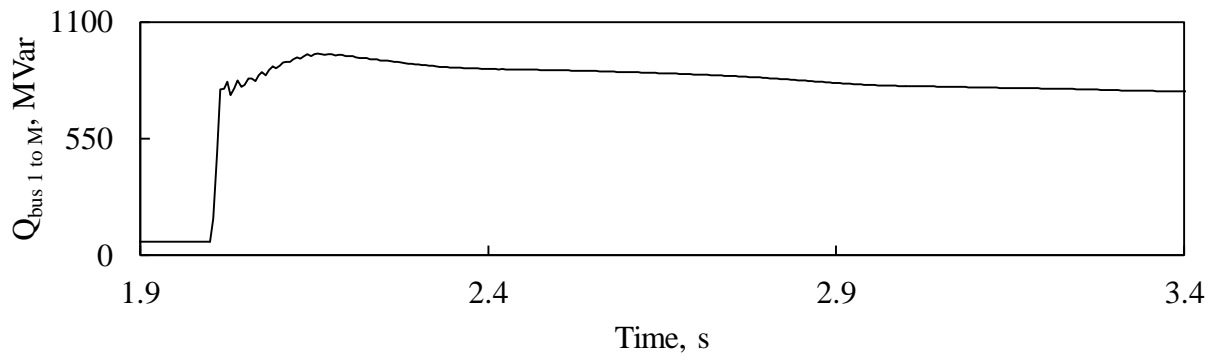
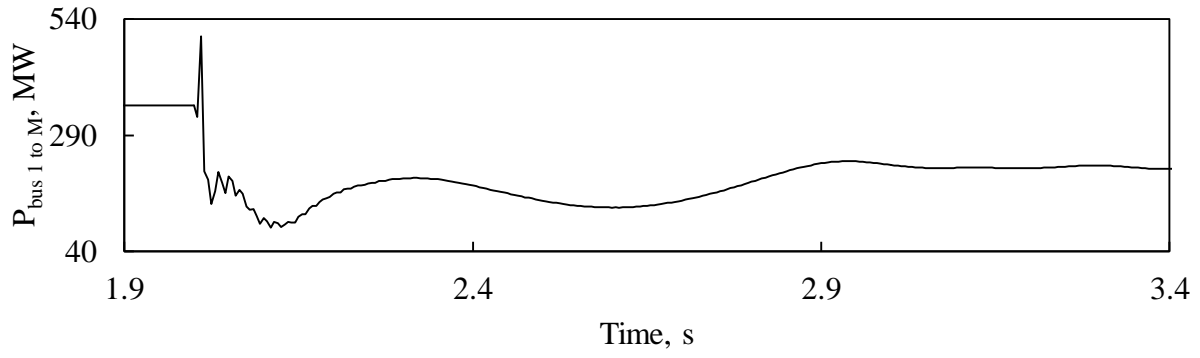


Figure 3.5: Continued.

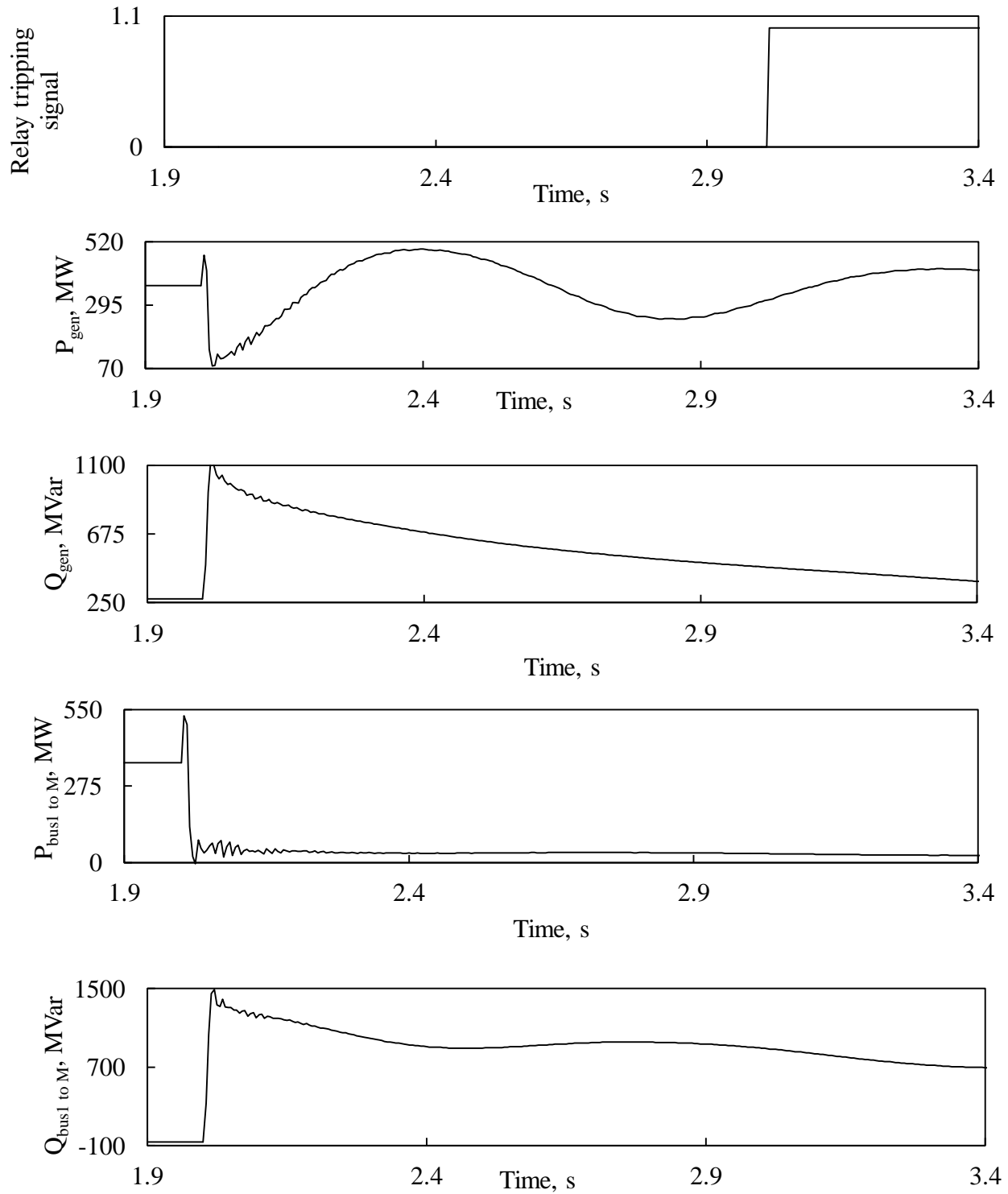


Figure 3.6: Relay (21) tripping signal, transient time responses of generator active and reactive powers, active and reactive power flows from Bus 1 to Bus M during a three-phase fault at F_1 (no wind farm in the system).

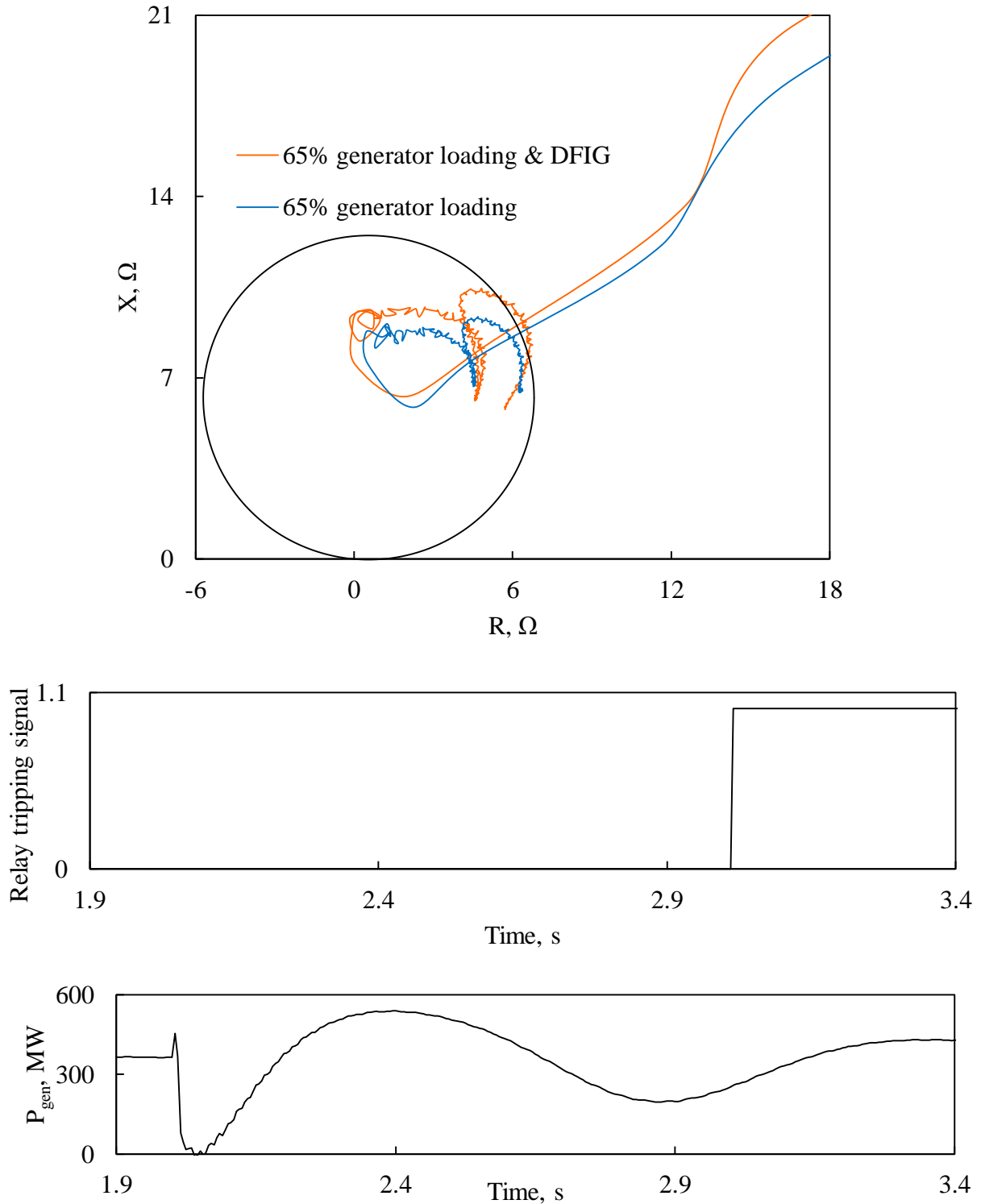


Figure 3.7: Relay (21) measured impedance trajectory and its tripping signal, transient time responses of generator active and reactive powers, active and reactive power flows from Bus 1 to Bus M, DFIG-based wind farm active and reactive powers during a three-phase at F_1 .

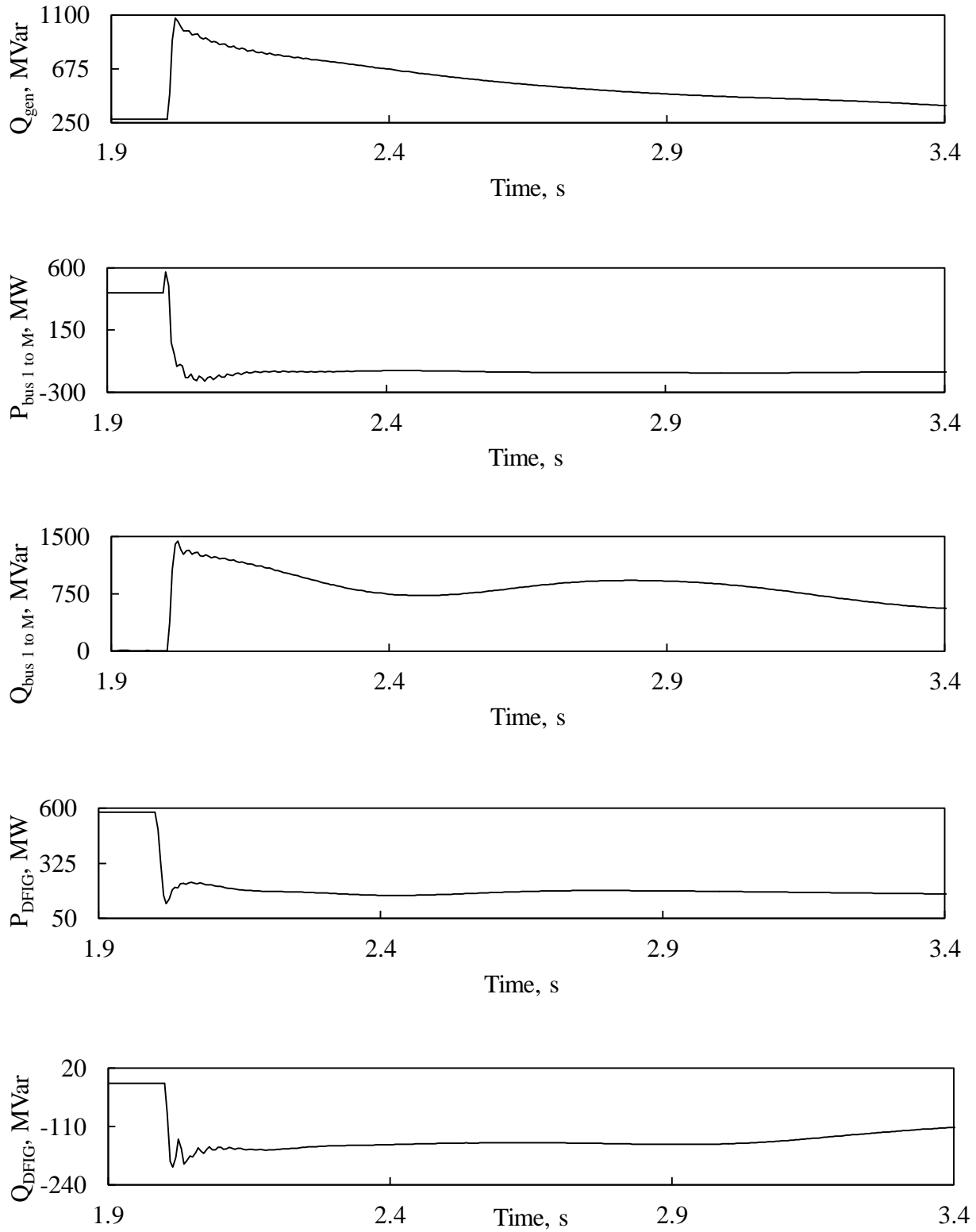


Figure 3.7: Continued.

Figure 3.8 illustrates the transient time responses of the generator active and reactive powers

as well as the active and reactive power flows from Bus 1 to Bus M during a line-to-line fault at F_2 when there is no wind farm in the system. After connecting the DFIG-based wind farm at Bus M, Figure 3.9 depicts Relay (21) measured impedance trajectories, transient time responses of the generator active and reactive powers, active and reactive power flows from Bus 1 to Bus M as well as the DFIG-based wind farm active and reactive powers during the same line-to-line fault at F_2 . Figures 3.10 and 3.11 show the same trajectories, signals in conjunction with transient time responses for the case of a three-phase fault at the same location.

The comparison between Figures 3.8 to 3.11 and Figures 3.4 to 3.7 yields the following observations:

- The system transient time responses to faults at F_2 are similar to the cases of faults at F_1 .
- As F_2 is far distant from the generator bus than F_1 , the sudden voltage drops in the generator terminal voltage are less than those during faults at F_1 . Therefore, the generator reactive power outputs during the faults are less than those in the cases of faults at F_1 .

The following observations are also noted from Figures 3.9 and 3.11:

- Relay (21) measured impedance trajectories during faults at F_2 penetrate momentarily the relay reach then stay outside it. For this reason, the relay does not issue a trip signal for faults at F_2 .
- For the case of a line-to-line fault at F_2 , Figure 3.9 shows that with the presence of the DFIG wind farm, the measured impedance trajectory moves a little closer to the relay reach. This, however, will not result in a tripping signal as the trajectory is still outside the relay reach.
- For the case of a three-phase faults, Figure 3.11 shows that the presence of the DFIG-based wind farm results in a slightly larger relay measured impedance. This makes the impedance trajectory to travel further outside the relay reach.

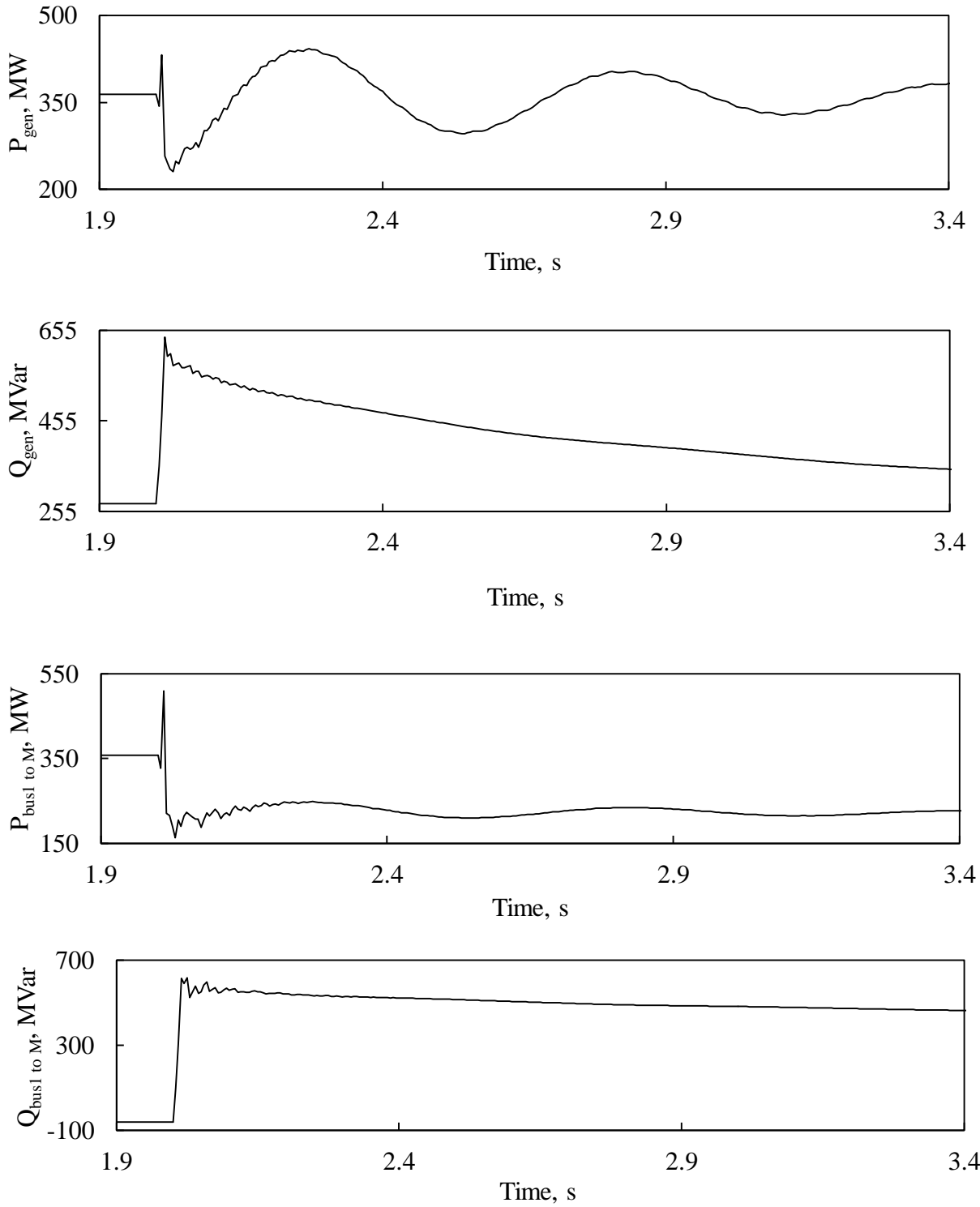


Figure 3.8: Transient time responses of generator active and reactive powers, active and reactive power flows from Bus 1 to Bus M during a line-to-line fault at F_2 (no wind farm in the system).

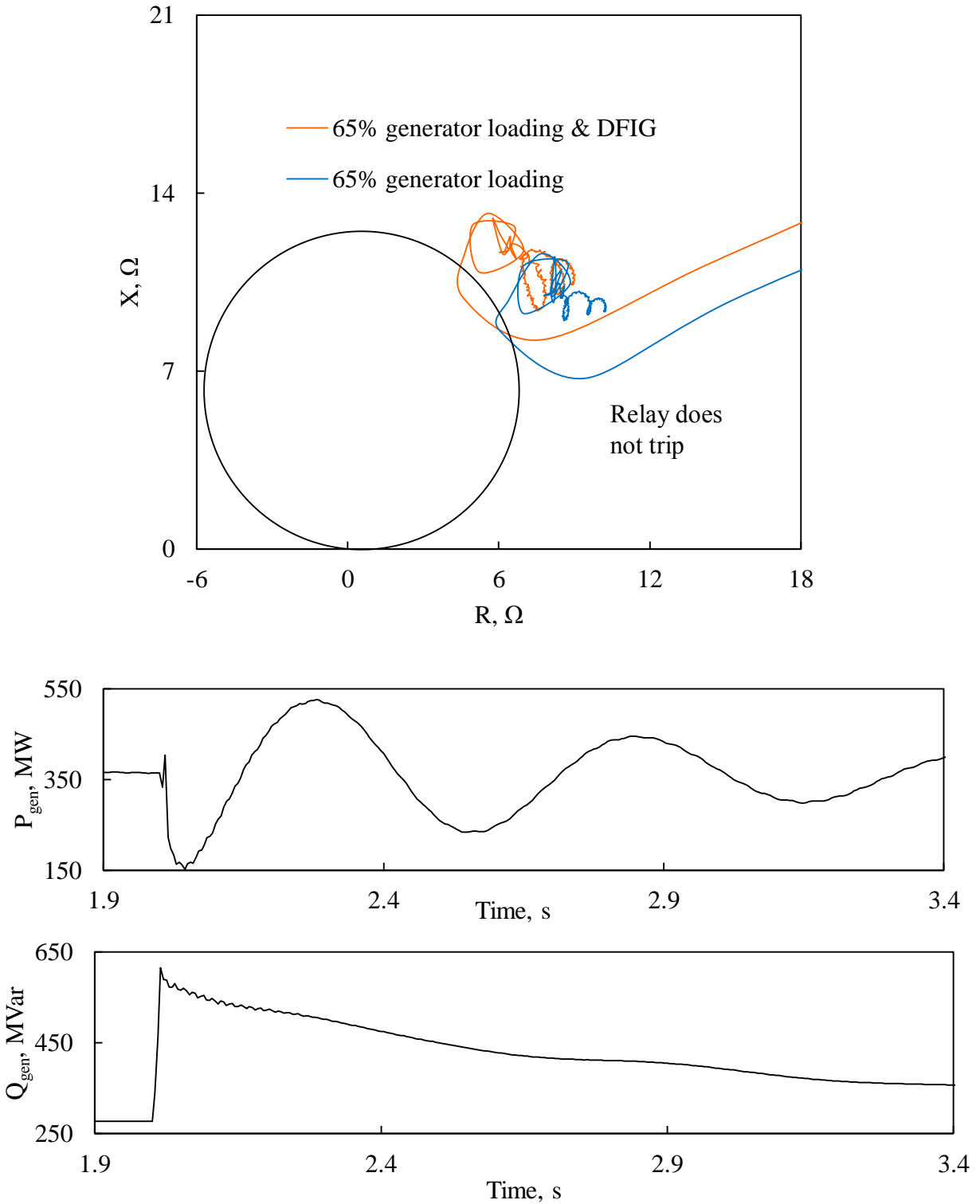


Figure 3.9: Relay (21) measured impedance, transient time responses of generator active and reactive powers, active and reactive power flows from Bus 1 to Bus M, DFIG-based wind farm active and reactive powers during a line-to-line fault at F_2 .

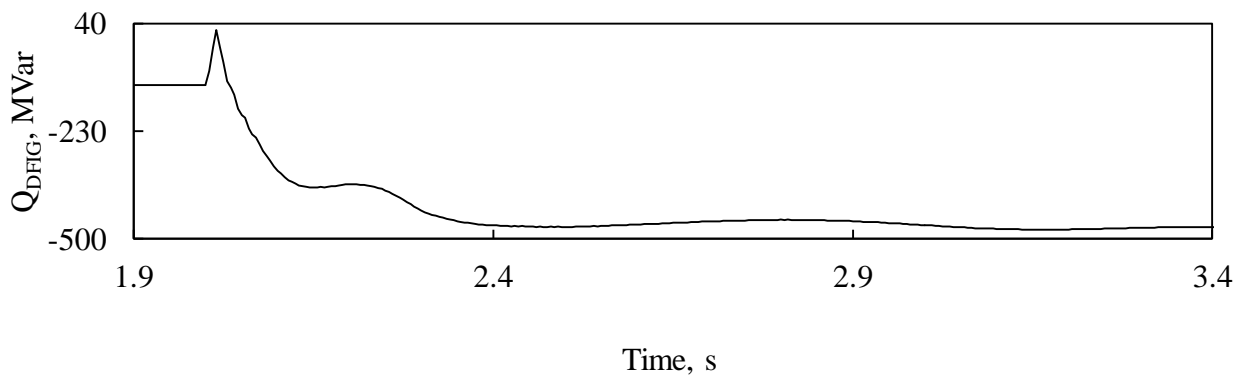
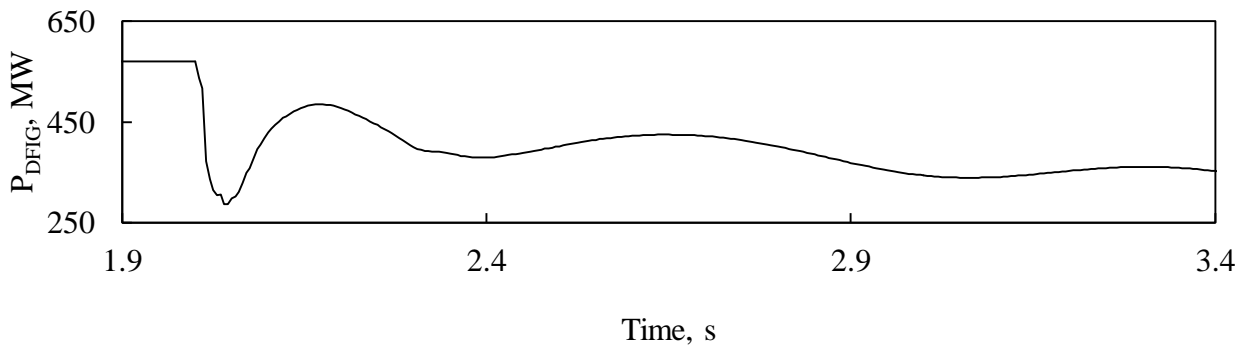
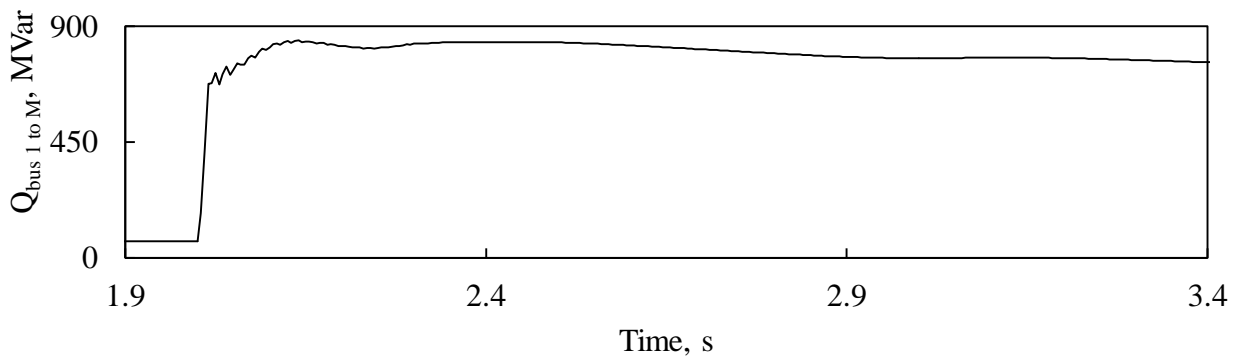
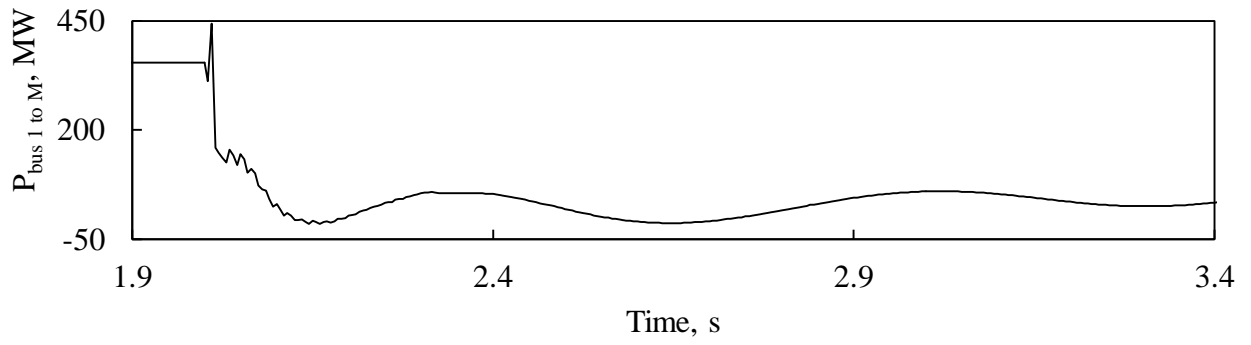


Figure 3.9: Continued.

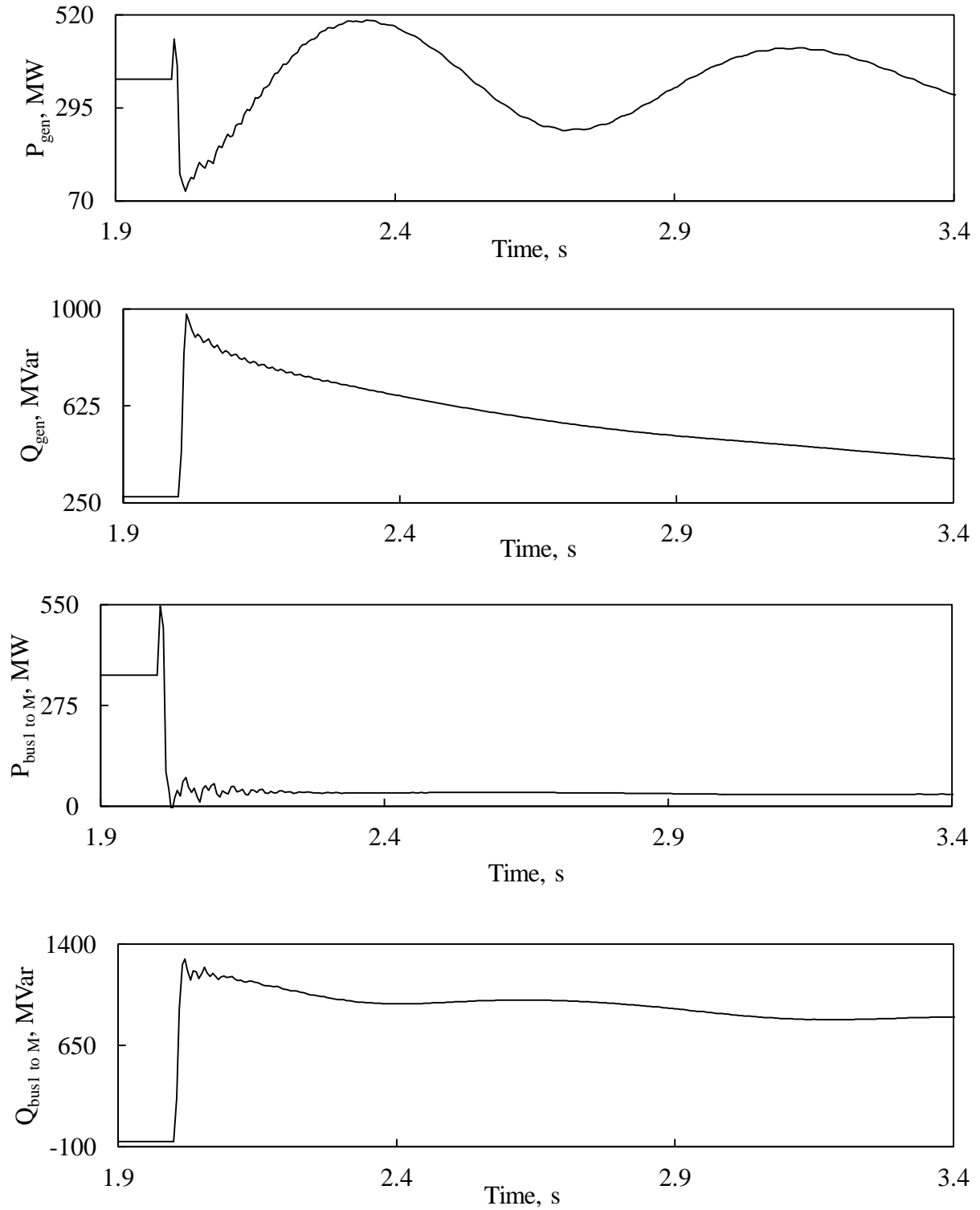


Figure 3.10: Transient time responses of generator active and reactive powers, active and reactive power flows from Bus 1 to Bus M during a three-phase fault at F_2 (no wind farm in the system).

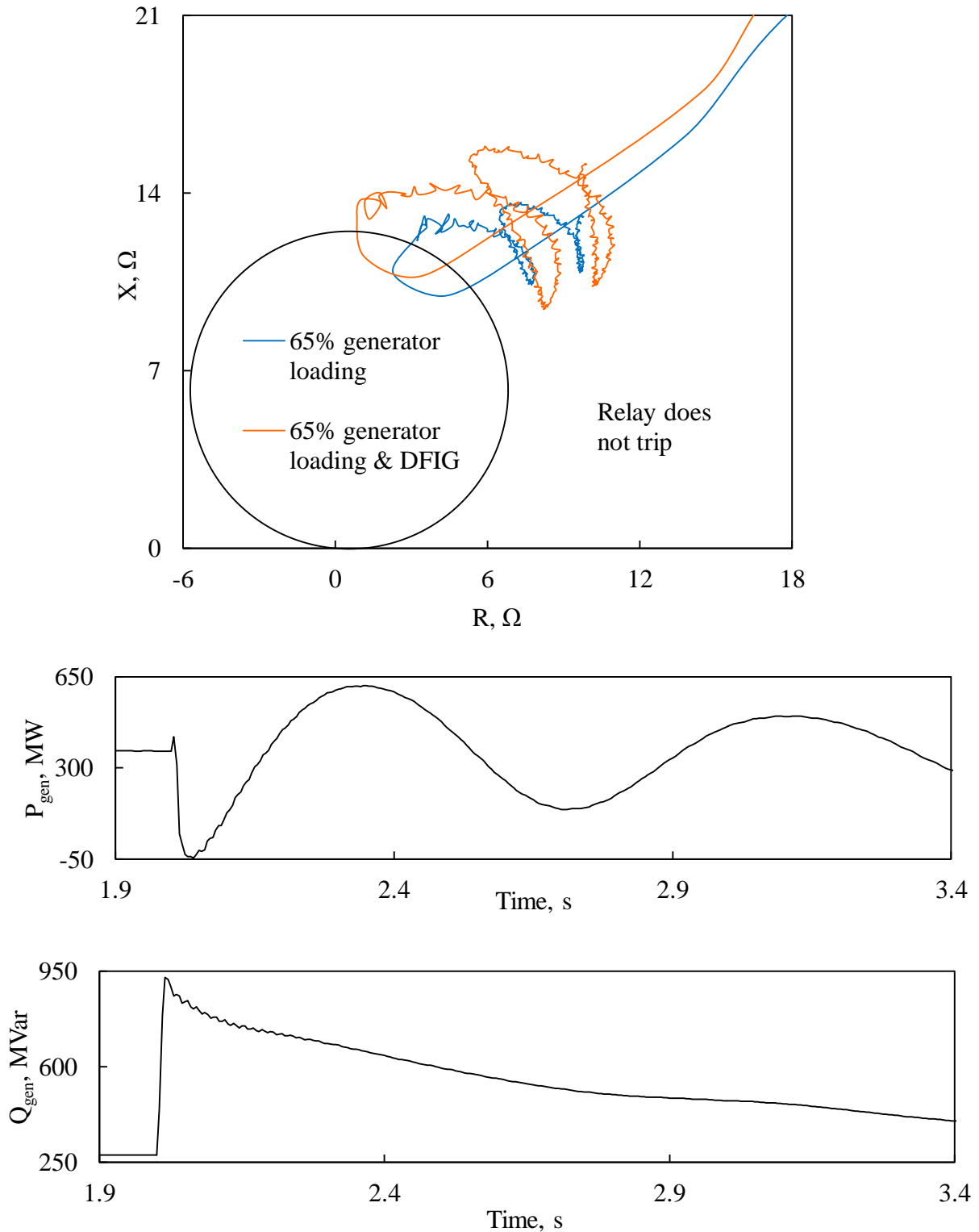


Figure 3.11: Relay (21) measured impedance trajectory, transient time responses of generator active and reactive powers, active and reactive power flows from Bus 1 to Bus M, DFIG-based wind farm active and reactive powers during a three-phase at F_2 .

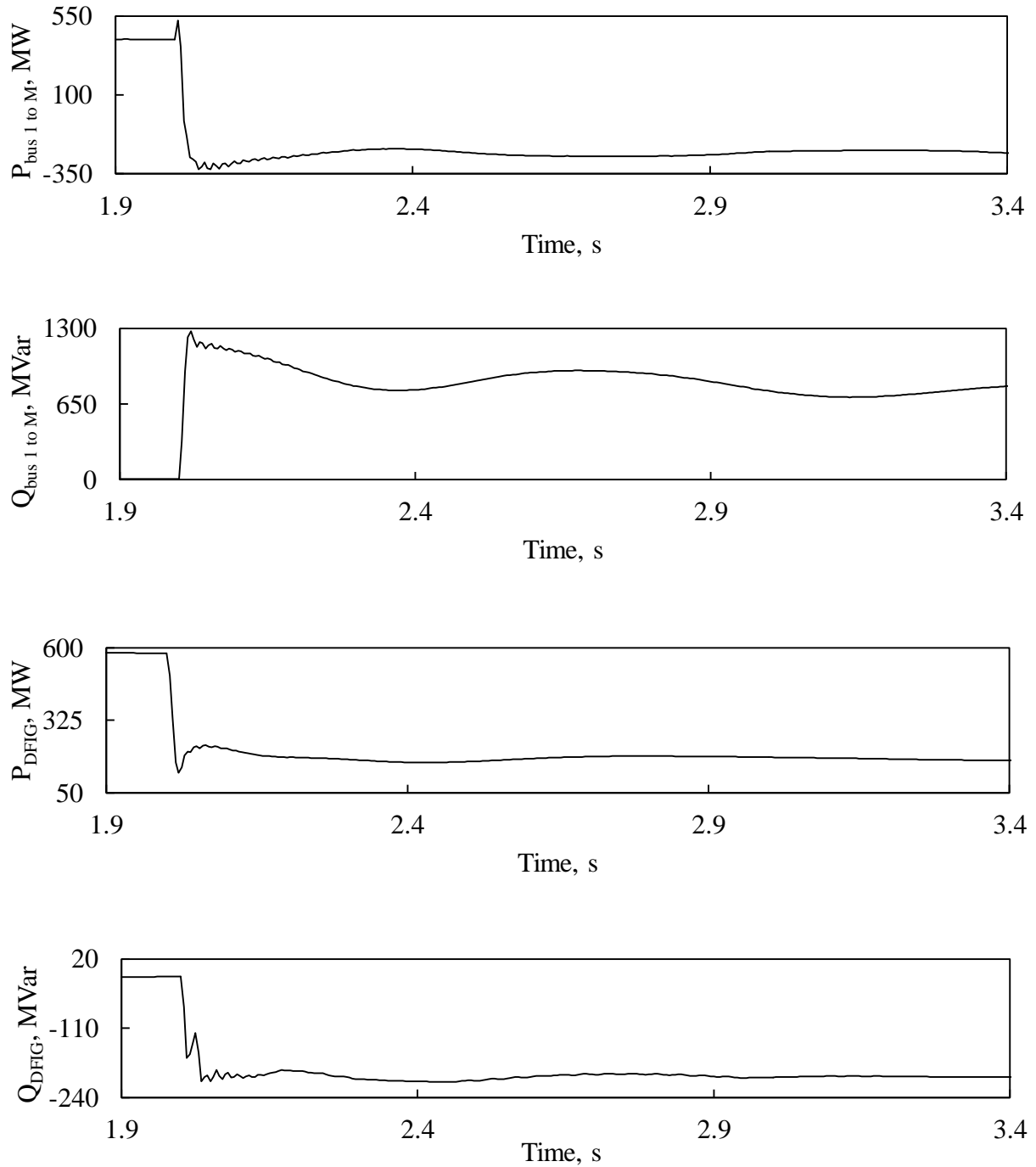


Figure 3.11: Continued.

The impact of the same faults on Relay (21) performance is also investigated for the fault location F_3 . The results of these investigations, which are very similar to the cases of faults at F_2 , are shown in Appendix C.

3.3.2 Performance of Relay (21) at 75% of the generator loading

At this loading, the generator delivers 420 MW and 315 MVAR to systems S_1 and S_2 . Figure 3.12 illustrates Relay (21) tripping signal, transient time responses of the generator active and reactive powers as well as the active and reactive power flows from Bus 1 to Bus M during a line-to-line fault occurs at F_1 when there is no wind farm in the system. Figure 3.13 depicts Relay (21) measured impedance trajectories, Relay (21) tripping signal, transient time responses of the generator active and reactive powers, active and reactive power flows from Bus 1 to Bus M as well as the DFIG-based wind farm active and reactive powers during the same line-to-line fault at F_1 with the DFIG-based wind farm connected to Bus M. Figures 3.14 and 3.15 show the same trajectories, signals in conjunction with transient time responses for the cases of three-phase fault at the same location.

The comparison between Figures 3.4 to 3.7 and Figures 3.12 to 3.15 shows that:

- The generator experiences the similar increase in the reactive power output as in the case of 65% generator loading for the same fault type and location. And it can be seen from Figures 3.13 and 3.15 that the grid and rotor-side converters protection system of DFIG-based is activated by the faults since the DFIG-based wind farm starts to absorb a large amount of reactive power from the system (negative values of Q_{DFIG}) after the occurrence of faults.

By examining the impedance trajectories shown in Figures 3.13 and 3.15, it can be seen that:

- The performance of Relay (21) during the two types of faults is not significantly affected by the DFIG-based wind farm since the trajectories stay inside relay zone and make relay trip at $t = 3.015$ seconds in the absence and presence of the DFIG-based wind farm.

The comparison between Figures 3.13 and 3.15 to Figures 3.5 and 3.7 reveals that:

- The relay measured impedance decreases as the generator loading increases as the trajectories in Figures 3.13 and 3.15 penetrates slightly further into the relay zone than those in Figures 3.5 and 3.7.

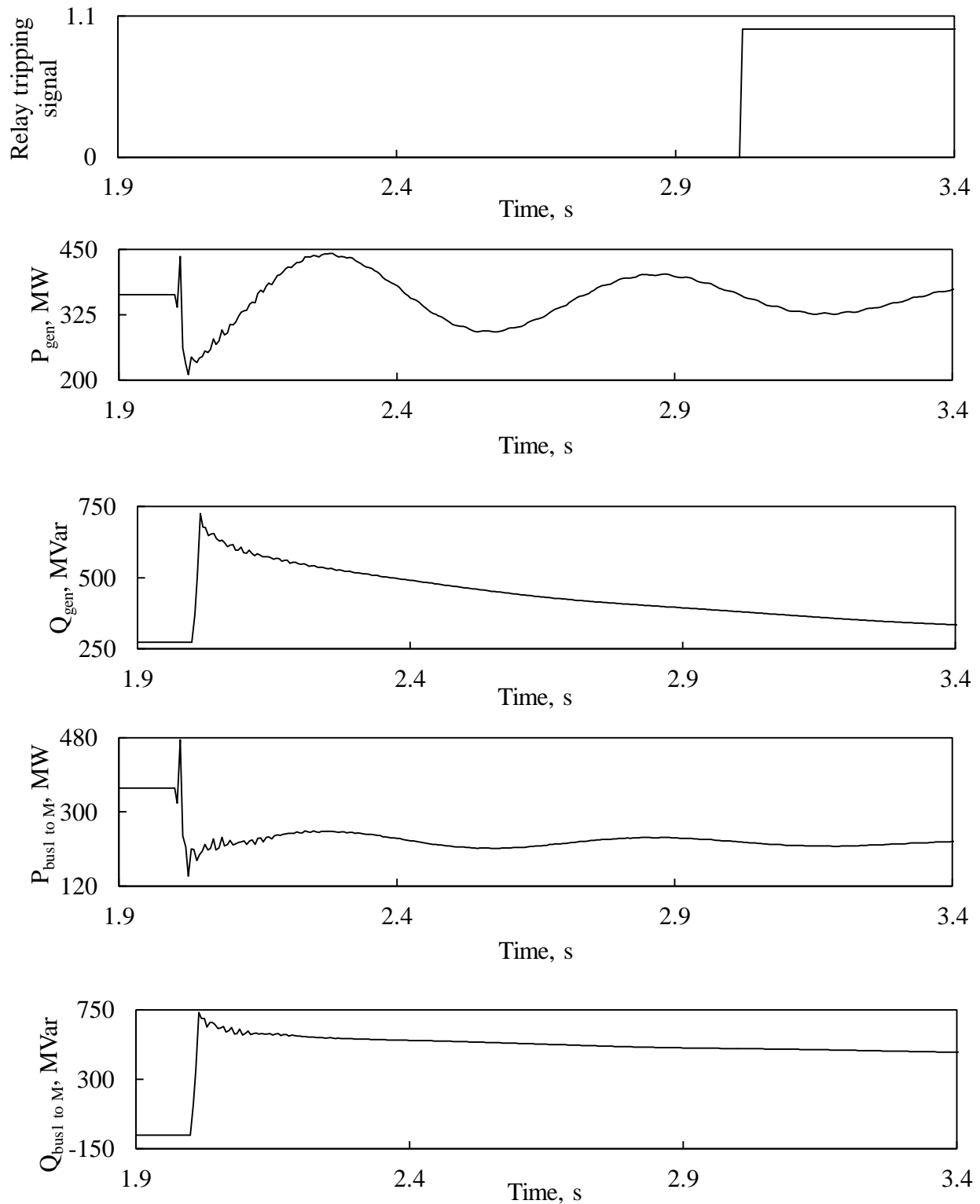


Figure 3.12: Relay (21) tripping signal, transient time responses of generator active and reactive powers, active and reactive power flows from Bus 1 to Bus M during a line-to-line fault at F_1 (no wind farm in the system).

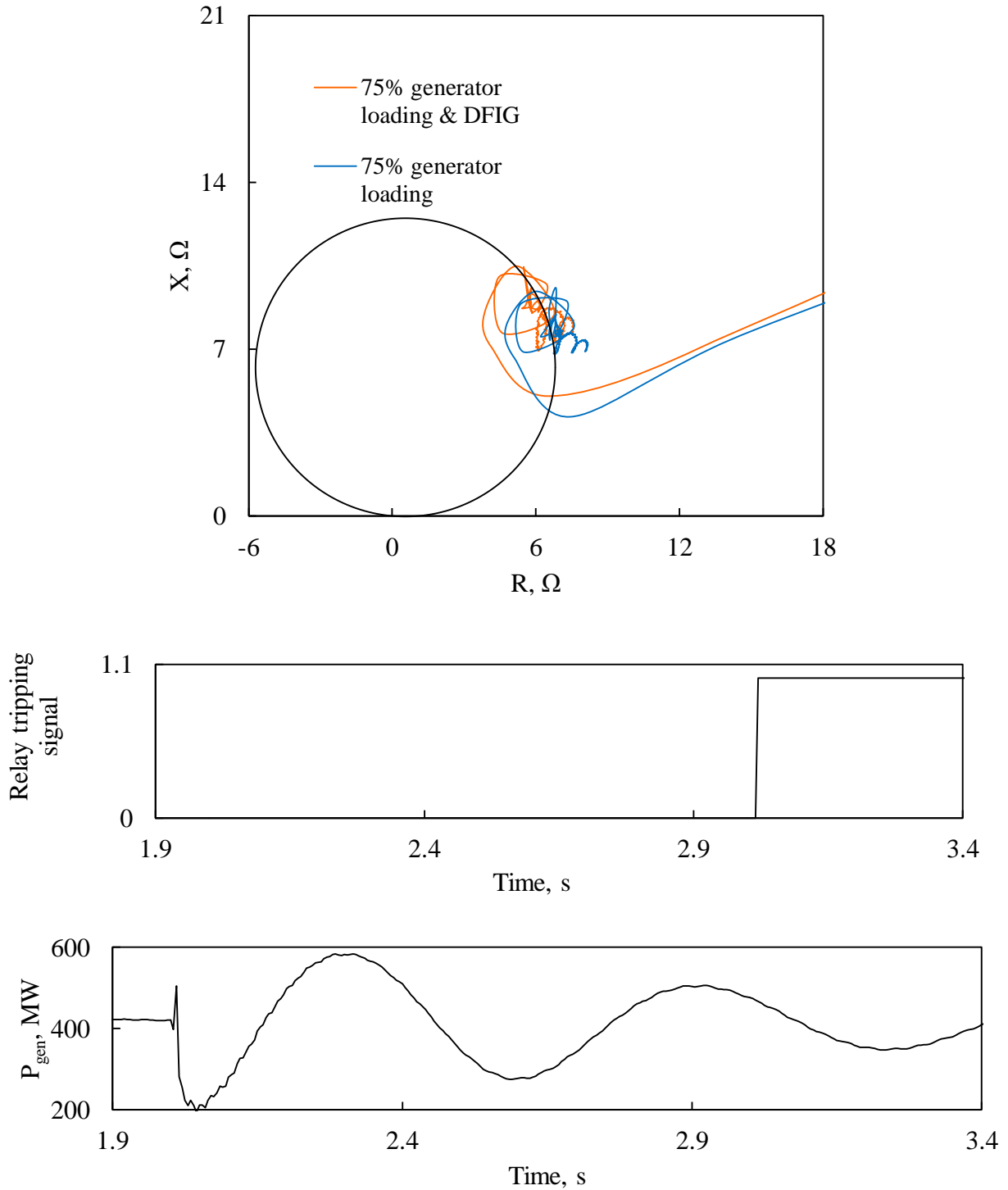


Figure 3.13: Relay (21) measured impedance trajectory and its tripping signal, transient time responses of generator active and reactive powers, active and reactive power flows from Bus 1 to Bus M, DFIG-based wind farm active and reactive powers during a line-to-line fault at F_1 .

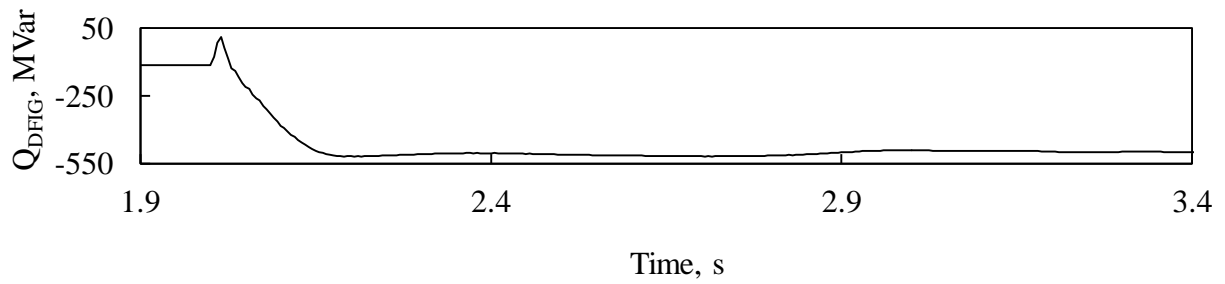
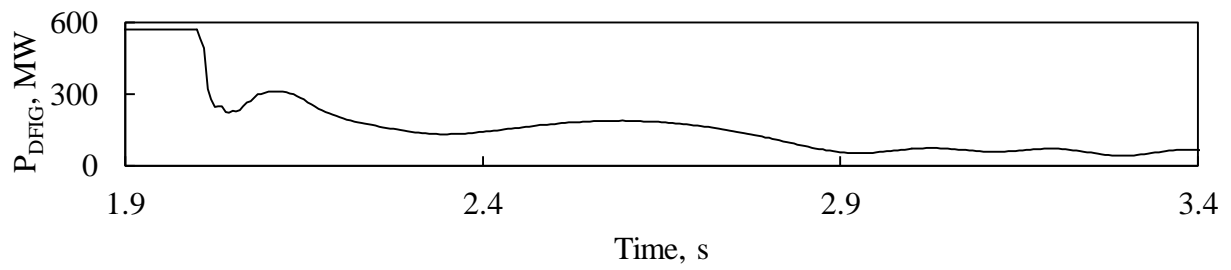
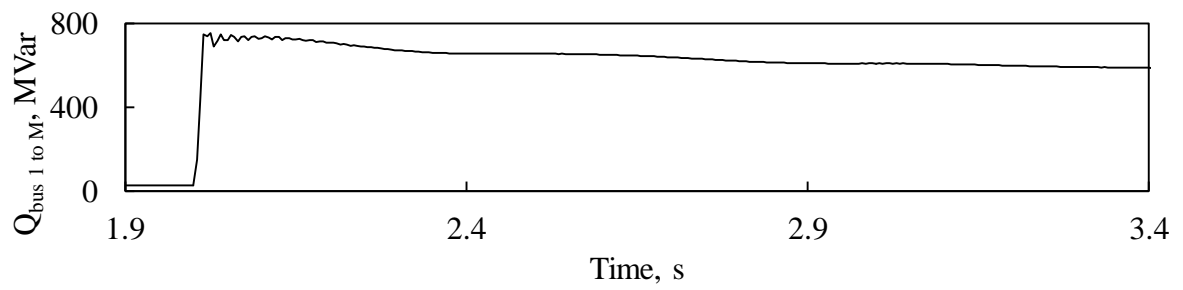
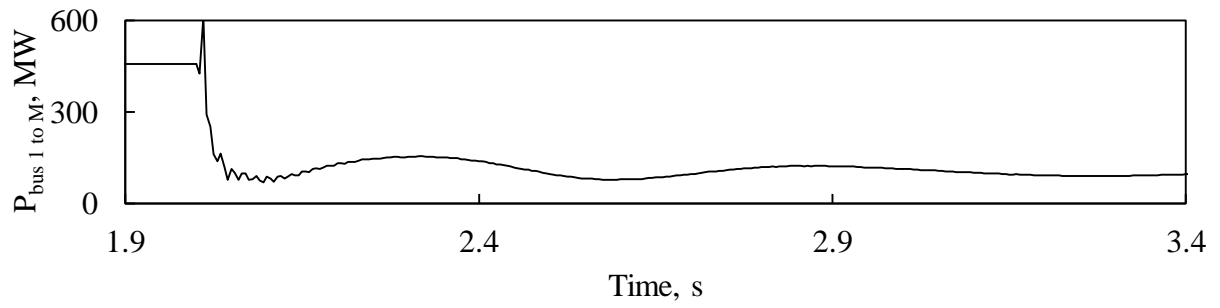
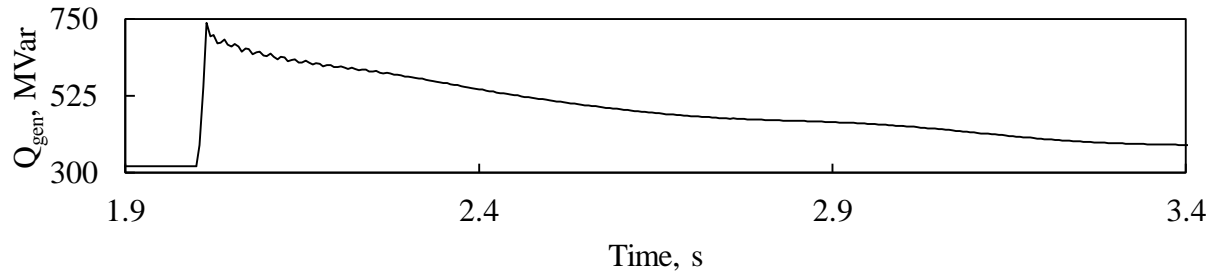


Figure 3.13: Continued.

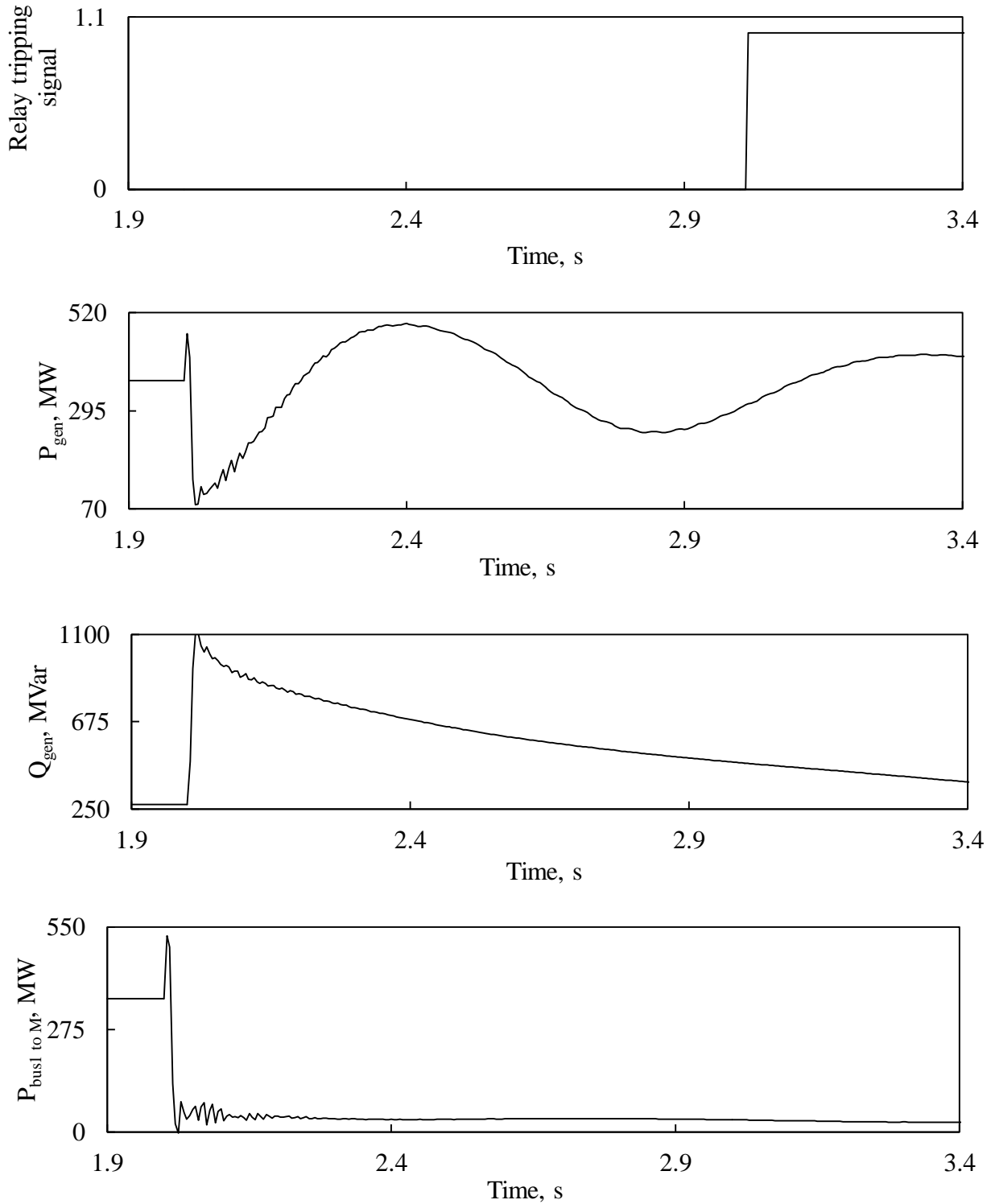


Figure 3.14: Relay (21) tripping signal, transient time responses of generator active and reactive powers, active and reactive power flows from Bus 1 to Bus M during a three-phase fault at F_1 (no wind farm in the system).

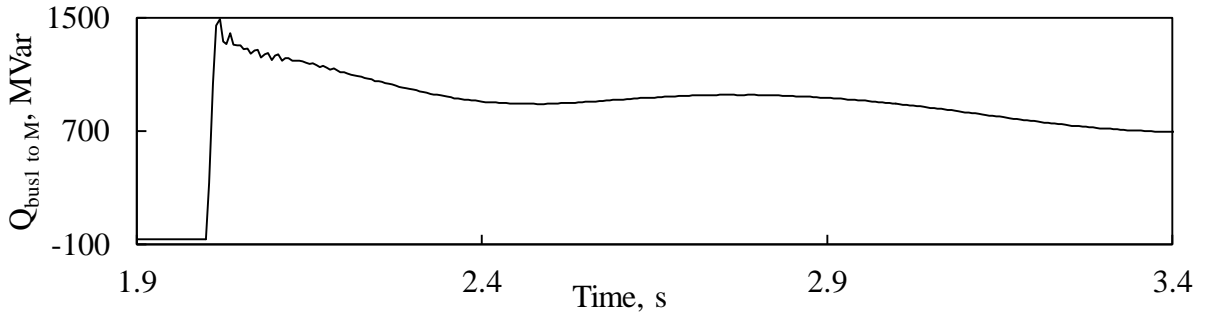


Figure 3.14: Continued.

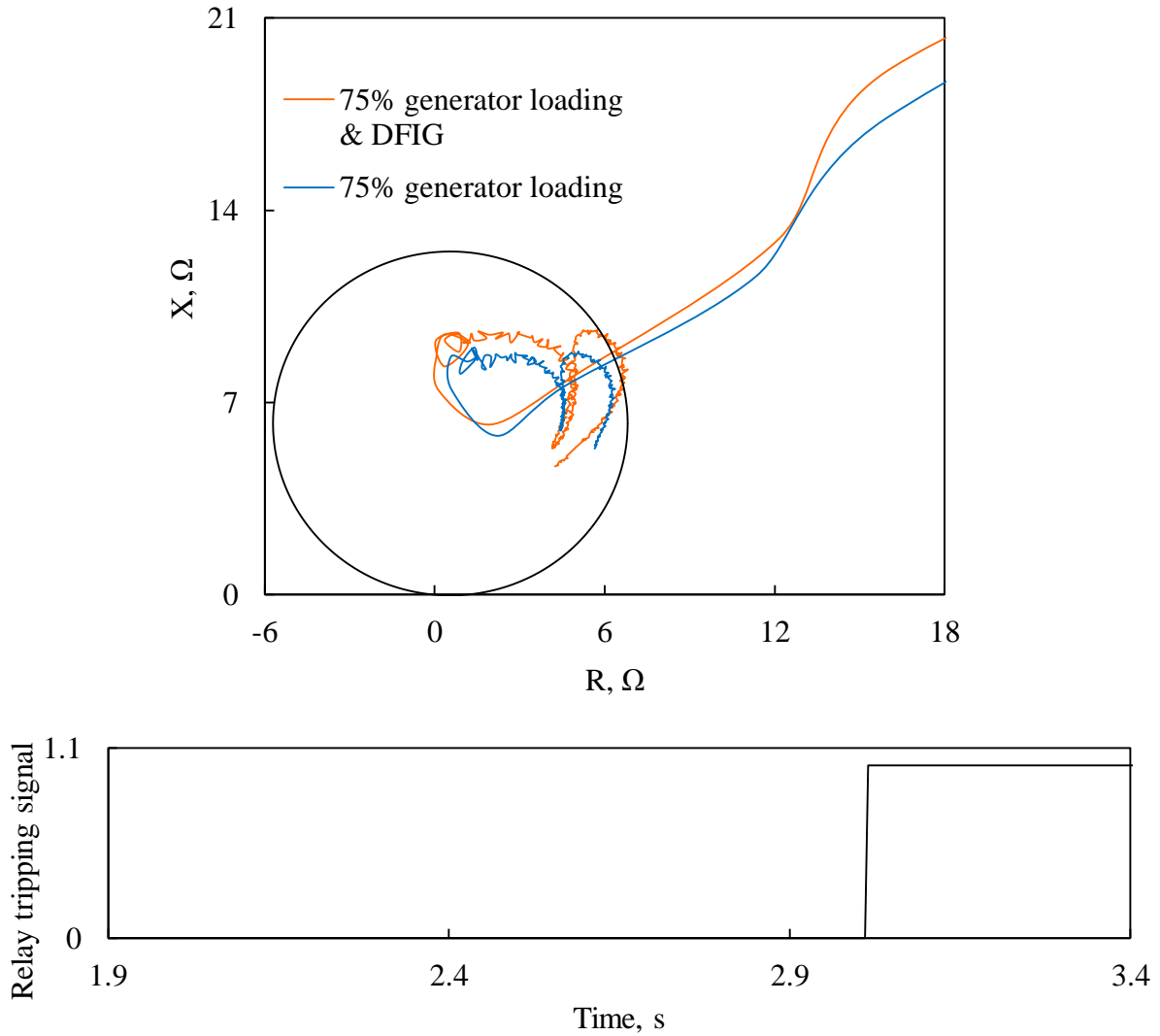


Figure 3.15: Relay (21) measured impedance trajectory and its tripping signal, transient time responses of generator active and reactive powers, active and reactive power flows from Bus 1 to Bus M, DFIG-based wind farm active and reactive powers during a three-phase at F_1 .

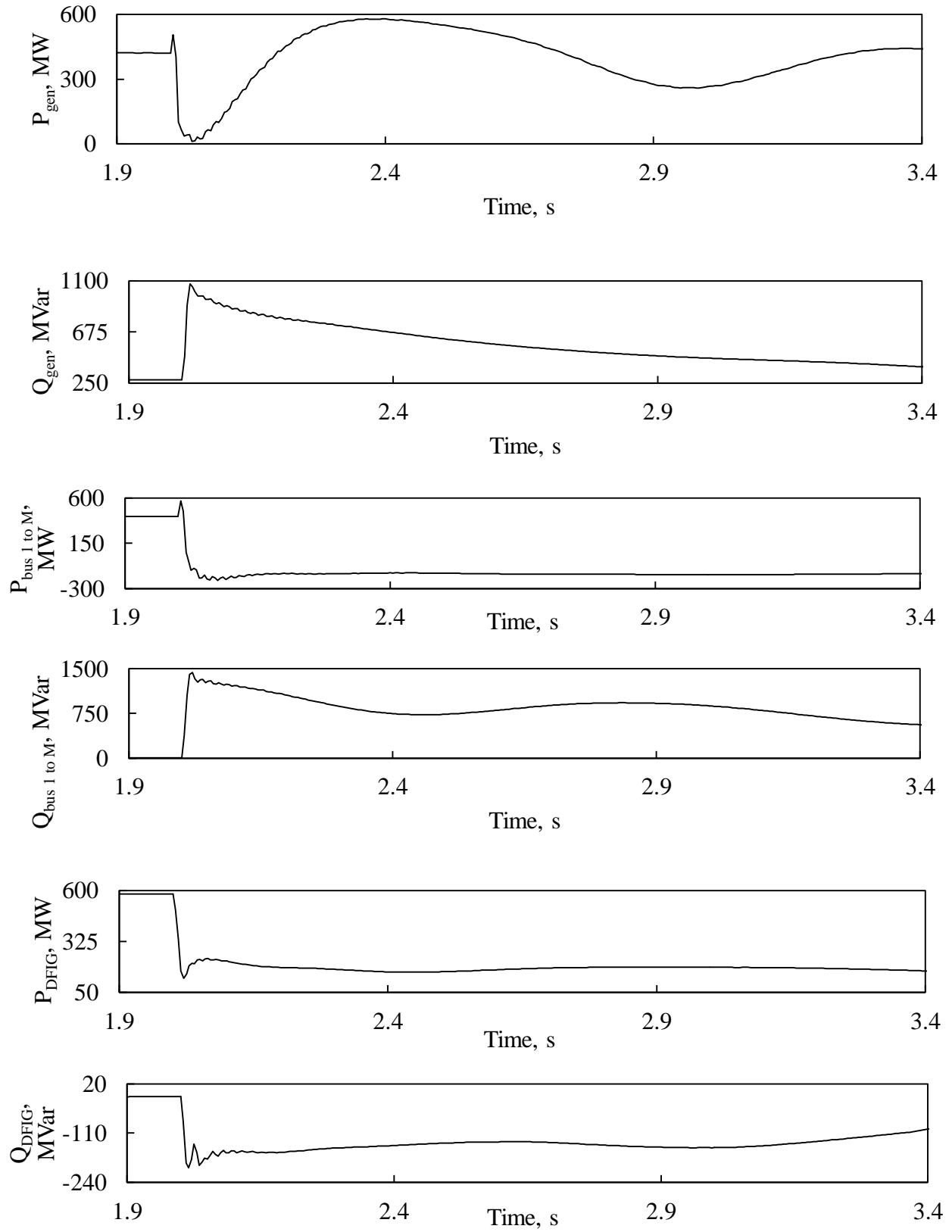


Figure 3.15: Continued.

Figure 3.16 illustrates the transient time responses of the generator active and reactive powers as well as the active and reactive power flows from Bus 1 to Bus M during a line-to-line fault at F_2 when there is no wind farm in the system. Figure 3.17 depicts the same responses in addition to the measured impedance trajectories of Relay (21) for the case of a DFIG-based wind farm at Bus M. Figures 3.21 and 3.22 show the same trajectories, signals in conjunction with transient time responses for the cases of three-phase faults at the same location. It can be observed through comparing Figures 3.16 to 3.19 with Figures 3.8 to 3.11 that:

- The responses of generator output and system load flow to the sudden system voltage drops caused by the high reactive power requirements due to the faults are similar to those presented for the 65% generator loading cases.
- The DFIG-based wind farm still operates as an induction generator just after the occurrence of faults as in the cases for 65% generator loading.
- Relay (21) measured impedance trajectories under 75% generator loading travels more within the relay zone than those in the 65% generator loading cases but only at a small degree. Even with these changes, the relay operations during and after the faults are the same as introduced in cases of 65% generator loading.

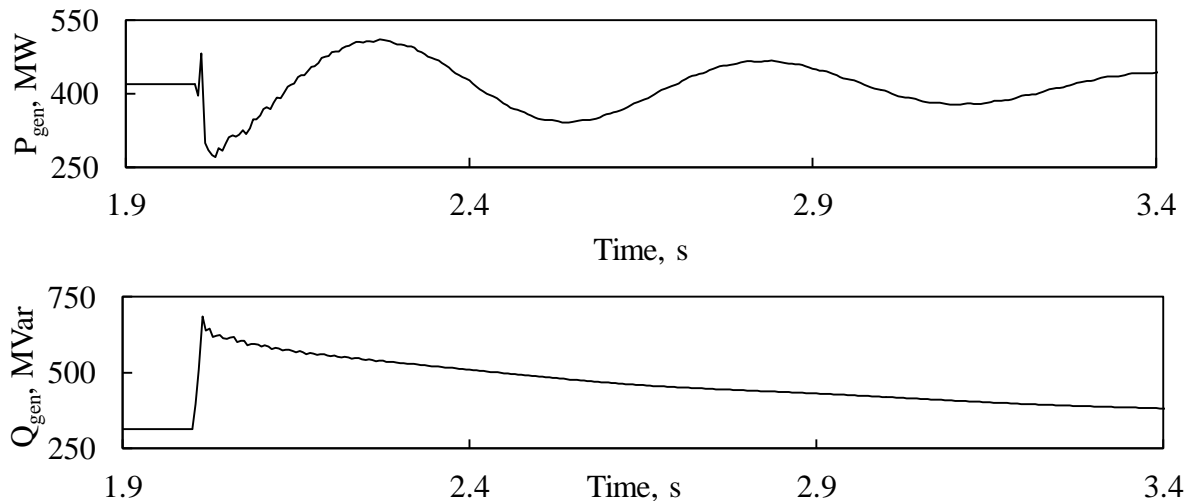


Figure 3.16: Transient time responses of generator active and reactive powers, active and reactive power flows from Bus 1 to Bus M during a line-to-line fault at F_2 (no wind farm in the system).

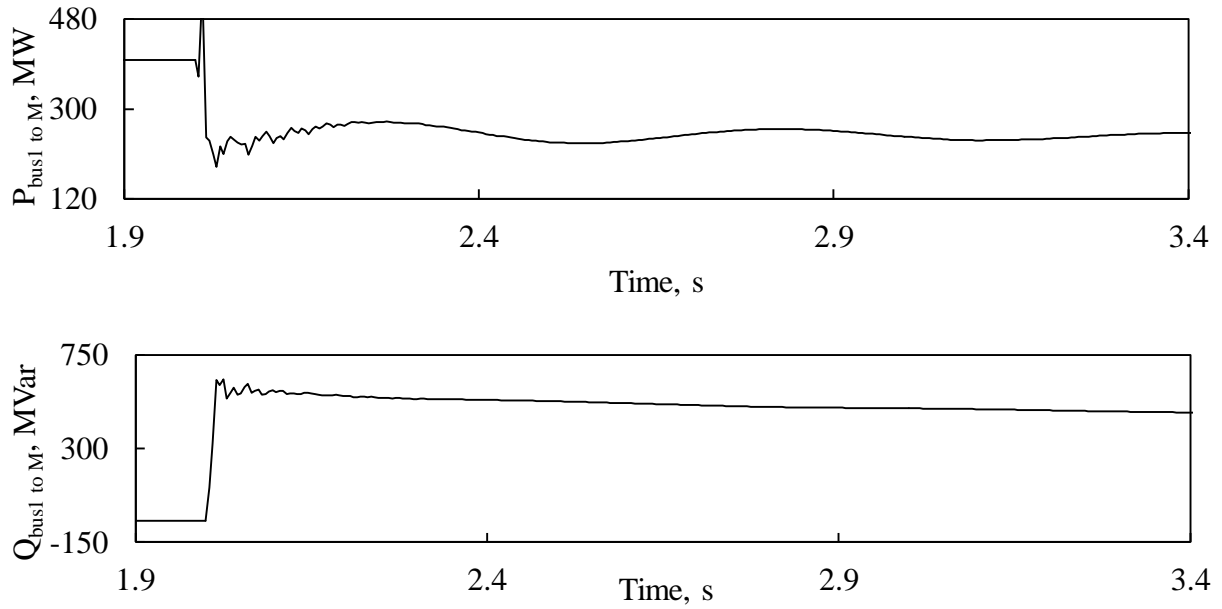


Figure 3.16: Continued.

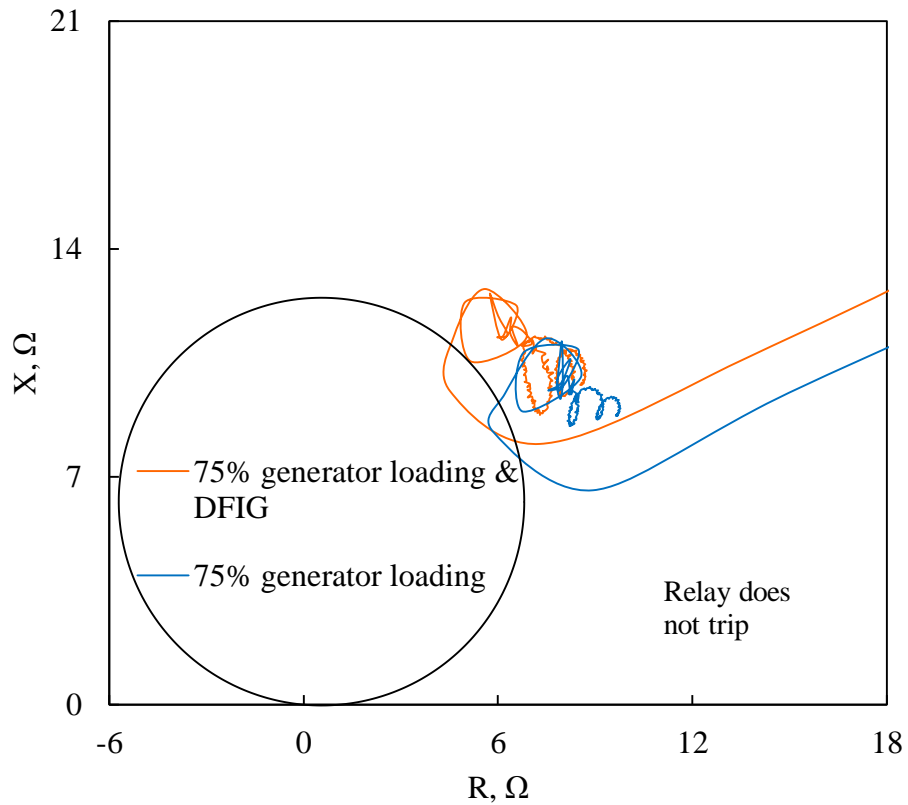


Figure 3.17: Relay (21) measured impedance trajectory, transient time responses of generator active and reactive powers, active and reactive power flows from Bus 1 to Bus M, DFIG-based wind farm active and reactive powers during a line-to-line fault at F_2 .

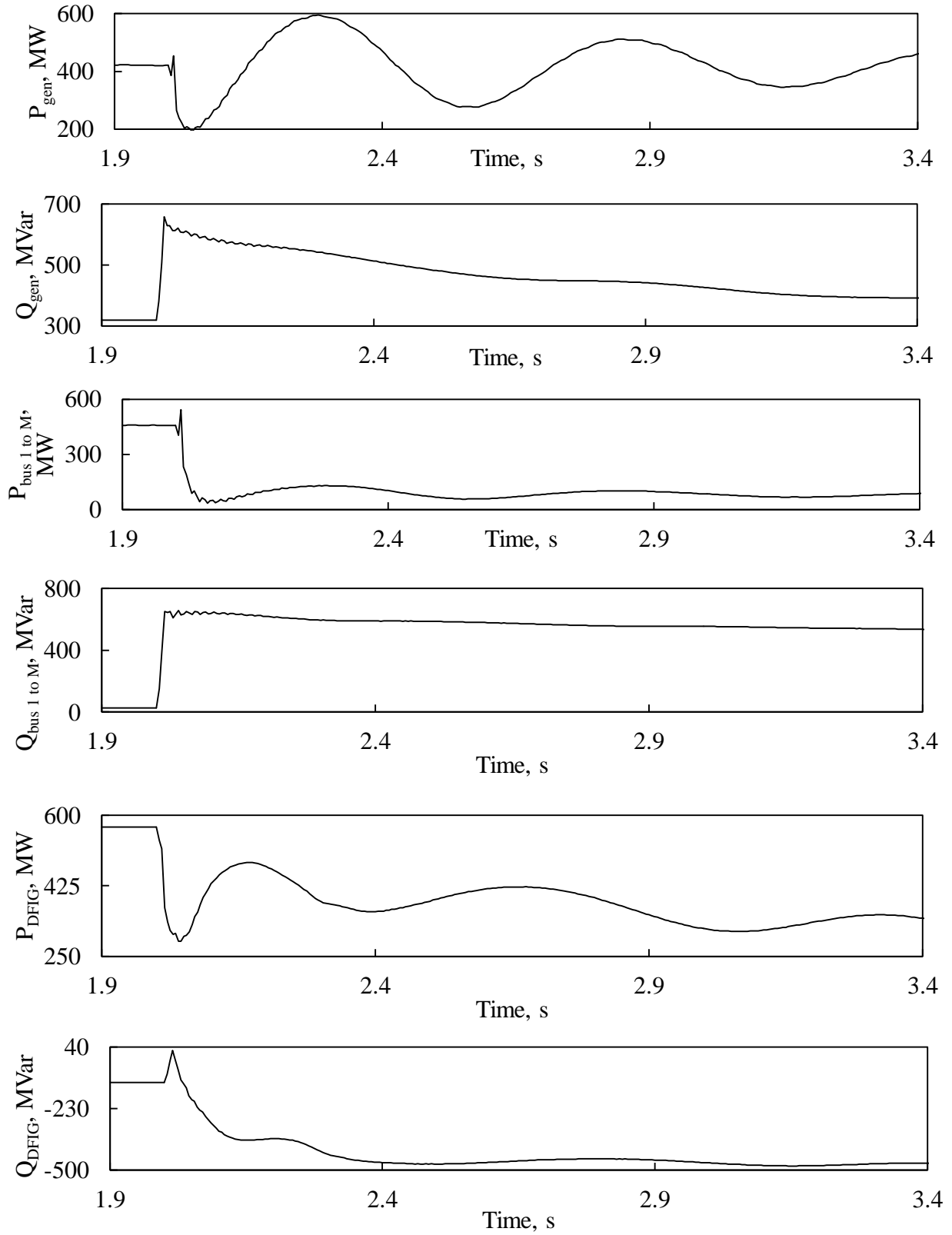


Figure 3.17: Continued.

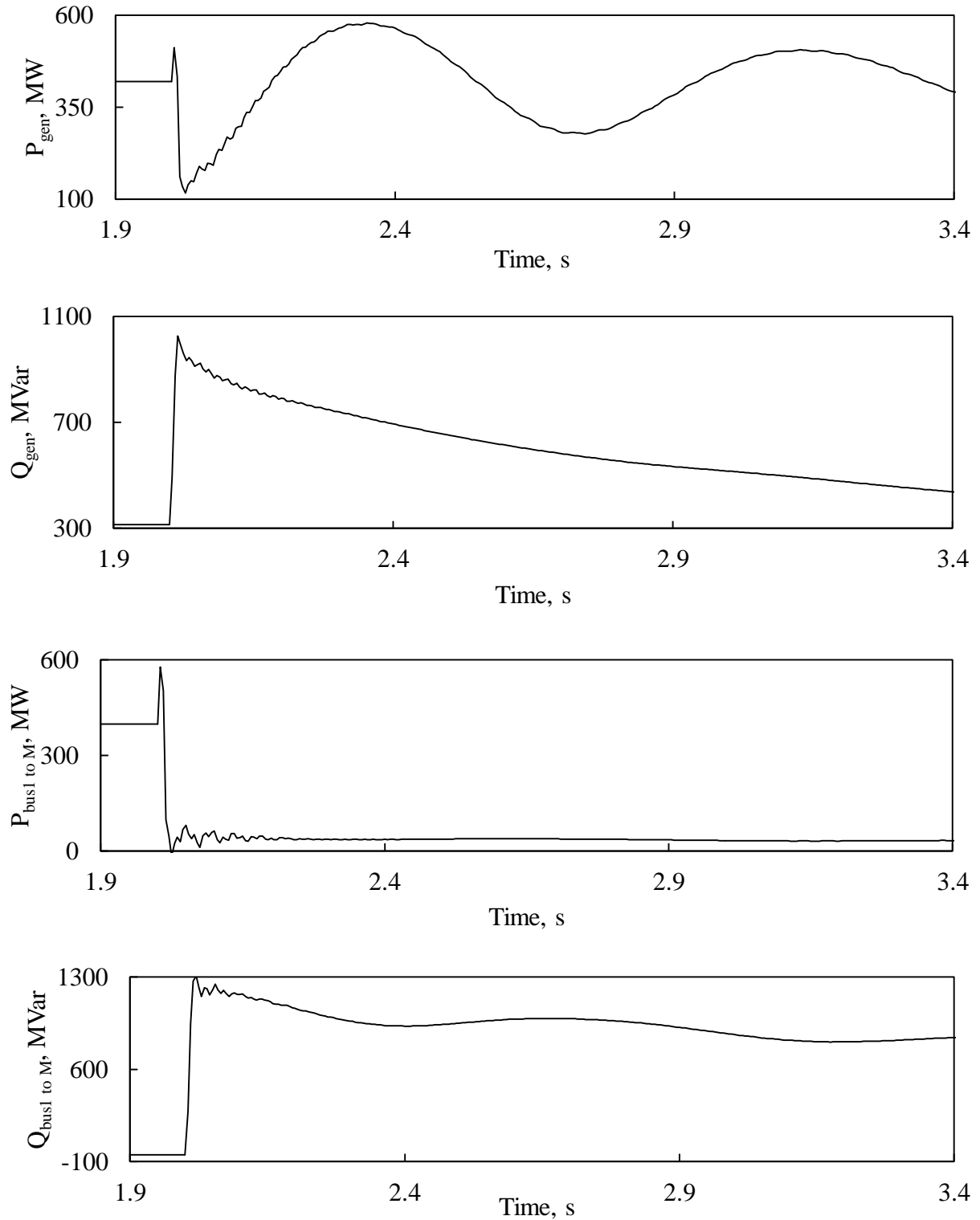


Figure 3.18: Transient time responses of generator active and reactive powers, active and reactive power flows from Bus 1 to Bus M during a three-phase fault at F_2 (no wind farm in the system).

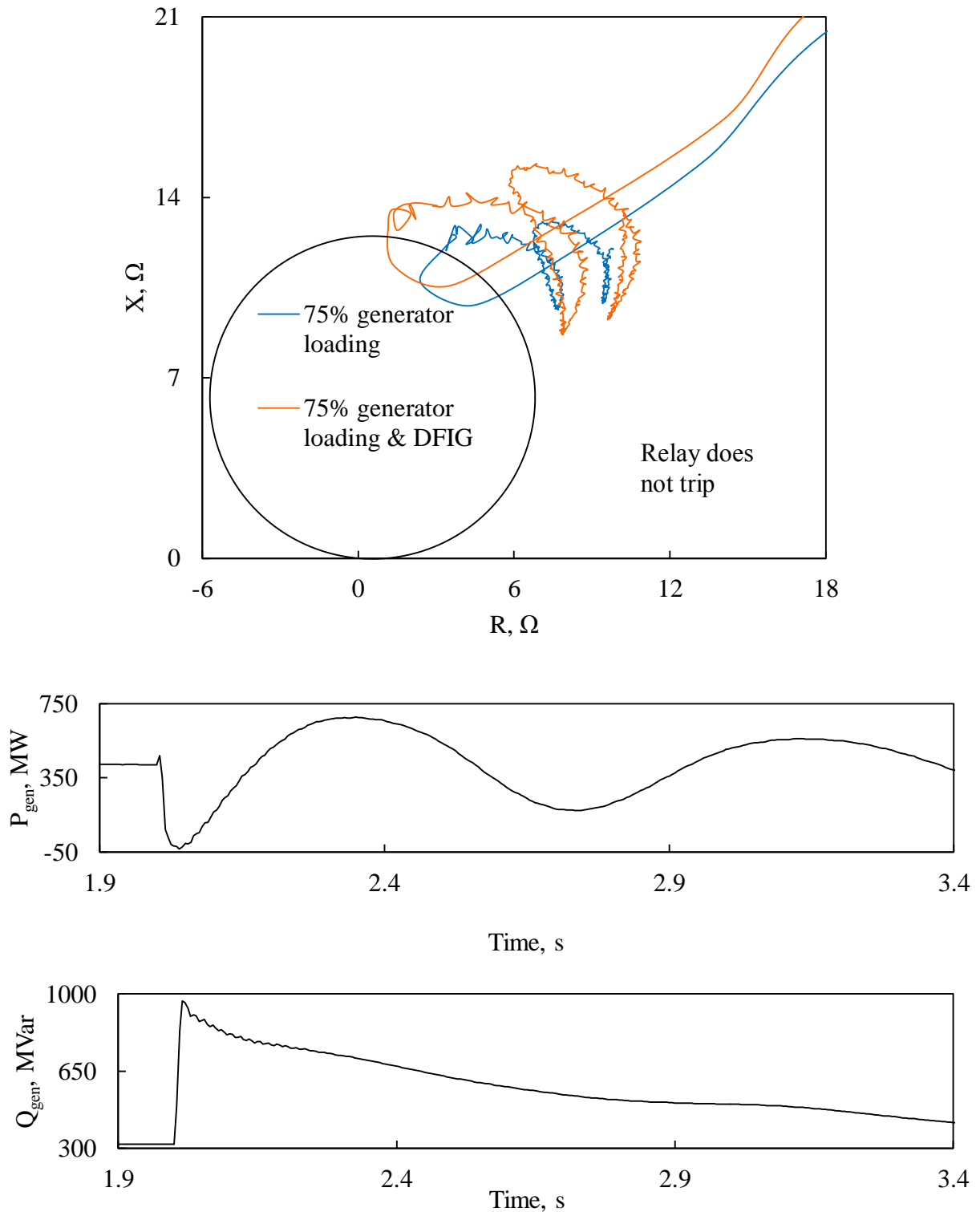


Figure 3.19: Relay (21) measured impedance trajectory, transient time responses of generator active and reactive powers, active and reactive power flows from Bus 1 to Bus M, DFIG-based wind farm active and reactive powers during a three-phase at F_2 .

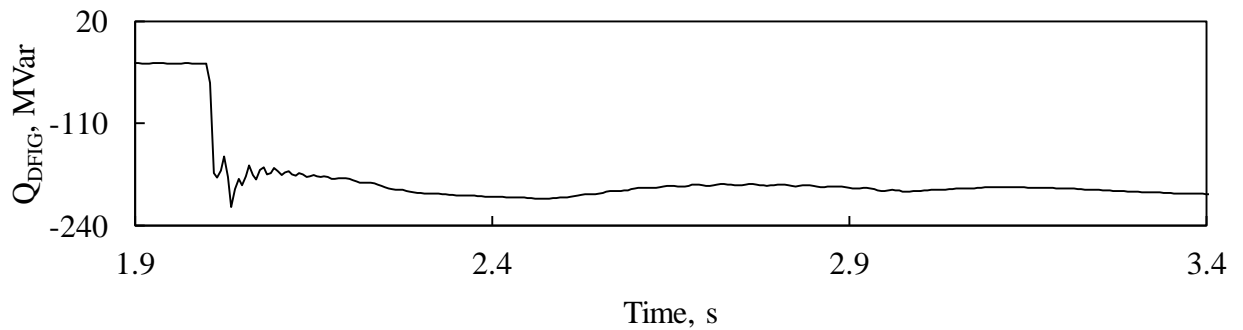
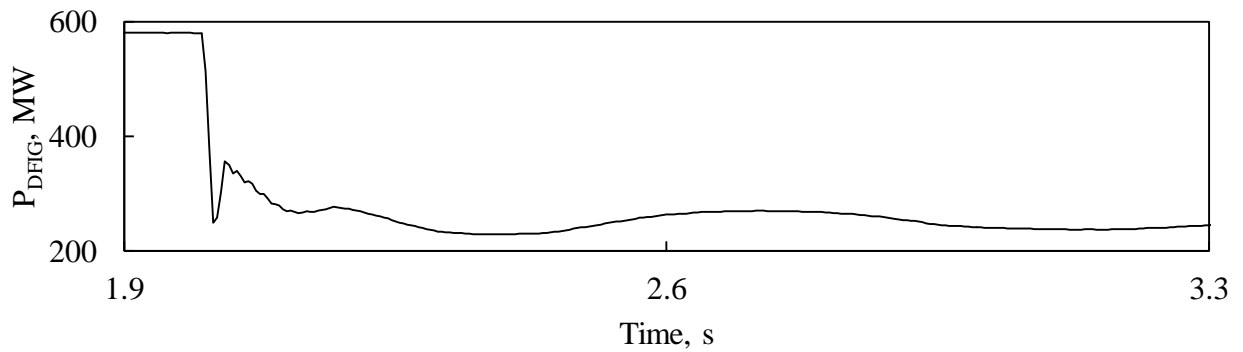
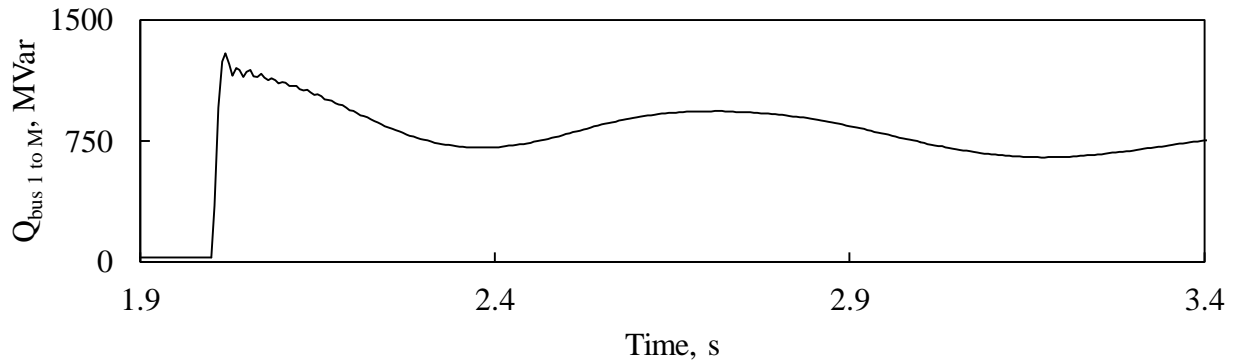
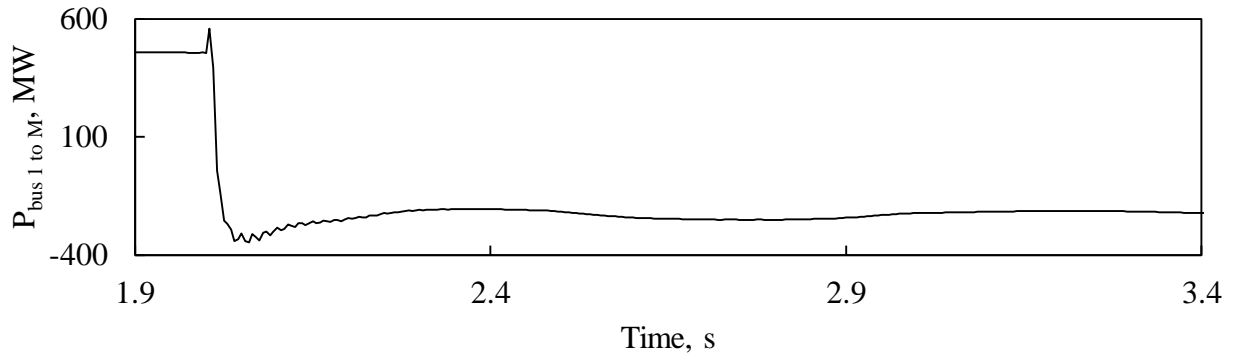


Figure 3.19: Continued.

The impact of the same faults on Relay (21) performance is also investigated for fault

location F_3 . The results of these investigations, which are very similar to the cases of faults at F_2 , are shown in Appendix C.

3.3.3 Performance of Relay (21) at 85% of the generator loading

At such a setting, the generator delivers 476 MW and 357 MVAR to systems S_1 and S_2 . Figures 3.20-3.27 depict the same transient time responses and impedance trajectories as it is displayed in the 65% and 75% generator loading cases. From all the results it can be seen that during the faults, the generator experience the same active power fluctuation, reactive power drop for the same fault location as results gained from 65% and 75% generator loading cases. The active and power flows on L_1 vary with the generator output accordingly. As for the DFIG-based wind farm, its absorbing of reactive power during the fault increases as the generator loading increases. Relay (21) operations are same as those in 65% and 75% generator loading cases with only a slightly smaller relay measured impedance than those with lower generator loadings.

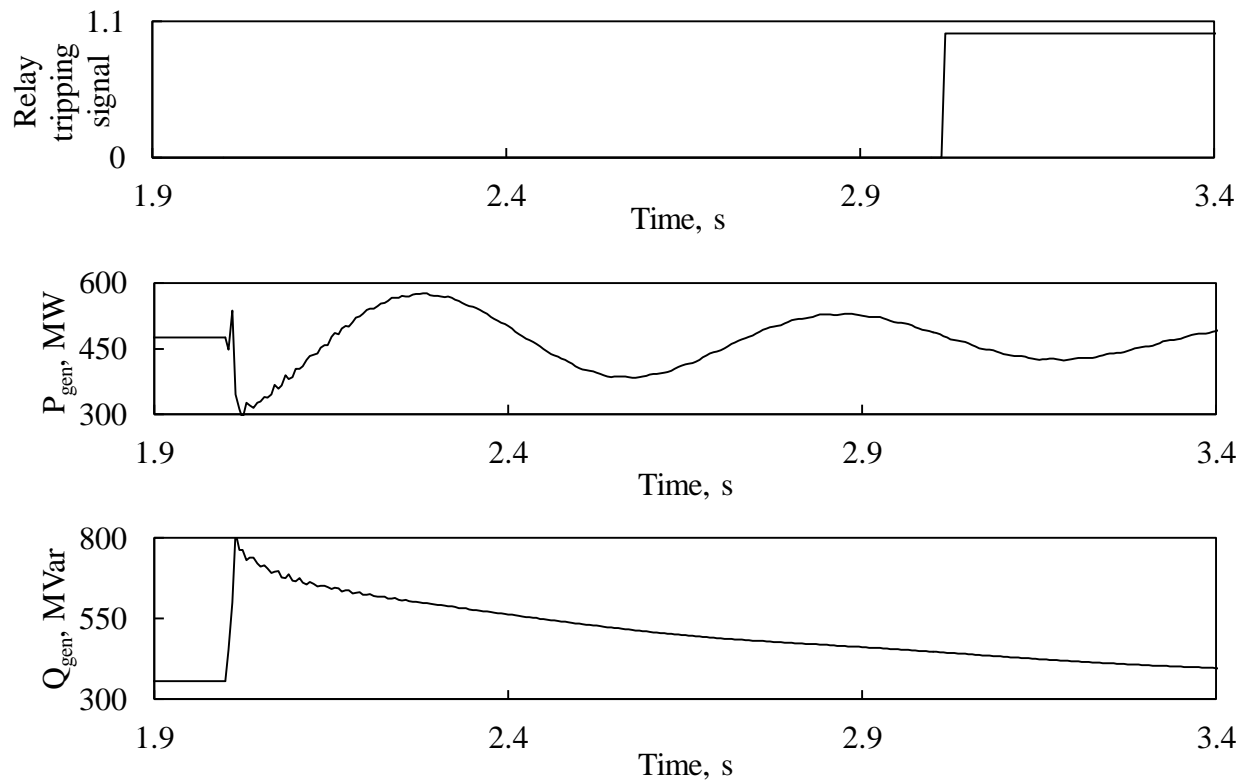


Figure 3.20: Relay (21) tripping signal, transient time responses of generator active and reactive powers, active and reactive power flows from Bus 1 to Bus M during a line-to-line fault at F_1 (no wind farm in the system).

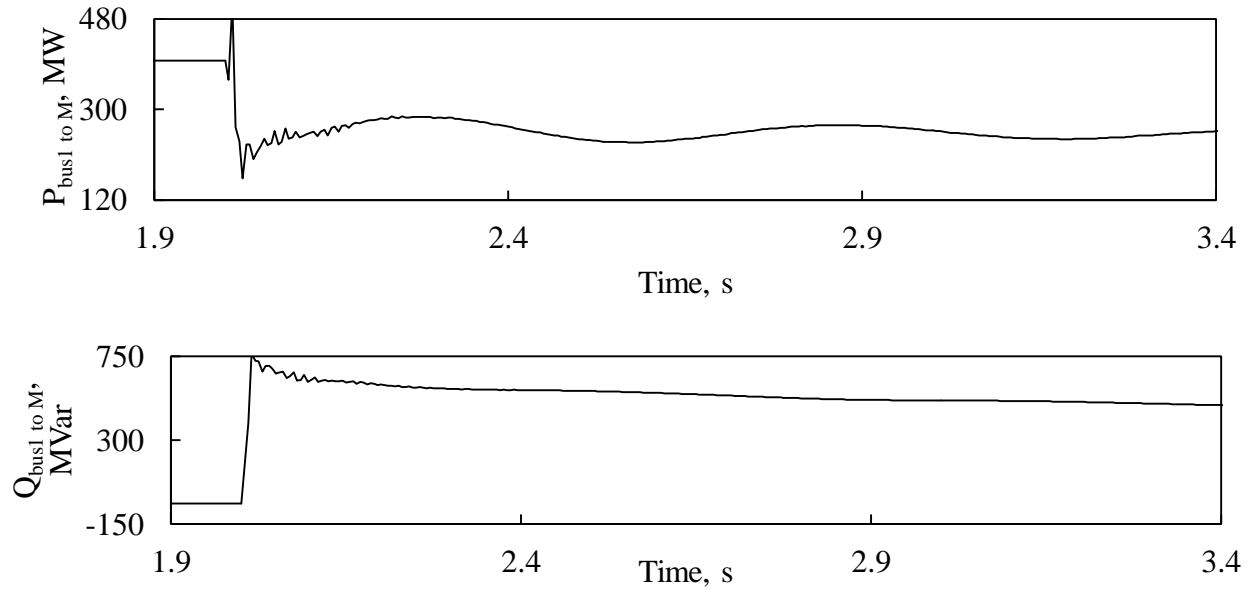


Figure 3.20: Continued.

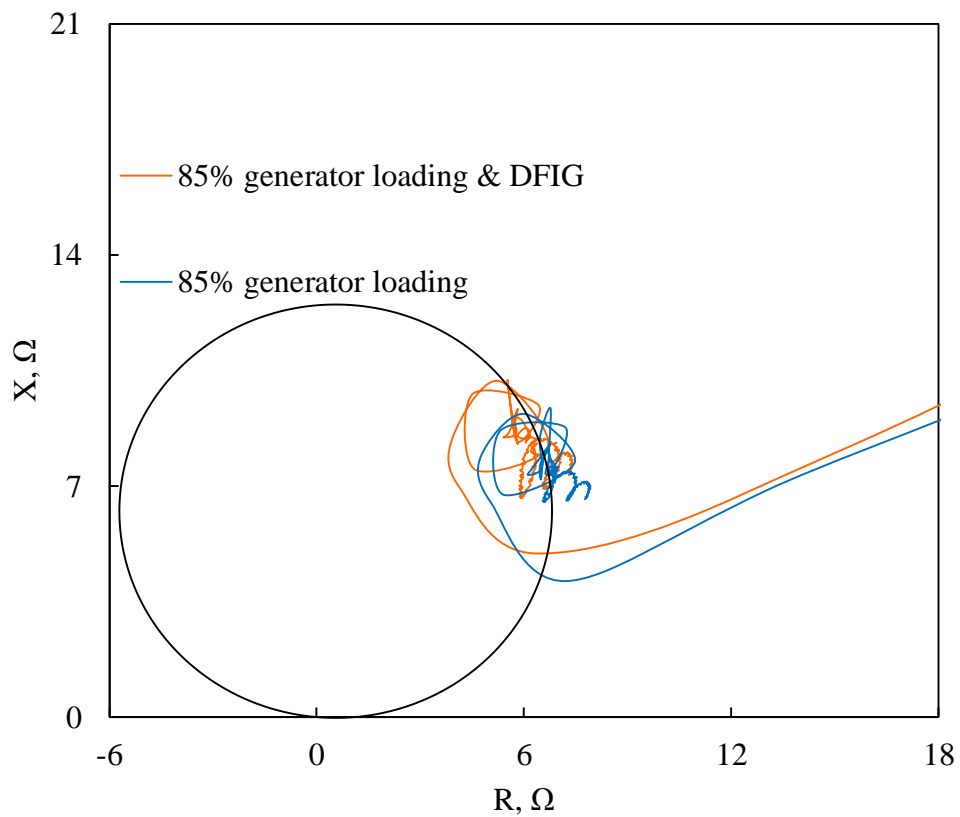


Figure 3.21: Relay (21) measured impedance trajectory and its tripping signal, transient time responses of generator active and reactive powers, active and reactive power flows from Bus 1 to Bus M, DFIG-based wind farm active and reactive powers during a line-to-line fault at F_1 .

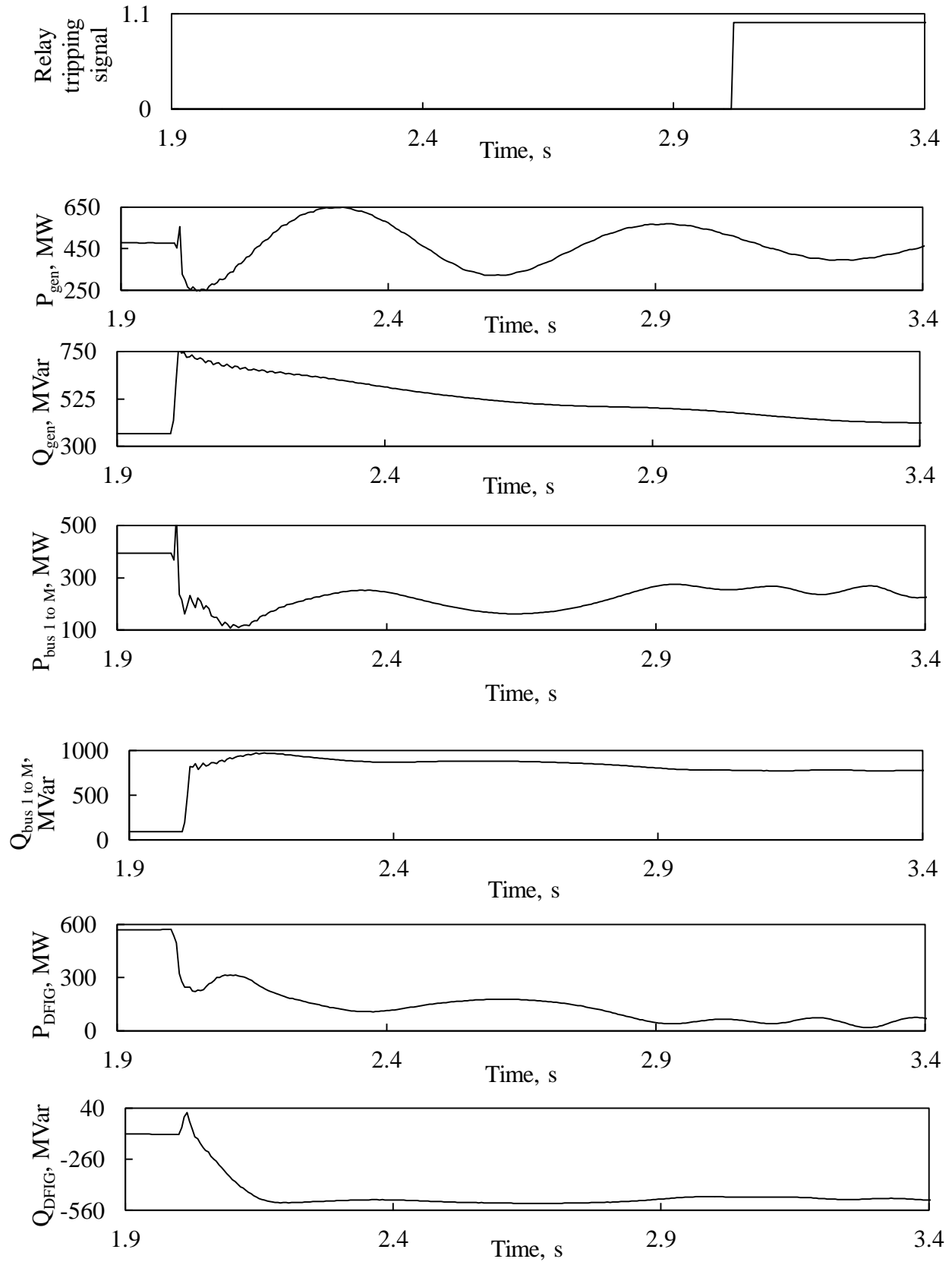


Figure 3.21: Continued.

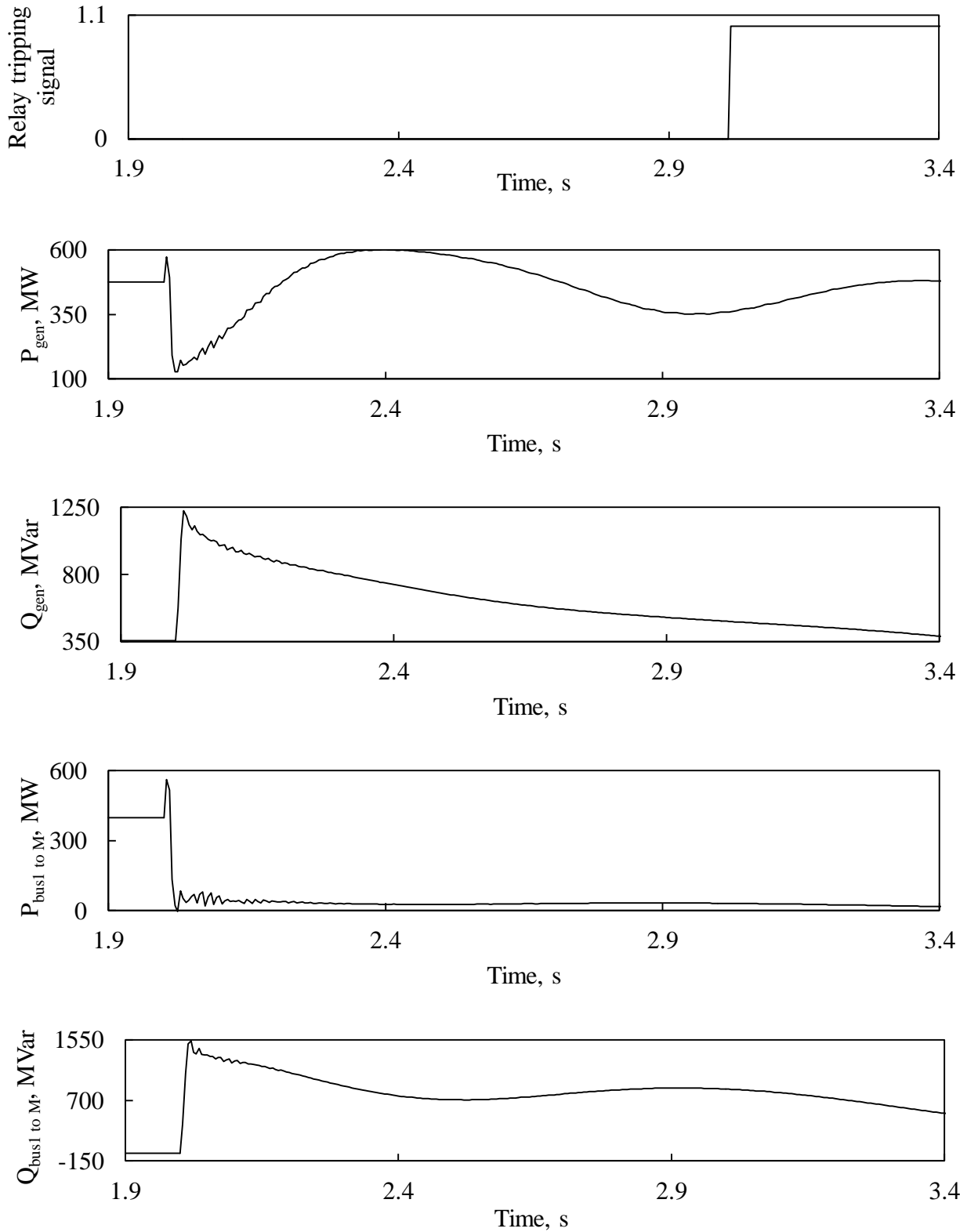


Figure 3.22: Relay (21) tripping signal, transient time responses of generator active and reactive powers, active and reactive power flows from Bus 1 to Bus M during a three-phase fault at F_1 (no wind farm in the system).

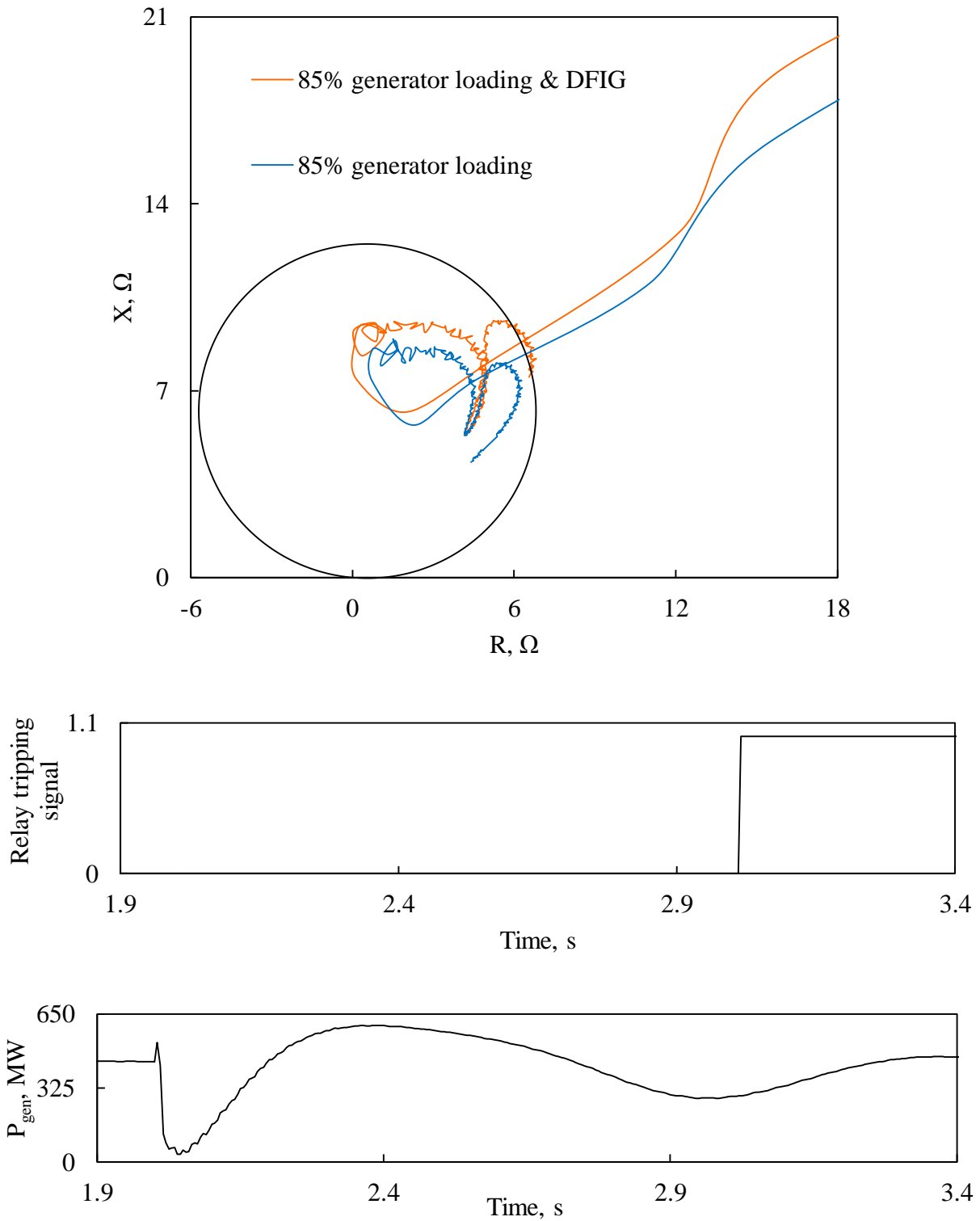


Figure 3.23: Relay (21) measured impedance trajectory and its tripping signal, transient time responses of generator active and reactive powers, active and reactive power flows from Bus 1 to Bus M, DFIG-based wind farm active and reactive powers during a three-phase at F_1 .

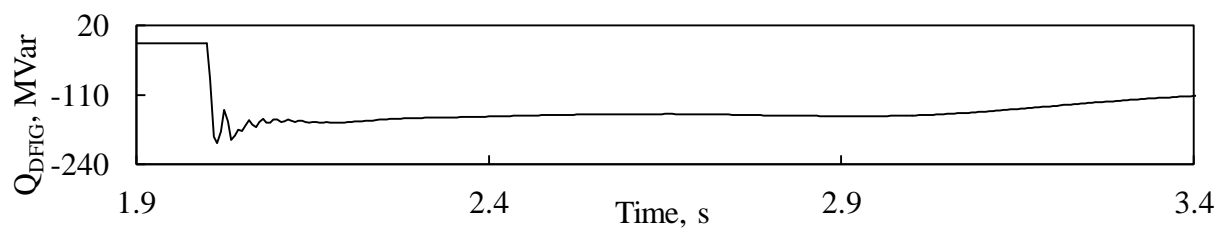
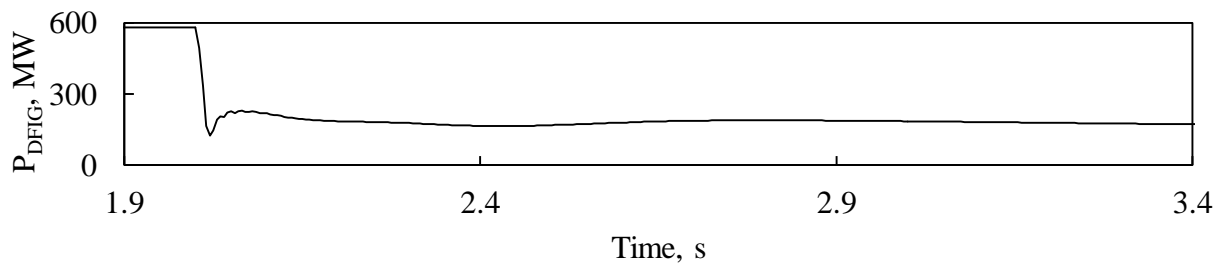
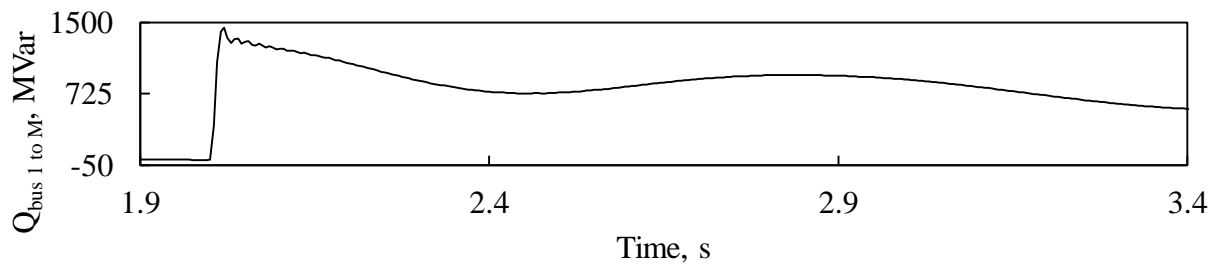
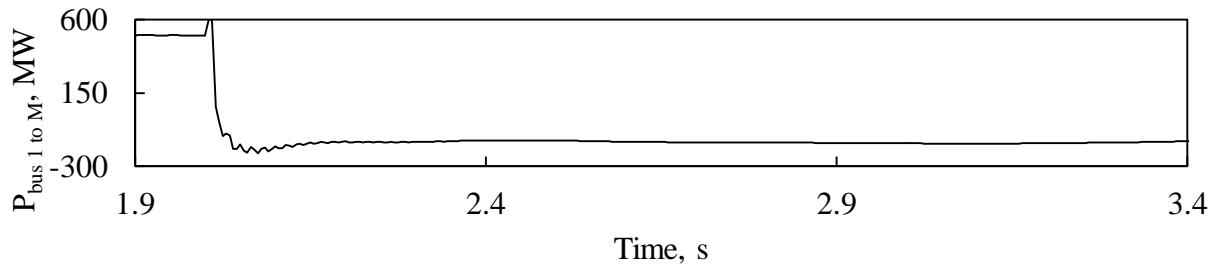
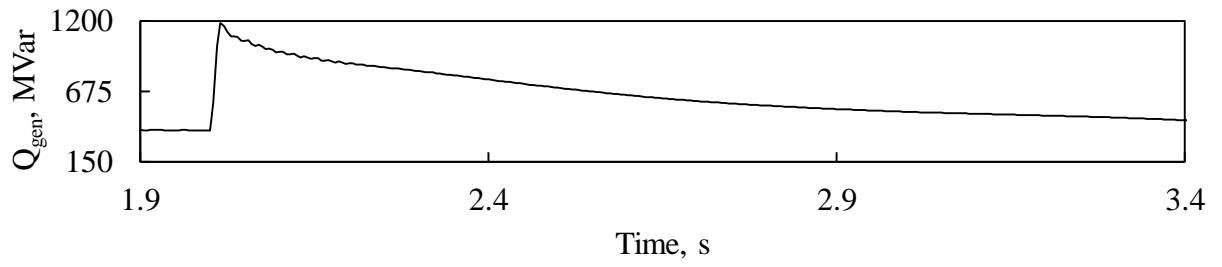


Figure 3.23: Continued.

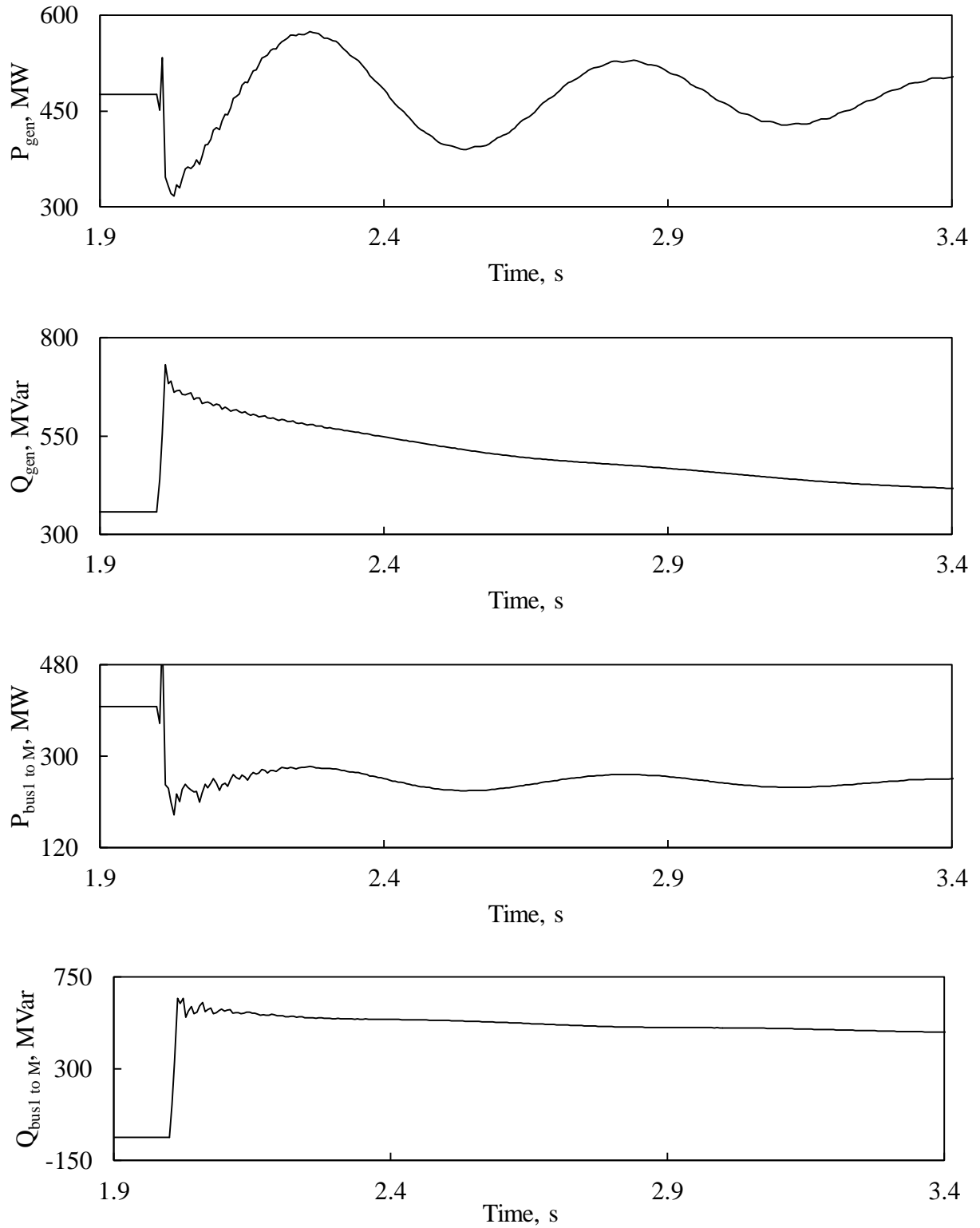


Figure 3.24: Transient time responses of generator active and reactive powers, active and reactive power flows from Bus 1 to Bus M during a line-to-line fault at F_2 (no wind farm in the system).

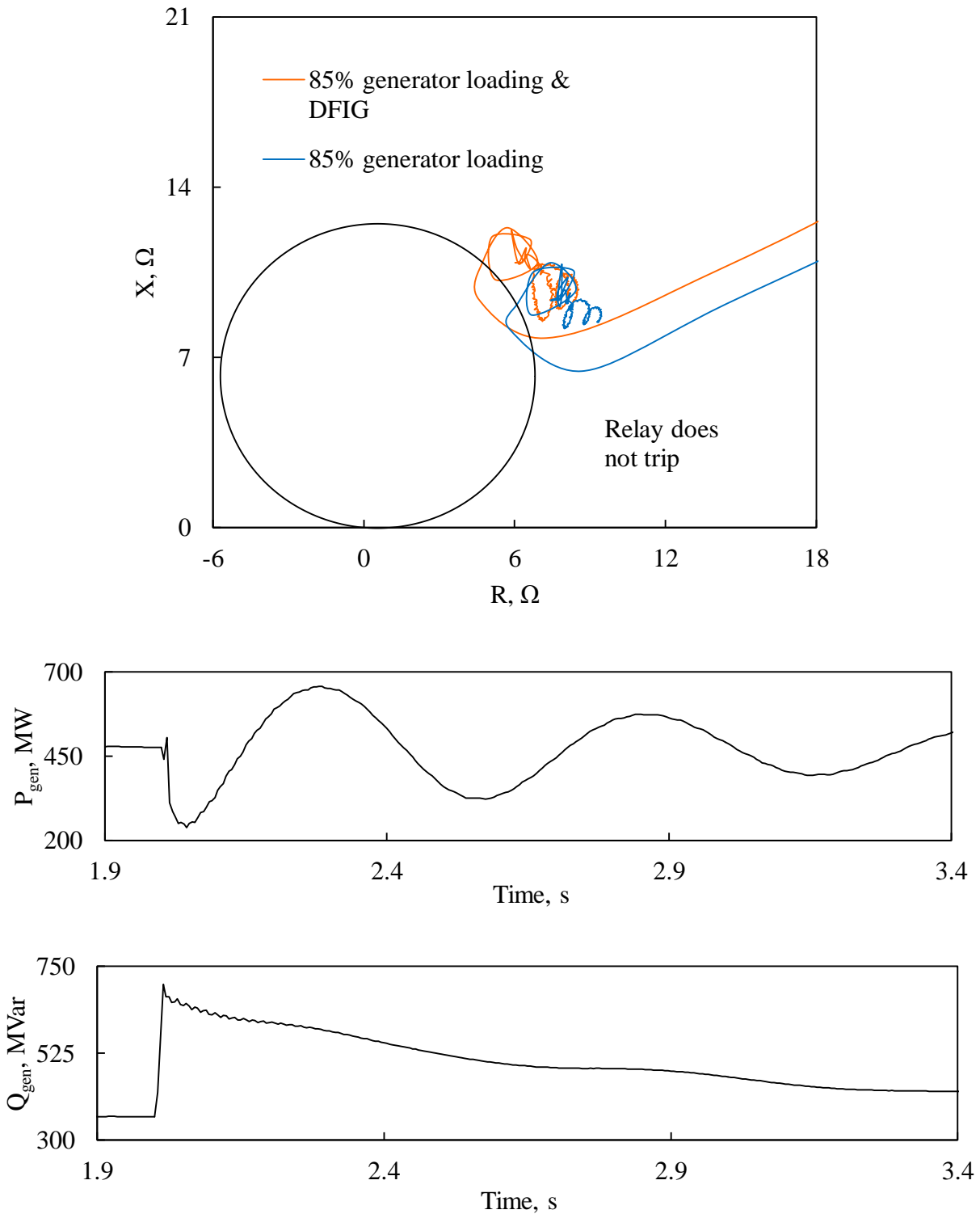


Figure 3.25: Relay (21) measured impedance trajectory, transient time responses of generator active and reactive powers, active and reactive power flows from Bus 1 to Bus M, DFIG-based wind farm active and reactive powers during a line-to-line fault at F_2 .

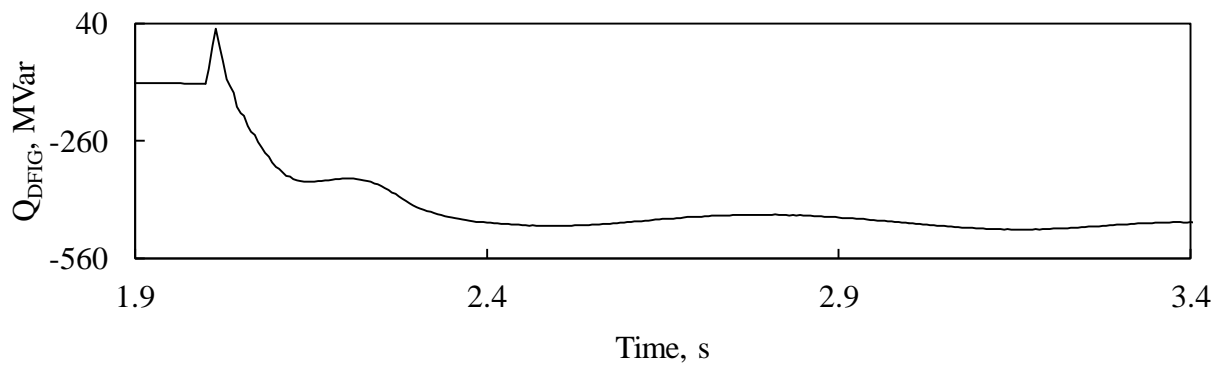
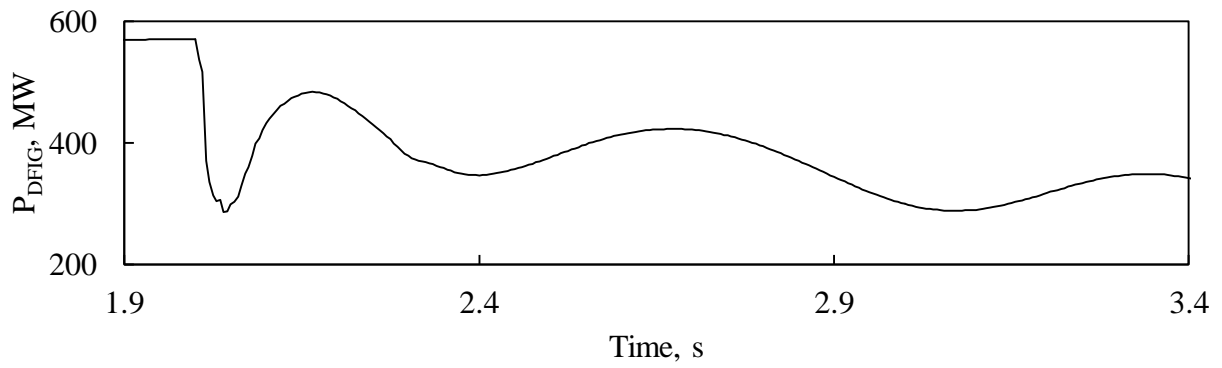
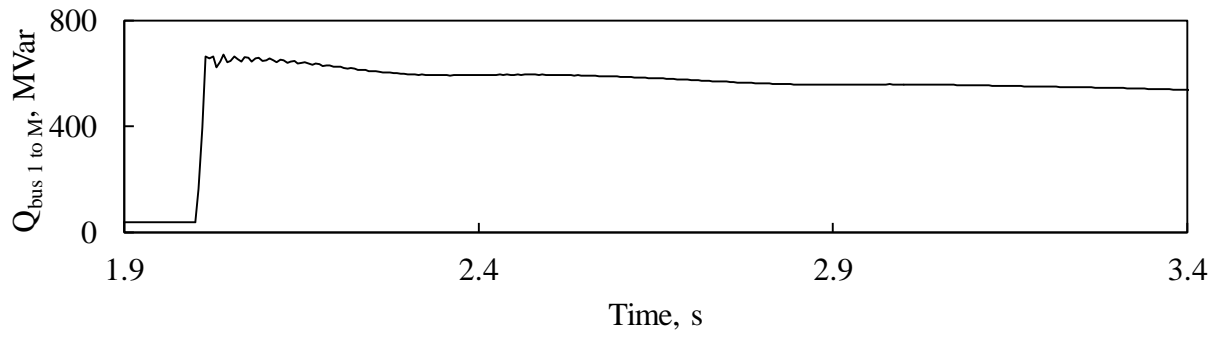
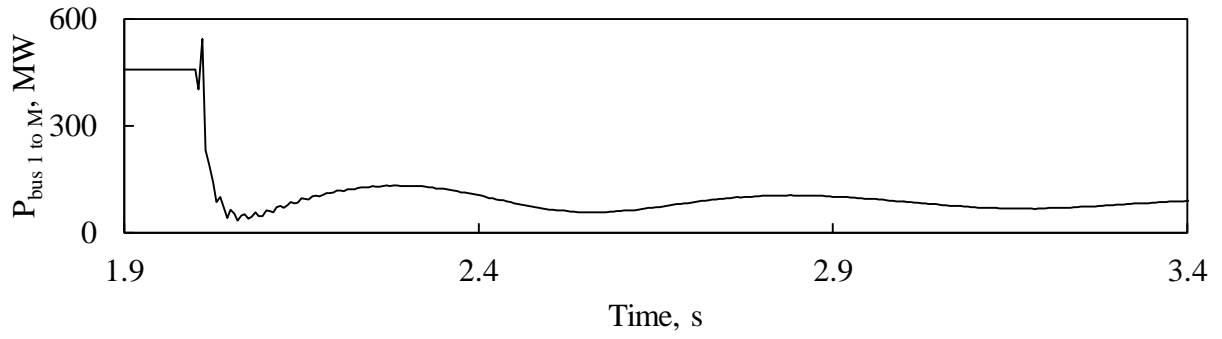


Figure 3.25: Continued.

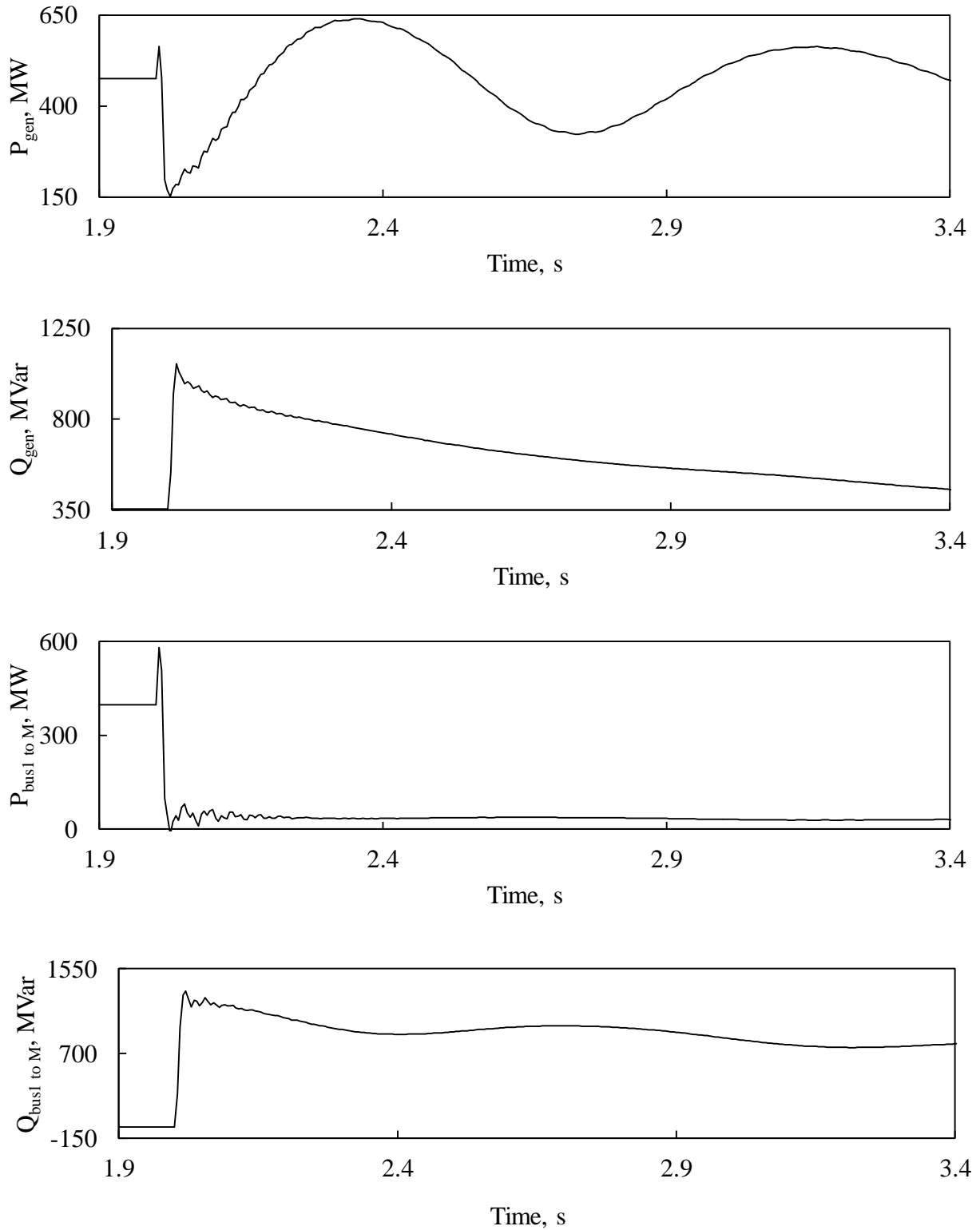


Figure 3.26: Transient time responses of generator active and reactive powers, active and reactive power flows from Bus 1 to Bus M during a three-phase fault at F_2 (no wind farm in the system).

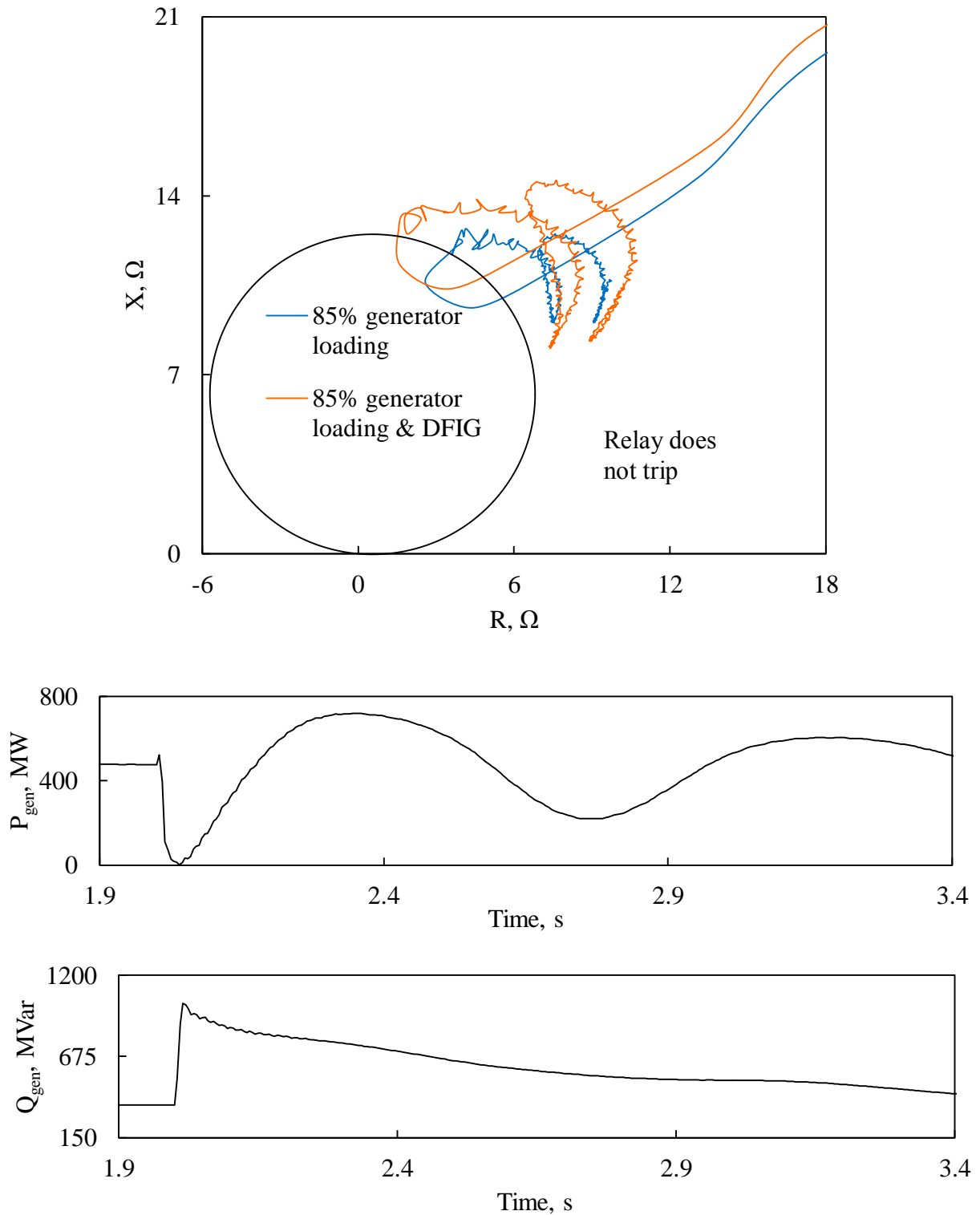


Figure 3.27: Relay (21) measured impedance trajectory, transient time responses of generator active and reactive powers, active and reactive power flows from Bus 1 to Bus M, DFIG-based wind farm active and reactive powers during a three-phase at F_2 .

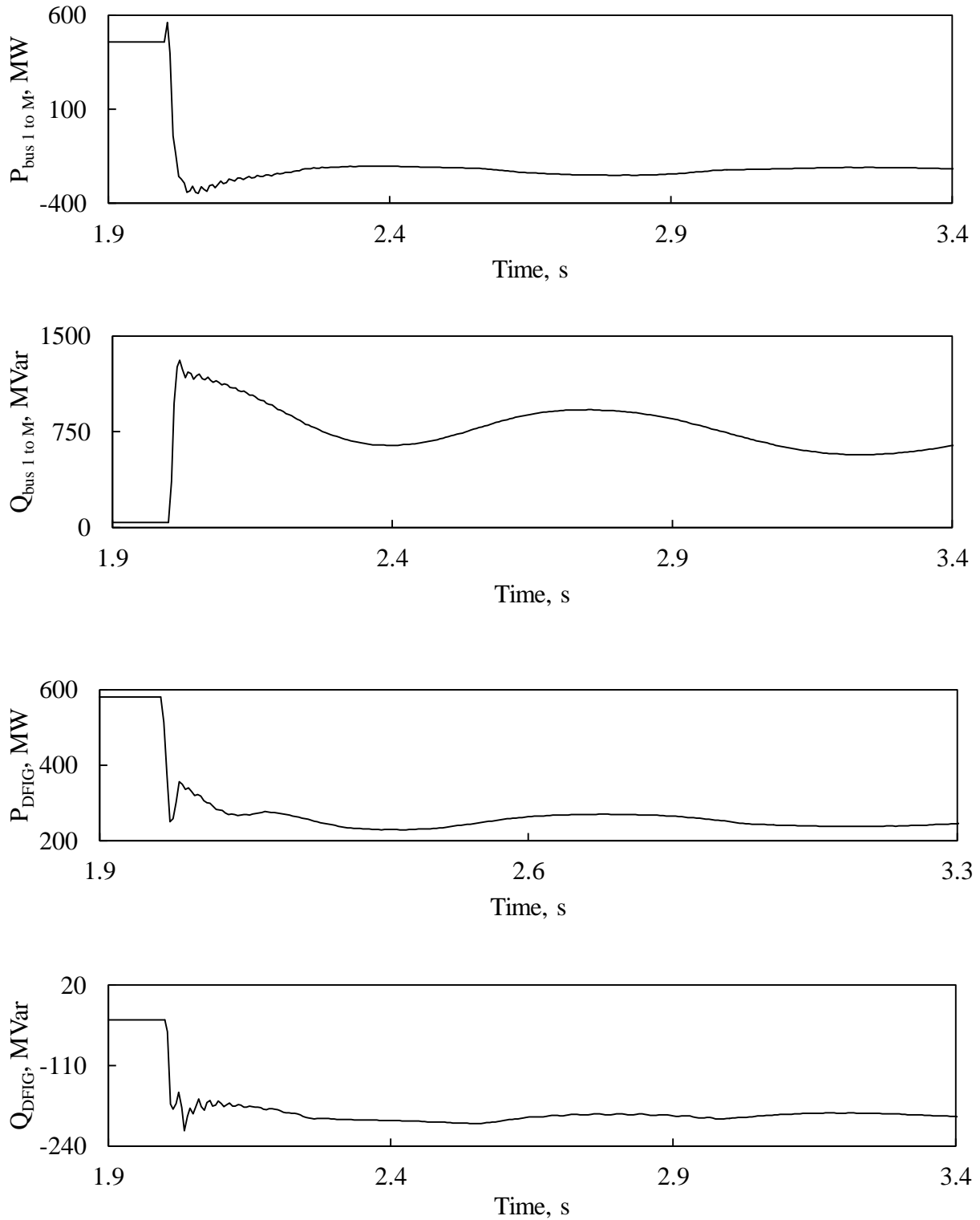


Figure 3.27: Continued.

3.3.4 Effect of the DFIG-based wind farm on Relay (21) measured impedance

In order to explore the impact of DFIG-based wind farm on Relay (21) measured impedance,

the percentage error in the measured impedance (*PEMI*) by Relay (21) is used. In this regard, *PEMI* is defined as:

$$PEMI, \% = 100 \times \frac{|Z_W| - |Z_N| \cos(\theta_N - \theta_W)}{|Z_N| \cos(\theta_N - \theta_W)} \quad (3.3)$$

where $Z_N \angle \theta_N$ and $Z_W \angle \theta_W$ are respectively, the measured impedances by the relay without or with the DFIG-based wind farm.

The impact of the DFIG-based wind farm is explained with respect to the variation of *PEMI*. The larger the *PEMI* value is, the more severe the effect of the wind farm is. The results presented in Figures 3.28 and 3.29 depict the effect of the DFIG-based wind farm on the relay measured impedance for three-phase and line-to-line faults respectively. The following observations can be stated from these figures.

3.3.4.1 Effect of the generator loading

For the same fault location, *PEMI* increases as the generator loading decreases in the cases of line-to-line faults. For three-phase faults, *PEMI* increases as the generator loading increases.

3.3.4.2 Effect of the fault type

The *PEMI* caused by the DFIG-based wind farm due to line-to-line faults is higher than those due to three-phase faults. In the cases of faults at F_1 , the maximum value of *PEMI* is -5.47% for line-to-line fault and 1.71% for three-phase fault. In the cases of faults at F_2 , the maximum value of *PEMI* is -7.43% for line-to-line fault and 2.13% for three-phase fault. In the cases of faults at F_3 , the maximum value of *PEMI* is -9.56% for line-to-line fault and 3.82% for three-phase fault.

3.3.4.3 Effect of the fault Location

PEMI decreases as the fault location varies from the upstream to the downstream of L_1 . For both line-to-line and three-phase faults, the maximum values of *PEMI* are observed for faults at F_3 .

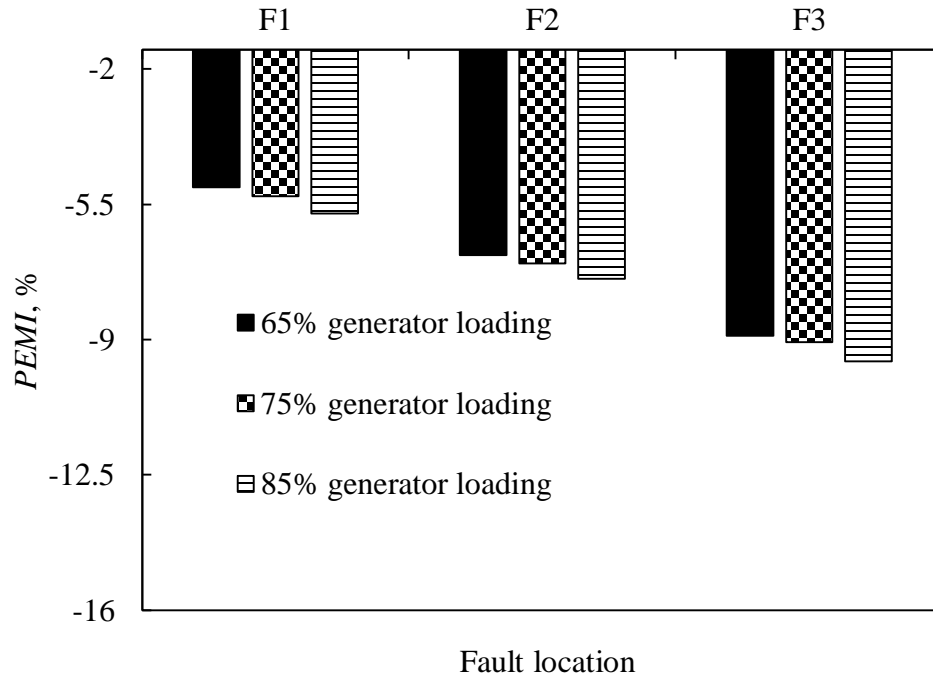


Figure 3.28: *PEMI* for line-to-line faults at different generator loading levels.

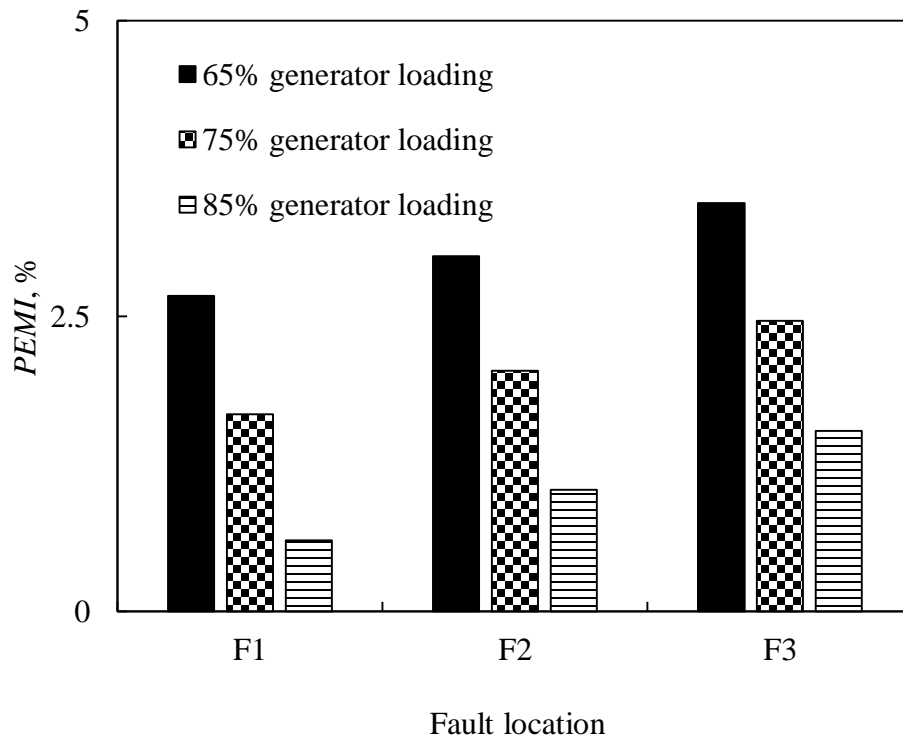


Figure 3.29: *PEMI* for three-phase faults at different generator loading levels.

3.3.5 Effect of the transmission line power flows

In all the previous study cases, it is assumed that most of the generator real power output flows in L_1 as illustrated in Figure 3.3. In order to explore the effect of the transmission line power flows on Relay (21) performance, the system power flow is adjusted such that most of the generator real power output at 65% of its loading would flow in L_2 as shown in Figure 3.30.

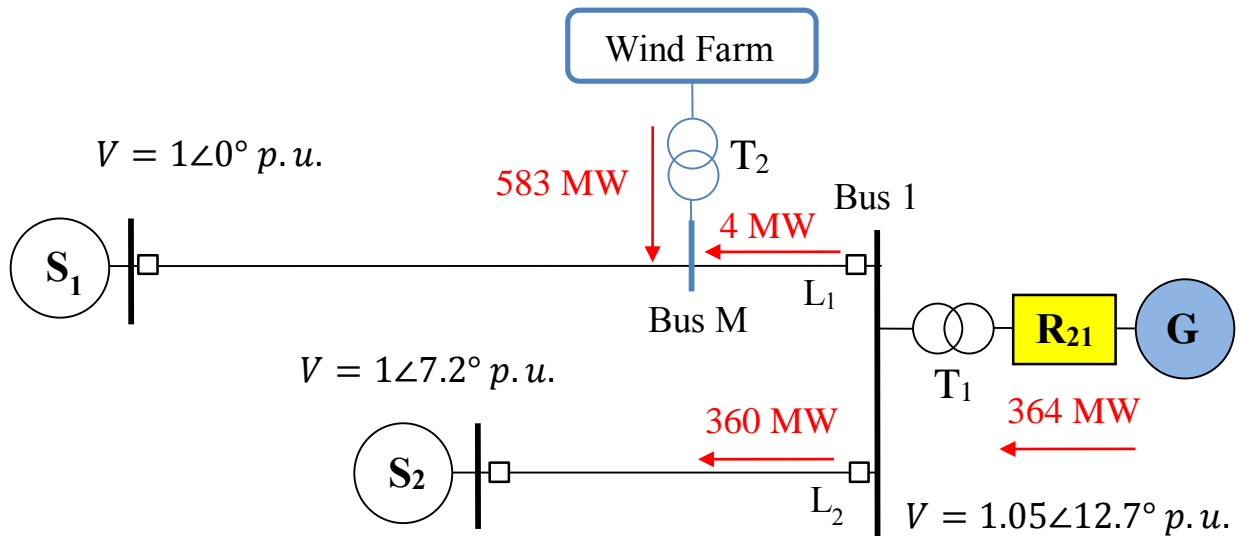


Figure 3.30: Load flow results of the bus voltages and real power flows of the system under 65% generator loading.

Figure 3.31 illustrates Relay (21) tripping signal, transient time responses of the generator active and reactive powers as well as the active and reactive power flows from Bus 1 to Bus M during a line-to-line fault at F_1 when there is no wind farm in the system. After connecting the DFIG-based wind farm at Bus M, Figure 3.32 depicts the same responses in addition to the measured impedance trajectories of Relay (21). Figures 3.33 and 3.34 show the same trajectories, signals in conjunction with transient time responses for the cases of three-phase fault at the same location.

Through observing Figures 3.31 to 3.34, it can be seen that with only 4 MW flowing on L_1 , the generator output, L_1 load flow situations and the DFIG-based wind farm output during faults are similar to those when 360 MW flow in L_1 (shown in Figures 3.4 to 3.7). Relay (21) operation and measured trajectories are not significantly affected by the presence of the wind farm.

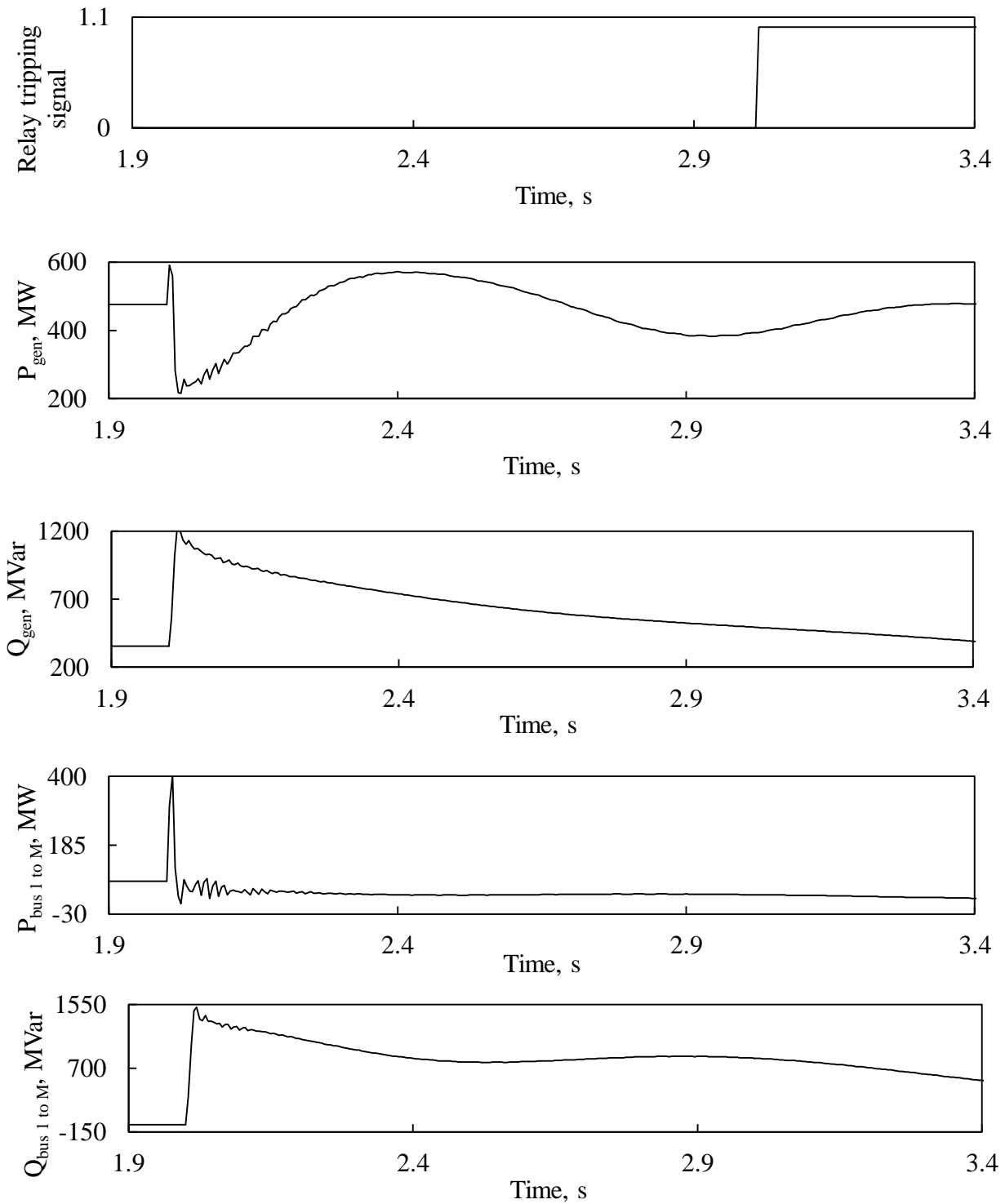


Figure 3.31: Relay (21) tripping signal, transient time responses of generator active and reactive powers, active and reactive power flows from Bus 1 to Bus M during a line-to-line fault at F_1 (no wind farm in the system).

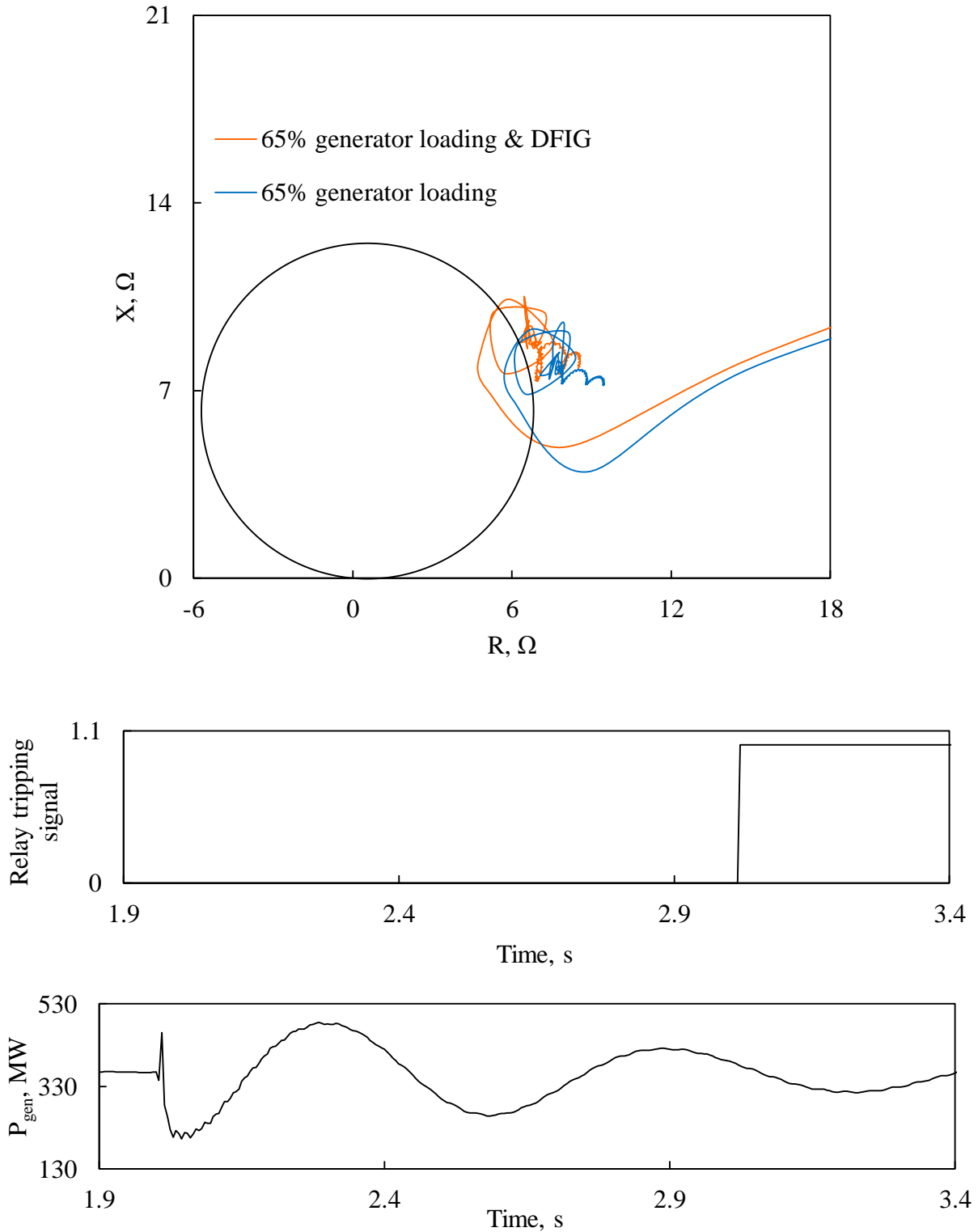


Figure 3.32: Relay (21) measured impedance trajectory and its tripping signal, transient time responses of generator active and reactive powers, active and reactive power flows from Bus 1 to Bus M, DFIG-based wind farm active and reactive powers during a line-to-line fault at F_1 .

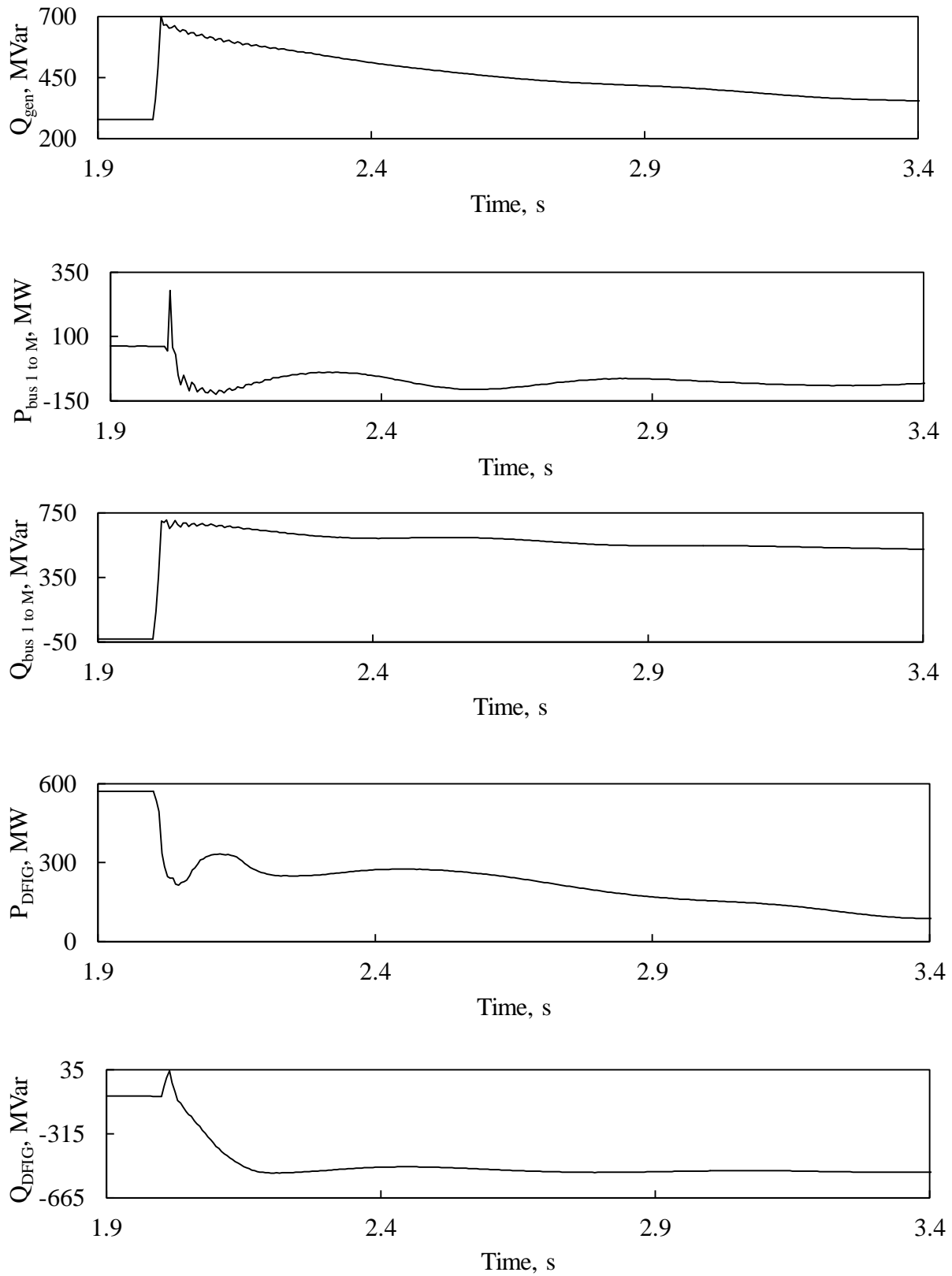


Figure 3.32: Continued.

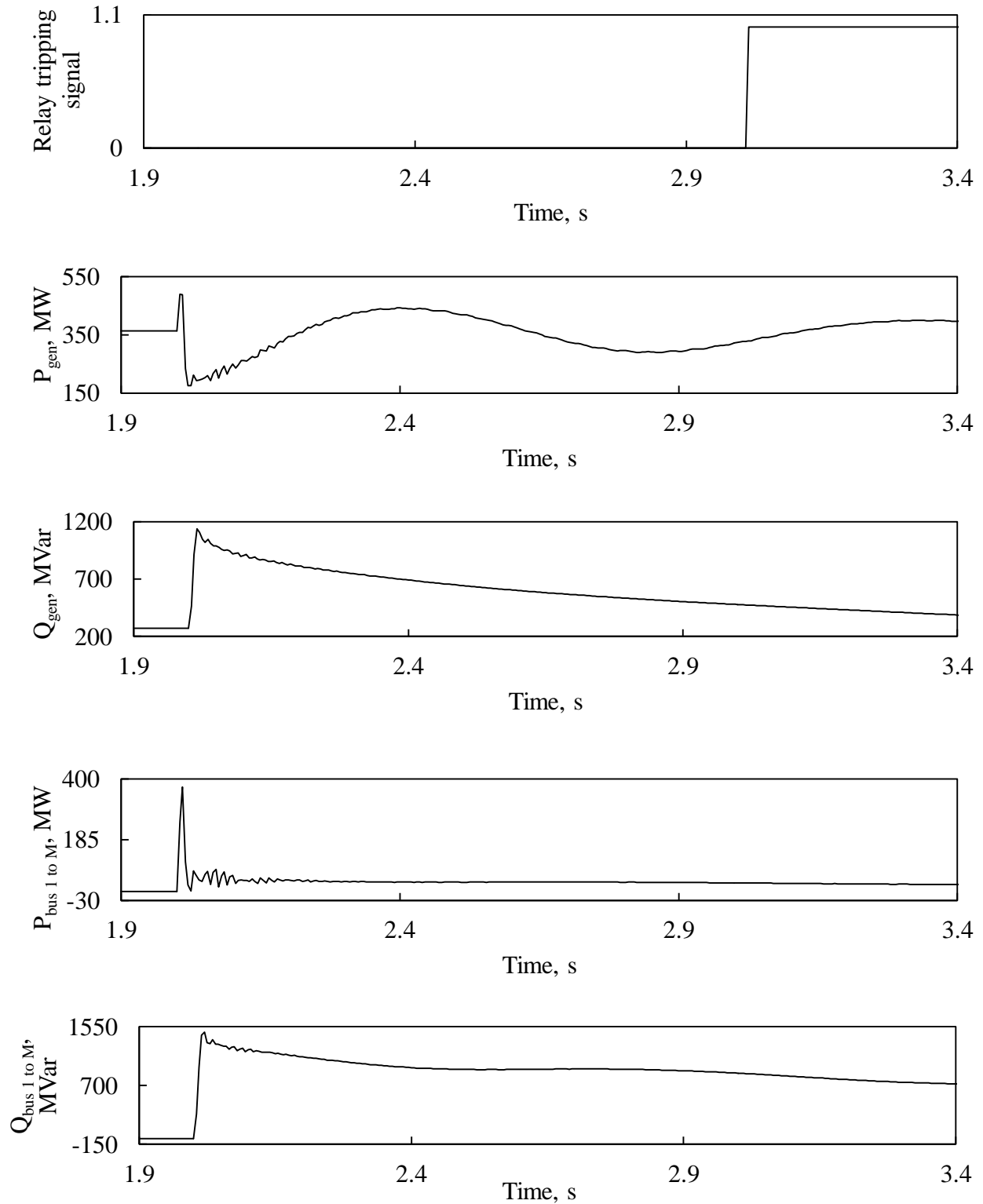


Figure 3.33: Relay (21) tripping signal, transient time responses of generator active and reactive powers, active and reactive power flows from Bus 1 to Bus M during a three-phase fault at F_1 (no wind farm in the system).

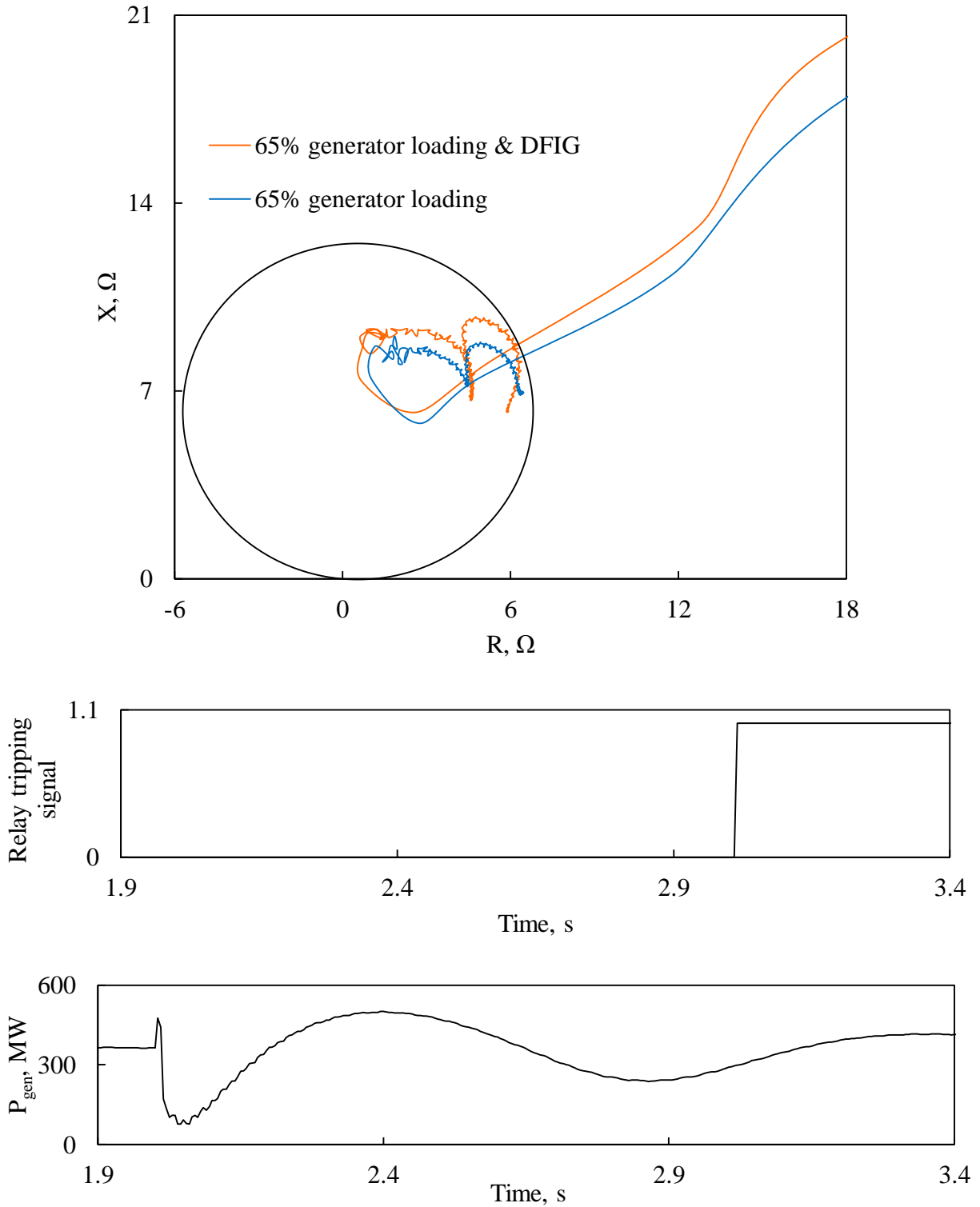


Figure 3.34: Relay (21) measured impedance trajectory and its tripping signal, transient time responses of generator active and reactive powers, active and reactive power flows from Bus 1 to Bus M, DFIG-based wind farm active and reactive powers during a three-phase at F_1 .

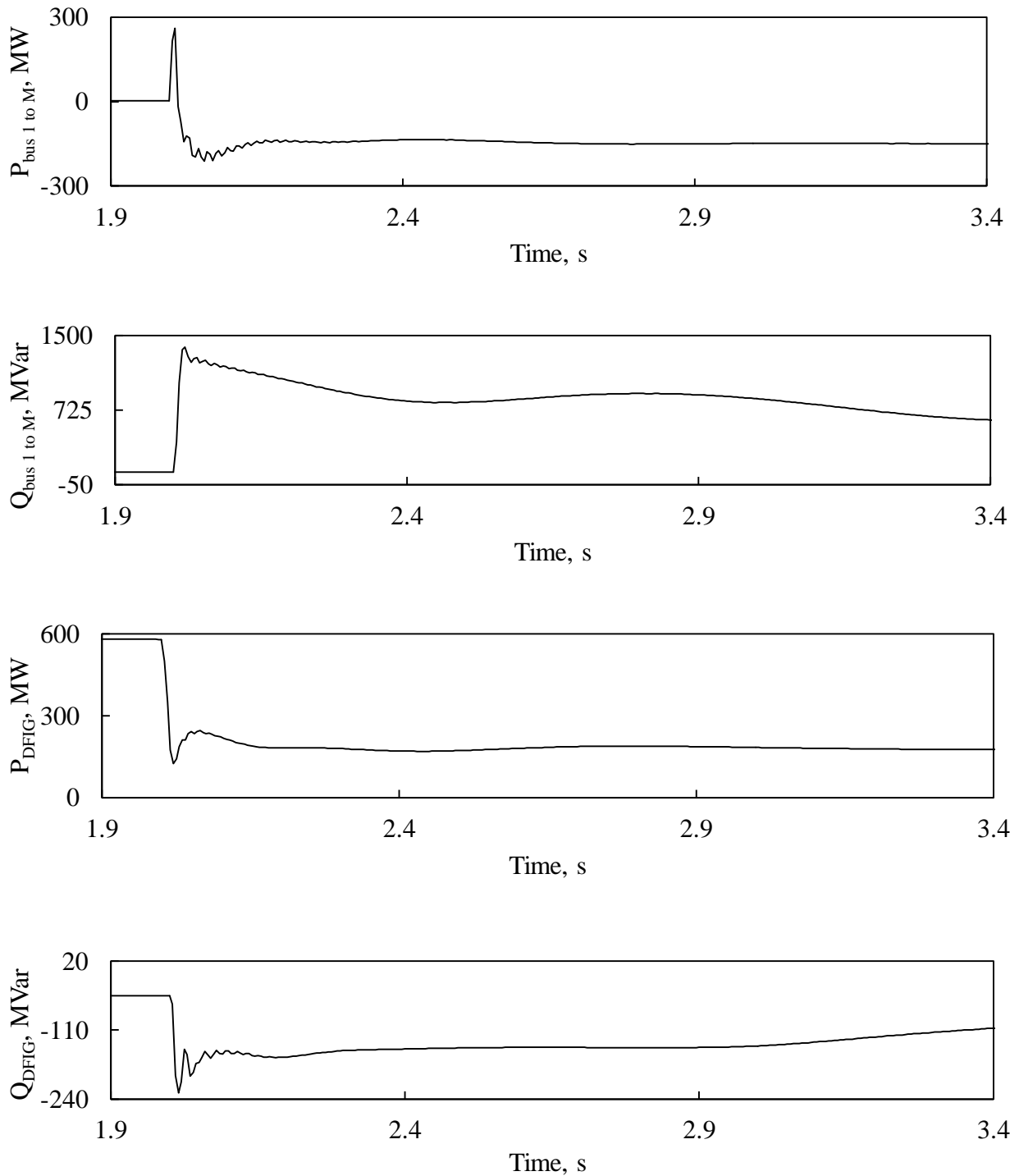


Figure 3.34: Continued.

Different *PEMI* values under different L_1 power flow conditions for line-to-line and three-phase faults are shown in Figures 3.35 and 3.36. It can be seen that *PEMI* decreases as the power flowing on L_1 decreases. This is true for both line-to-line and three-phase faults.

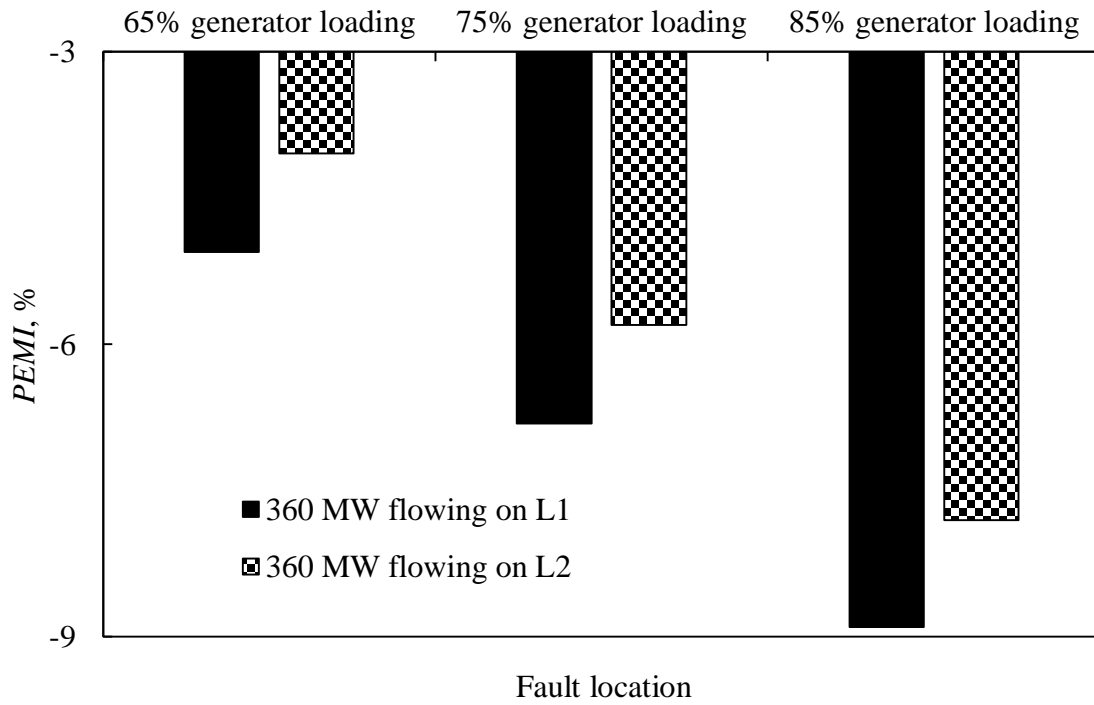


Figure 3.35: *PEMI* for line-to-line faults at different L_1 power flow conditions.

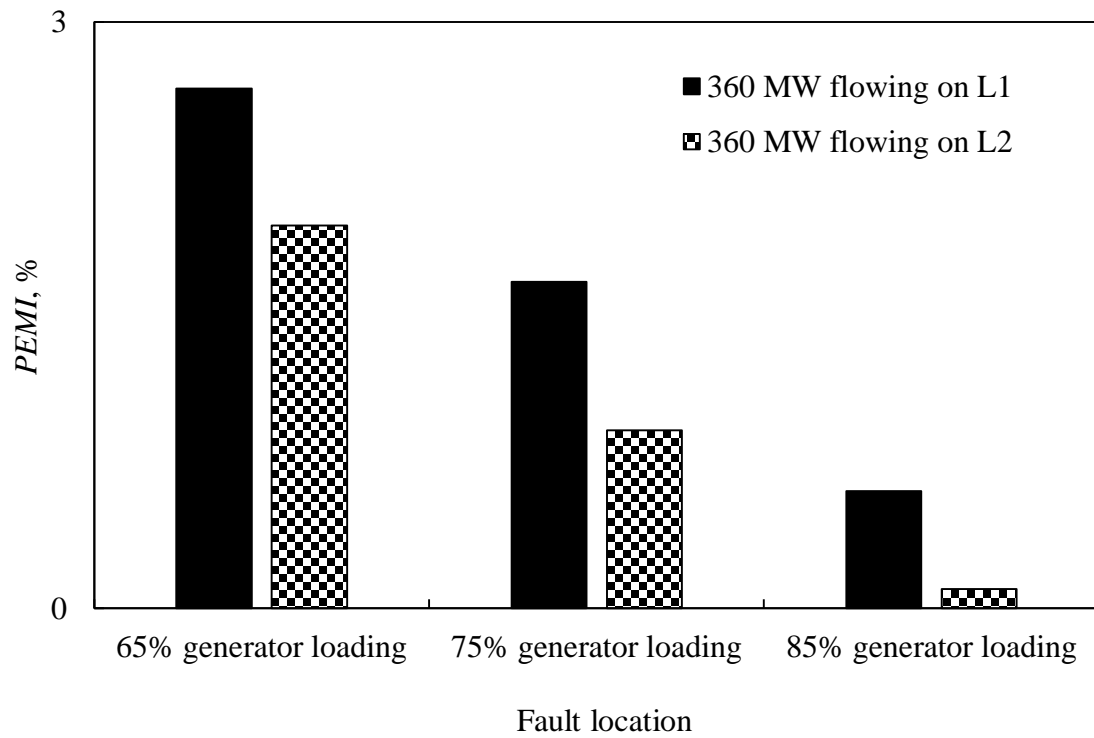


Figure 3.36: *PEMI* for three-phase faults at different L_1 power flow conditions.

3.3.6 Effect of the DFIG-based wind farm rating and location

In order to examine the effect of the DFIG-based wind farm rating and location on Relay (21) performance, a 1200 MW wind farm (twice the rating of the original wind farm in Figure 3.3) is assumed to be tapped to the middle of L_1 (Bus K, 200 km from bus 1) as shown in Figure 3.37.

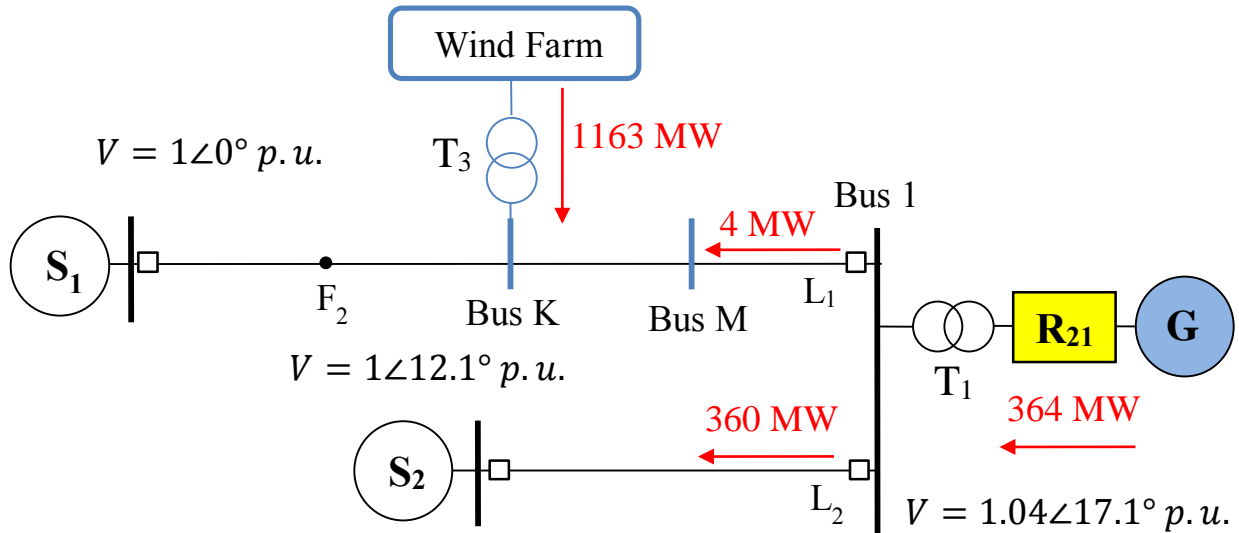


Figure 3.37: Load flow results of the bus voltages and real power flows of the system under 65% generator loading.

From comparing Figures 3.38 - 3.41 with Figures 3.8 - 3.11, the following observations are noted:

- The DFIG-based wind farm still absorbs a large amount of reactive power during both line-to-line and three-phase faults.
- For the case of a 1200 MW DFIG-based wind farm at Bus K, the generator loses its stability during a three-phase fault at F_2 . Notice the system oscillations in Figure 3.41. This is in contrast to the case of a 600 MW wind farm at Bus M which is shown in Figure 3.11.

For the performance of Relay (21), in the cases of line-to-line faults, it can be seen by comparing the trajectories in Figures 3.39 and 3.9 that:

- Relay (21) experiences a more significant effect caused by the DFIG-based wind farm when its rating is raised from 600 MW to 1200 MW and moved from Bus M to Bus K during the same fault at F_2 .

In cases of the three-phase faults, comparing Figures 3.41 and 3.11, it can be seen that:

- Although the system goes out of step with the 1200 MW wind farm, the overall location of relay trajectories in two wind farm rating and location cases are still similar.

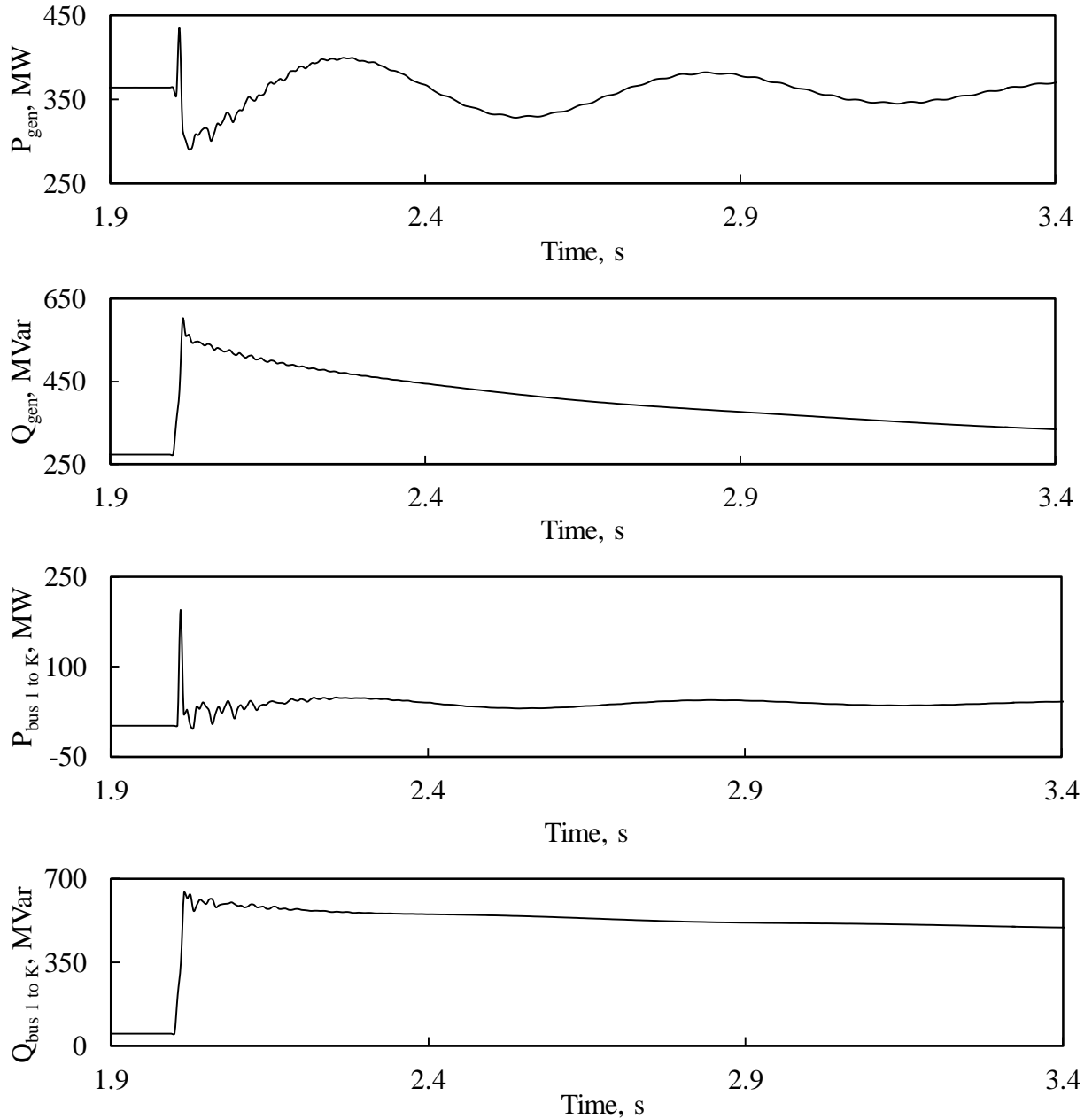


Figure 3.38: Transient time responses of generator active and reactive powers, active and reactive power flows from Bus 1 to Bus K, during a line-to-line fault at F_2 (no wind farm in the system).

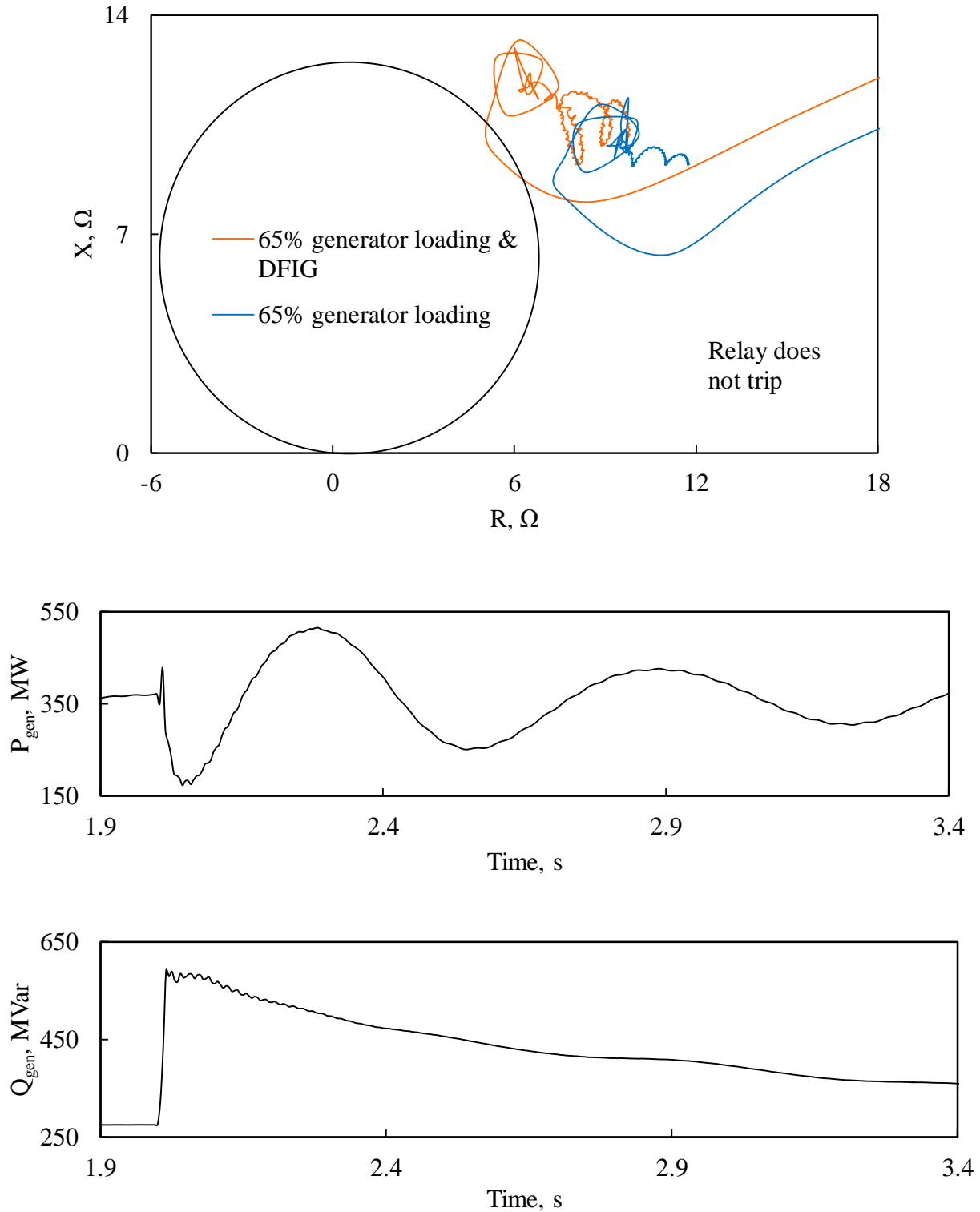


Figure 3.39: Relay (21) measured impedance, transient time responses of generator active and reactive powers, active and reactive power flows from Bus 1 to Bus K, DFIG-based wind farm active and reactive powers during a line-to-line fault at F_2 .

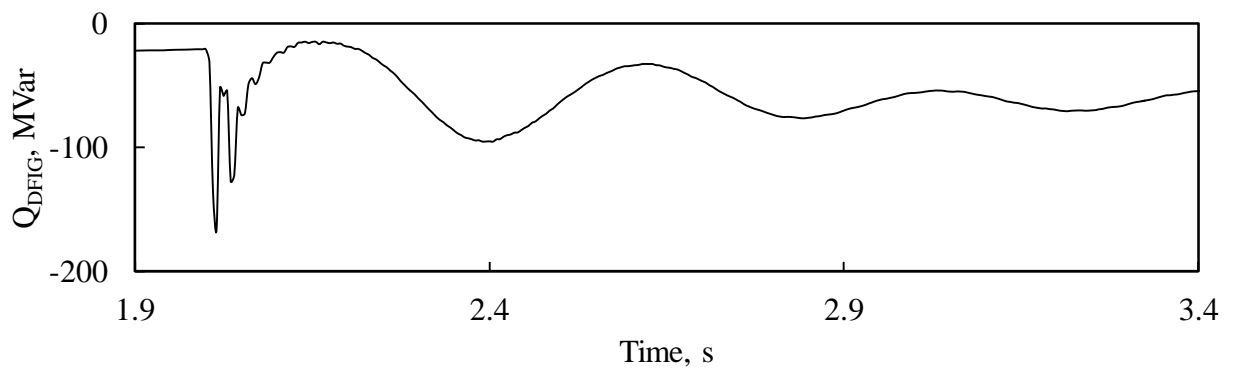
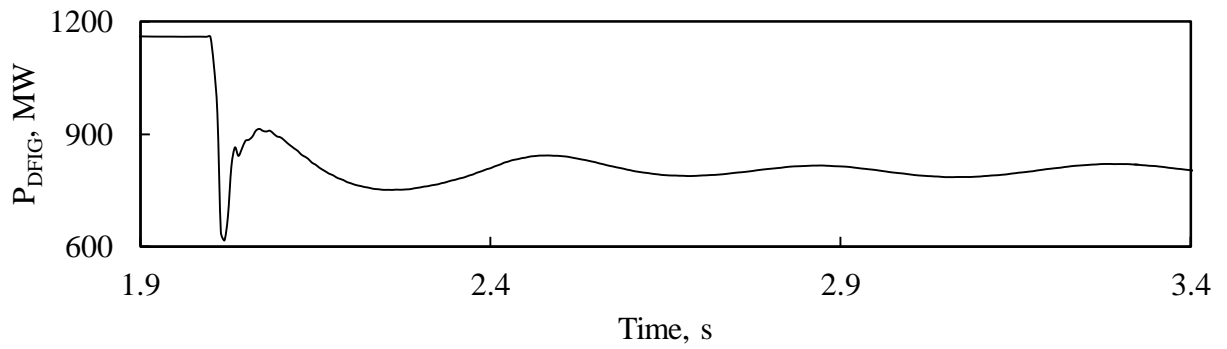
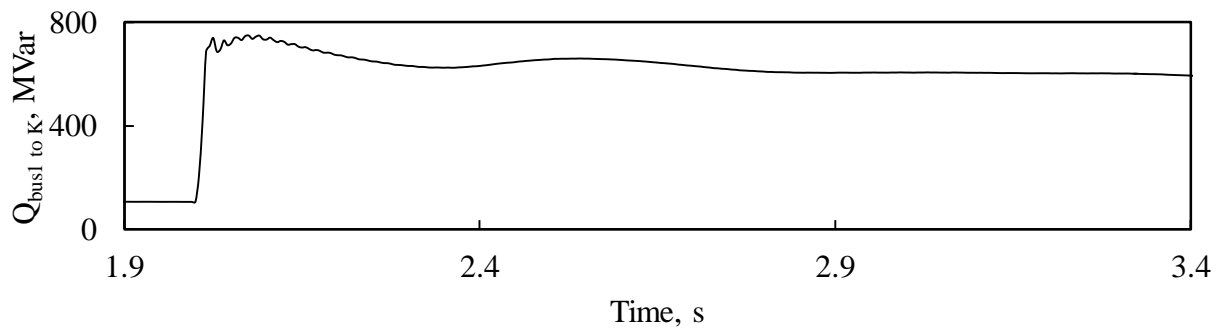
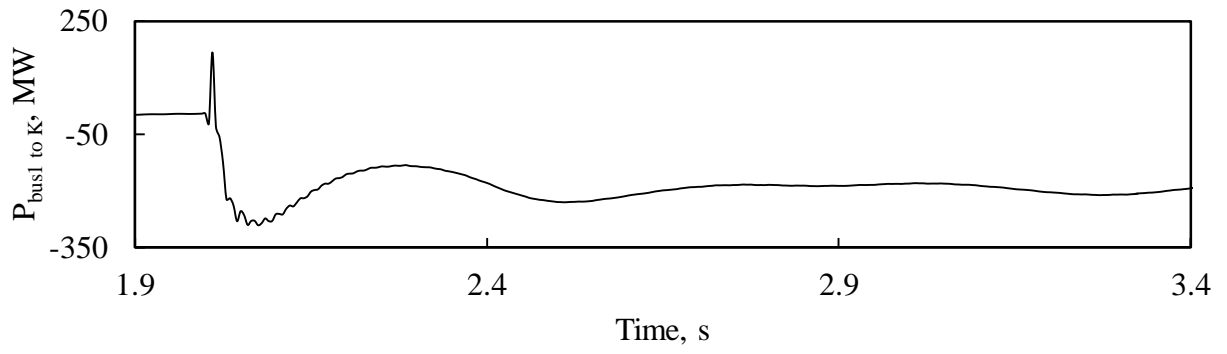


Figure 3.39: Continued.

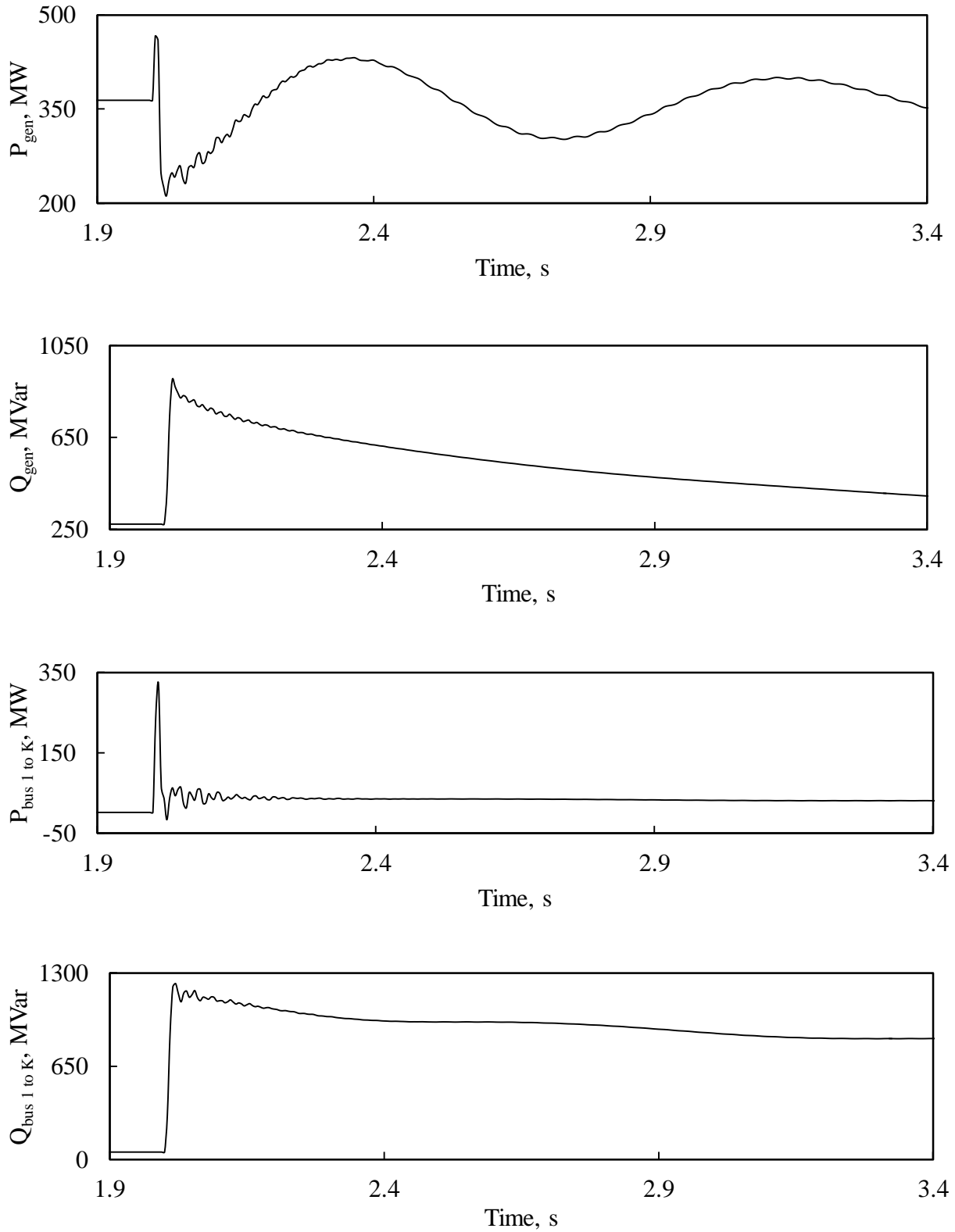


Figure 3.40: Transient time responses of generator active and reactive powers, active and reactive power flows from Bus 1 to Bus K, during a three-phase fault at F_2 (no wind farm in the system).

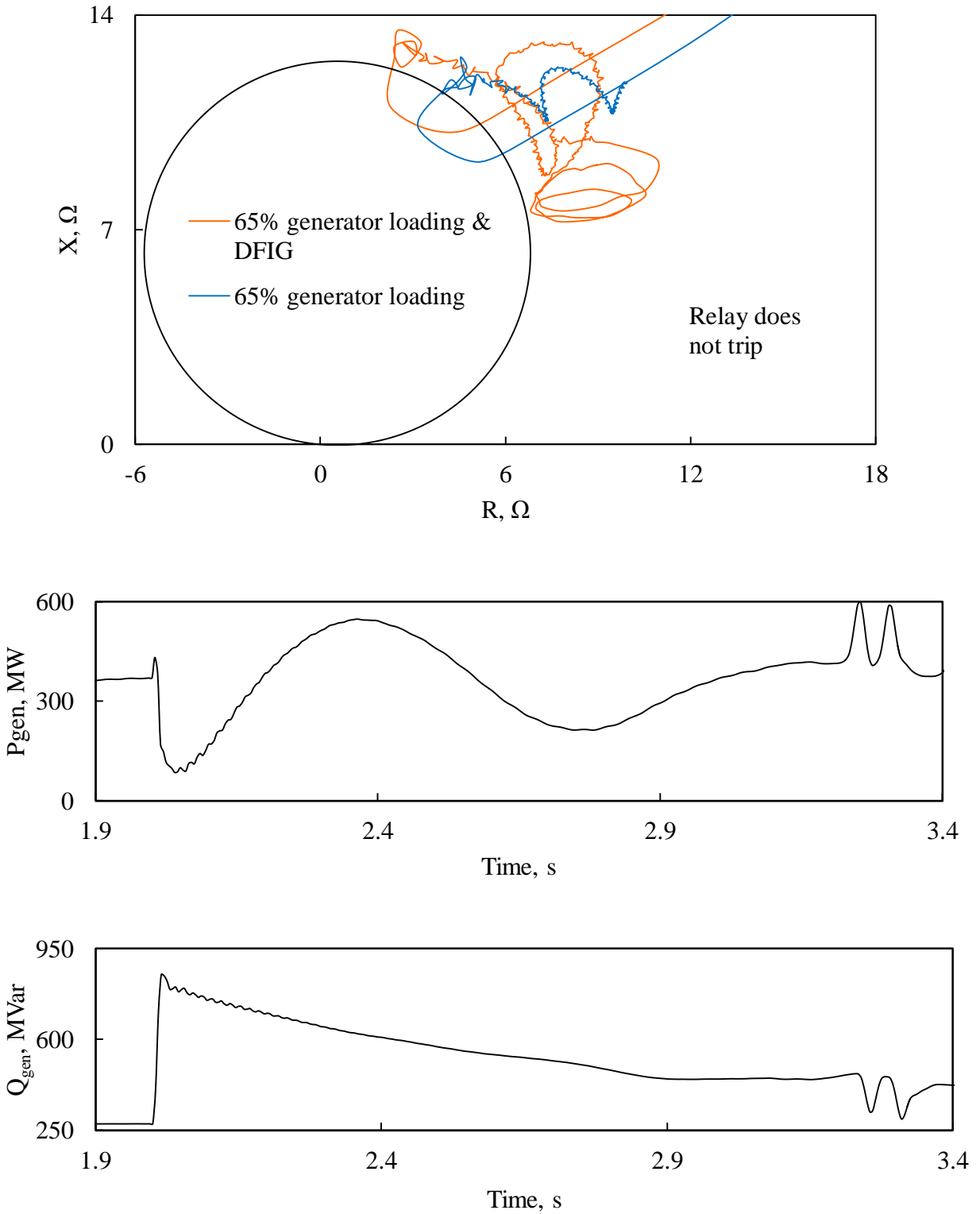


Figure 3.41: Relay (21) measured impedance trajectory, transient time responses of generator active and reactive powers, active and reactive power flows from Bus 1 to Bus K, DFIG-based wind farm active and reactive powers during a three-phase at F_2 .

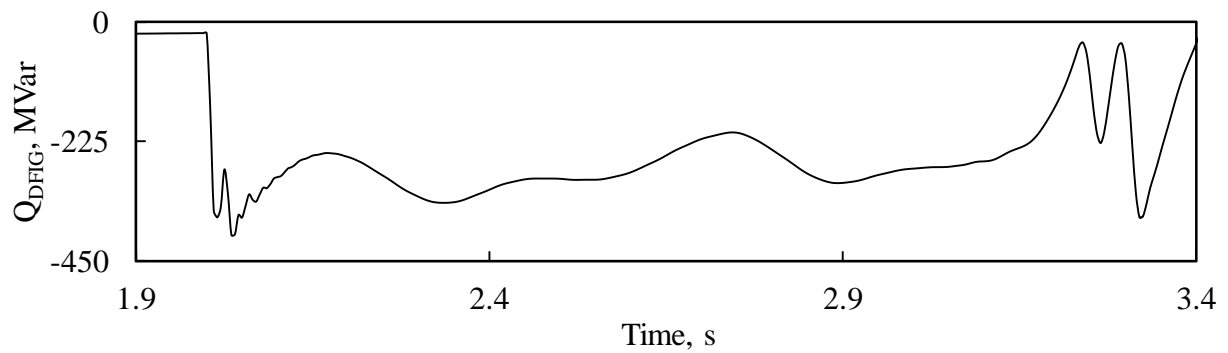
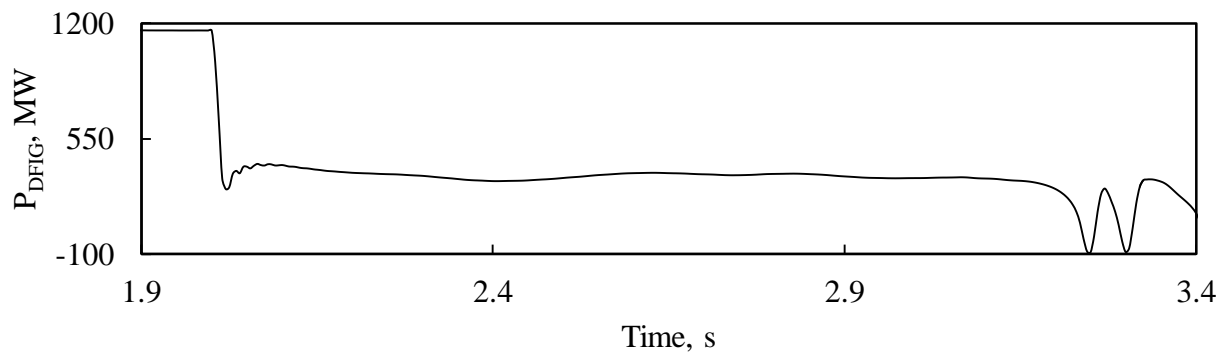
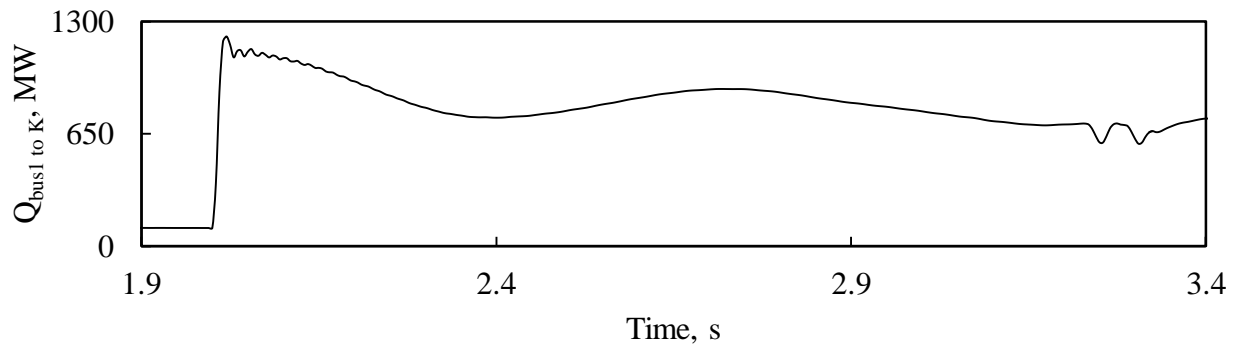
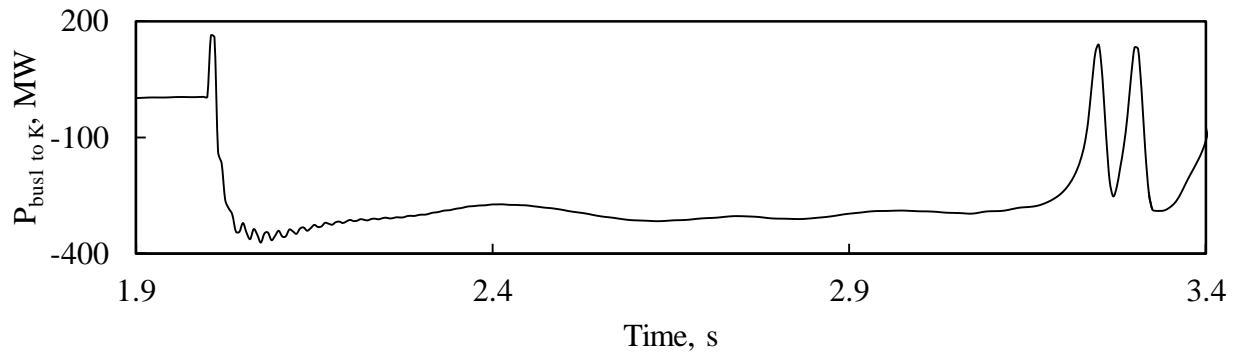


Figure 3.41: Continued.

3.4 Setting Relay (21) According to 67% of the Generator Load Impedance at the Rated Power Factor Angle of the Generator

As mentioned in Section 3.3, Relay (21) elements are set at the smallest of the three criteria outlined in Section 3.2. In the studies conducted in this thesis, the relay is set according to Criterion 2 (50% to 67% of the generator load impedance at the rated power factor angle of the generator). In Section 3.3, the impact of the DFIG-based wind farm on Relay (21) when the relay is set at 50% of RPFA of the generator is studied. In order to fulfill the 50% to 67% margin, Relay (21) protective zone reach is now set at 67% of RPFA of the generator, which yields to $Z_{21} = 16.77 \Omega$ at $MTA = 85^\circ$ (as shown in Appendix B).

Results from the cases due to a 16.77Ω relay setting is quite similar to those from the cases due to a 15.52Ω , which have been detailed in Section 3.3. One difference is, instead of only trip for faults at F_1 in the 15.52Ω relay setting cases, in cases of the 16.77Ω relay setting, Relay (21) trips for all line-to-line and three phase faults at F_1 , F_2 and F_3 . And after connecting the DFIG-based wind farm to Bus M, Relay (21) still trips for all faults. A full display of results for cases of setting Relay (21) according to 67% of the generator loading impedance at the RPFA of the generator can be found in Appendix C. Furthermore, same conclusions about effect of fault type, fault location and generator loading as those revealed from Section 3.3 can as well be draw from results in Section 3.4.

3.5 Summary

In this chapter, the effect of the DFIG-base wind farm on the generator distance phase backup protection element Relay (21) is presented. The investigations of such effect are carried out through several case of studies of time-domain simulations for different fault type, fault location, generator loading and Relay (21) setting. The main conclusions drawn from the results of these studies are presented in Chapter 4.

4. SUMMARY AND CONCLUSIONS

4.1 Summary

Due to the growth of interest in the use of renewable energy, many large wind farms have been built and integrated into the power grid during the past few years in order to cope with the environmental concerns, as well as the global energy shortage problem. Wind power is poised to deliver an essential contribution to a clean, robust, and diversified energy portfolio. Capturing and using this large and inexhaustible resource has the potential to mitigate climate change, improve the environment, increase energy security, and stimulate the world economy.

Integration of large wind farms into the bulk power system presents multiple challenges to power system operation and security. One particular challenge to the system security is the misoperation of protective relays. This thesis reports the results of the investigations that were carried out to explore the impact of large Doubly-Fed Induction Generator (DFIG)-based wind farms on the performance of the generator distance phase backup protection (Relay (21)).

Chapter 1 briefly introduces the concepts of DFIG-based wind farm as well as generator distance phase backup protection. The objective of the research is also presented in this chapter.

In Chapter 2, the system used in the studies conducted in this thesis is introduced and the mathematical models of its components are presented. The results of digital time-domain simulations of a case study for the system without the presence of wind farms during three-phase and line-to-line faults are also presented in this chapter.

In Chapter 3, comprehensive studies are carried out to explore the effect of a large DFIG-based wind farm tapped to the transmission system on the performance of generator distance phase backup protection (Relay (21)).

4.2 Conclusion

The studies conducted in this thesis yield the following conclusions for the system under study:

1. Large DFIG-based wind farms have the potential to adversely affect the existing generator distance phase backup protection relays. Such an effect varies with the wind

farm rating and location, generator loading, fault type, fault location and transmission line power flows.

2. During line-to-line and three-phase faults, the occurrence of the fault activates the DFIG-based wind farm grid and rotor-side converters protection system which causes the crowbar to isolate the converters. As a result, the DFIG-based wind farm operates as an induction generator and starts to absorb a large amount of reactive power from the system.
3. The presence of DFIG-based wind farms and its contribution to the fault current during system faults changes the measured impedance of Relay (21). This is due to the changes in both the voltages and currents measured by the relay elements. Moreover, these changes in the measured impedance vary with the fault type, fault location and generator loading.
4. The highest error in the measured impedance of Relay (21) occurred at the lowest generator loading, namely 65% of the rated MVA. This is true for both line-to-line and three-phase faults.
5. For the same setting of Relay (21), fault location and generator loading, the absolute values of error in the measured impedance by the relay during line-to-line faults are higher than those during three-phase faults.
6. In all the studied fault cases, the error in the measured impedance by Relay (21) increases as the fault location varies from the upstream to the downstream of the transmission line.

The studies conducted in this thesis give an insight on the impact of integrating a large DFIG-based wind farm into the power system on generator distance phase backup protection. The results of these investigations highlight the need for more research in this area, particularly for the cases of multiple wind farms that are tapped to several transmission lines near generating stations.

REFERENCES

- [1] Global Wind Energy Council, *Global Wind Report Annual market update 2015*, April 2016.
- [2] https://en.wikipedia.org/wiki/Wind_power.
- [3] O. Anaya-Lara, N. Jenkins, J. Ekanayake, P. Cartwright, and M. Hughes, *Wind Energy Generation: Modelling and Control*, John Wiley & Sons, Ltd, 2009.
- [4] P. Gipe, *Wind Energy Basics A Guide to Home and Community-Scale Wind-Energy Systems*, 2th edn., USA: Chelsea Green Publishing. 2009.
- [5] Thomas Ackermann, *Wind Power in Power Systems*, Britain: John Wiley & Sons, 2005.
- [6] J. G. Slootweg, S. W. H. de Haan, H. Polinder, W. L. Kling, “General Model for Representing Variable Speed Wind Turbines in Power System Dynamics Simulations”, *IEEE Transactions On Power Systems*, 18(1), pp. 144 – 151, 2003.
- [7] K. Patil, B. Mehta, “Modeling and Simulation of Variable Speed Wind Turbine with Direct Drive Permanent Magnet Synchronous Generator”, *Green Computing Communication and Electrical Engineering (ICGCCEE)*, pp. 1 – 6, 2009.
- [8] S. Li, T. A. Haskew, R. P. Swatloski, W. Gathings, “Optimal and Direct-Current Vector Control of Direct-Driven PMSG Wind Turbines”, *IEEE Transactions on Power Electronics*, 27(5), pp. 2325 – 2337, 2012.
- [9] X. Gao, *Simultaneous Mitigation of Subsynchronous Resonance And Subsynchronous Interaction Using Full-Scale Frequency Converter- And Doubly-Fed Induction Generator-Based Wind Farms*, a thesis for master of science in electrical engineering, University of Saskatchewan, Saskatoon, Canada, 2014.
- [10] H. Lee Willis, *Protective Relaying Principles and Applications*, CRC Press, Third Edition, 2006.
- [11] P. M. Anderson, *Power System Protection*, Canada: John Wiley & Sons, Inc., the Institute of Electrical and Electronics Engineers, Inc, 1999.
- [12] M. Elsamahy, *Impacts Of Midpoint Facts Controllers On The Coordination Between Generator Phase Backup Protection And Generator Capability Limits*, a thesis for doctor of philosophy in electrical engineering, University of Saskatchewan, Saskatoon, Canada, 2011.
- [13] K. Tseng, W. Kao, J. Lin, “Load model effects on distance relay settings”, *IEEE Transactions on Power Delivery*, 18(4), pp. 1140 – 1146, 2003.
- [14] G. Klempner, I. Kerszenbaum, *Operation and Maintenance of Large Turbo-Generators*, Wiley-IEEE Press, Second Edition, 2008.
- [15] IEEE Std 67, “IEEE Guide for Operation and Maintenance of Turbine Generators”, 2010.

- [16] M.V.Bakshi, U.A.Bakshi, *Electrical Machines III*, Technical Publications, 2009.
- [17] M. Elsamahy, S.O. Faried, T. S. Sidhu, “Impact of Superconducting Fault Current Limiters on the Coordination Between Generator Distance Phase Backup Protection and Generator Capability Curves”, *IEEE Transactions on Power Delivery*, vol.26, no. 3, pp. 1854 – 1863, 2011.
- [18] W. Elmore, *Protective Relaying Theory and Applications*, CRC Press, second edition, 2004.
- [19] Charles Mozina, “Power Plant Protection and Control Strategies for Blackout Avoidance,” *Proceedings of the IEEE Power Systems Conference: Advanced Metering, Protection, Control, Communication, and Distributed Resources*, Clemson, SC, March 14-17, 2006, pp. 200-218.
- [20] R. Dubey, S.R. Samantaray, B.K. Panigrahi, “Adaptive distance protection scheme for shunt-FACTS compensated line connecting wind farm”, *IET Generation, Transmission & Distribution*, vol. 10, no. 1, pp. 247–256, 2016.
- [21] R. Dubey, S.R. Samantaray, B.K. Panigrahi, “Adaptive distance protection scheme for shunt-FACTS compensated line connecting wind farm”, *IET Generation, Transmission & Distribution*, vol. 10, no. 1, pp. 247–256, 2016.
- [22] A.K. Pradhan, G. Jóos, “Adaptive distance relay setting for lines connecting wind farms”, *IEEE Transactions On Energy Conversion*, vol. 22, no. 1, pp. 206–213, 2007.
- [23] H. Sadeghi, “A novel method for adaptive distance protection of transmission line connected to wind farms”, *International Journal of Electrical Power & Energy Systems*, vol. 43, pp. 1376–1382, 2012.
- [24] R. K. Dubey, S. R. Samantaray, B. K. Panigrahi, “Adaptive distance relaying scheme for transmission network connecting wind farms”, *Electric Power Components and Systems*, vol. 42, no. 11, pp. 181–1193, 2014.
- [25] L. He, C. Liu, “Impact of LVRT Capability of Wind Turbines on Distance Protection of AC Grids”, *Innovative Smart Grid Technologies (ISGT), 2013 IEEE PES*, pp. 24-27, 2013.
- [26] RIA Lúcio, “Behavior of Distance Protections near Wind Farms”. [online] Available: https://fenix.tecnico.ulisboa.pt/downloadFile/395143996730/Artigo_Rita.pdf. [Accessed 24 August 24, 2016].
- [27] M. Khoddam, H. Karegar, “Effect of Wind Turbines Equipped with Doubly-Fed Induction Generators on Distance Protection”, *2011 The International Conference on Advanced Power System Automation and Protection*, pp. 1349-1353, 2011.
- [28] S De Rijcke, J. Driesen “Impact of wind turbines equipped with doubly-fed induction generators on distance relaying”, *Power and Energy Society General Meeting, 2010 IEEE*, 2010.

- [29] P. Kundur, *Power System Stability and Control*, New York, McGraw-Hill, 1994.
- [30] Y. Yu, *Electric Power System Dynamics*, New York, Academic Press, 1983.
- [31] A.D. Hansen, G. Michalke, P. Sorensen, T. Lund and Florin Iov, "Co-ordinated Voltage Control of DFIG Wind Turbines in Uninterrupted Operation during Grid Faults," *Wind Energy*, Vol. 10, No. 1, January/February 2007, pp. 51-68, published online, DOI: 10.1002/we.207.
- [32] J. Morren, S. W. H. de Haan, P. Bauer, J. Pierik, and J. Bozelie, "Comparison of Complete and Reduced Models of a Wind Turbine with Doubly-fed Induction Generator," in Proc. 10th European Conference on Power Electronics and Applications., Toulouse, France, September 2-4, 2003, pp. 1-10.
- [33] J. G. Slootweg, H. Polinder, and W. L. Kling, "Representing Wind Turbine Electrical Generating Systems in Fundamental Frequency Simulations," *IEEE Transactions on Energy Conversion*, Vol. 18, No. 4, December 2003, pp. 516-524.
- [34] <http://www.emtp-software.com/>
- [35] IEEE Std. C37.102, "IEEE Guide for AC Generator Protection," 2006.
- [36] IEEE Tutorial PES Tutorial 95 TP 102 "IEEE Tutorial on the Protection of Synchronous Generators," 1995.

APPENDIX A

DATA OF THE SYSTEM UNDER STUDY

A.1 Synchronous Generator

Table A.1: Synchronous generator data.

Rating, MVA	700
Rated voltage, kV	22
Armature resistance, r_a , p.u.	0.0045
Leakage reactance, x_l , p.u.	0.12
Direct-axis synchronous reactance, x_d , p.u.	1.54
Quadrature-axis synchronous reactance, x_q , p.u.	1.50
Direct-axis transient reactance, x'_d , p.u.	0.23
Quadrature-axis transient reactance, x'_q , p.u.	0.42
Direct-axis subtransient reactance, x''_d , p.u.	0.18
Quadrature-axis subtransient reactance, x''_q , p.u.	0.18
Direct-axis transient open-circuit time constant, T'_{do} , s	3.70
Quadrature-axis transient open-circuit time constant, T'_{qo} , s	0.43
Direct-axis subtransient open-circuit time constant, T''_{do} , s	0.04
Quadrature-axis subtransient open-circuit time constant, T''_{qo} , s	0.06
Zero-sequence reactance, x_o , p.u.	0.36
Inertia constant, M, p.u.	2625.22013

A.2 Transformers

Table A.2: Transformer data.

	T ₁ (Generator)	T ₂ (Wind farm)	T ₃ (Wind farm)
Rating, MVA	700	600	1200
Rated voltage, kV	22/500	34.5/500	34.5/500
Resistance, r_T , p.u.	0.0012	0.005	0.005
Leakage reactance, x_T , p.u.	0.12	0.15	0.15

A.3 DFIG-based Wind Farm

Table A.3: Wind farm parameters.

Number of wind turbine generators	400
System frequency, Hz	60
Rated capacity of each wind farm generator, MVA	1.67
Rated capacity of turbine, MW	1.5
Generator rated voltage, kV	0.575
DC nominal voltage, V	1150
Number of poles	6
Average wind speed, m/s	11.24

A.4 Transmission Lines

All transmission lines have the same series impedance and shunt admittance per unit length.

$$Z_{T.L.series} = 0.0118 + j0.3244 \Omega/km$$

$$Y_{T.L.shunt} = 5.0512 \mu s/km$$

Transmission voltage = 500 kV

APPENDIX B

CALCULATIONS OF RELAY (21) REACH

1. 120% of the longest line with system infeed currents:

The equivalent circuit of the system under study with infeed current is shown in Figure B.1.

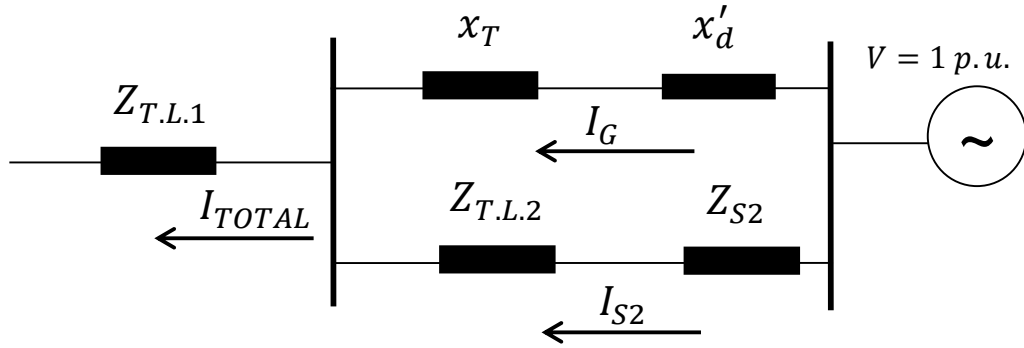


Figure B.1: Equivalent circuit of the system under study.

$$\text{Transmission lines: } 500 \text{ kV, } Z_{T.L.1} = 0.32461 \angle 87.917^\circ \Omega/\text{km} \quad (\text{B.1})$$

$$L_1: 400 \text{ km, } Z_{T.L.1} = 129.844 \angle 87.917^\circ \Omega \quad (\text{B.2})$$

$$Z_{S_2} = 5 + j35 \Omega = 35.3553 \angle 81.8699^\circ \Omega \quad (\text{B.3})$$

$$Z_{T.L.2} = 64.922 \angle 87.917^\circ \Omega \quad (\text{B.4})$$

$$Z_{T.L.BASE} = \frac{(500)^2}{700} = 357.1429 \Omega \quad (\text{B.5})$$

$$Z_{T.L.1} = 0.3636 \angle 87.917^\circ \text{ p.u.} \quad (\text{B.6})$$

$$Z_{T.L.2} = 0.1818 \angle 87.917^\circ \text{ p.u.} \quad (\text{B.7})$$

$$Z_{S_2} = 0.099 \angle 81.8699^\circ \text{ p.u.} \quad (\text{B.8})$$

$$Z_\alpha = x_T + x'_d = 0.37 \angle 90^\circ \text{ p.u.} \quad (\text{B.9})$$

$$Z_\beta = Z_{T.L.2} + Z_{S_2} = 0.2804 \angle 85.7858^\circ \text{ p.u.} \quad (\text{B.10})$$

$$Z_{TOTAL} = 0.5232 \angle 87.8211^\circ \text{ p.u.} \quad (\text{B.11})$$

$$I_{TOTAL} = 1.9112 \angle -87.8211^\circ \text{ p.u.} \quad (\text{B.12})$$

$$I_{S2} = I_{TOTAL} \frac{Z_{\alpha}}{Z_{\alpha}+Z_{\beta}} \quad (B.13)$$

$$I_G = I_{TOTAL} \frac{Z_{\beta}}{Z_{\alpha}+Z_{\beta}} \quad (B.14)$$

$$\frac{I_{S2}+I_G}{I_G} = \frac{Z_{\alpha}+Z_{\beta}}{Z_{\beta}} = 2.318 \angle 2.3975^{\circ} \quad (B.15)$$

$$\left| \frac{I_{S2}+I_G}{I_G} \right| = 2.318 \quad (B.16)$$

If there is no infeed (the short line does not exist), the above ratio is 1.

$$I_{Generator_base} = \frac{700 \times 10^6}{\sqrt{3} \times 22 \times 10^3} = 18370 \text{ A} \quad (B.17)$$

$$R_C = \frac{18370 \times 1.25}{5} = 4592 \quad (B.18)$$

$$V_{Ph_GEN} = \frac{22 \times 10^3}{\sqrt{3}} = 12702.7059 \text{ V} \quad (B.19)$$

$$R_v = \frac{12702.7059}{67} = 190 \quad (B.20)$$

$$Z_{base_relay} = \frac{(kV_{Gen-Base})^2}{700} \times \frac{R_C}{R_v} = \frac{22^2}{700} \times \frac{4592}{190} = 16.7128 \Omega \quad (B.21)$$

$$Z_{21} = [0.12 + (1.2 \times 2.3228 \times 0.36357)] \times 16.7128 = 18.9425 \Omega \quad (B.22)$$

2. 50% to 67% of the generator load impedance (Z_{load}) at the rated power factor angle (RPFA) of the generator:

$$Z_{Max_loading_at_RPF} = \frac{22^2}{700} \times \frac{4592}{190} = 16.71 \Omega \quad (B.23)$$

$$Z_{21_50\%} = 0.5 \times \frac{16.71}{\cos(85^{\circ} - 36.8699^{\circ})} = 12.52 \Omega \quad (B.24)$$

$$Z_{21_67\%} = 0.67 \times \frac{16.71}{\cos(85^{\circ} - 36.8699^{\circ})} = 16.77 \Omega \quad (B.25)$$

3. 90% of the generator load impedance at the maximum torque angle:

$$Z_{21} = 0.9 \times Z_{GCCMTA} = 0.9 \times \frac{22^2}{587.54} \times \frac{4592}{190} = 17.918 \Omega \quad (B.26)$$

APPENDIX C

SETTING RELAY (21) ACCORDING TO 50% TO 67% OF RPFA OF THE GENERATOR

C.1 Setting Relay (21) According to 50% of RPFA of the Generator

C.1.1 Performance of Relay (21) at 65% of the generator loading

Figure C.1 illustrates the transient time responses of the generator active and reactive powers as well as active and reactive power flows from Bus 1 to Bus M during a line-to-line fault occurs at F_3 when there is no wind farm in the system. After connecting DFIG-based wind farm to Bus M, Figure C.2 depicts the Relay (21) measured impedance trajectories, transient time responses of the generator active and reactive powers, active and reactive power flows from Bus 1 to Bus M as well as the DFIG-based wind farm active and reactive powers during the same line-to-line fault at F_3 . Figures C.3 and C.4 show the same trajectories, signals in conjunction with transient time responses for the cases of three-phase fault at the same location. Note that the relay does not trip for faults at F_3 .

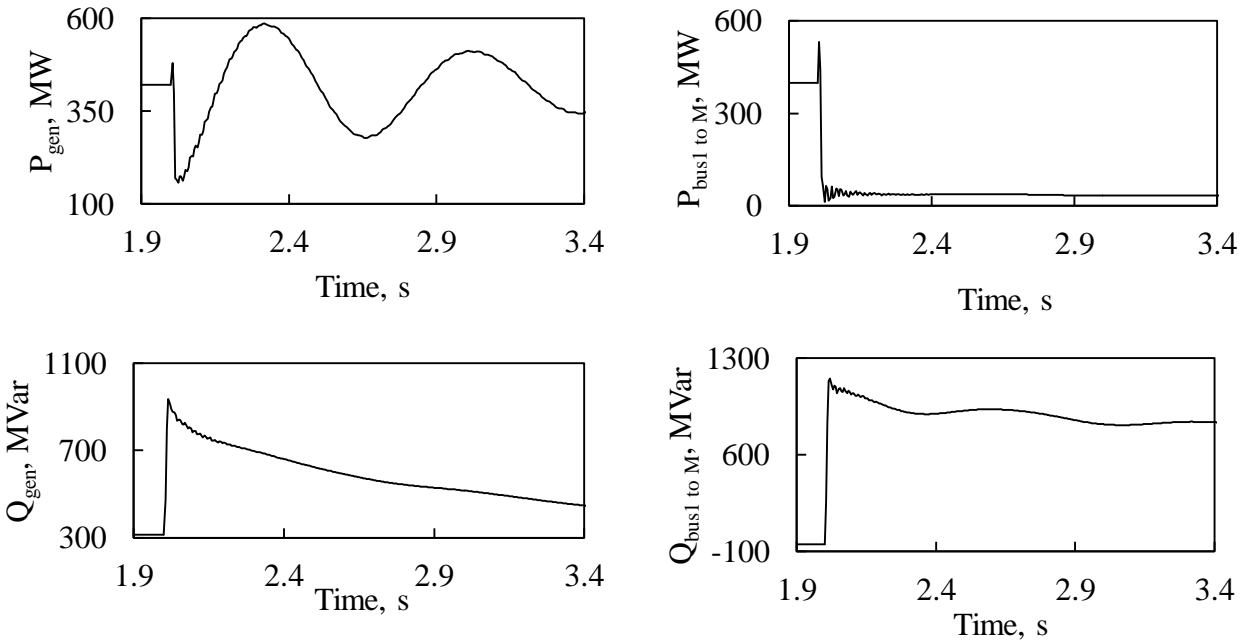


Figure C.1: Transient time responses of generator active and reactive powers, active and reactive power flows from Bus 1 to Bus M during a line-to-line fault at F_3 (no wind farm in the system).

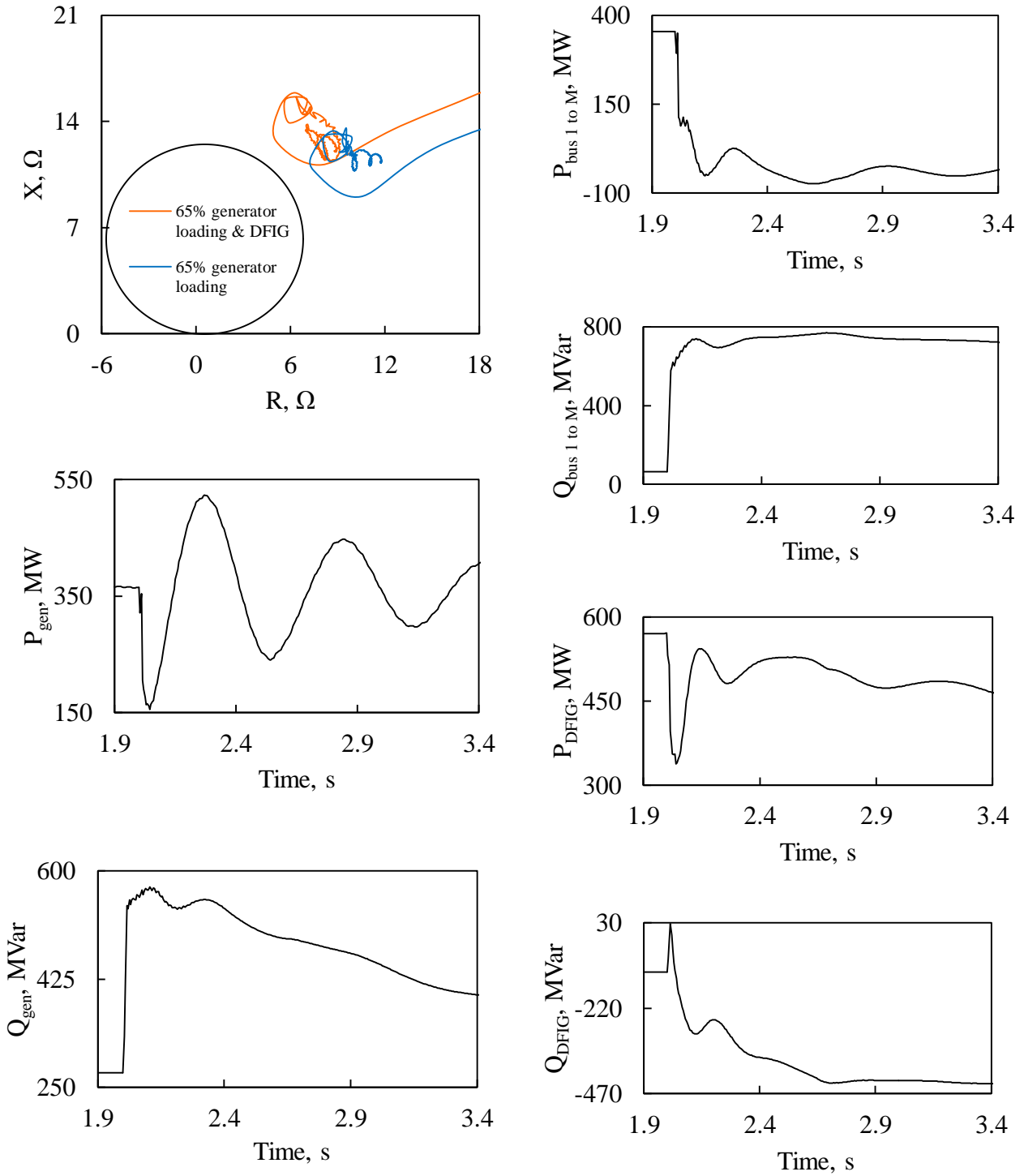


Figure C.2: Relay (21) measured impedance trajectory, transient time responses of generator active and reactive powers, active and reactive power flows from Bus 1 to Bus M, DFIG-based wind farm active and reactive powers during a line-to-line fault at F_3 .

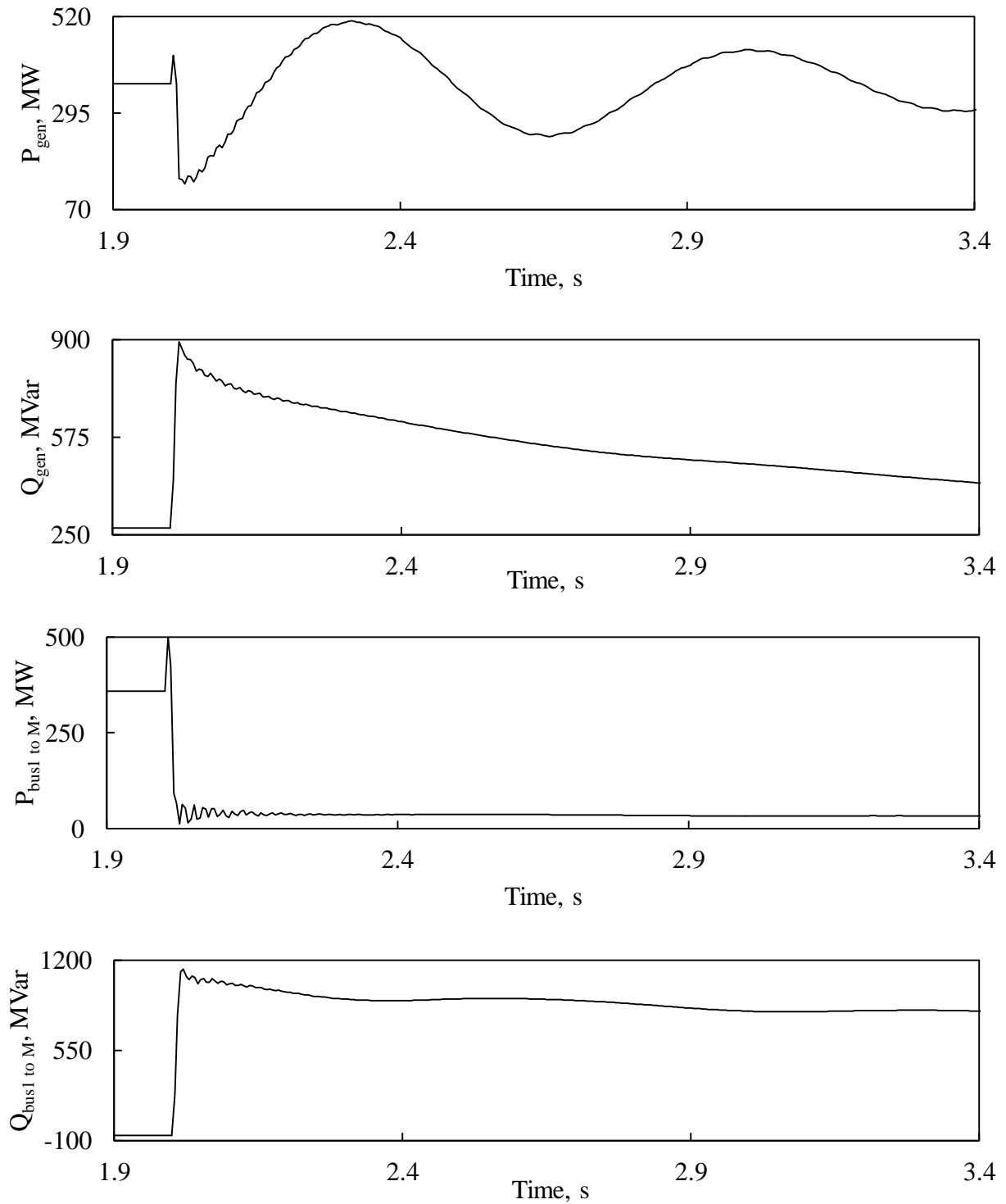


Figure C.3: Transient time responses of generator active and reactive powers, active and reactive power flows from Bus 1 to Bus M during a three-phase fault at F_3 (no wind farm in the system).

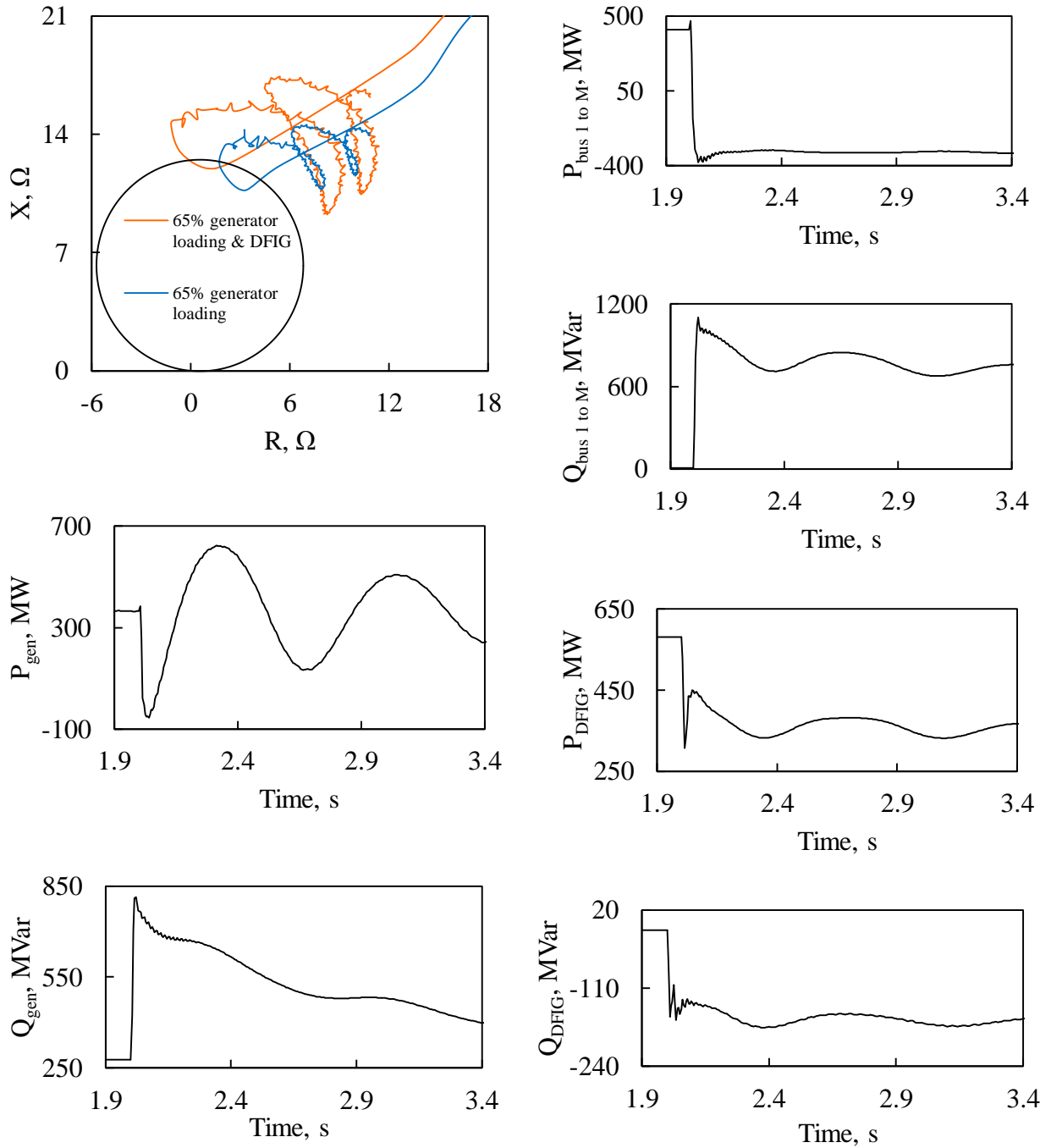


Figure C.4: Relay (21) measured impedance trajectory, transient time responses of generator active and reactive powers, active and reactive power flows from Bus 1 to Bus M, DFIG-based wind farm active and reactive powers during a three-phase at F_3 .

C.1.2 Performance of Relay (21) at 75% of the generator loading

Figures C.5 to C.8 depict the same trajectories and transient time responses for cases for the same faults as the cases where generator outputting 65% of its rated power.

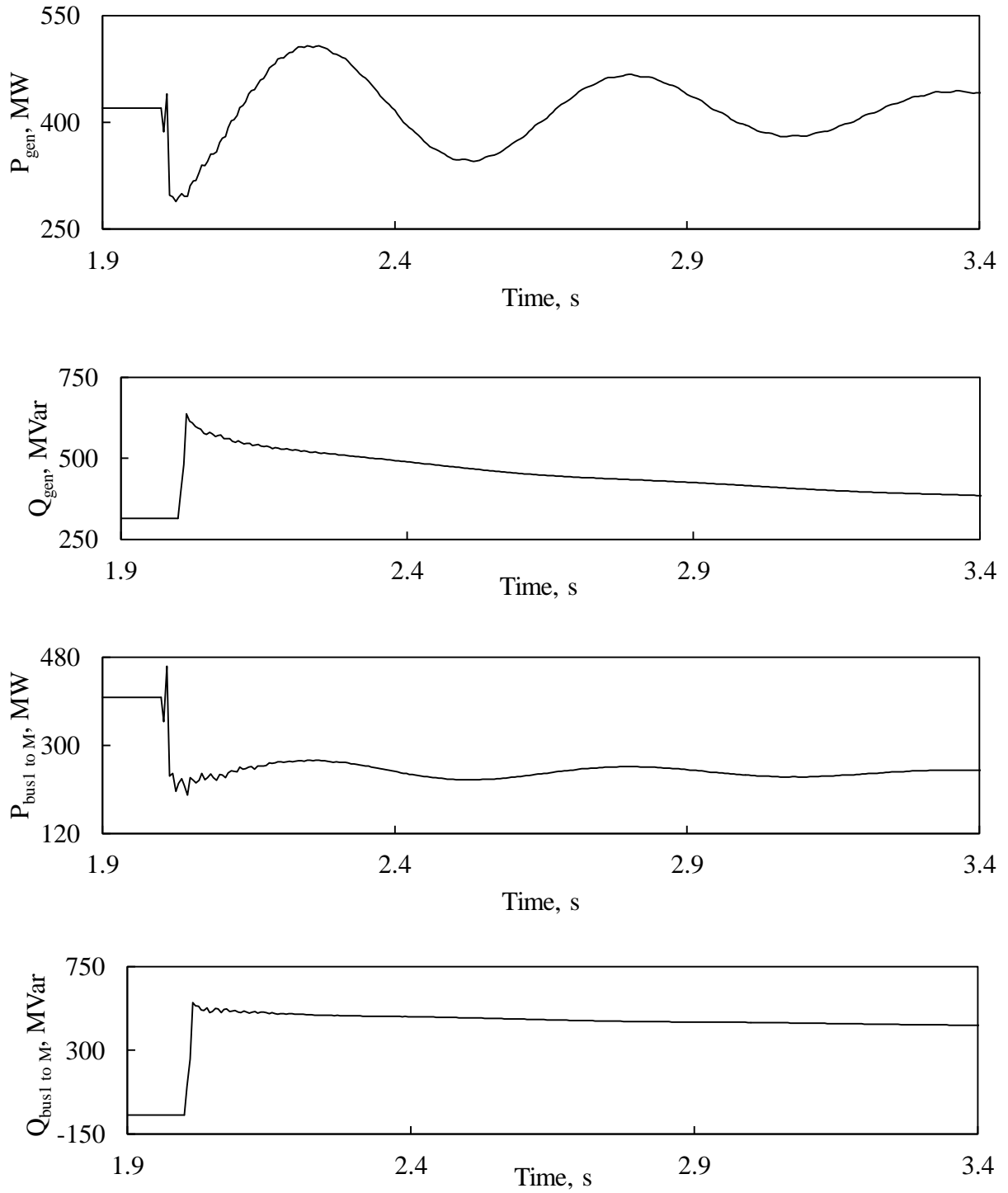


Figure C.5: Transient time responses of generator active and reactive powers, active and reactive power flows from Bus 1 to Bus M during a line-to-line fault at F_3 (no wind farm in the system).

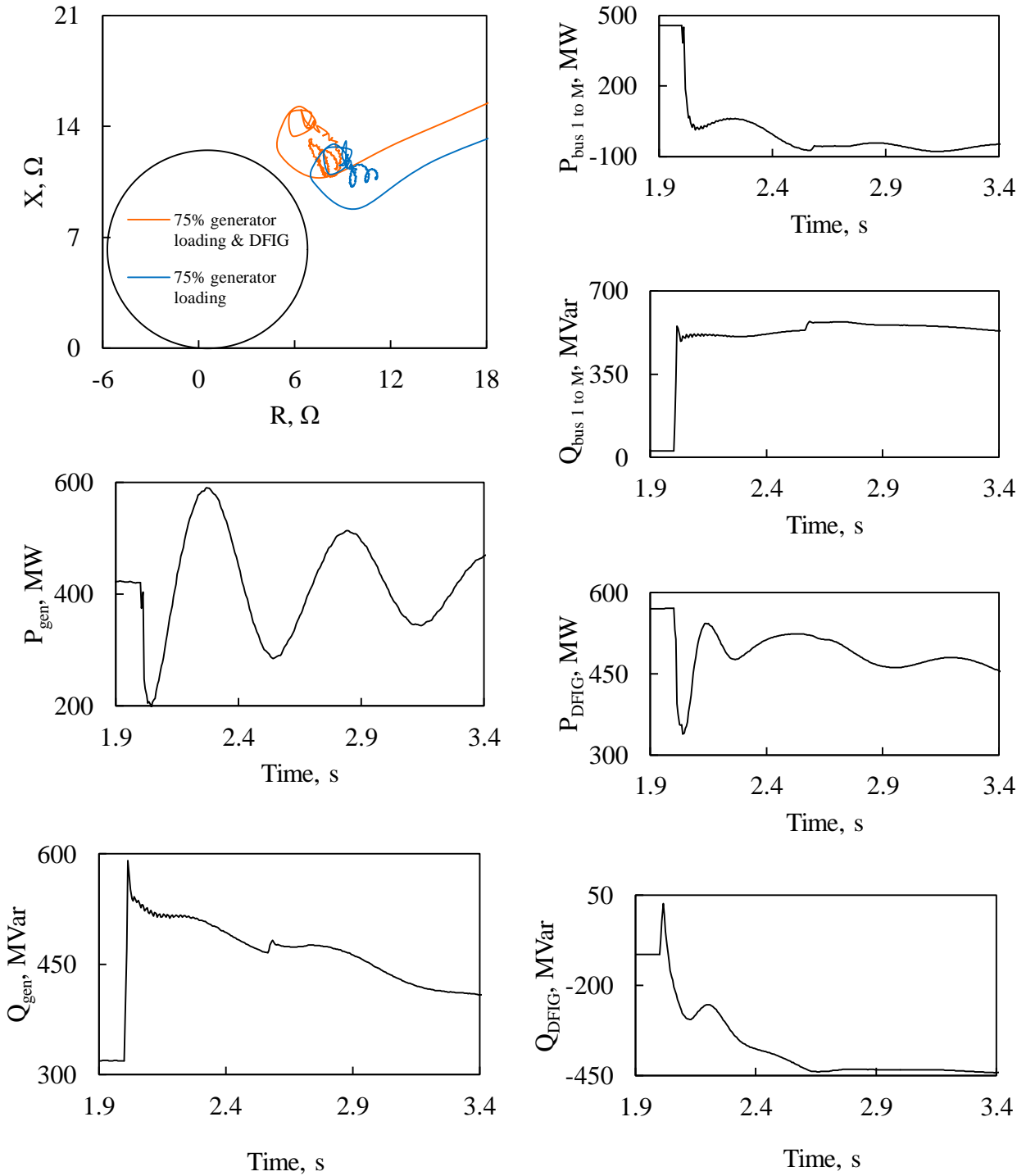


Figure C.6: Relay (21) measured impedance trajectory, transient time responses of generator active and reactive powers, active and reactive power flows from Bus 1 to Bus M, DFIG-based wind farm active and reactive powers during a line-to-line fault at F_3 .

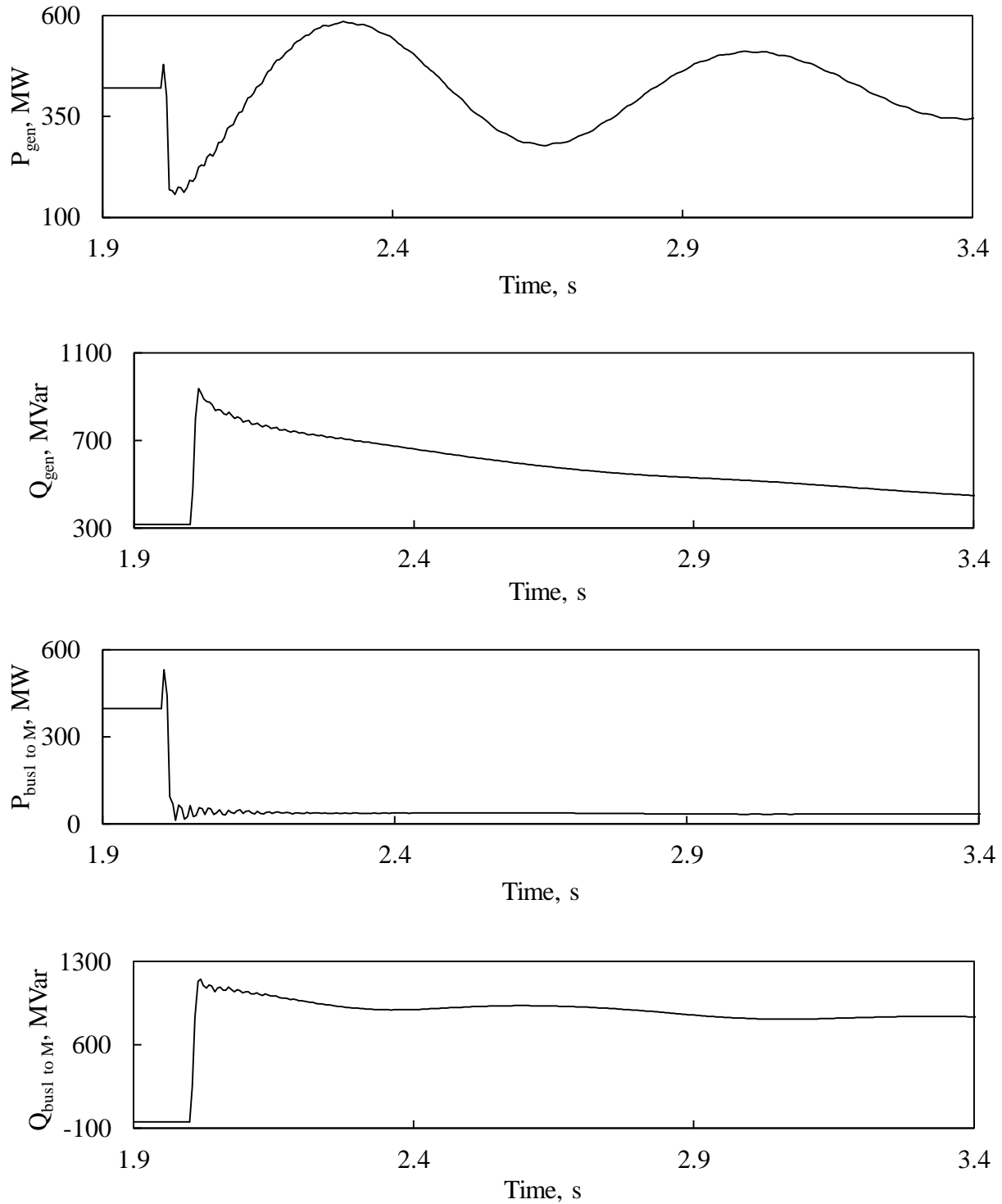


Figure C.7: Transient time responses of generator active and reactive powers, active and reactive power flows from Bus 1 to Bus M during a three-phase fault at F_3 (no wind farm in the system).

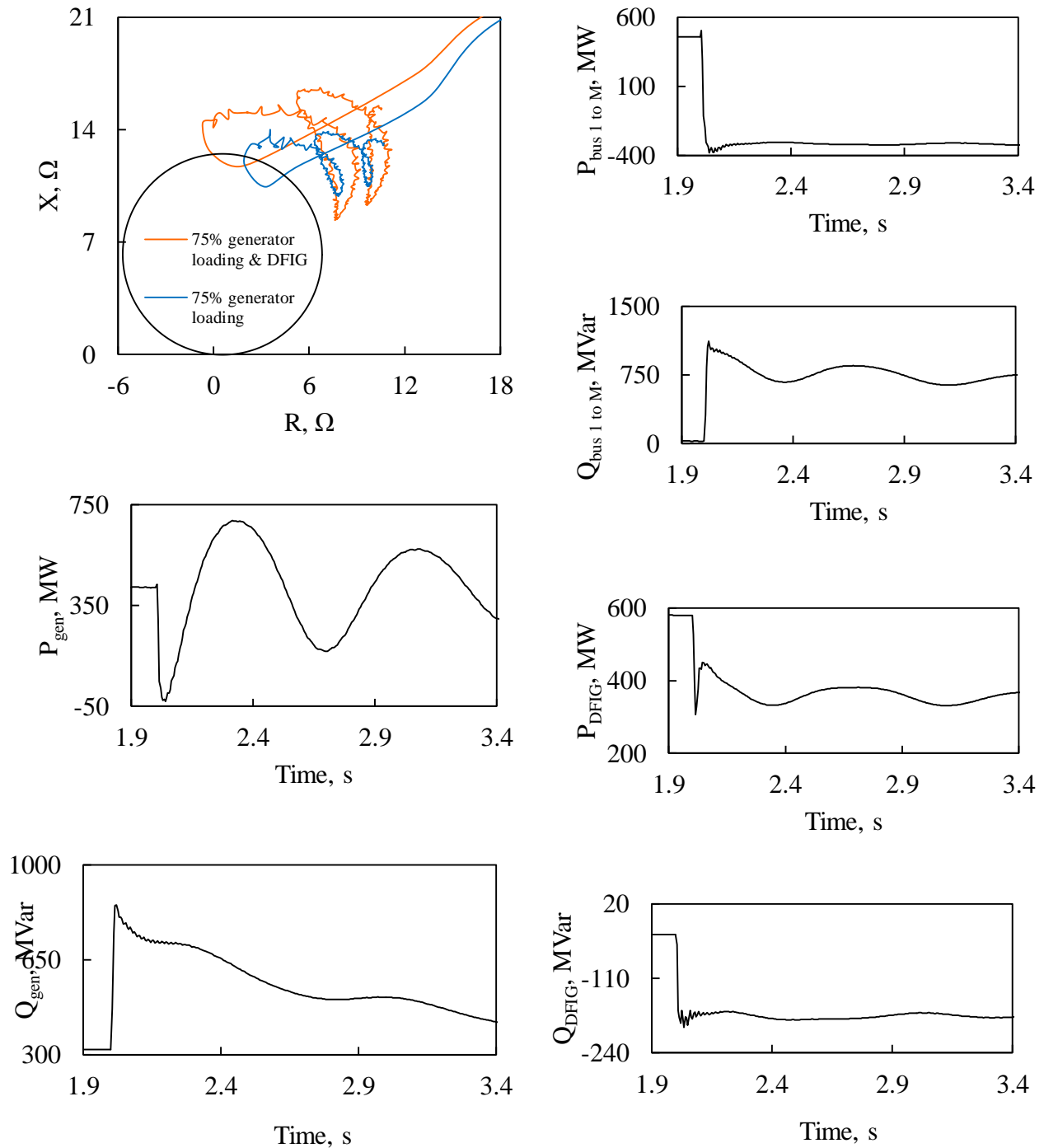


Figure C.8: Relay (21) measured impedance trajectory, transient time responses of generator active and reactive powers, active and reactive power flows from Bus 1 to Bus M, DFIG-based wind farm active and reactive powers during a three-phase at F₃.

C.1.3 Performance of Relay (21) at 85% of the generator loading

Figures C.9 to C.12 depict the same trajectories and transient time responses for cases for the same faults as the cases where generator outputting 65% of its rated power.

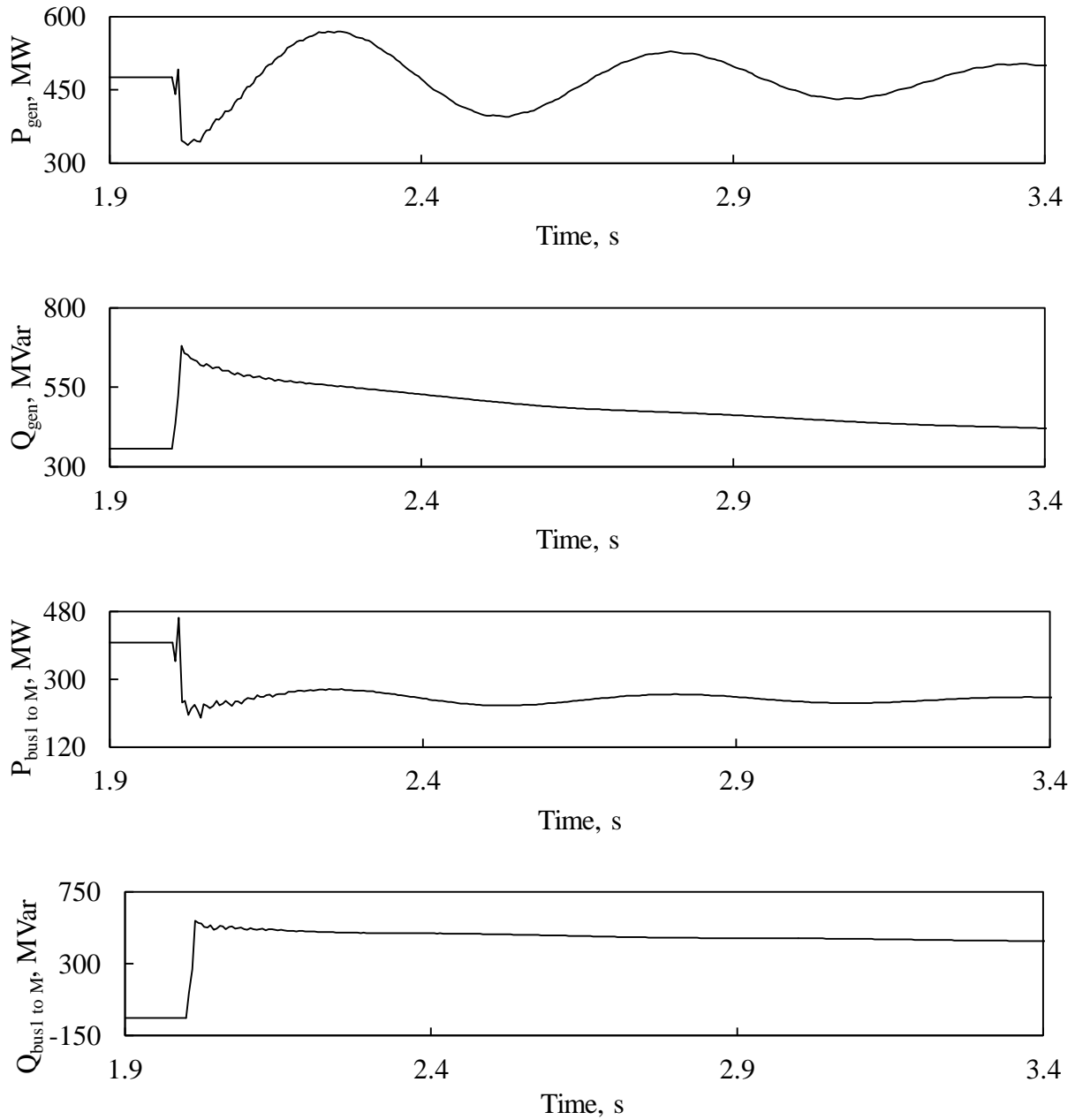


Figure C.9: Transient time responses of generator active and reactive powers, active and reactive power flows from Bus 1 to Bus M during a line-to-line fault at F_3 (no wind farm in the system).

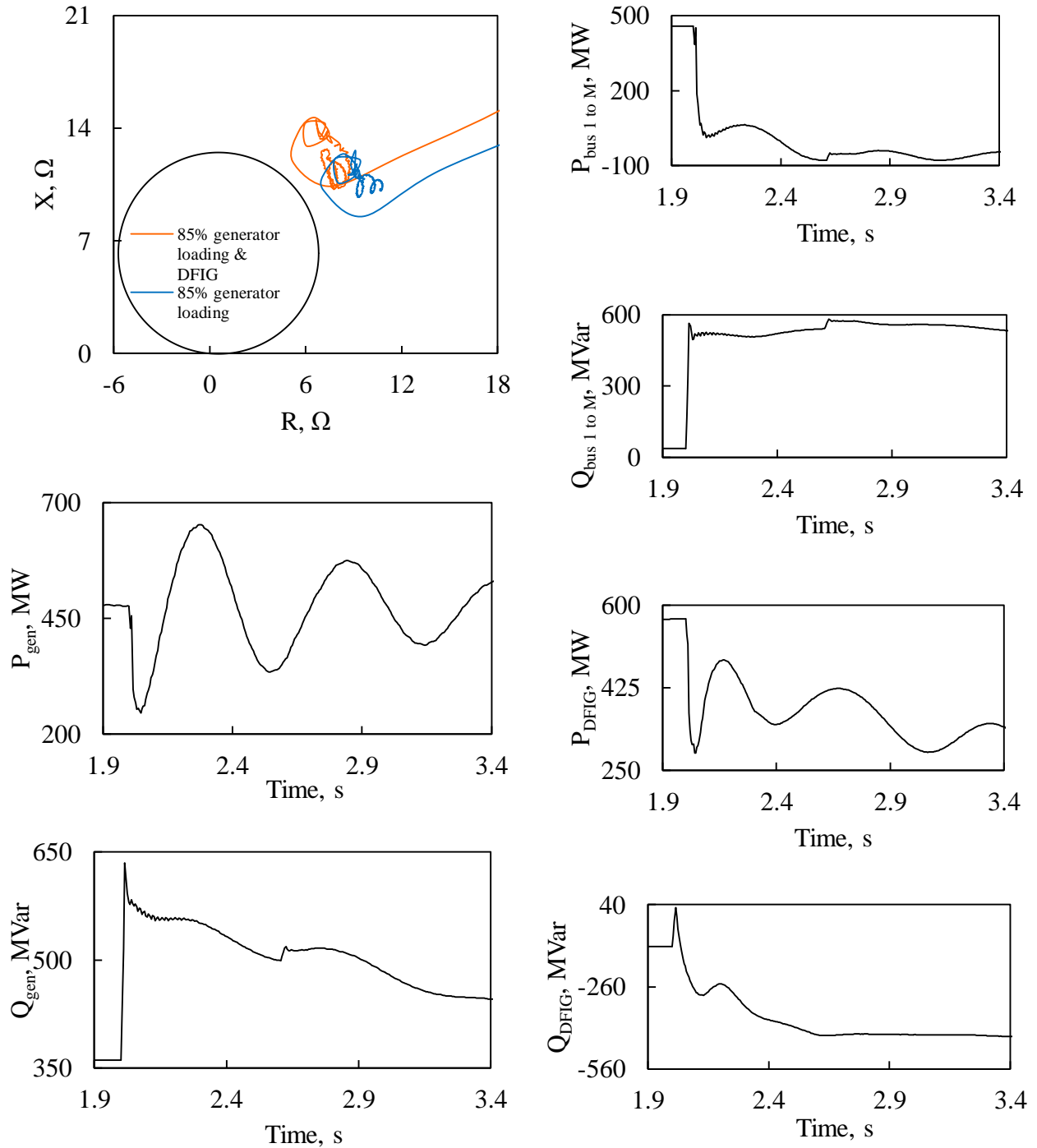


Figure C.10: Relay (21) measured impedance trajectory, transient time responses of generator active and reactive powers, active and reactive power flows from Bus 1 to Bus M, DFIG-based wind farm active and reactive powers during a line-to-line fault at F_3 .

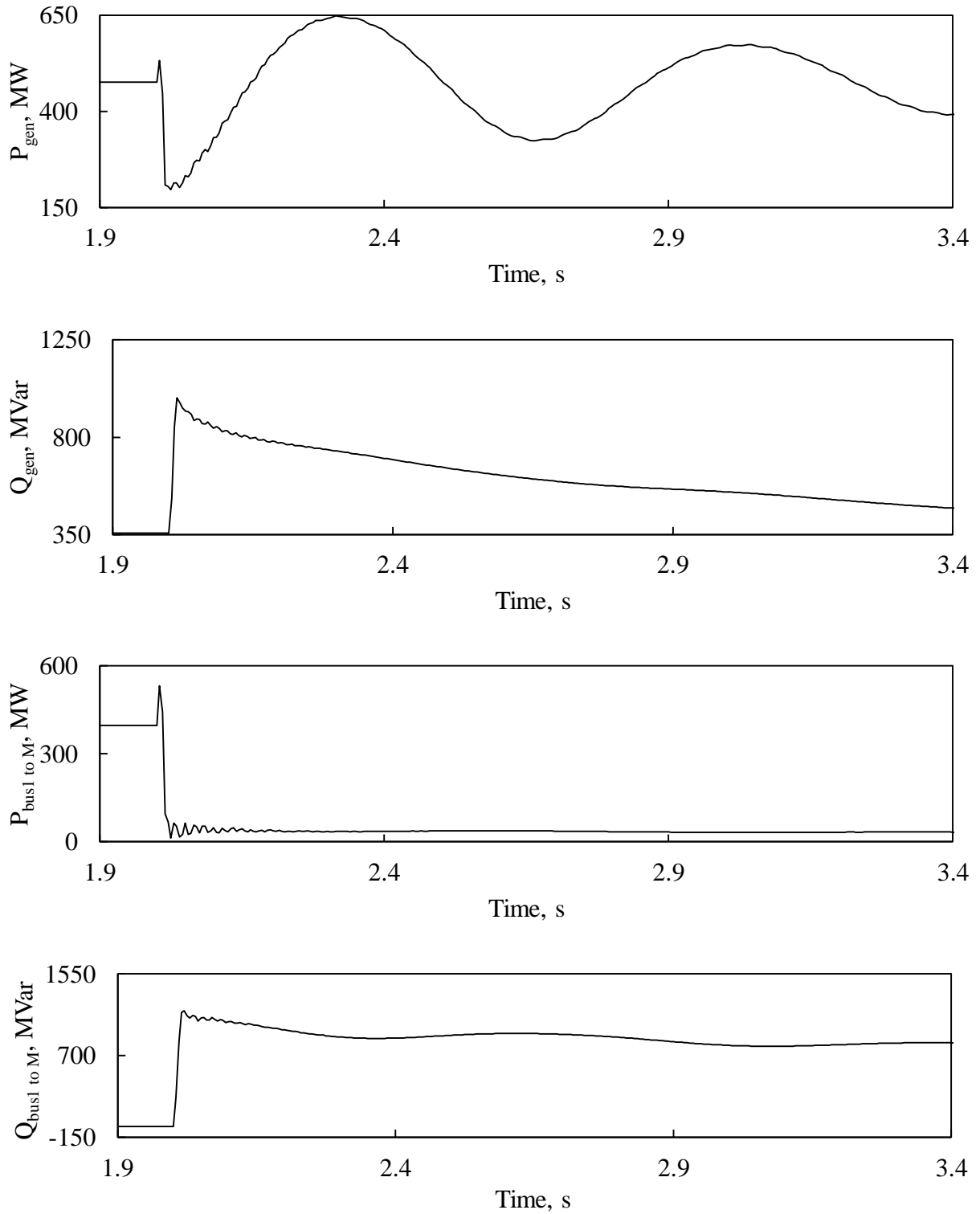


Figure C.11: Transient time responses of generator active and reactive powers, active and reactive power flows from Bus 1 to Bus M during a three-phase fault at F_3 (no wind farm in the system).

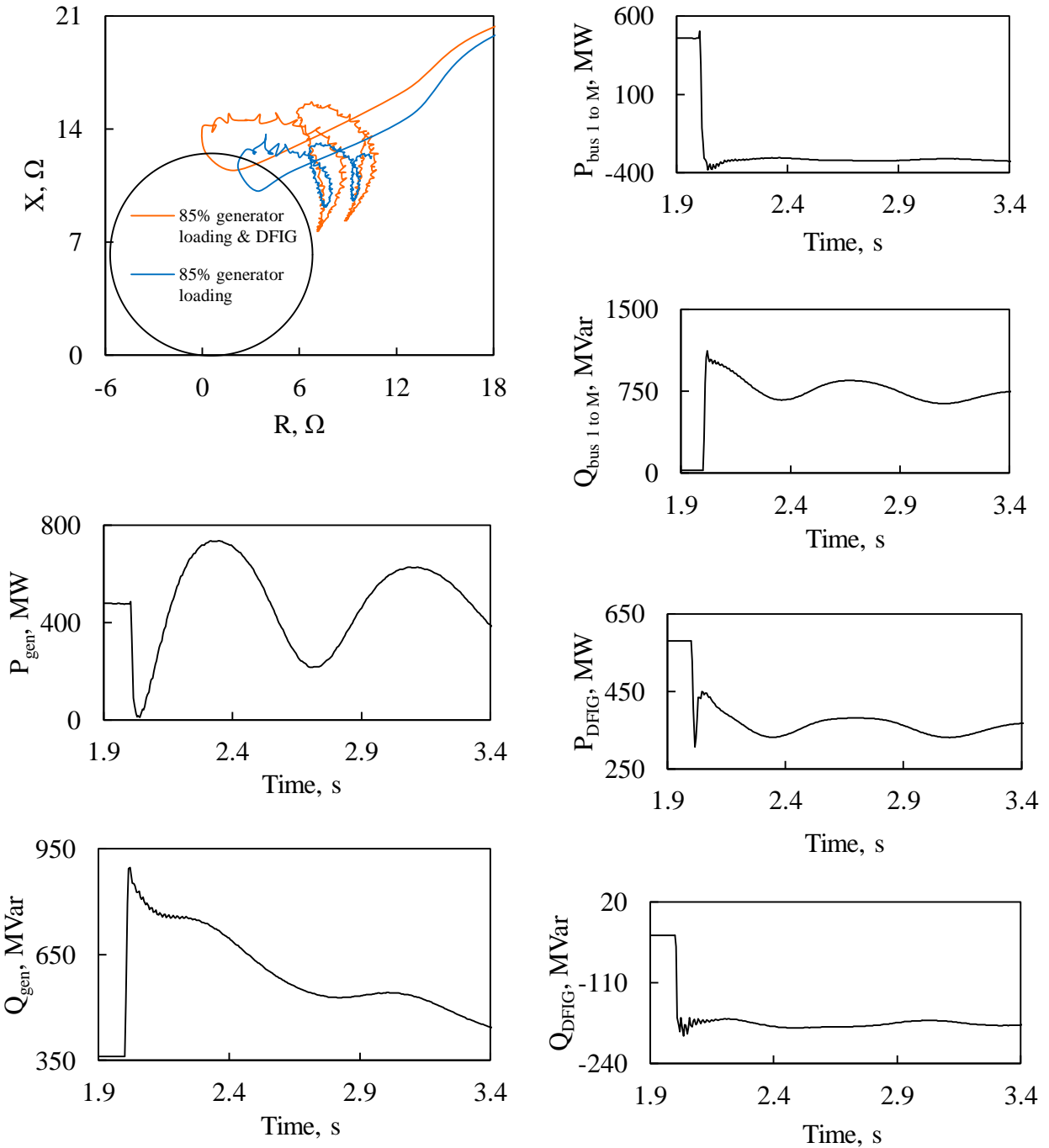


Figure C.12: Relay (21) measured impedance trajectory, transient time responses of generator active and reactive powers, active and reactive power flows from Bus 1 to Bus M, DFIG-based wind farm active and reactive powers during a three-phase at F_3 .

C.1.4 Effect of transmission line power flows

Figures C.13 to C.20 illustrate Relay tripping signal and its measured impedance trajectories as well as transient time responses of the generator active and reactive powers, active and reactive

power flows from Bus 1 to Bus M during line-to-line and three-phase faults occur at F_1 for the cases of 75% and 85% generator loading mentioned in Section 3.3.5.

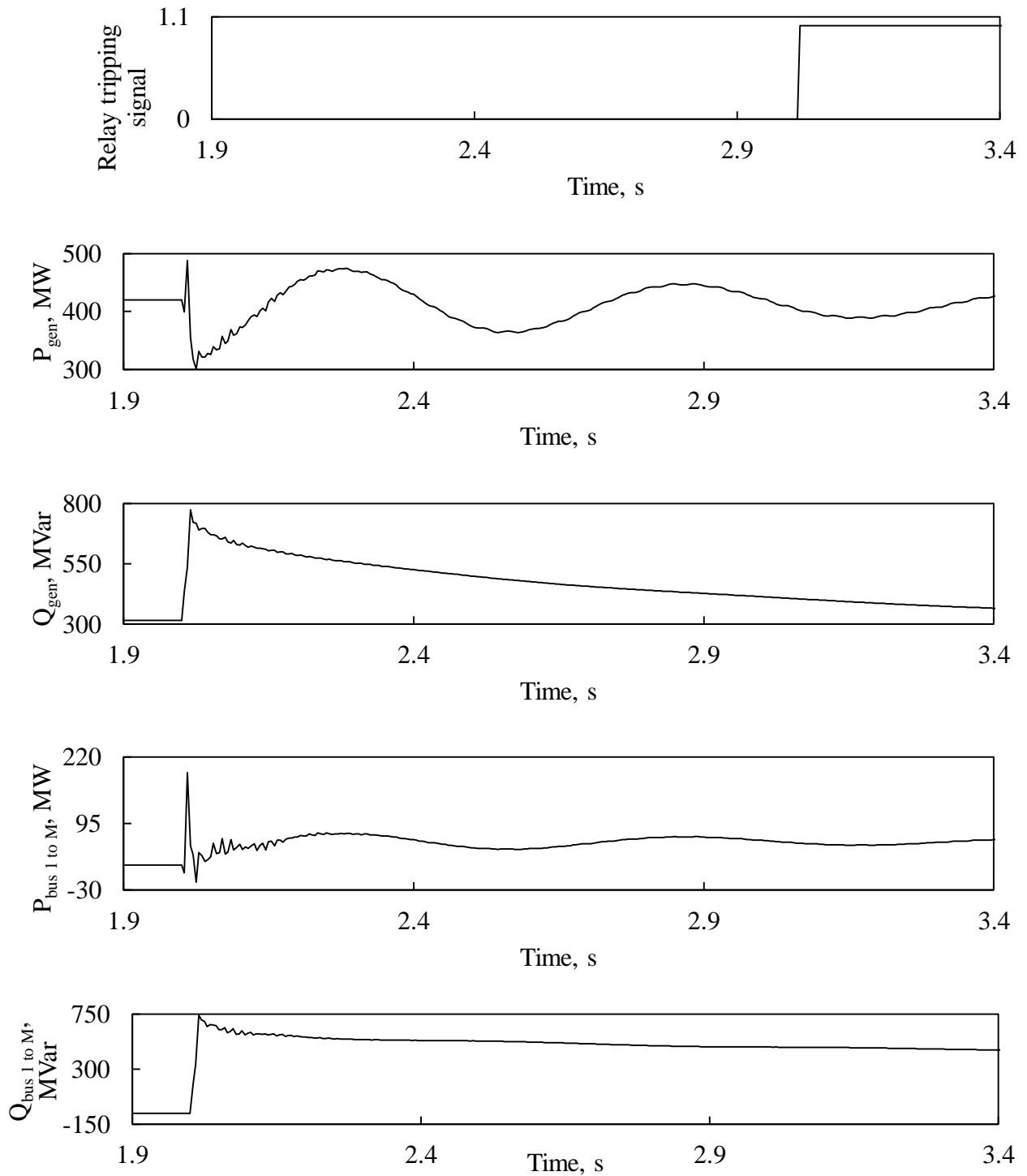


Figure C.13: Relay (21) tripping signal, transient time responses of generator active and reactive powers, active and reactive power flows from Bus 1 to Bus M during a line-to-line fault at F_1 (no wind farm in the system).

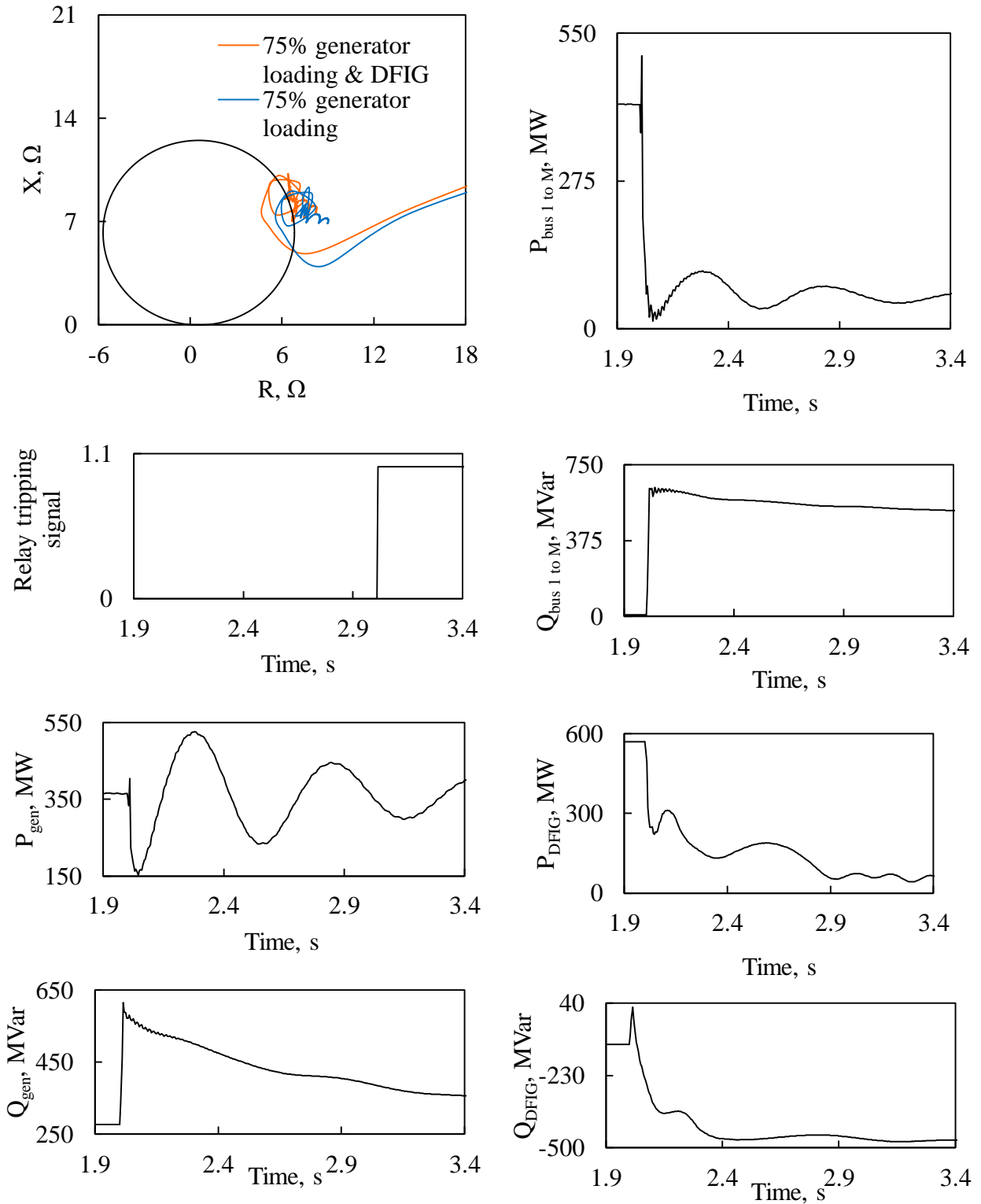


Figure C.14: Relay (21) measured impedance trajectory and its tripping signal, transient time responses of generator active and reactive powers, active and reactive power flows from Bus 1 to Bus M, DFIG-based wind farm active and reactive powers during a line-to-line fault at F_1 .

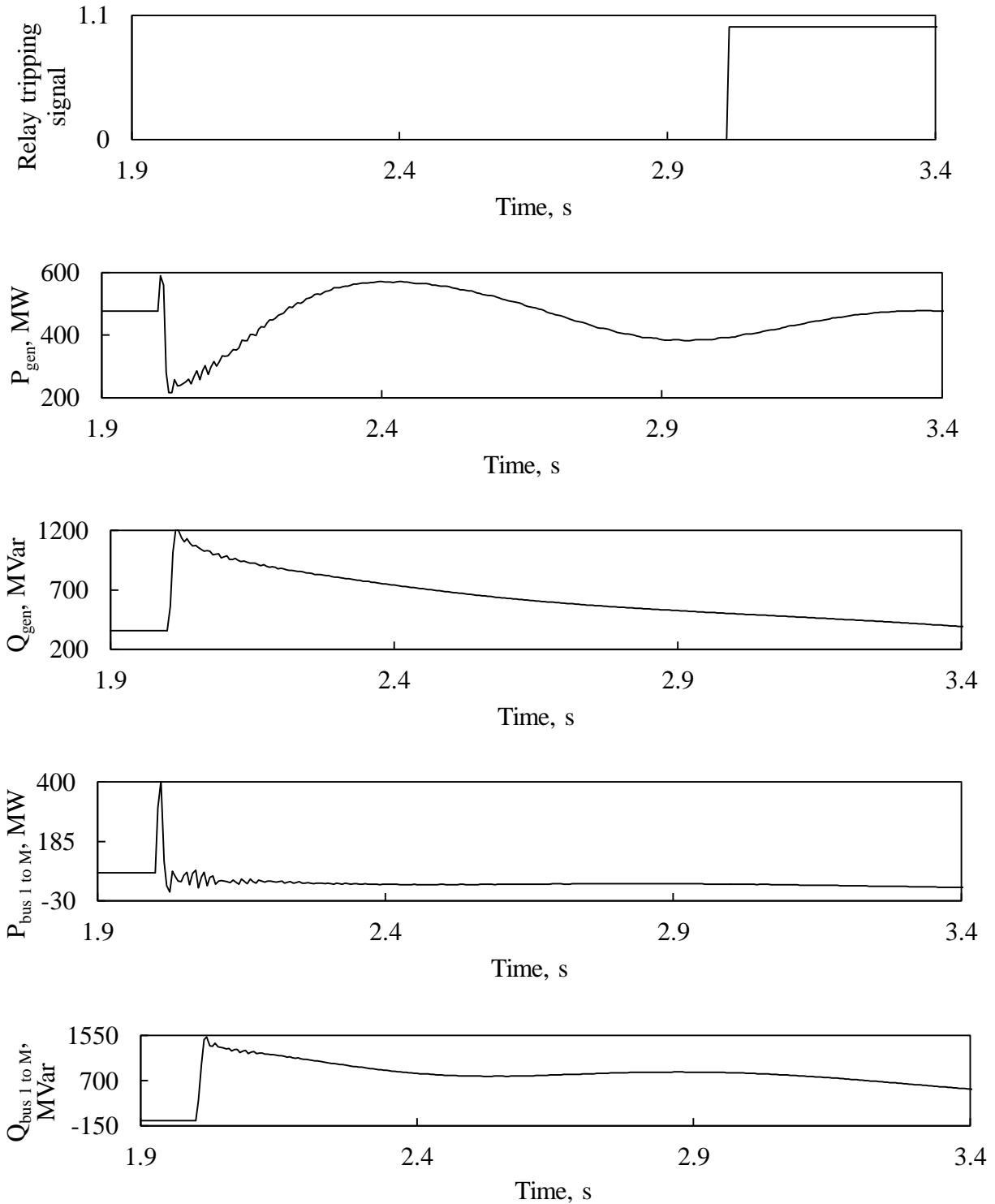


Figure C.15: Relay (21) tripping signal, transient time responses of generator active and reactive powers, active and reactive power flows from Bus 1 to Bus M during a three-phase fault at F_1 (no wind farm in the system).

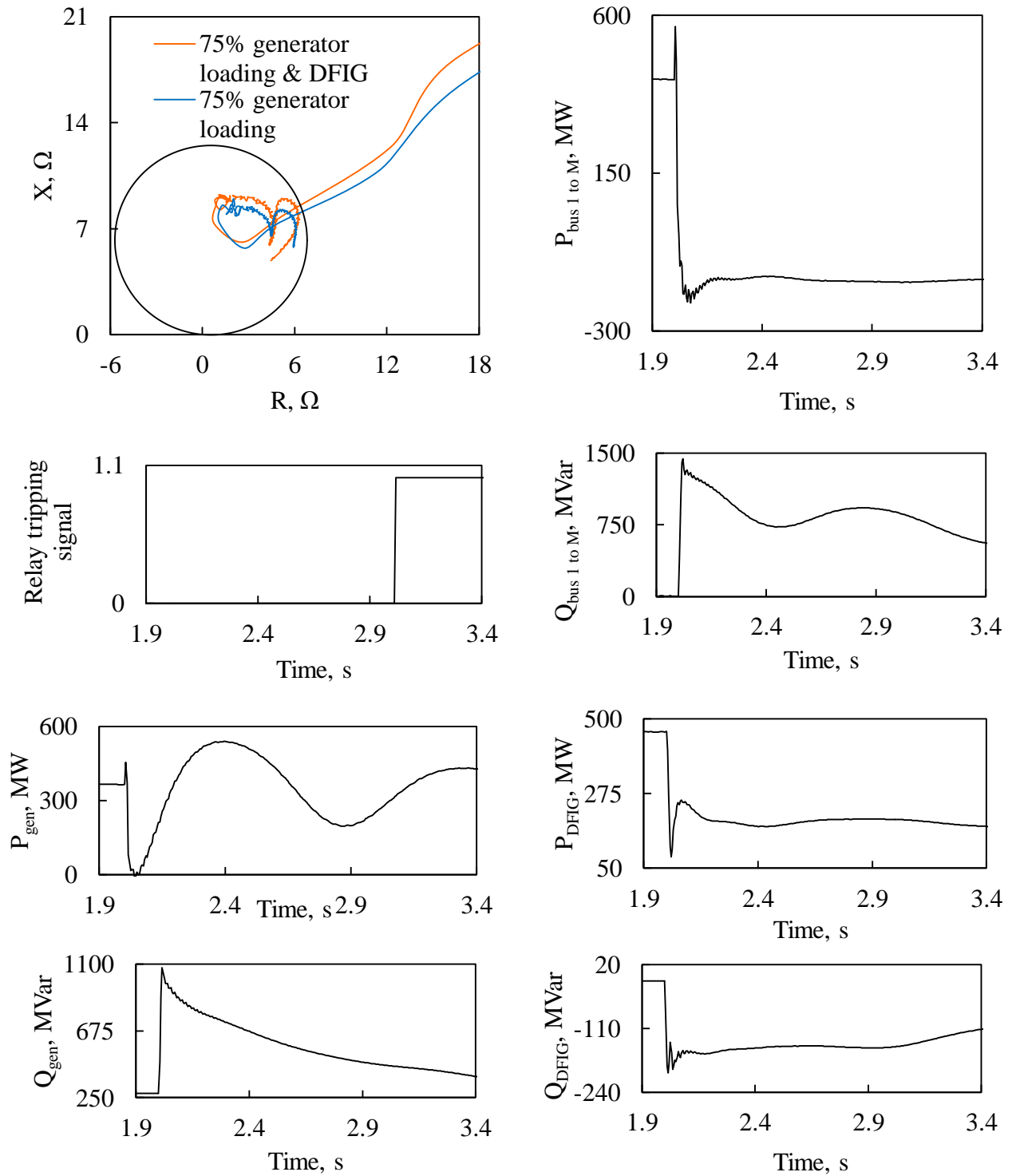


Figure C.16: Relay (21) measured impedance trajectory and its tripping signal, transient time responses of generator active and reactive powers, active and reactive power flows from Bus 1 to Bus M, DFIG-based wind farm active and reactive powers during a three-phase at F_1 .

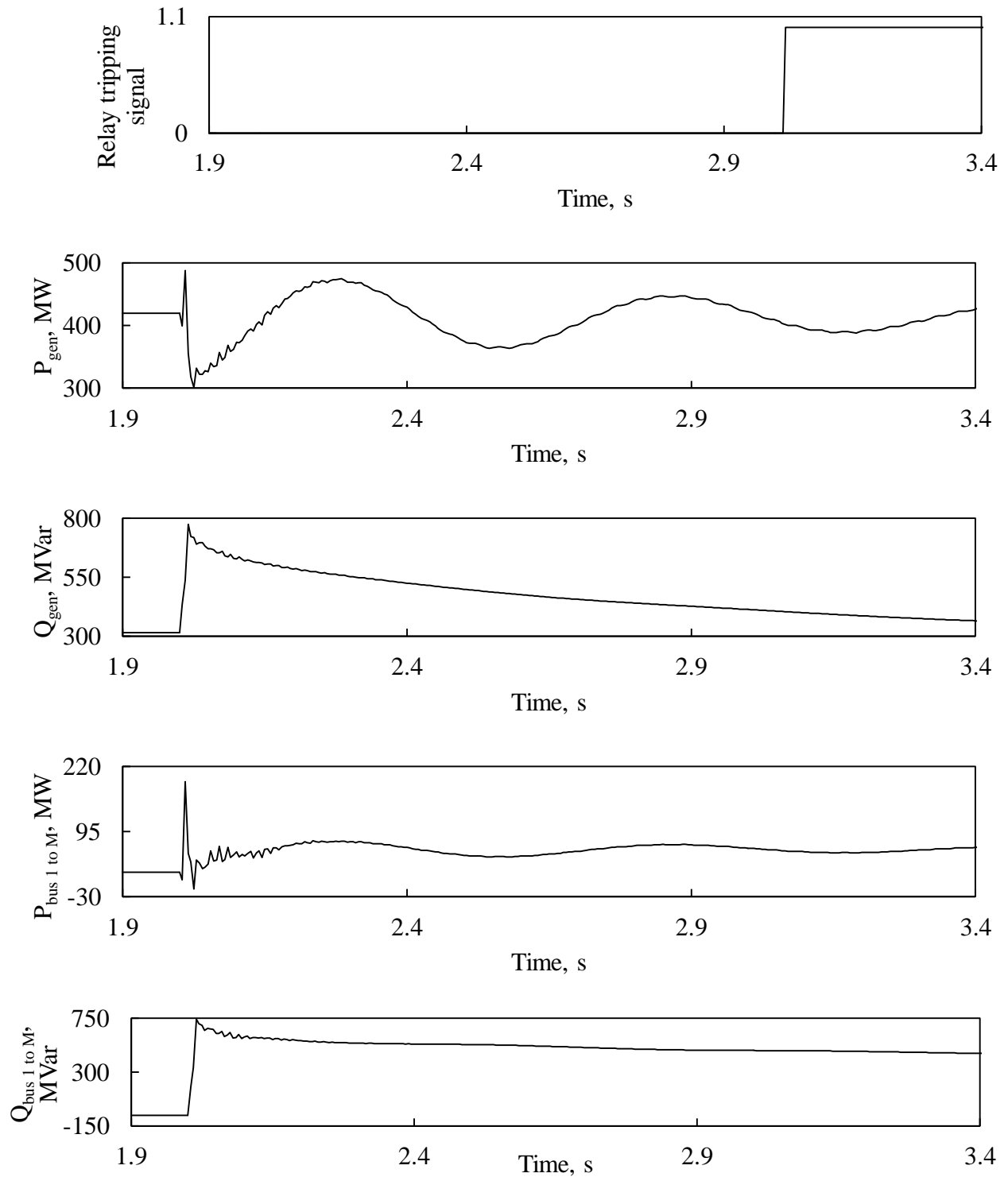


Figure C.17: Relay (21) tripping signal, transient time responses of generator active and reactive powers, active and reactive power flows from Bus 1 to Bus M during a line-to-line fault at F_1 (no wind farm in the system).

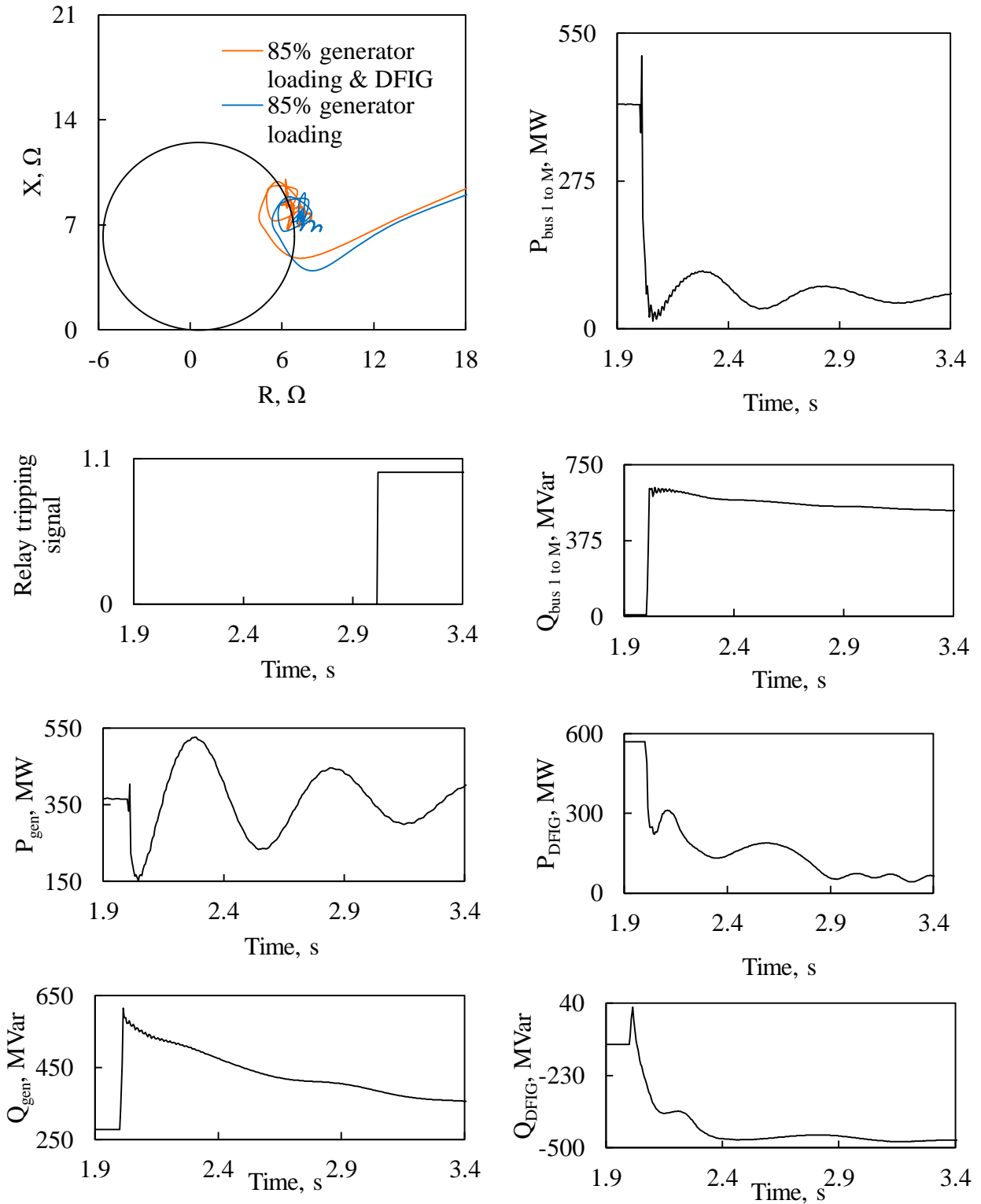


Figure C.18: Relay (21) measured impedance trajectory and its tripping signal, transient time responses of generator active and reactive powers, active and reactive power flows from Bus 1 to Bus M, DFIG-based wind farm active and reactive powers during a line-to-line fault at F_1 .

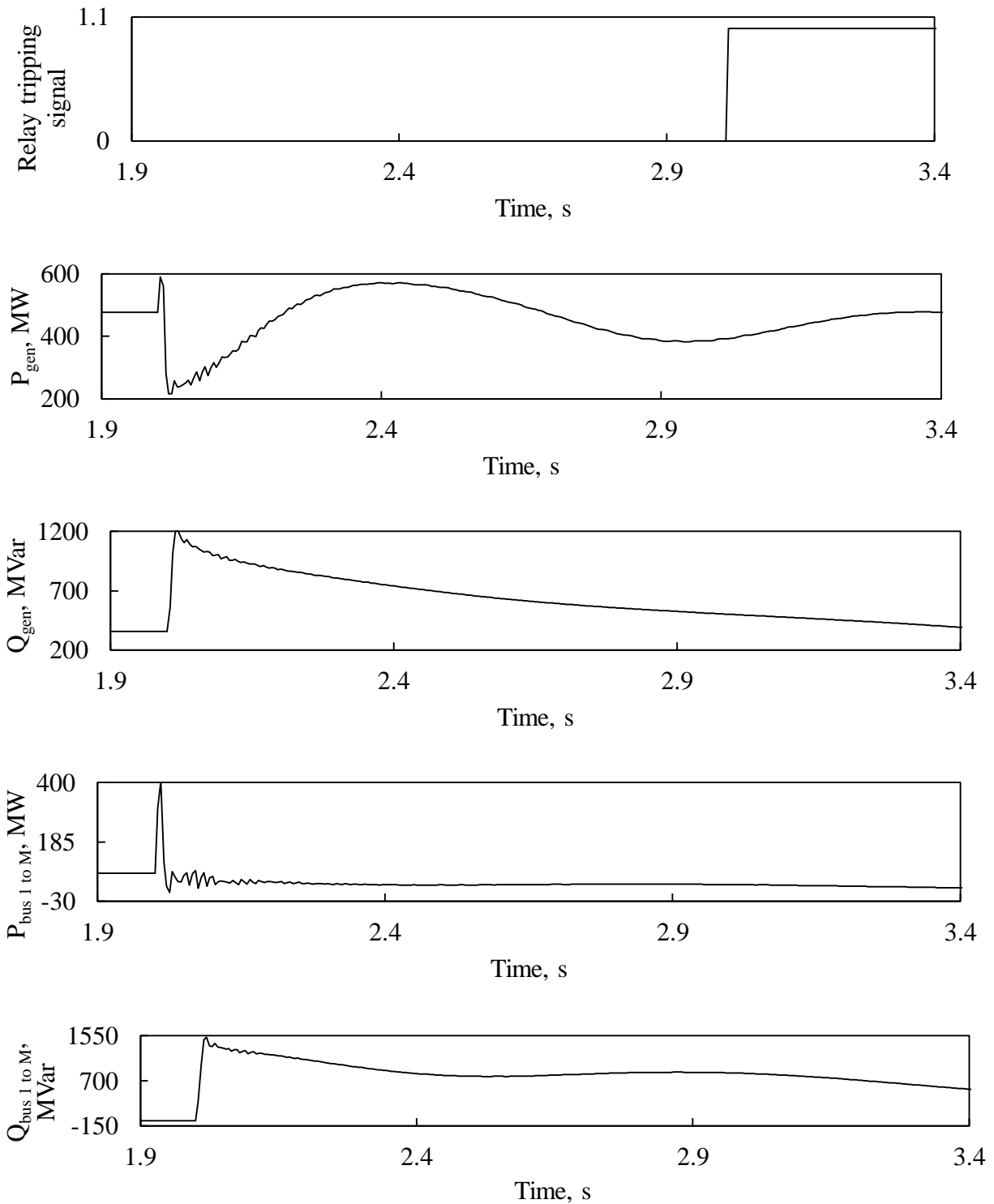


Figure C.19: Relay (21) tripping signal, transient time responses of generator active and reactive powers, active and reactive power flows from Bus 1 to Bus M during a three-phase fault at F_1 (no wind farm in the system).

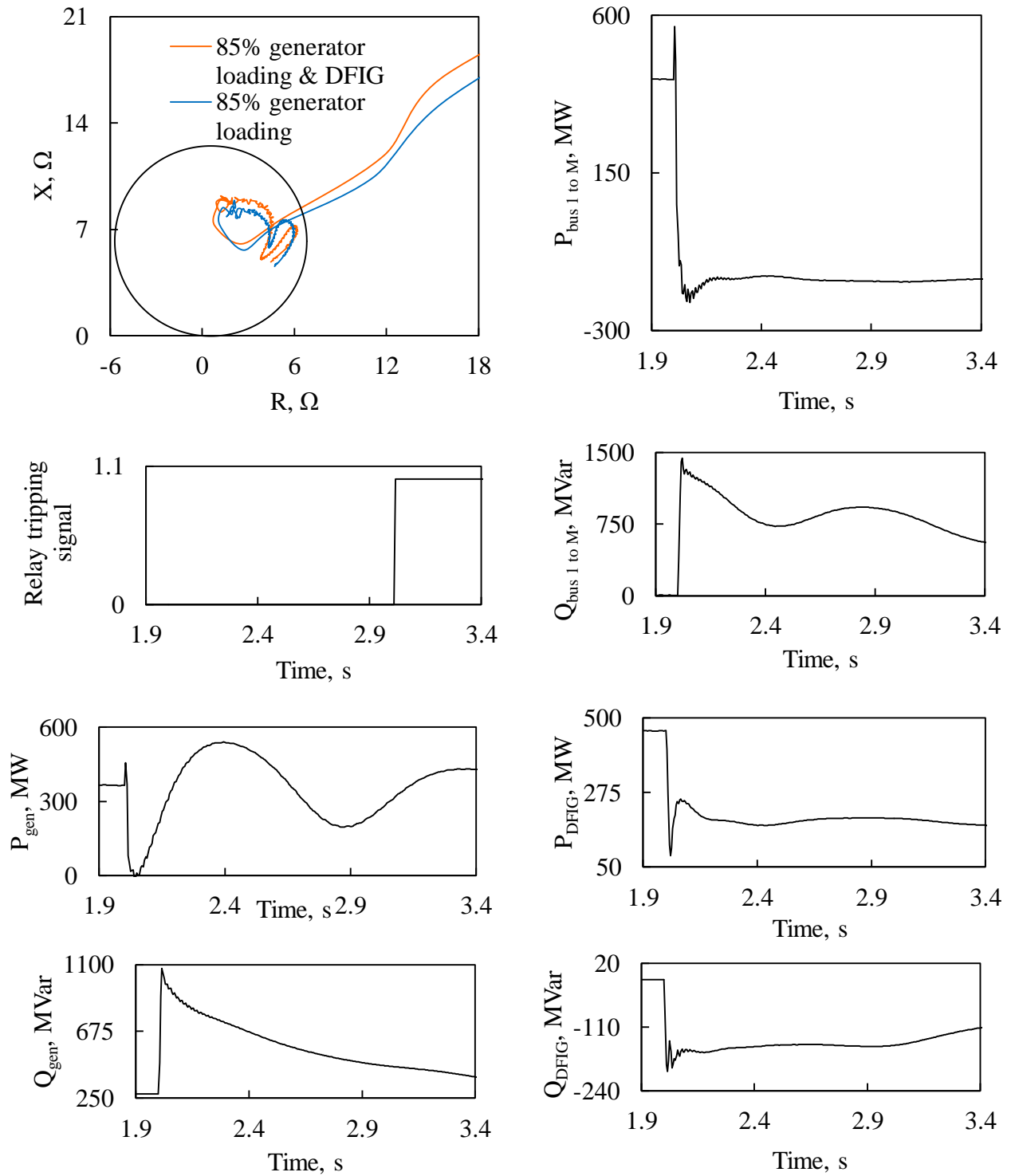


Figure C.20: Relay (21) measured impedance trajectory and its tripping signal, transient time responses of generator active and reactive powers, active and reactive power flows from Bus 1 to Bus M, DFIG-based wind farm active and reactive powers during a three-phase at F_1 .

C.2 Setting Relay (21) According to 67% of RPPA of the Generator

C.2.1 Performance of Relay (21) at 65% of the generator loading

Figure C.21 illustrates the Relay (21) tripping signal, transient time responses of the generator active and reactive powers as well as active and reactive power flows from Bus 1 to Bus M during a line-to-line fault occurs at F_1 when there is no wind farm in the system. After connecting DFIG-based wind farm to Bus M, Figure C.22 depicts the Relay (21) measured impedance trajectories, Relay (21) tripping signal, transient time responses of the generator active and reactive powers, active and reactive power flows from Bus 1 to Bus M as well as the DFIG-based wind farm active and reactive powers during the same line-to-line fault at F_1 . Figures C.23 and C.24 show the same trajectories, signals in conjunction with transient time responses for the cases of three-phase fault at the same location.

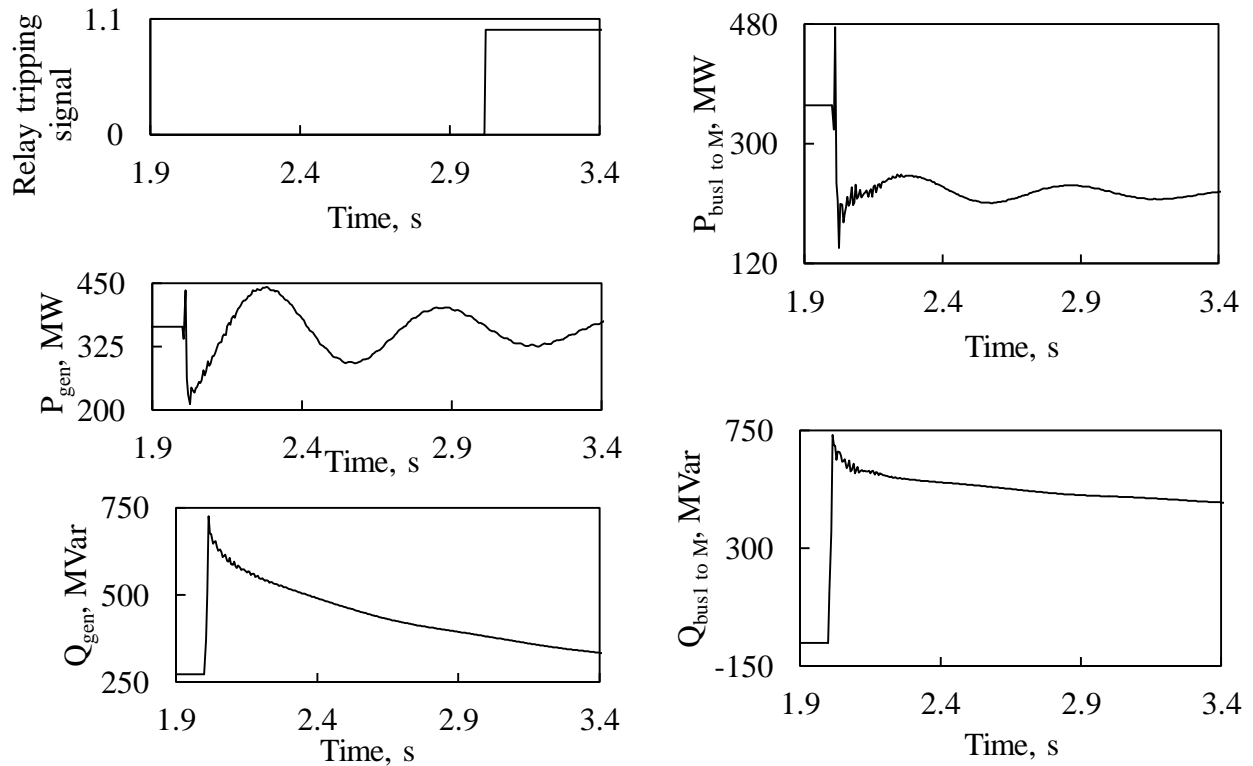


Figure C.21: Relay (21) tripping signal, transient time responses of generator active and reactive powers, active and reactive power flows from Bus 1 to Bus M during a line-to-line fault at F_1 (no wind farm in the system).

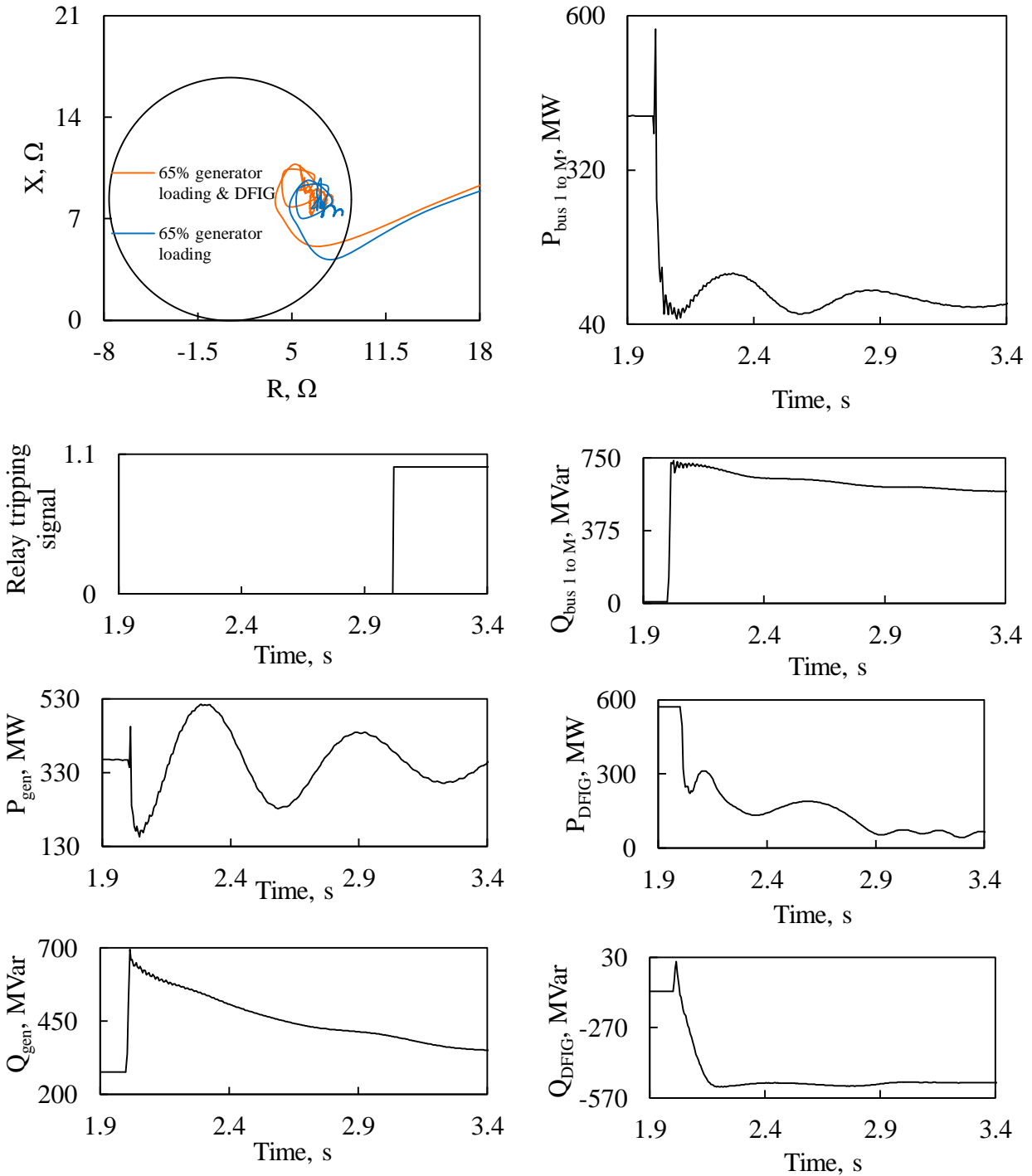


Figure C.22: Relay (21) measured impedance trajectory and its tripping signal, transient time responses of generator active and reactive powers, active and reactive power flows from Bus 1 to Bus M, DFIG-based wind farm active and reactive powers during a line-to-line fault at F₁.

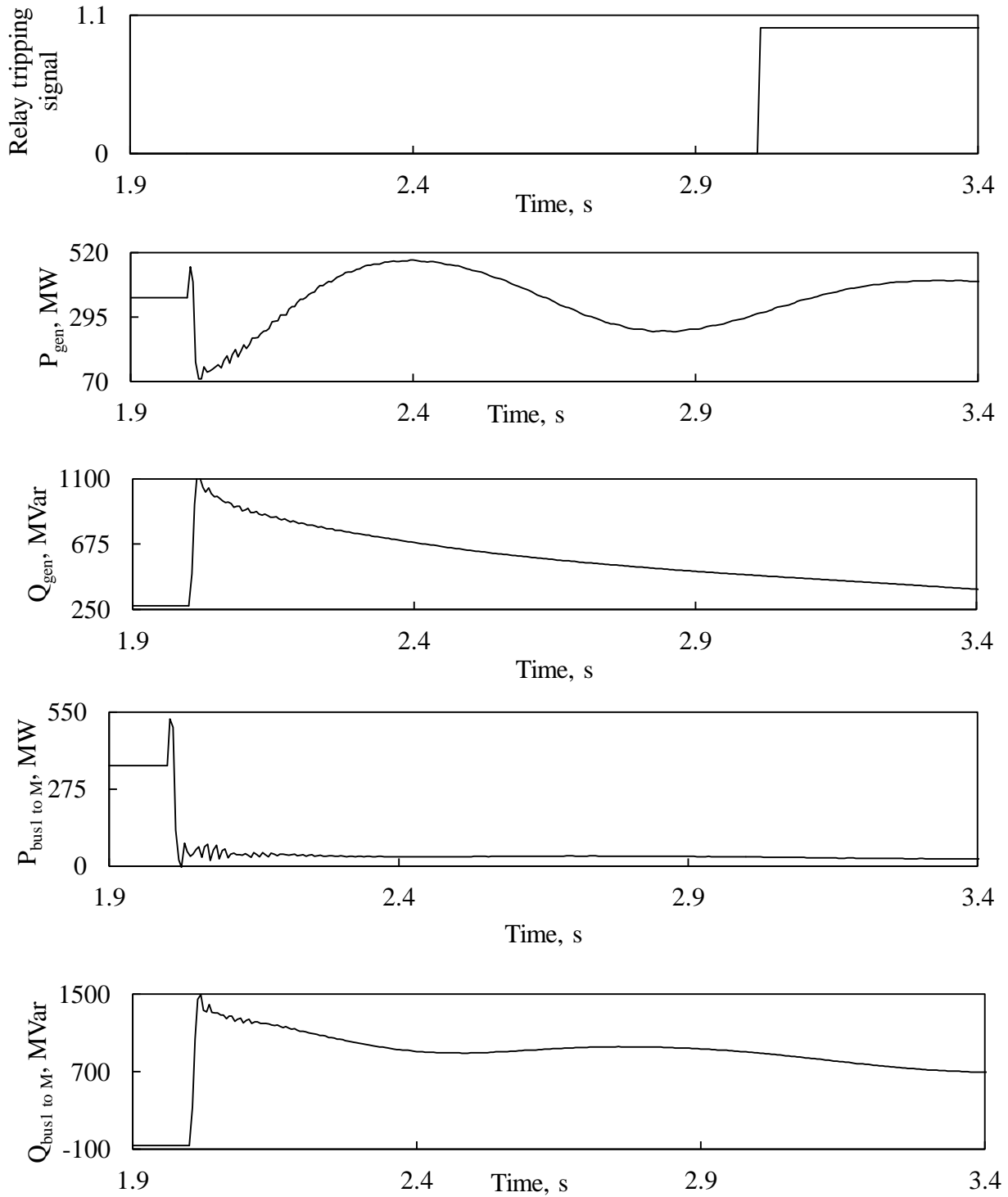


Figure C.23: Relay (21) tripping signal, transient time responses of generator active and reactive powers, active and reactive power flows from Bus 1 to Bus M during a three-phase fault at F_1 (no wind farm in the system).

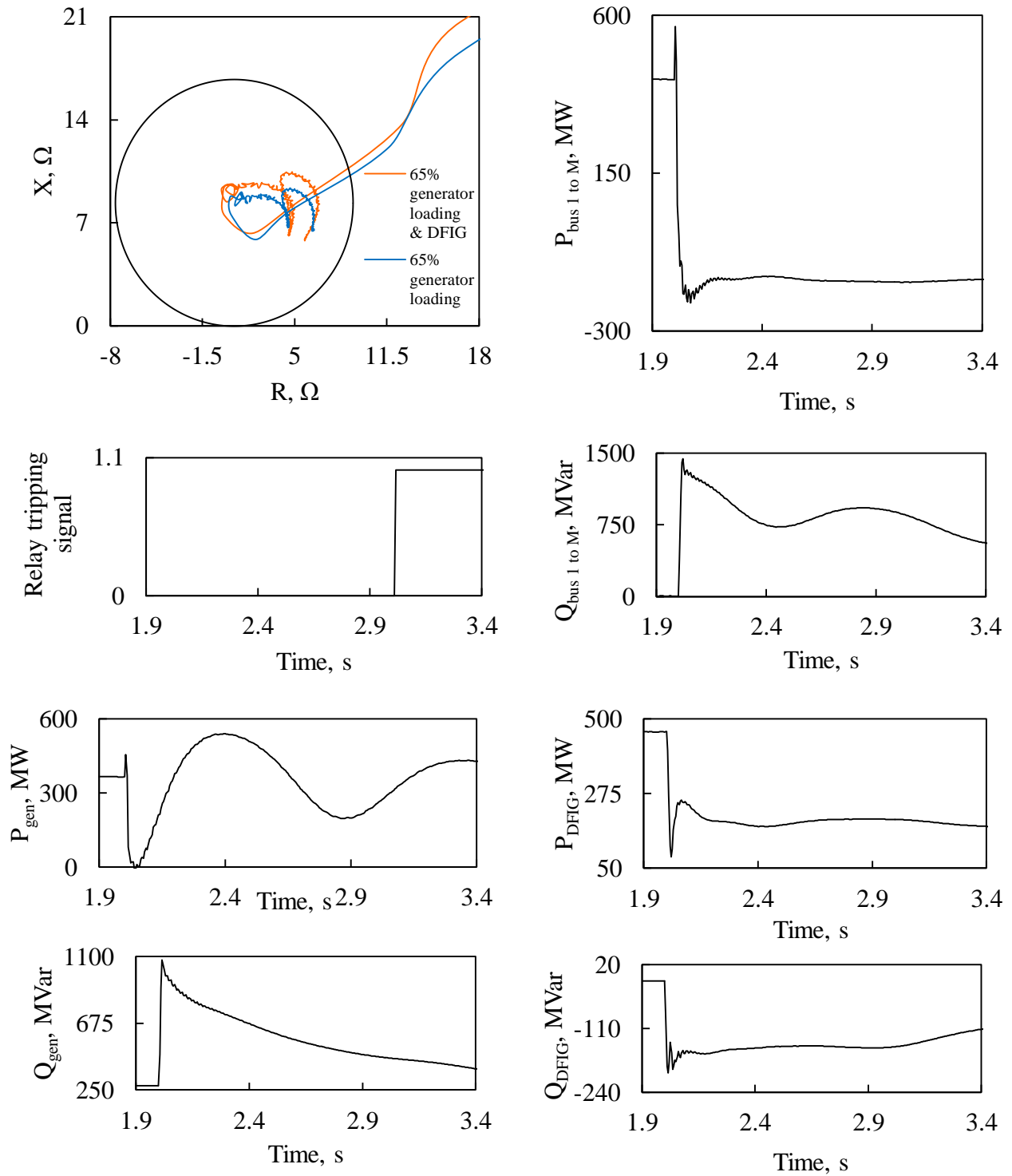


Figure C.24: Relay (21) measured impedance trajectory and its tripping signal, transient time responses of generator active and reactive powers, active and reactive power flows from Bus 1 to Bus M, DFIG-based wind farm active and reactive powers during a three-phase at F_1 .

Figure C.25 illustrates the Relay (21) tripping signal, transient time responses of the generator active and reactive powers as well as active and reactive power flows from Bus 1 to Bus M during a line-to-line fault occurs at F_2 when there is no wind farm in the system. After connecting DFIG-based wind farm to Bus M, Figure C.26 depicts the Relay (21) measured impedance trajectories and its tripping signal, transient time responses of the generator active and reactive powers, active and reactive power flows from Bus 1 to Bus M as well as the DFIG-based wind farm active and reactive powers during the same line-to-line fault at F_2 . Figures C.27 and C.28 show the same trajectories, signals in conjunction with transient time responses for the cases of three-phase fault at the same location.

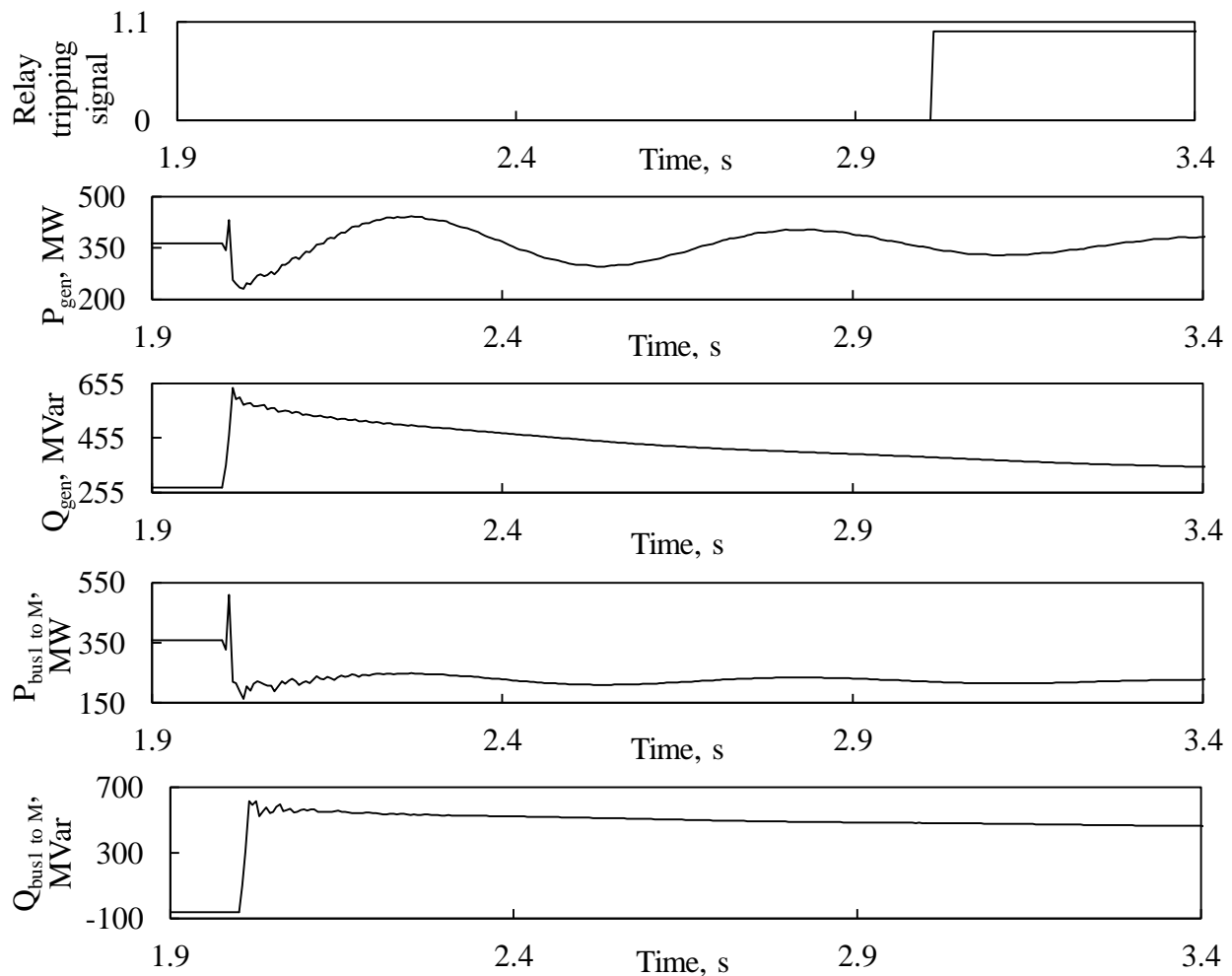


Figure C.25: Relay (21) tripping signal, transient time responses of generator active and reactive powers, active and reactive power flows from Bus 1 to Bus M during a line-to-line fault at F_2 (no wind farm in the system).

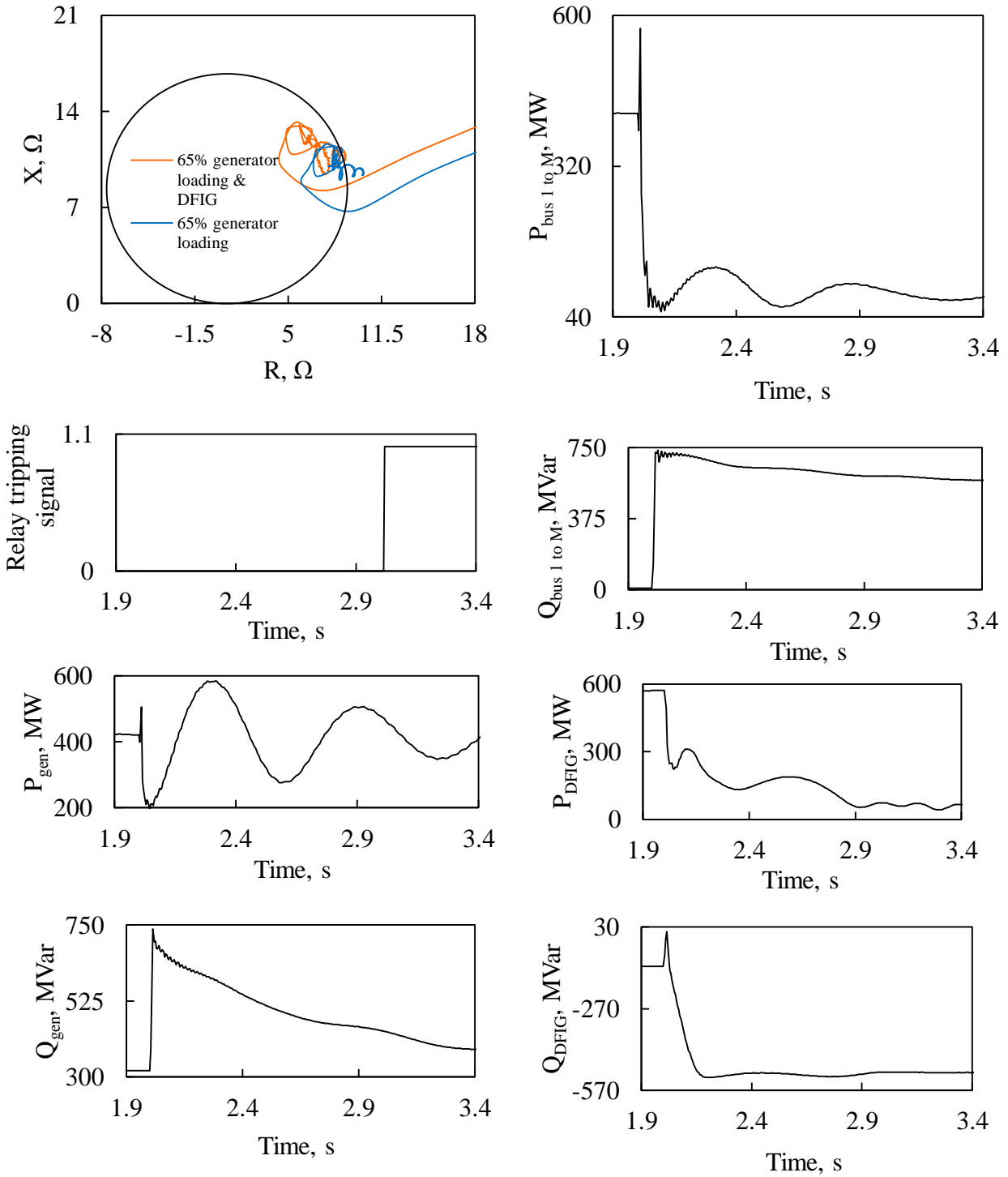


Figure C.26: Relay (21) measured impedance trajectory and its tripping signal, transient time responses of generator active and reactive powers, active and reactive power flows from Bus 1 to Bus M, DFIG-based wind farm active and reactive powers during a line-to-line fault at F_2 .

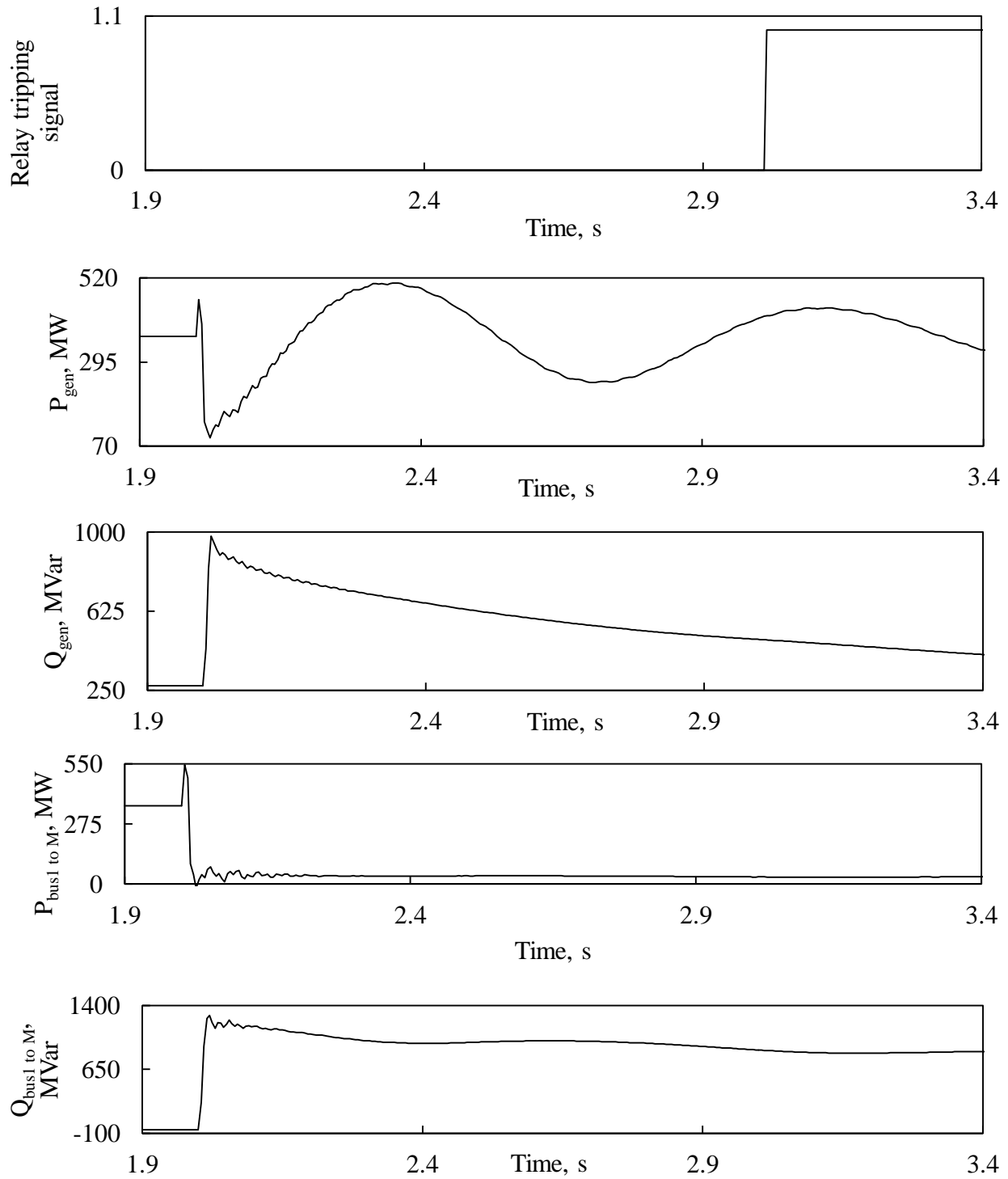


Figure C.27: Relay (21) tripping signal, transient time responses of generator active and reactive powers, active and reactive power flows from Bus 1 to Bus M during a three-phase fault at F_2 (no wind farm in the system).

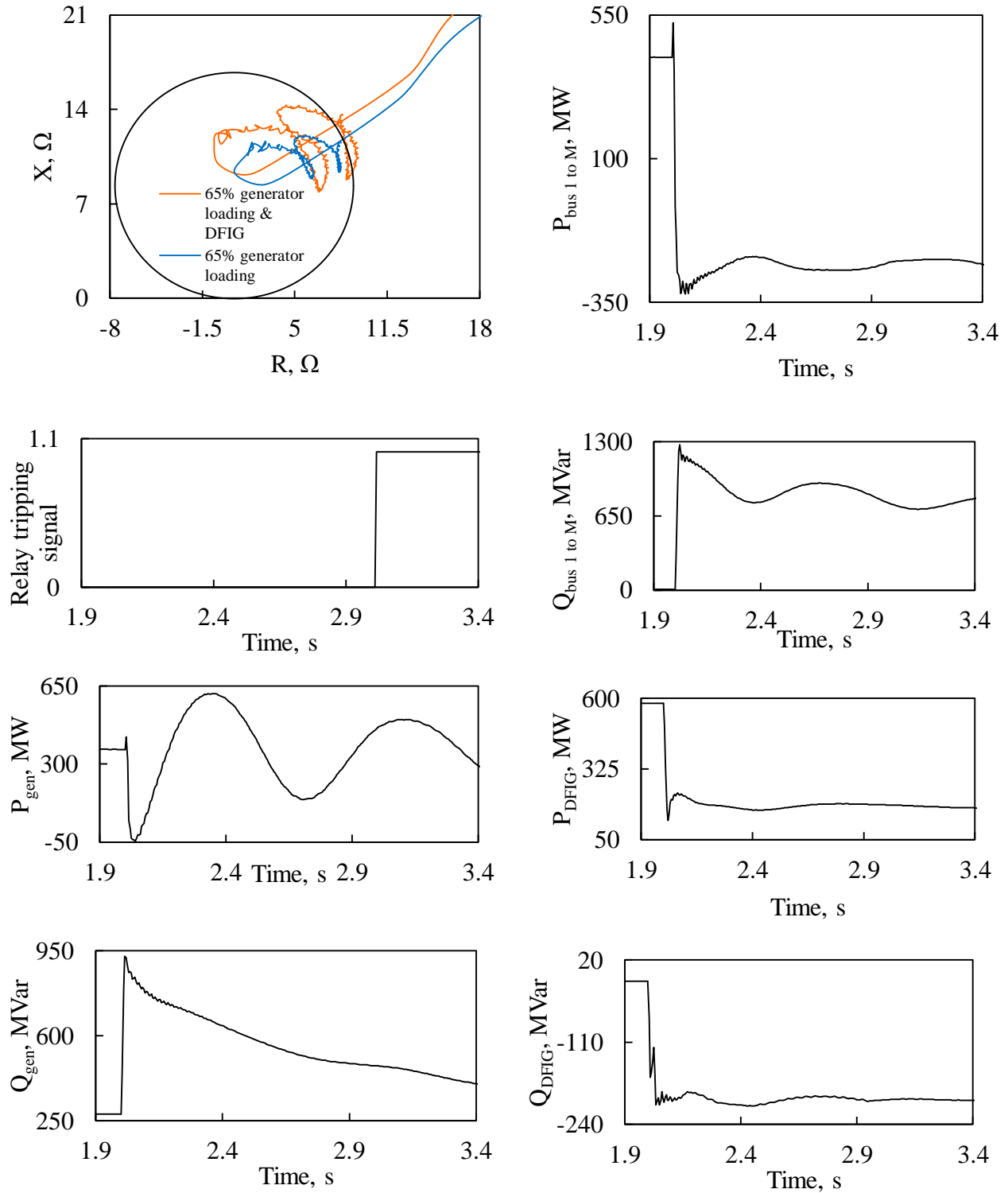


Figure C.28: Relay (21) measured impedance trajectory and its tripping signal, transient time responses of generator active and reactive powers, active and reactive power flows from Bus 1 to Bus M, DFIG-based wind farm active and reactive powers during a three-phase at F₂.

Figure C.29 illustrates the Relay (21) tripping signal, transient time responses of generator active and reactive powers as well as active and reactive power flows from Bus 1 to Bus M during a line-to-line fault occurs at F_3 when there is no wind farm in the system. After connecting DFIG-based wind farm to Bus M, Figure C.30 depicts the Relay (21) measured impedance trajectories and its tripping signal, transient time responses of the generator active and reactive powers, active and reactive power flows from Bus 1 to Bus M as well as the DFIG-based wind farm active and reactive powers during the same line-to-line fault at F_3 . Figures C.31 and C.32 show the same trajectories, signals in conjunction with transient time responses for the cases of three-phase fault at the same location.

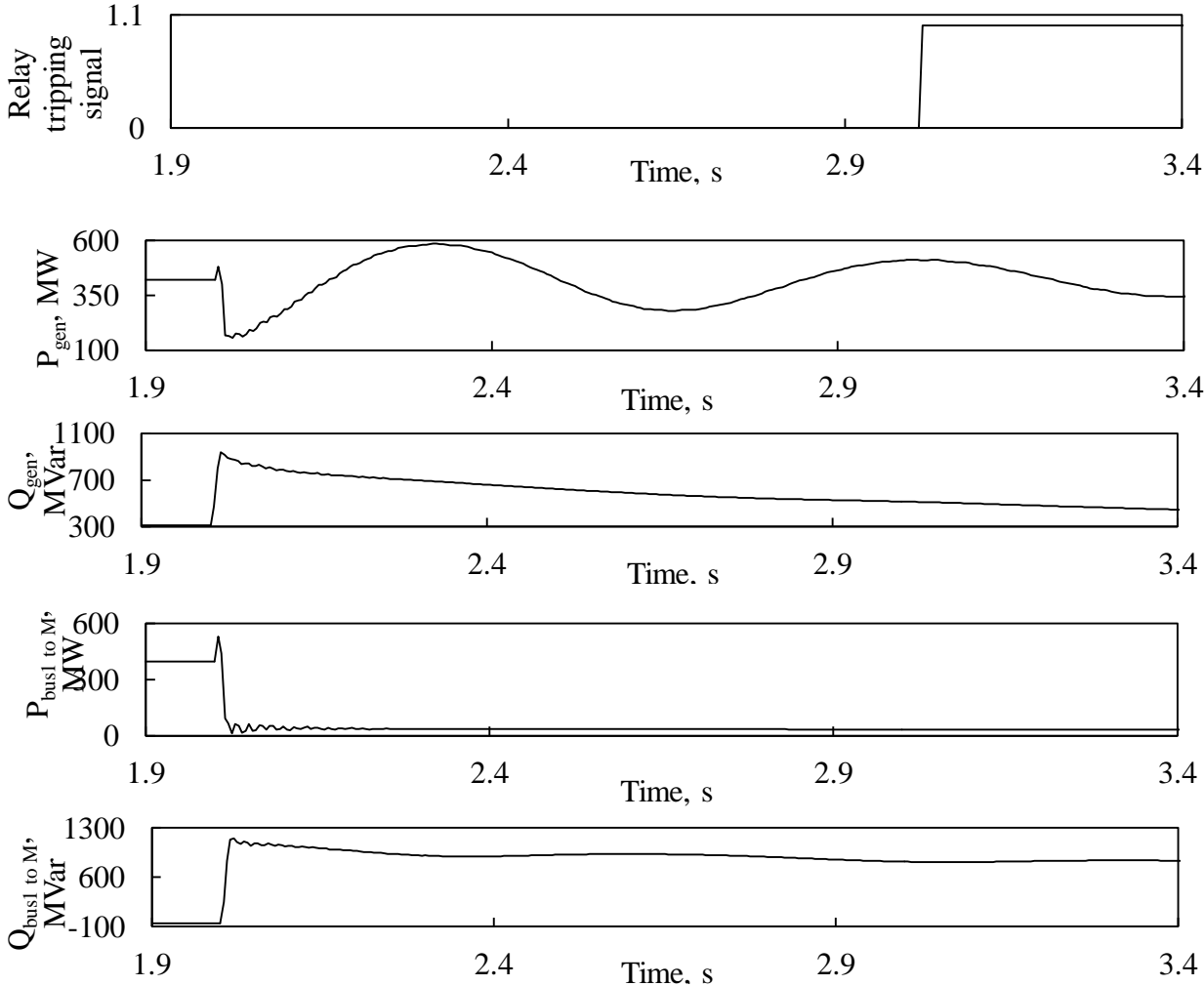


Figure C.29: Relay (21) tripping signal, Transient time responses of generator active and reactive powers, active and reactive power flows from Bus 1 to Bus M during a line-to-line fault at F_3 (no wind farm in the system).

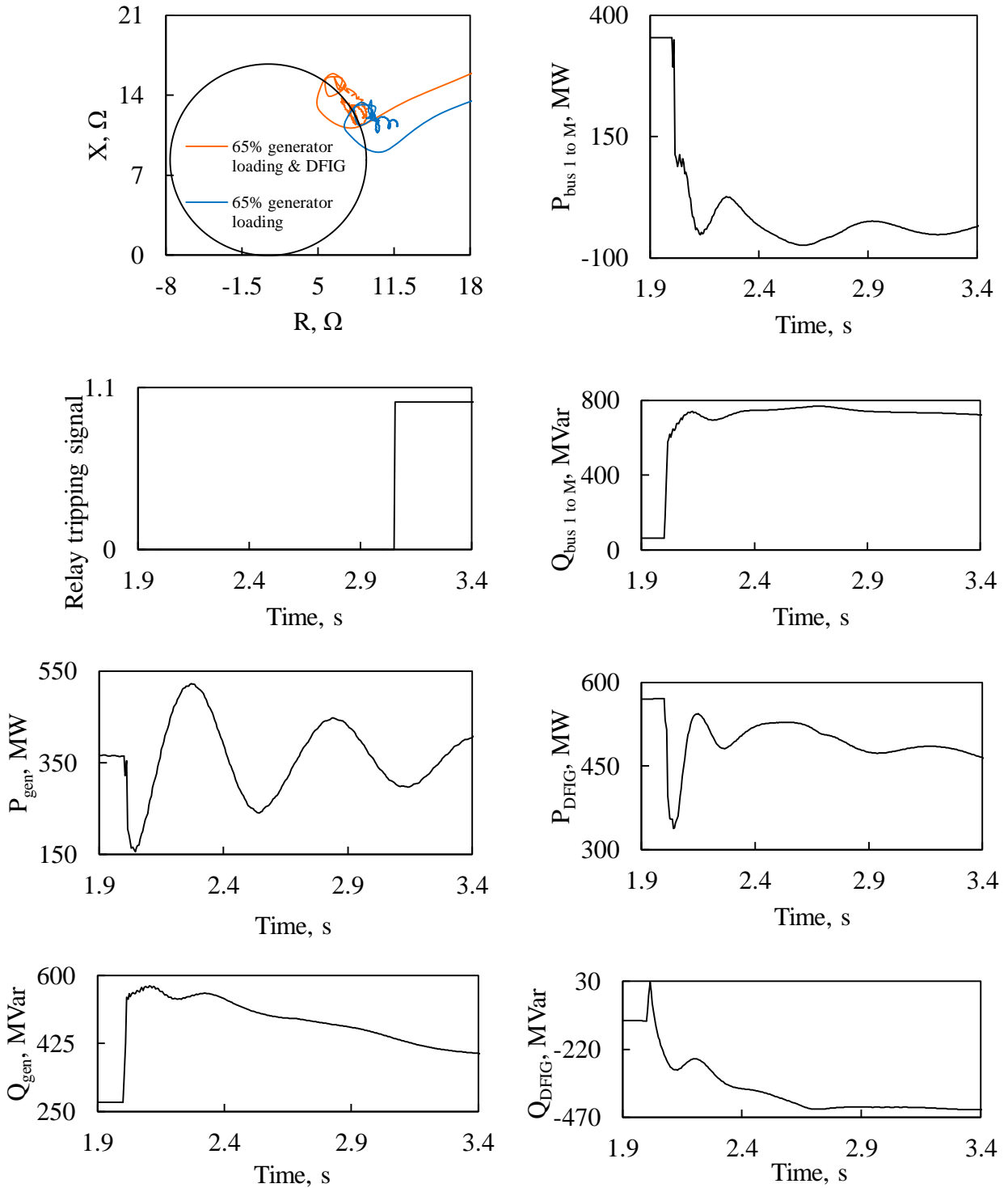


Figure C.30: Relay (21) measured impedance trajectory and its tripping signal, transient time responses of generator active and reactive powers, active and reactive power flows from Bus 1 to Bus M, DFIG-based wind farm active and reactive powers during a line-to-line fault at F₃.

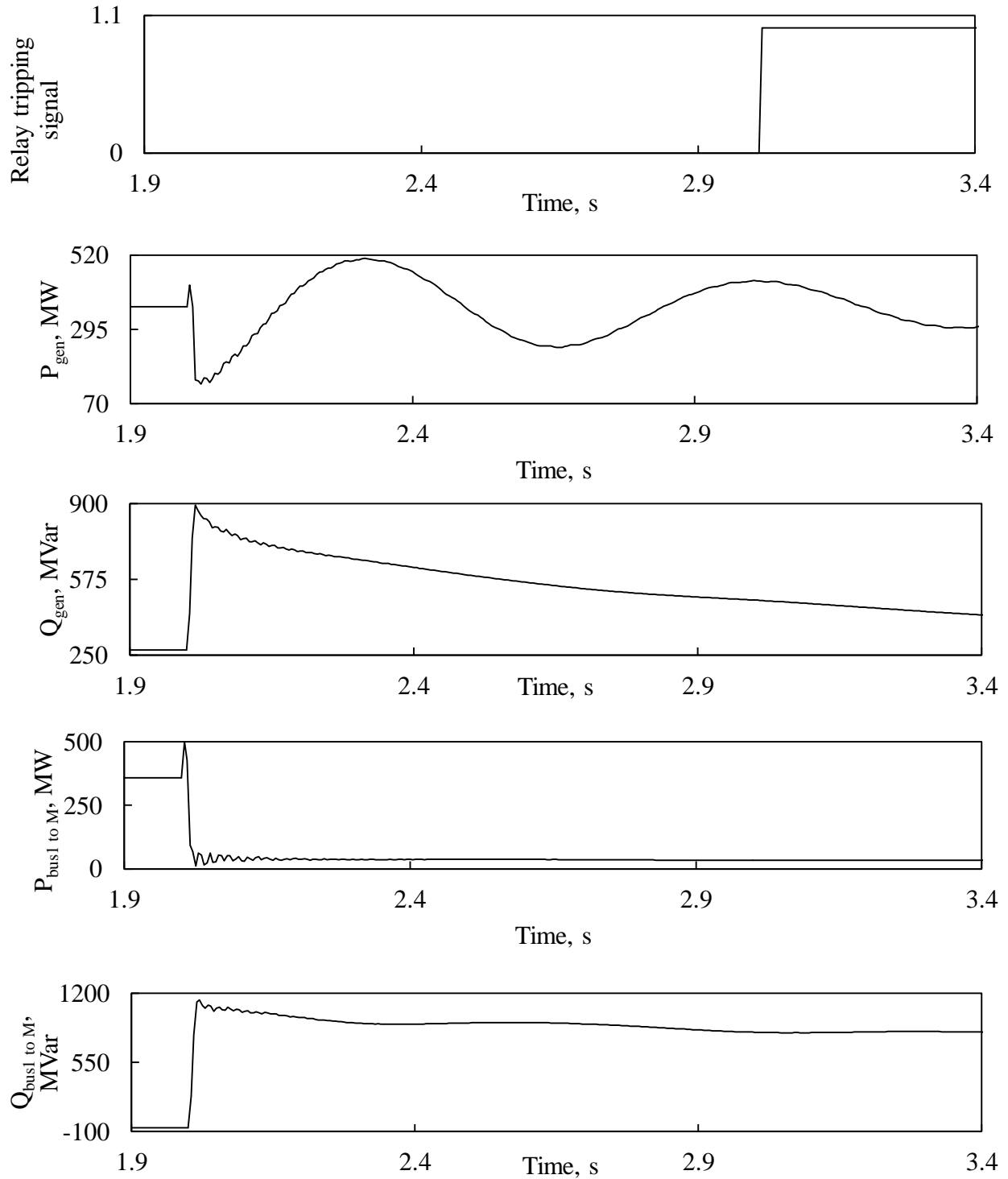


Figure C.31: Relay (21) tripping signal, transient time responses of generator active and reactive powers, active and reactive power flows from Bus 1 to Bus M during a three-phase fault at F_3 (no wind farm in the system).

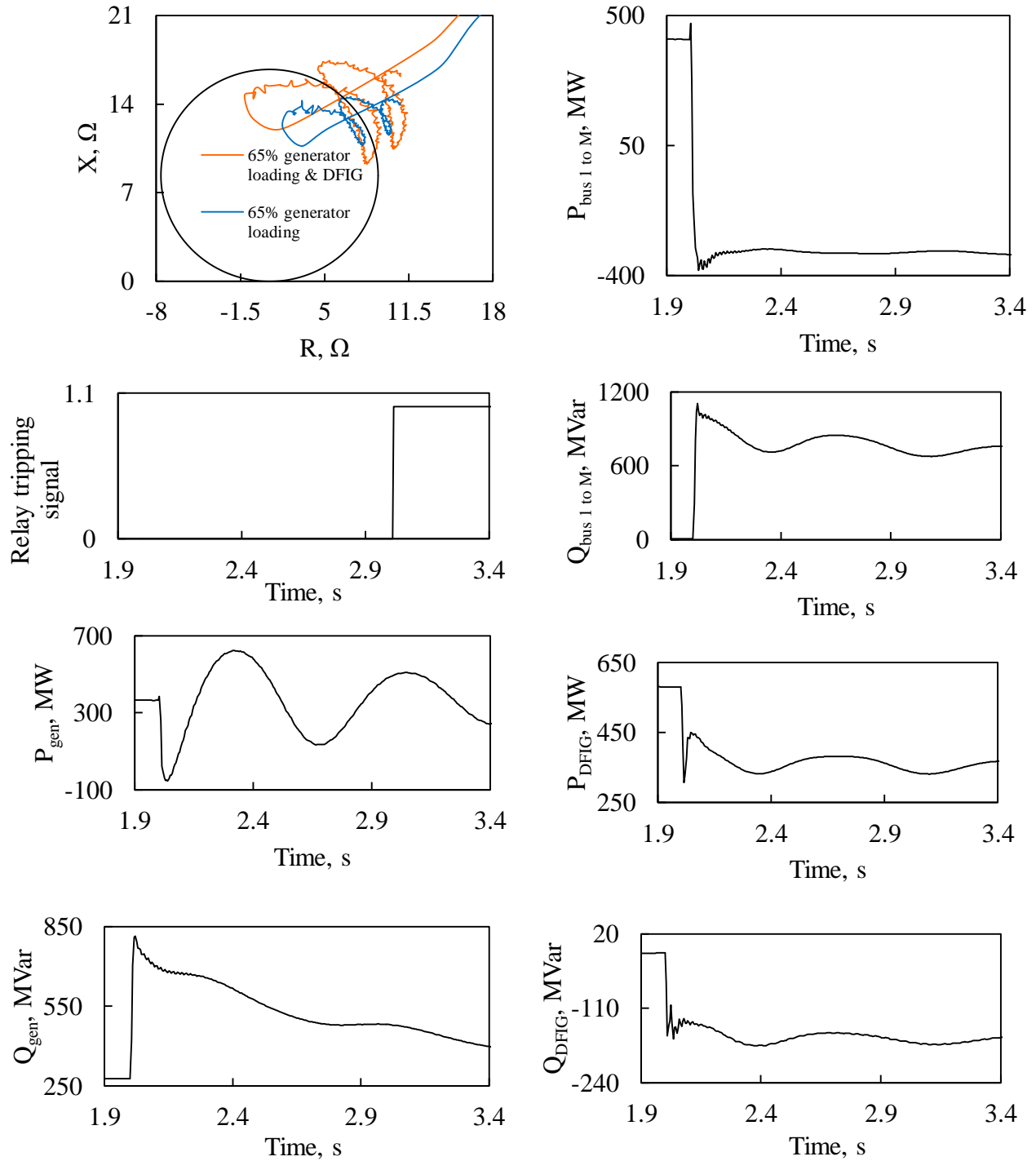


Figure C.32: Relay (21) measured impedance trajectory and its tripping signal, transient time responses of generator active and reactive powers, active and reactive power flows from Bus 1 to Bus M, DFIG-based wind farm active and reactive powers during a three-phase at F_3 .

C.2.2 Performance of Relay (21) at 75% of the generator loading

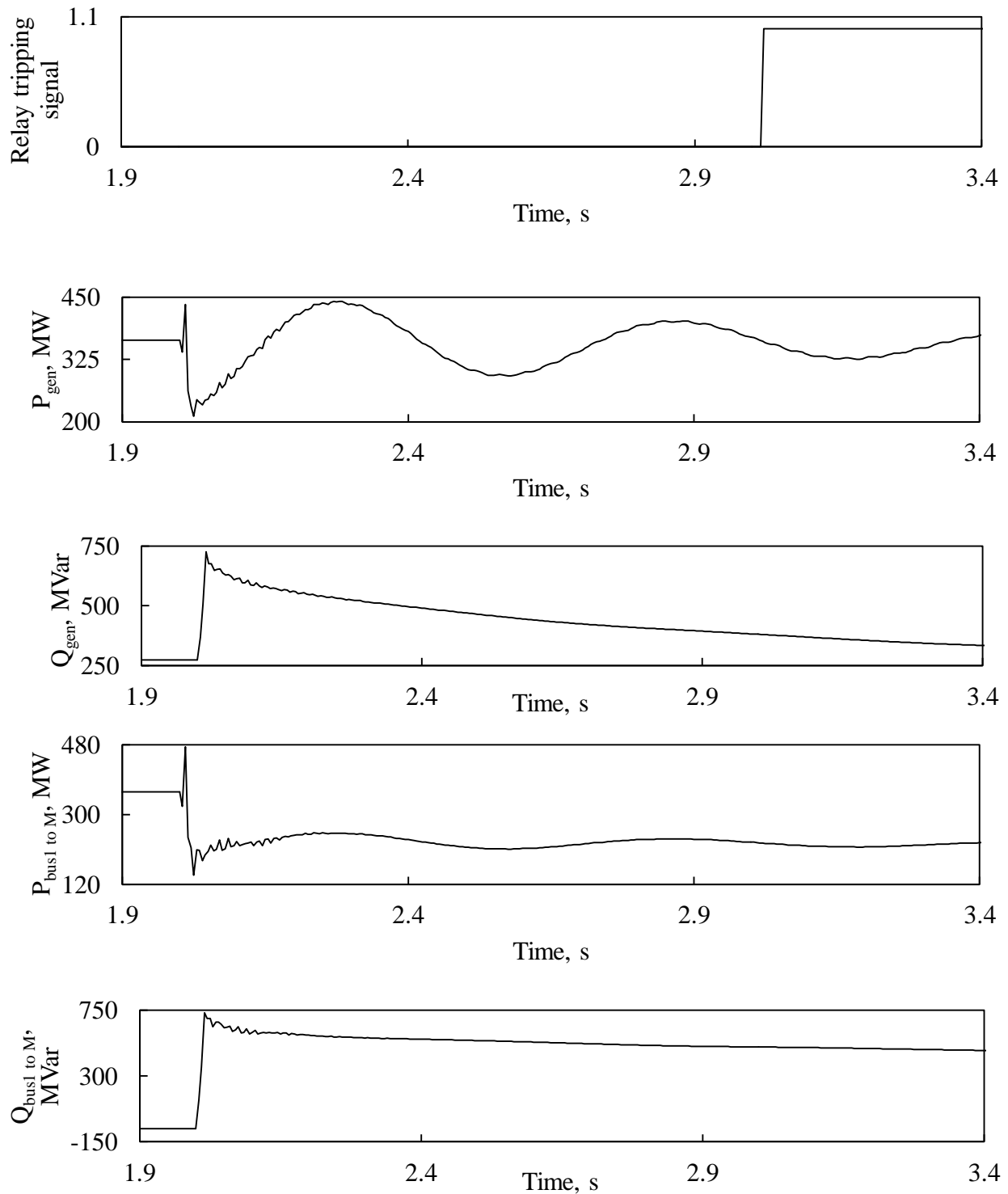


Figure C.33: Relay (21) tripping signal, transient time responses of generator active and reactive powers, active and reactive power flows from Bus 1 to Bus M during a line-to-line fault at F_1 (no wind farm in the system).

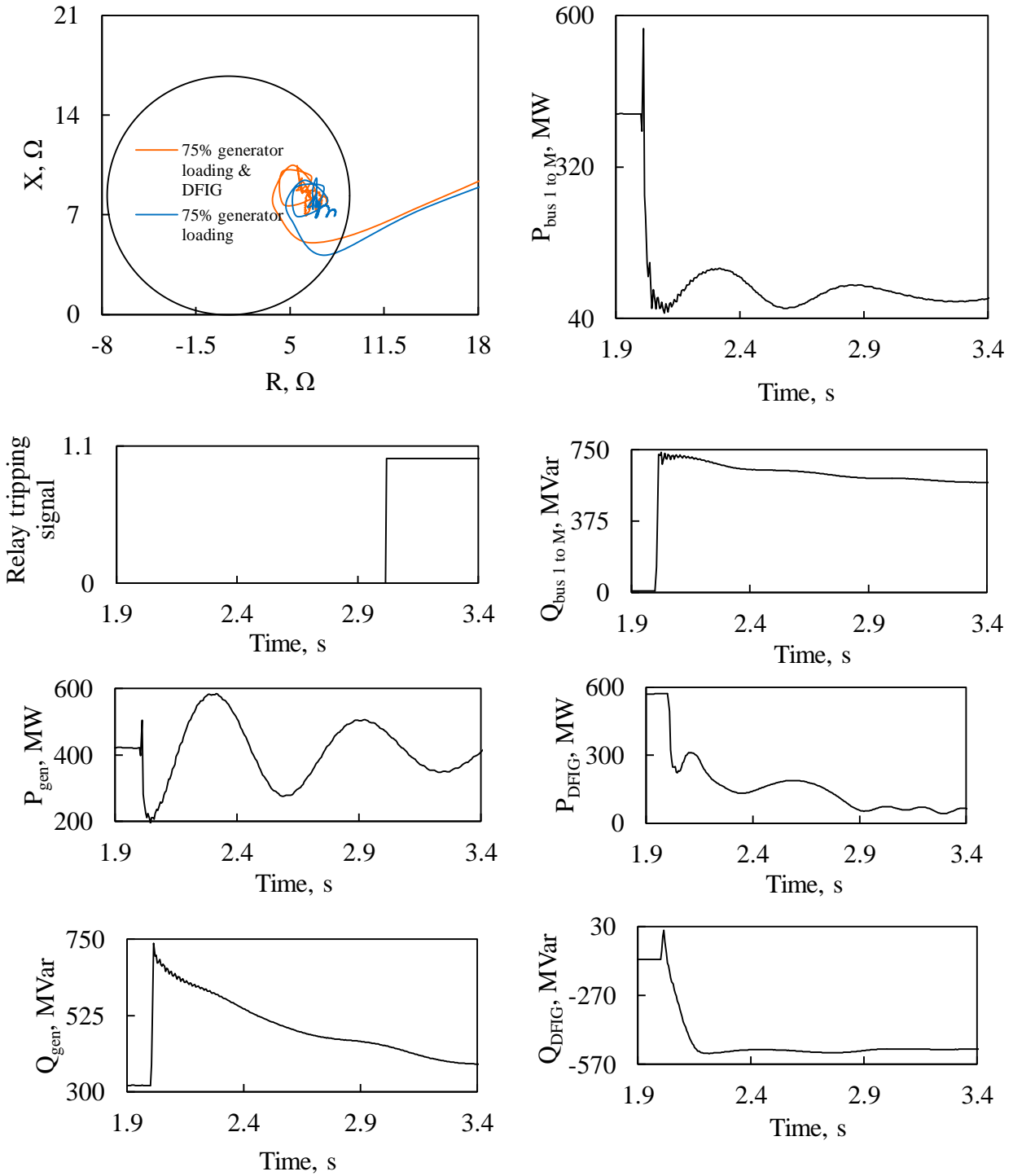


Figure C.34: Relay (21) measured impedance trajectory and its tripping signal, transient time responses of generator active and reactive powers, active and reactive power flows from Bus 1 to Bus M, DFIG-based wind farm active and reactive powers during a line-to-line fault at F_1 .

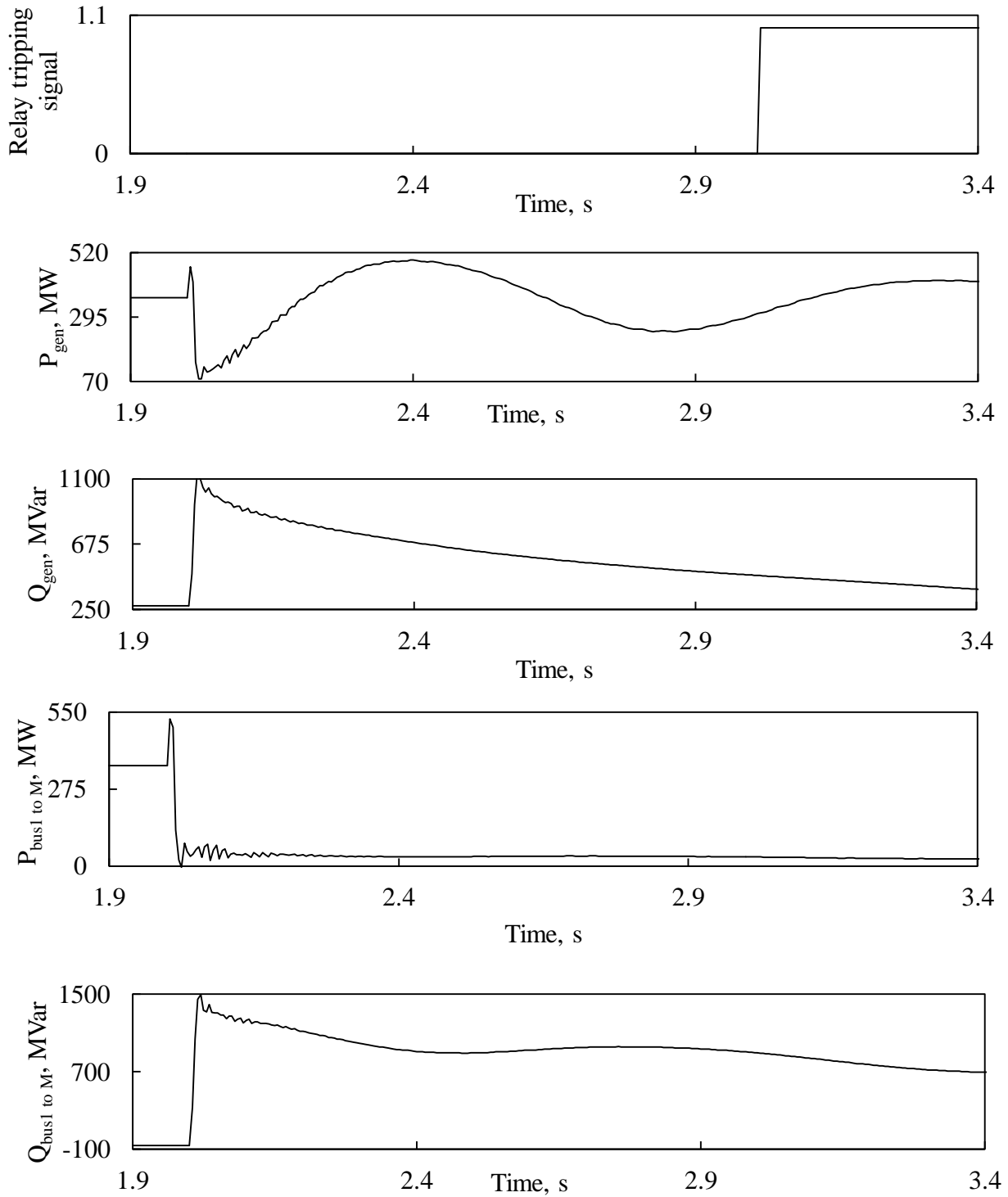


Figure C.35: Relay (21) tripping signal, transient time responses of generator active and reactive powers, active and reactive power flows from Bus 1 to Bus M during a three-phase fault at F_1 (no wind farm in the system).

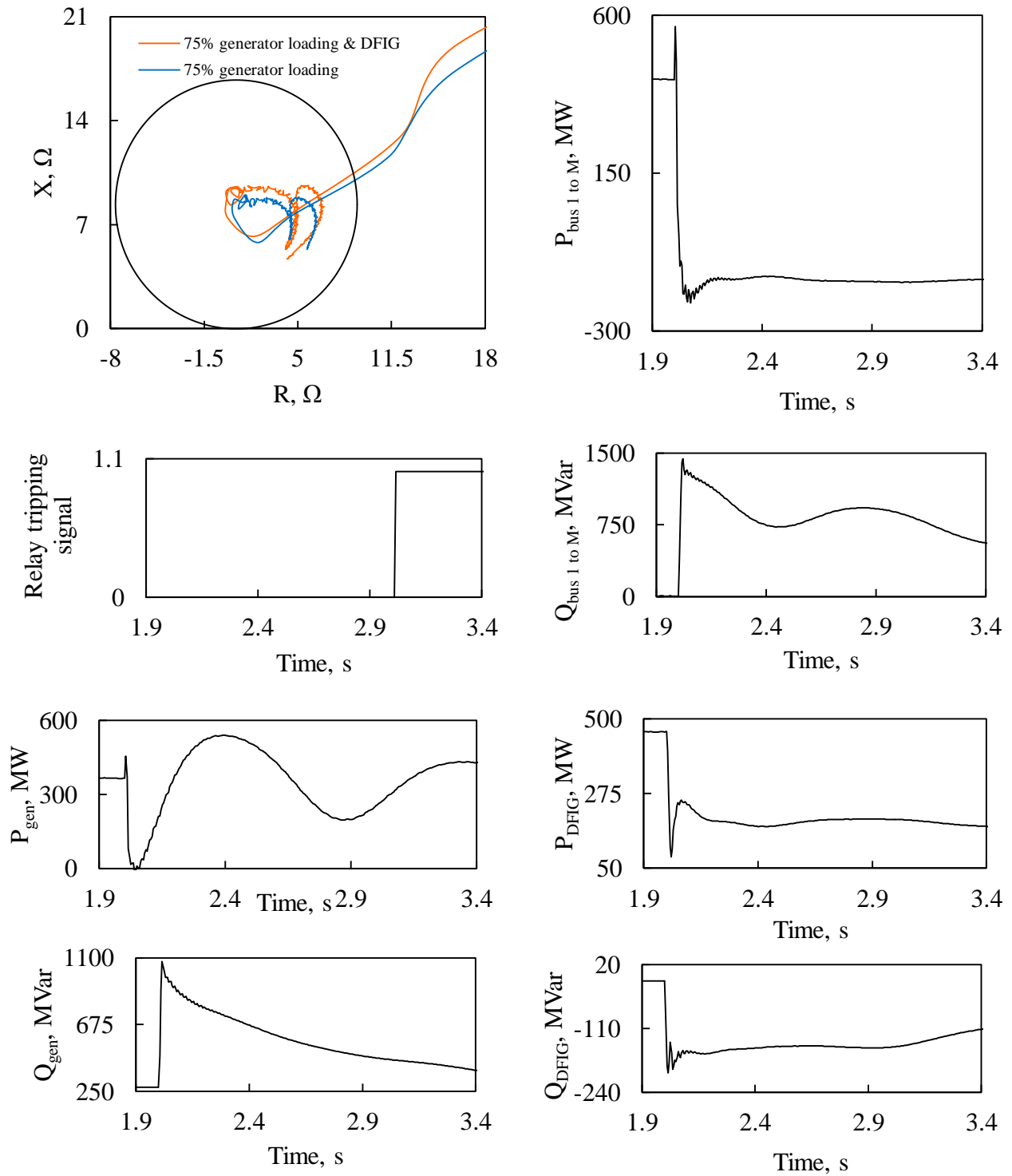


Figure C.36: Relay (21) measured impedance trajectory and its tripping signal, transient time responses of generator active and reactive powers, active and reactive power flows from Bus 1 to Bus M, DFIG-based wind farm active and reactive powers during a three-phase at F_1 .

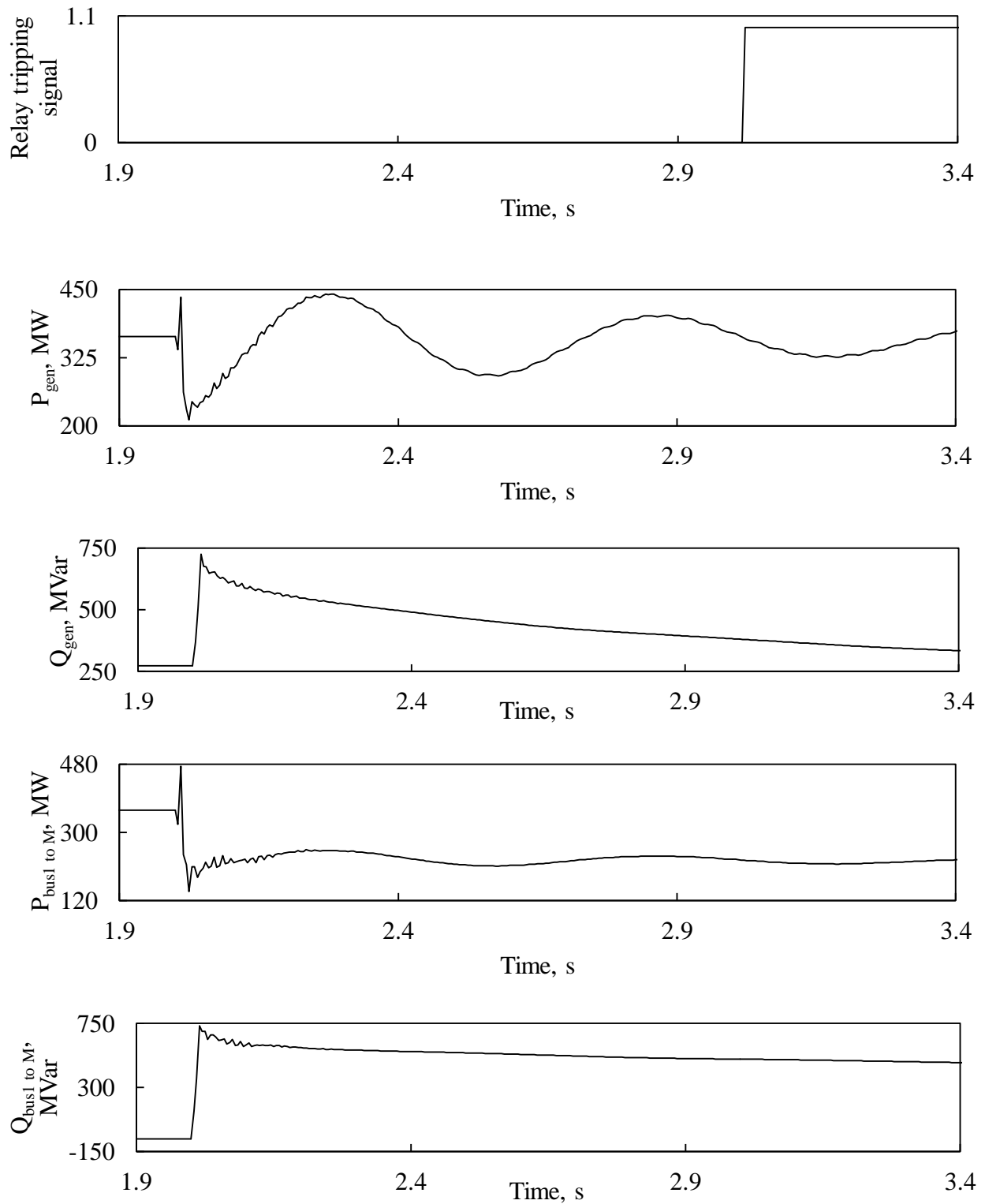


Figure C.37: Relay (21) tripping signal, transient time responses of generator active and reactive powers, active and reactive power flows from Bus 1 to Bus M during a line-to-line fault at F_2 (no wind farm in the system).

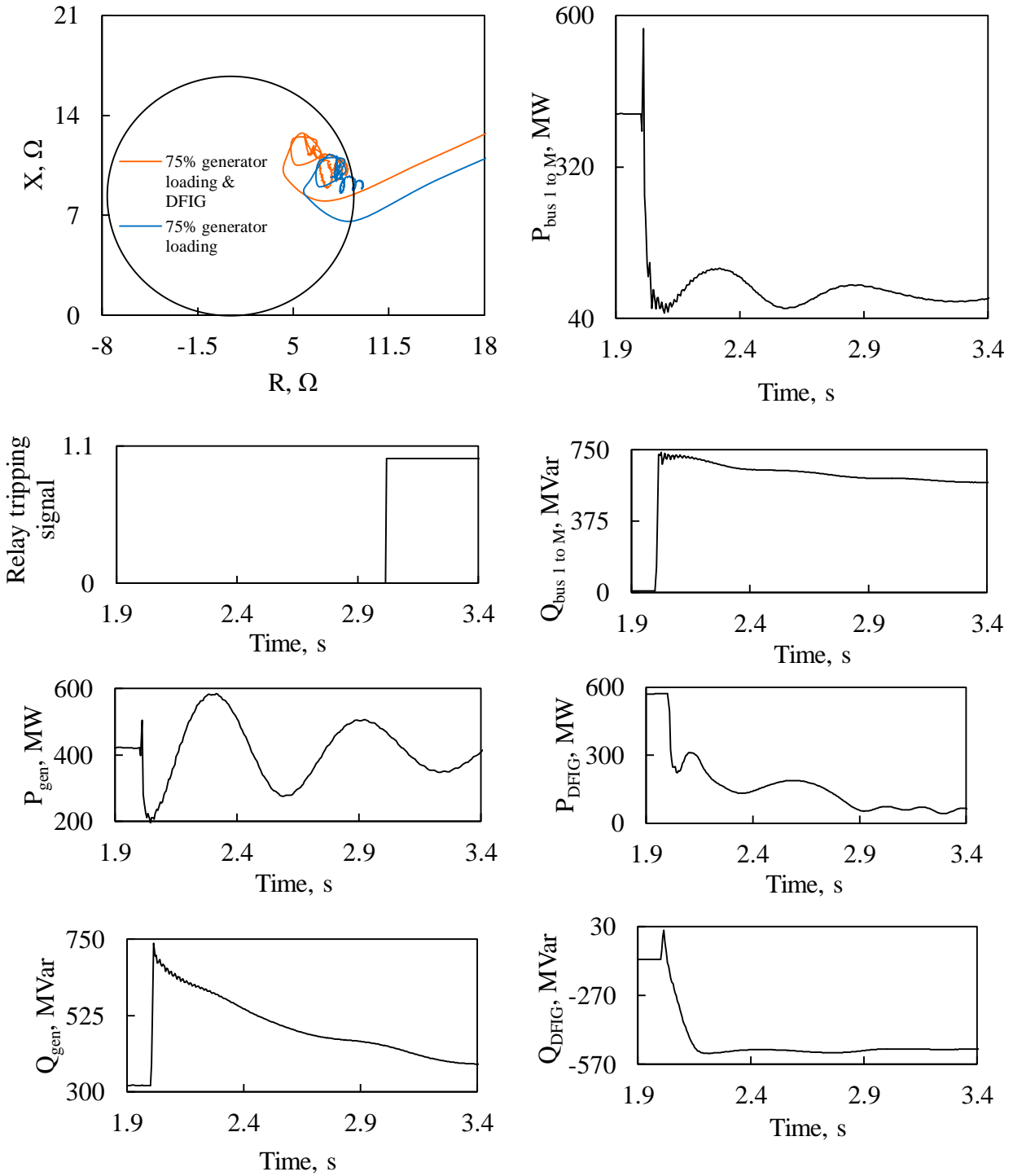


Figure C.38: Relay (21) measured impedance trajectory and its tripping signal, transient time responses of generator active and reactive powers, active and reactive power flows from Bus 1 to Bus M, DFIG-based wind farm active and reactive powers during a line-to-line fault at F₂.

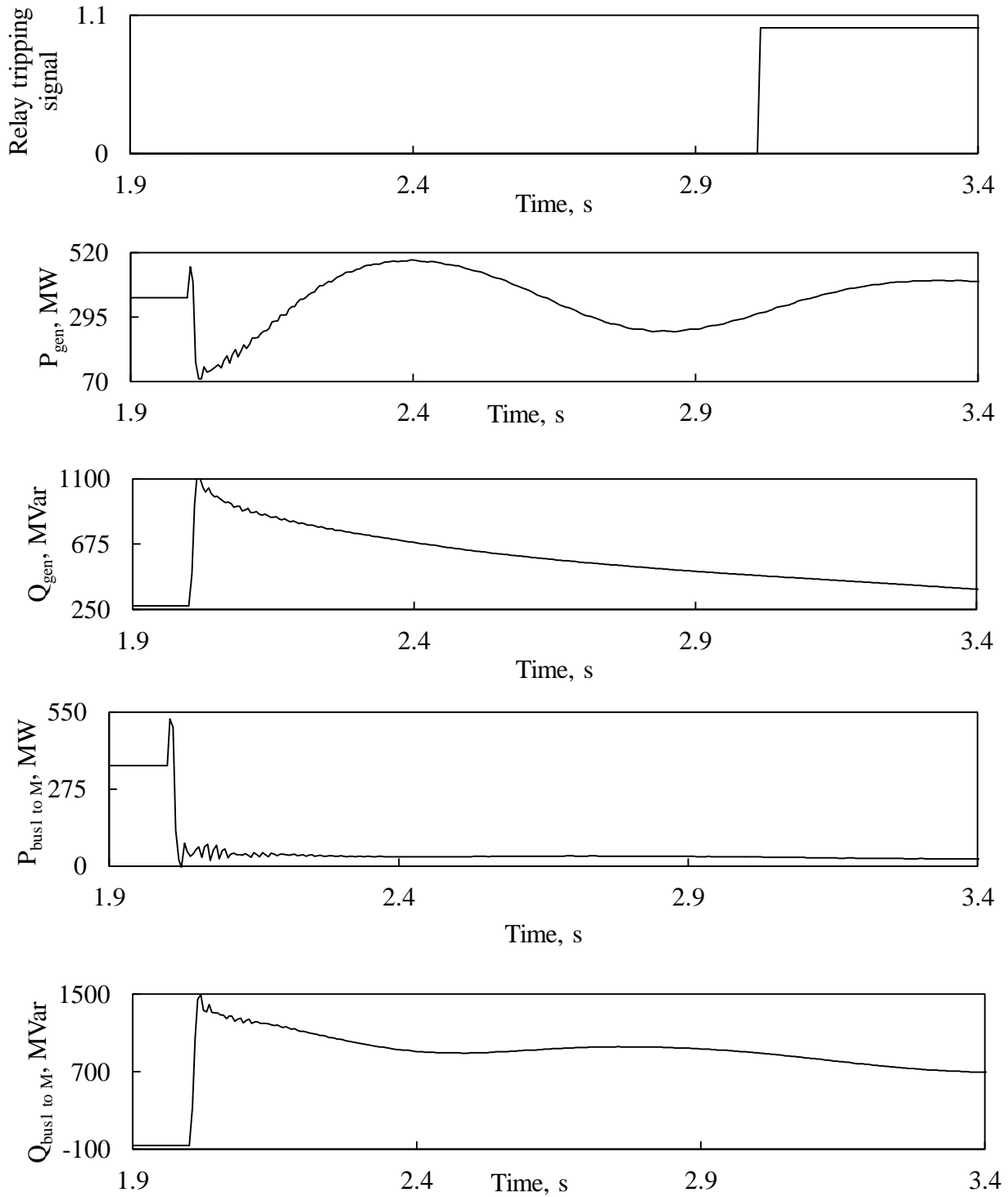


Figure C.39: Relay (21) tripping signal, transient time responses of generator active and reactive powers, active and reactive power flows from Bus 1 to Bus M during a three-phase fault at F_2 (no wind farm in the system).

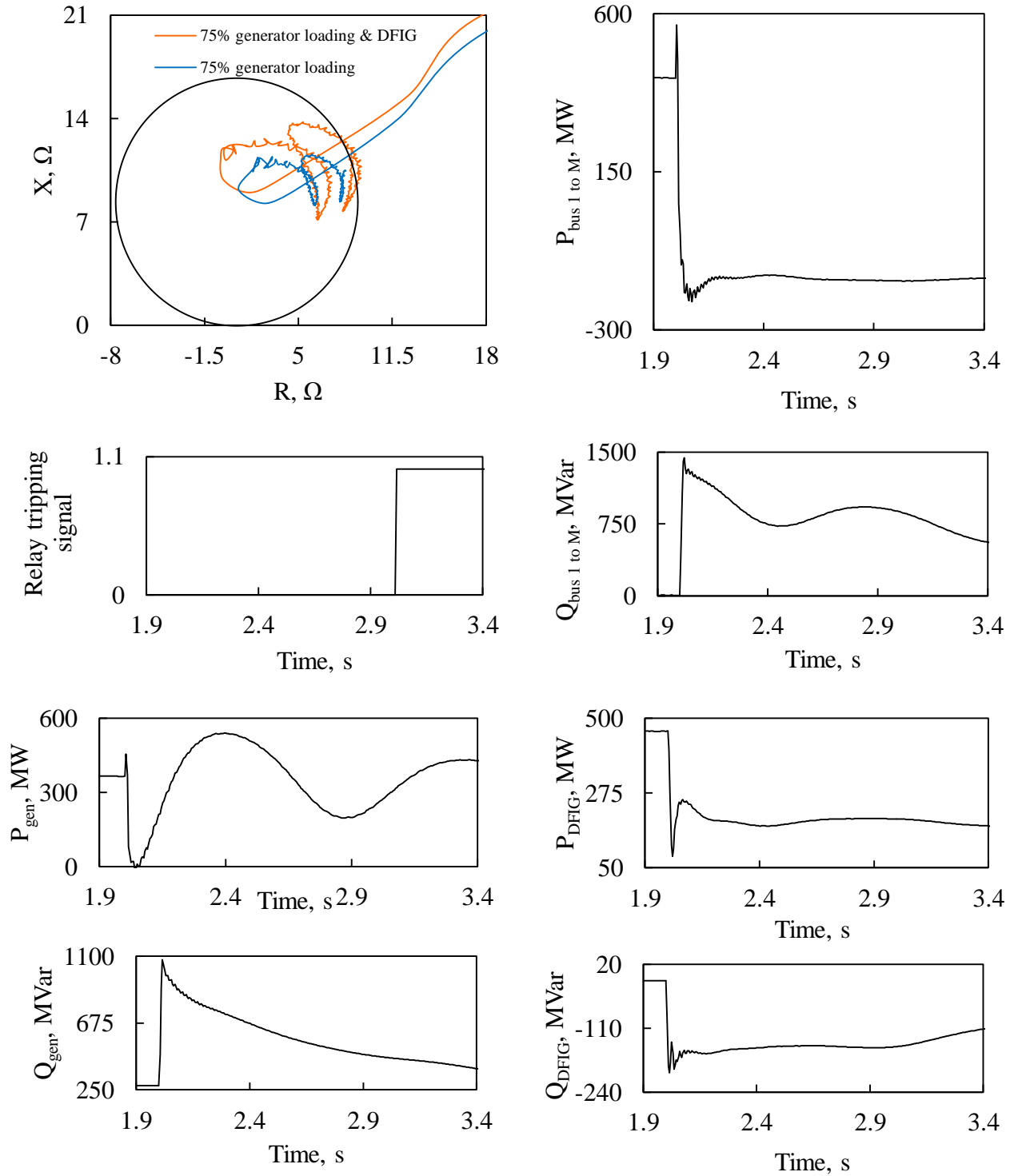


Figure C.40: Relay (21) measured impedance trajectory and its tripping signal, transient time responses of generator active and reactive powers, active and reactive power flows from Bus 1 to Bus M, DFIG-based wind farm active and reactive powers during a three-phase at F_2 .

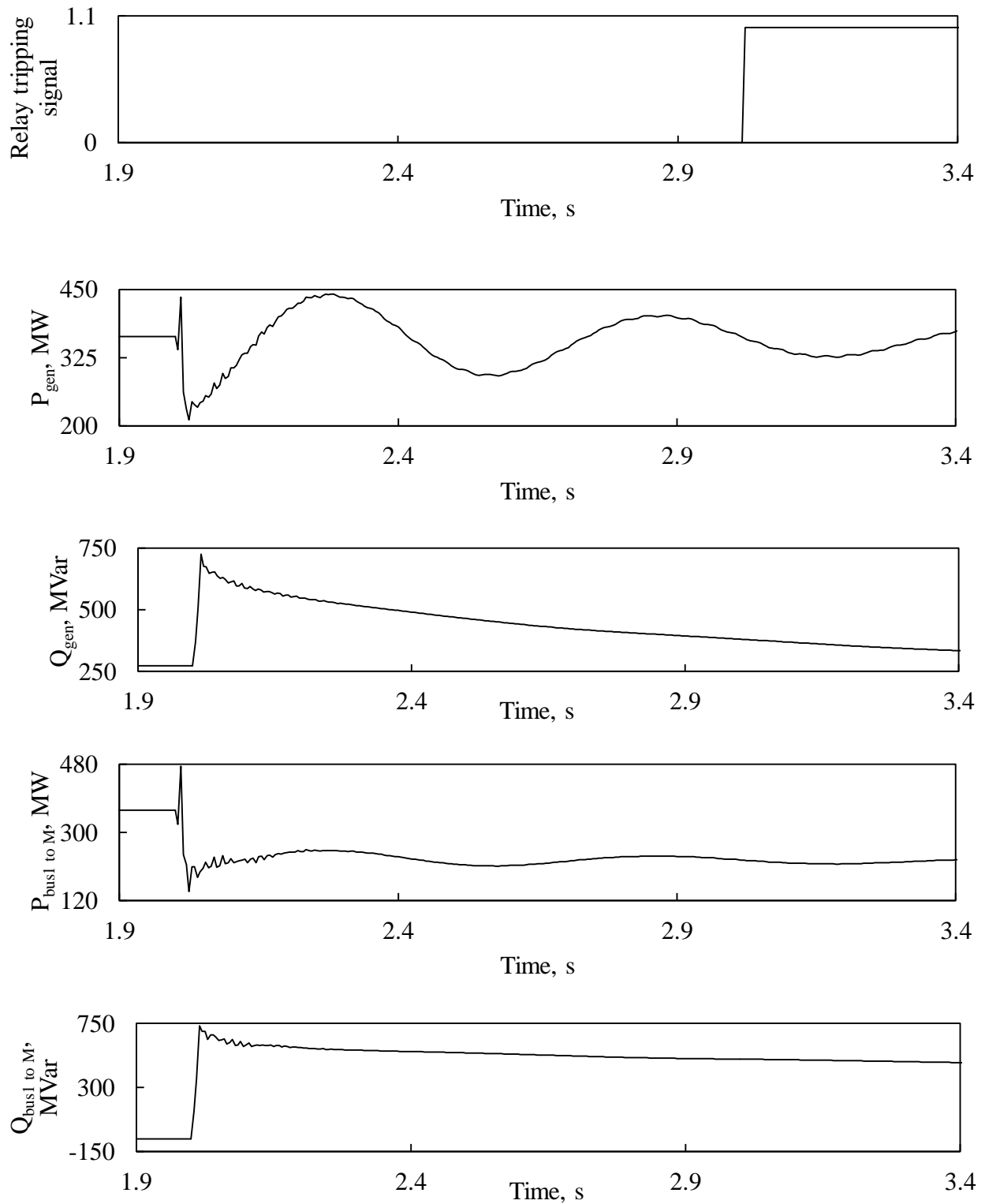


Figure C.41: Relay (21) tripping signal, transient time responses of generator active and reactive powers, active and reactive power flows from Bus 1 to Bus M during a line-to-line fault at F_3 (no wind farm in the system).

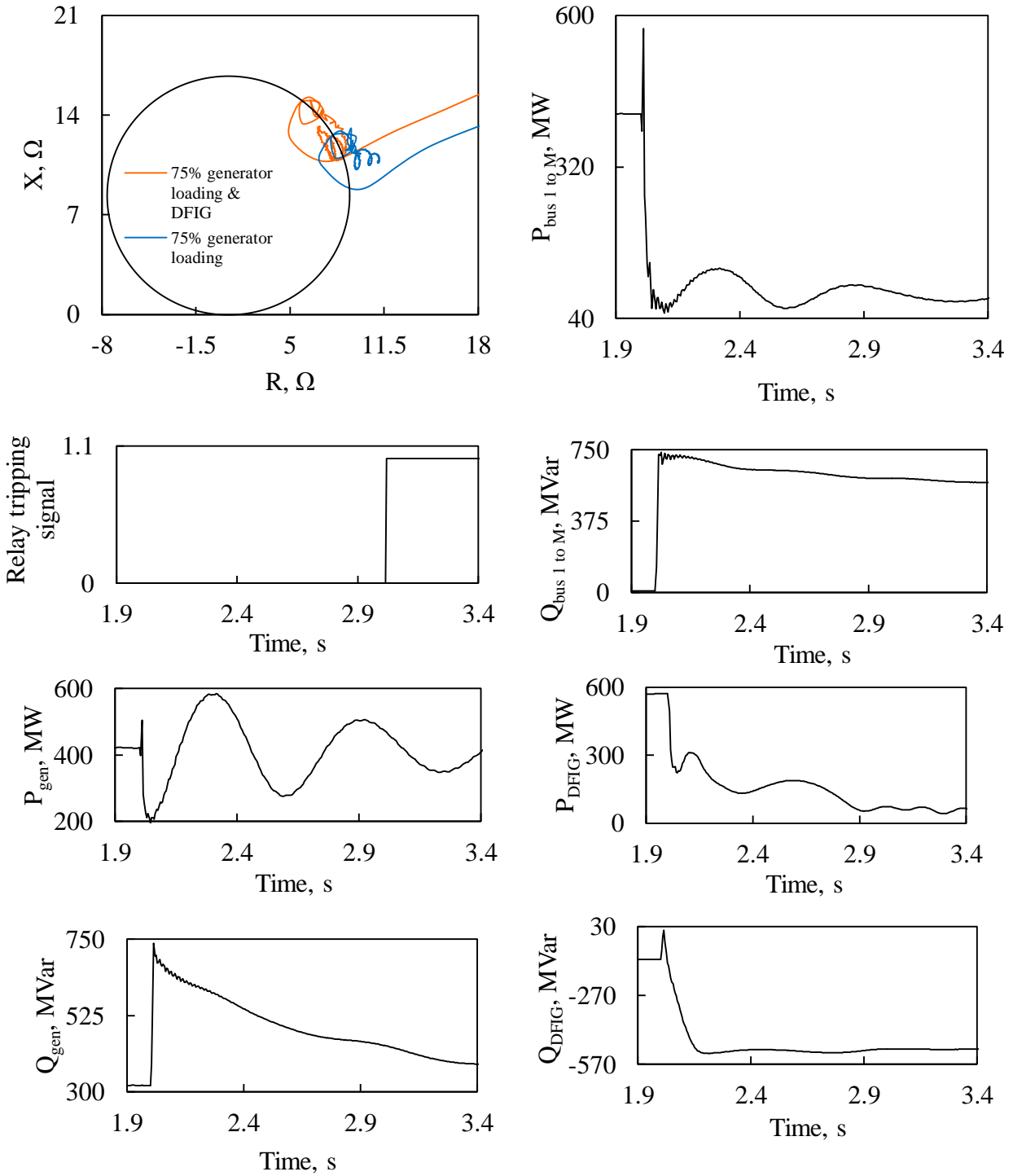


Figure C.42: Relay (21) measured impedance trajectory and its tripping signal, transient time responses of generator active and reactive powers, active and reactive power flows from Bus 1 to Bus M, DFIG-based wind farm active and reactive powers during a line-to-line fault at F₃.

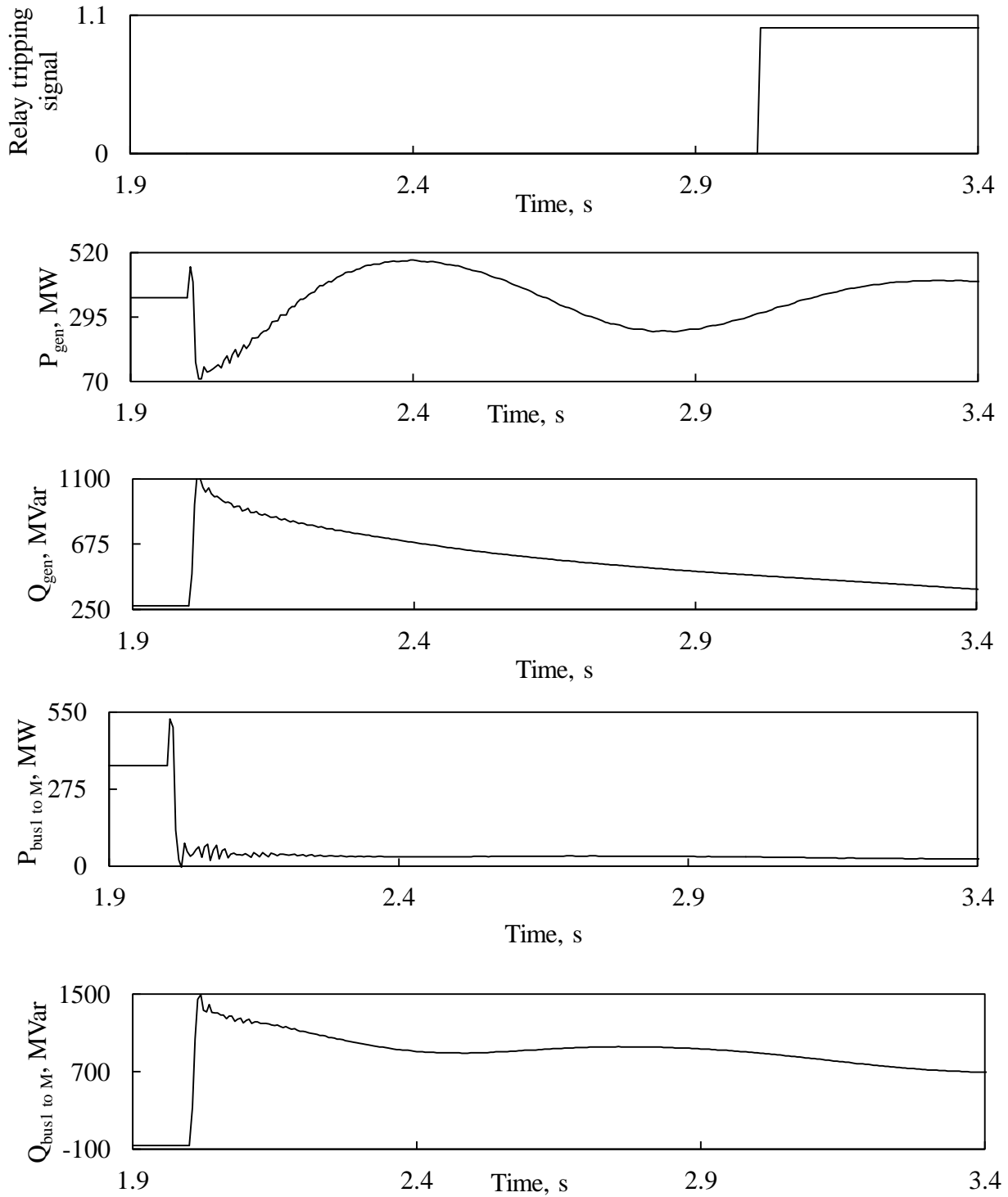


Figure C.43: Relay (21) tripping signal, transient time responses of generator active and reactive powers, active and reactive power flows from Bus 1 to Bus M during a three-phase fault at F_3 (no wind farm in the system).

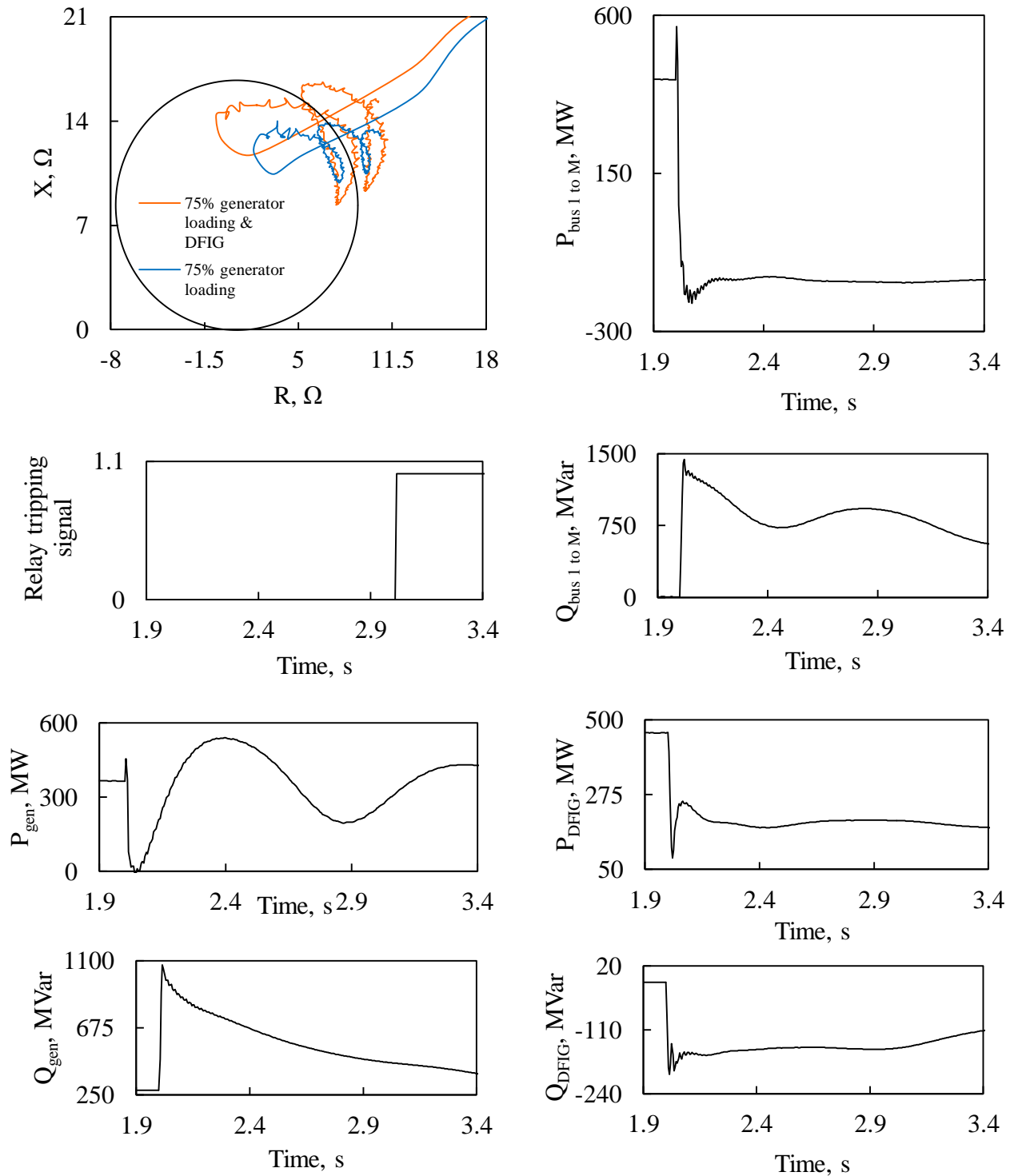


Figure C.44: Relay (21) measured impedance trajectory and its tripping signal, transient time responses of generator active and reactive powers, active and reactive power flows from Bus 1 to Bus M, DFIG-based wind farm active and reactive powers during a three-phase at F_3 .

C.2.3 Performance of Relay (21) at 85% of the generator loading

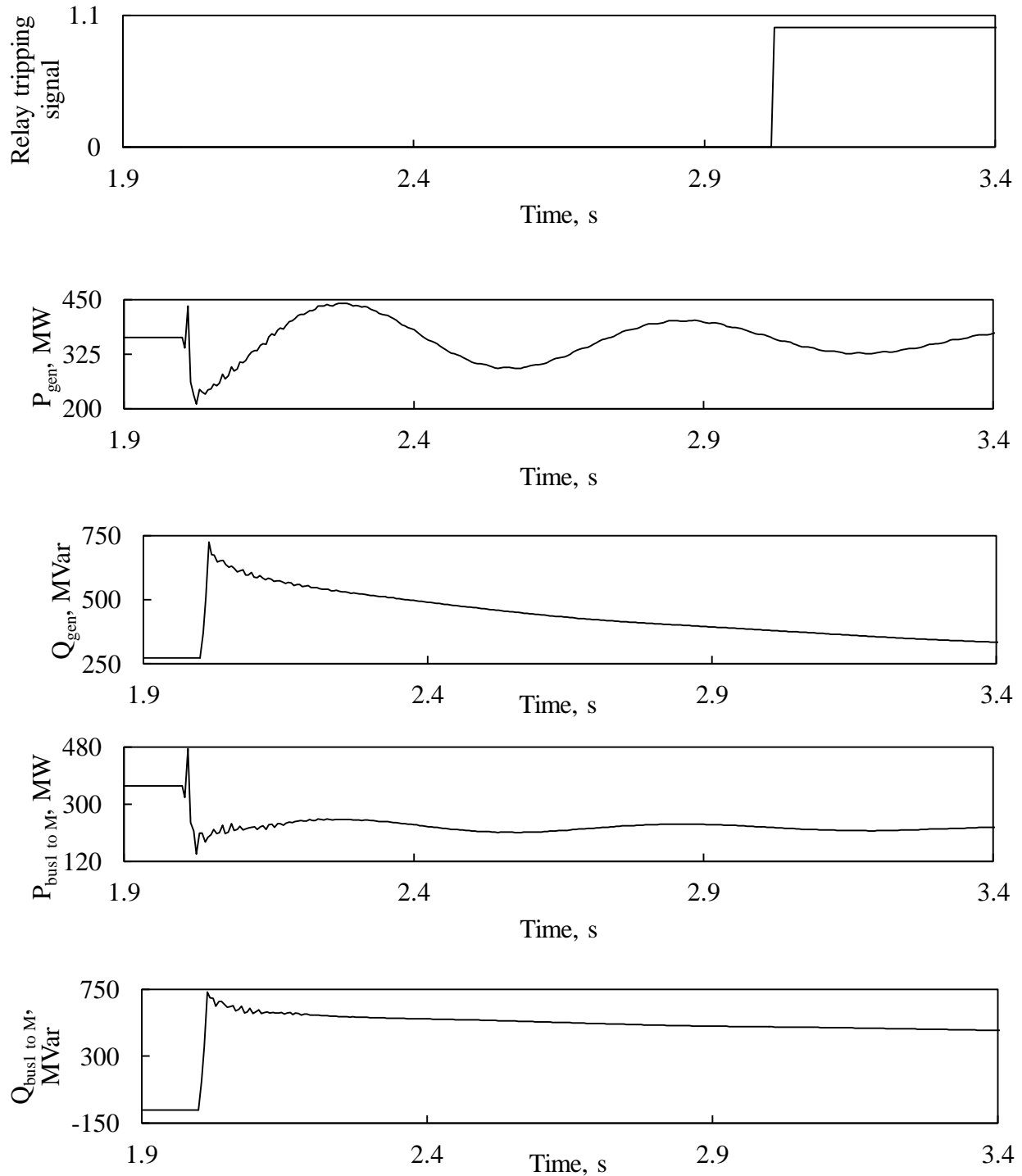


Figure C.45: Relay (21) tripping signal, transient time responses of generator active and reactive powers, active and reactive power flows from Bus 1 to Bus M during a line-to-line fault at F_1 (no wind farm in the system).

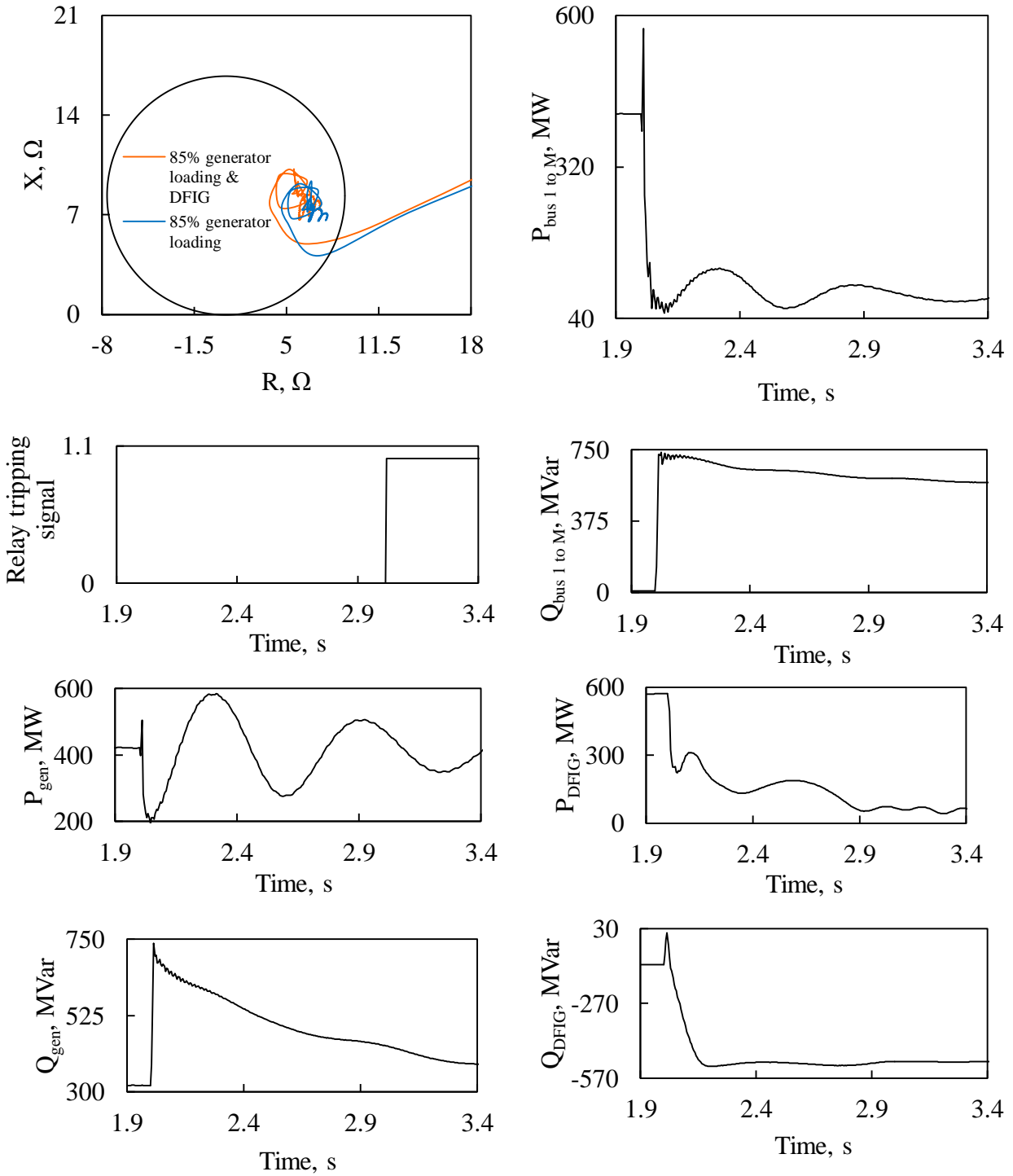


Figure C.46: Relay (21) measured impedance trajectory and its tripping signal, transient time responses of generator active and reactive powers, active and reactive power flows from Bus 1 to Bus M, DFIG-based wind farm active and reactive powers during a line-to-line fault at F₁.

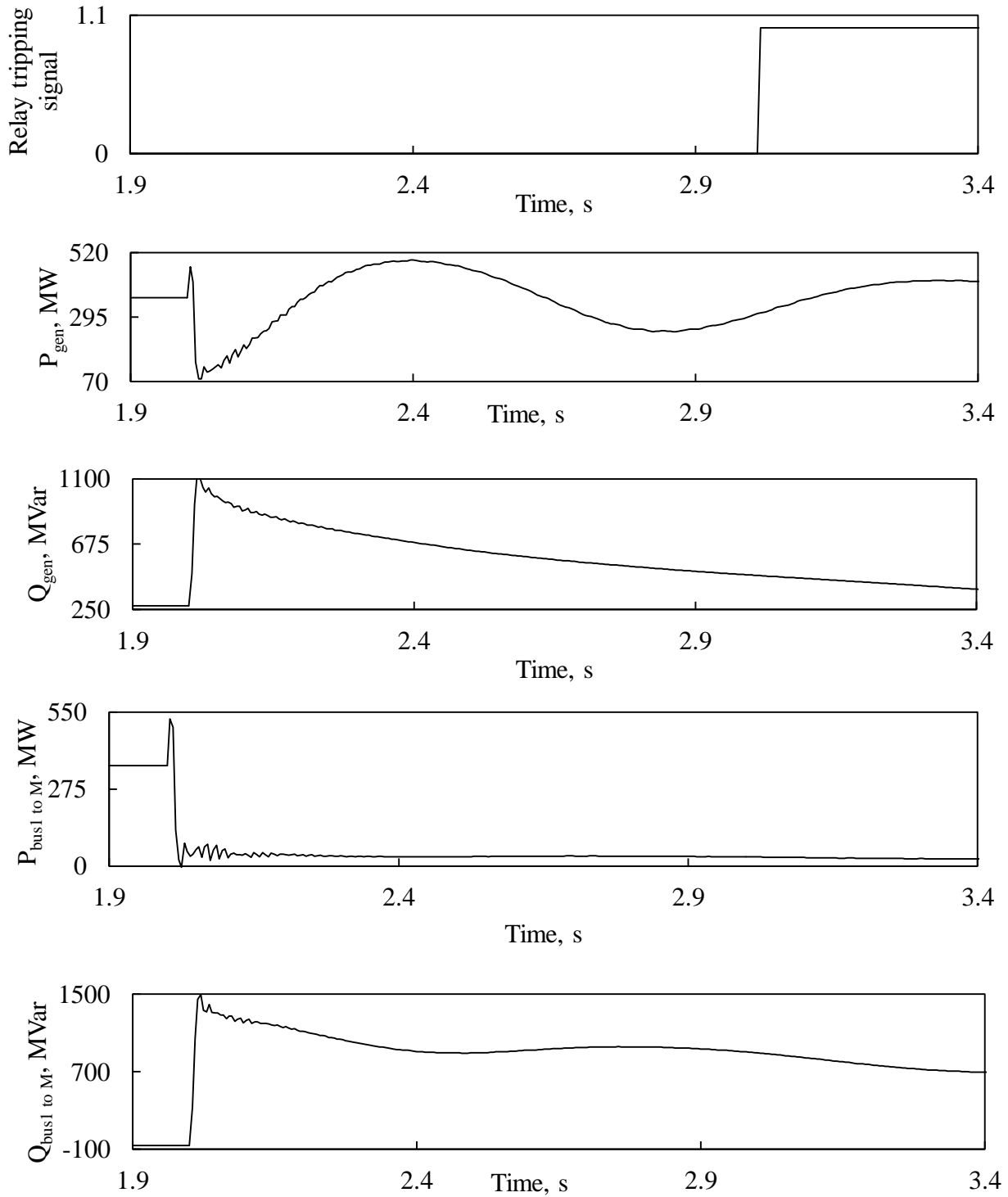


Figure C.47: Relay (21) tripping signal, transient time responses of generator active and reactive powers, active and reactive power flows from Bus 1 to Bus M during a three-phase fault at F_1 (no wind farm in the system).

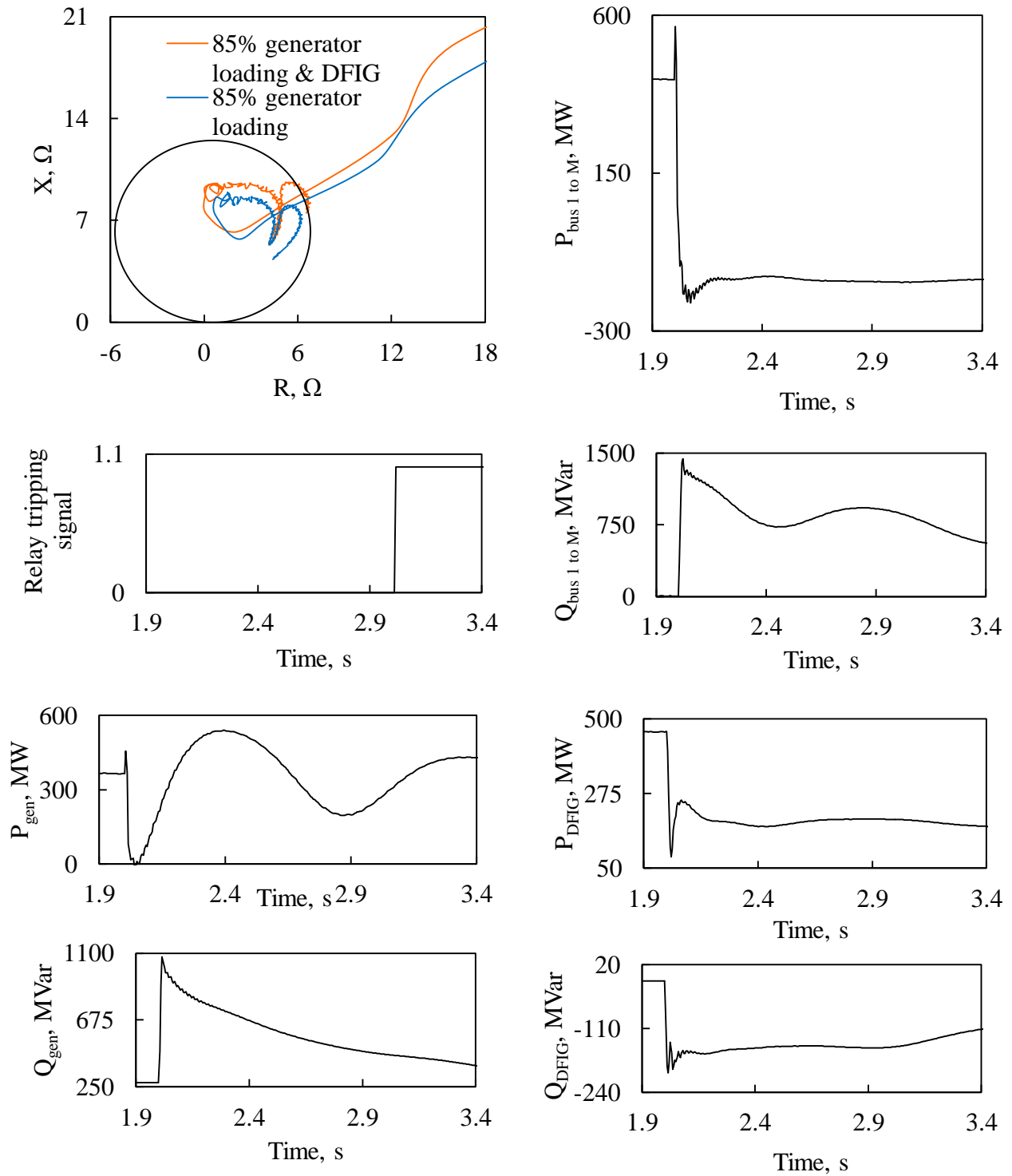


Figure C.48: Relay (21) measured impedance trajectory and its tripping signal, transient time responses of generator active and reactive powers, active and reactive power flows from Bus 1 to Bus M, DFIG-based wind farm active and reactive powers during a three-phase at F₁.

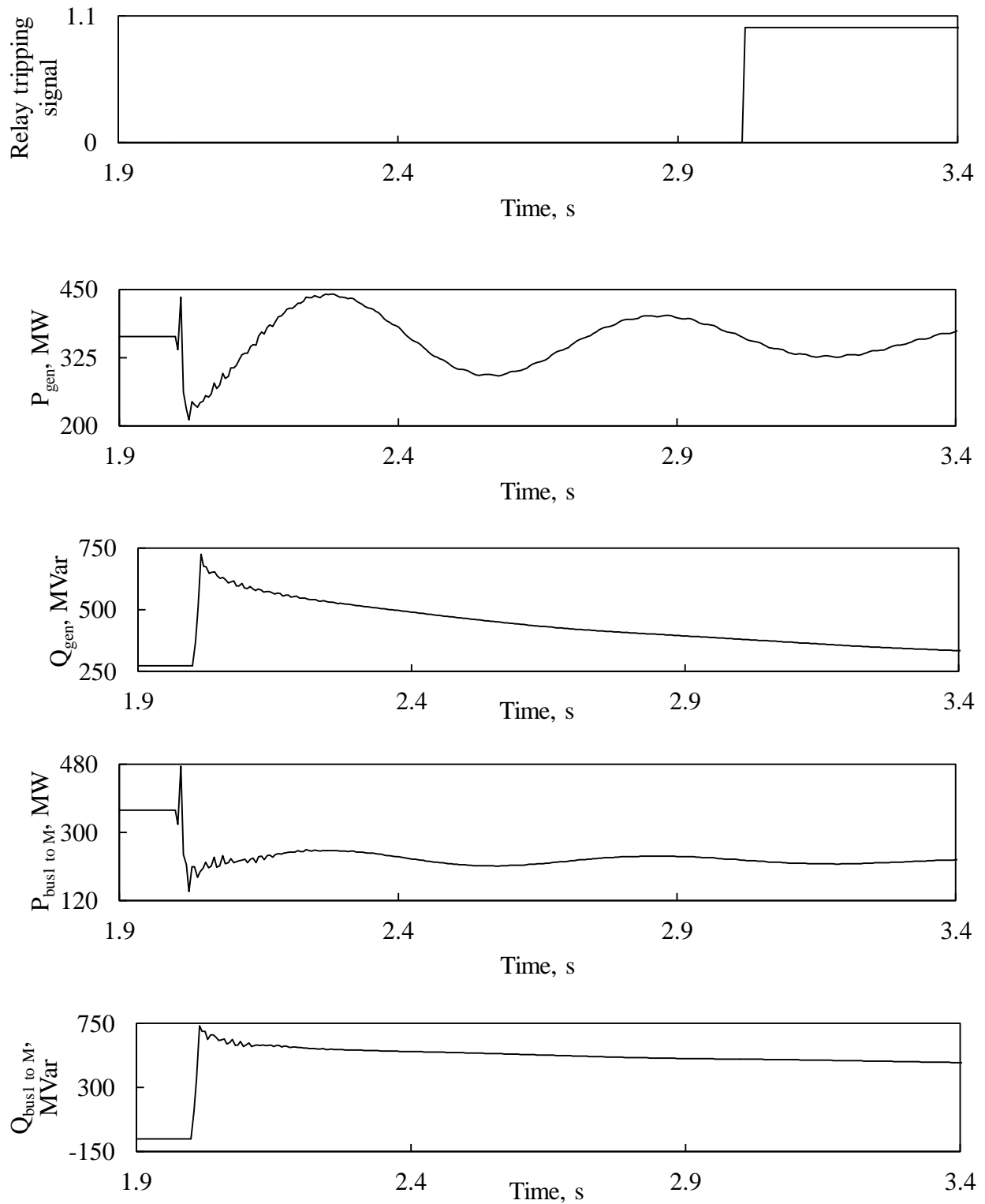


Figure C.49: Relay (21) tripping signal, transient time responses of generator active and reactive powers, active and reactive power flows from Bus 1 to Bus M during a line-to-line fault at F_2 (no wind farm in the system).

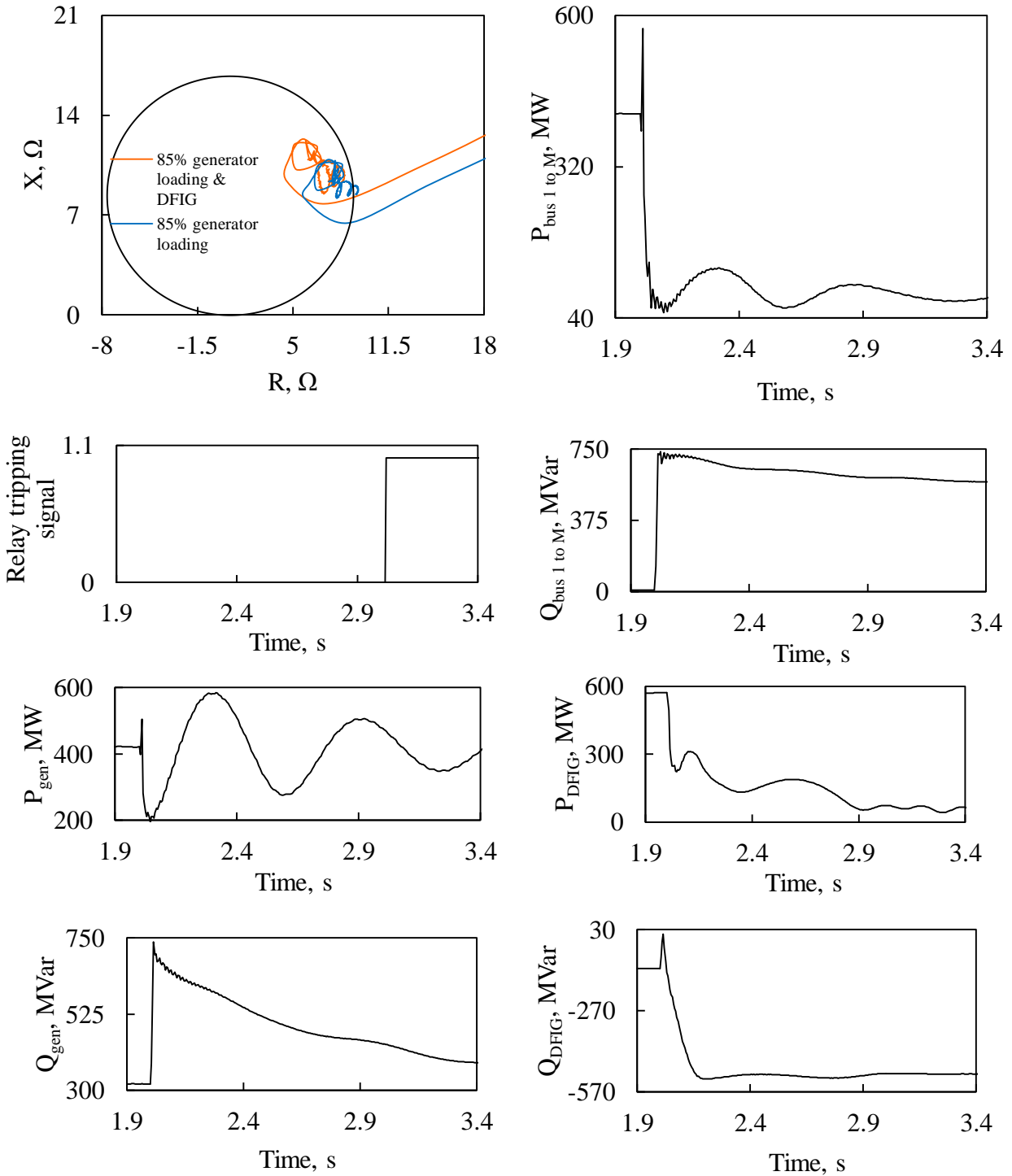


Figure C.50: Relay (21) measured impedance trajectory and its tripping signal, transient time responses of generator active and reactive powers, active and reactive power flows from Bus 1 to Bus M, DFIG-based wind farm active and reactive powers during a line-to-line fault at F_2 .

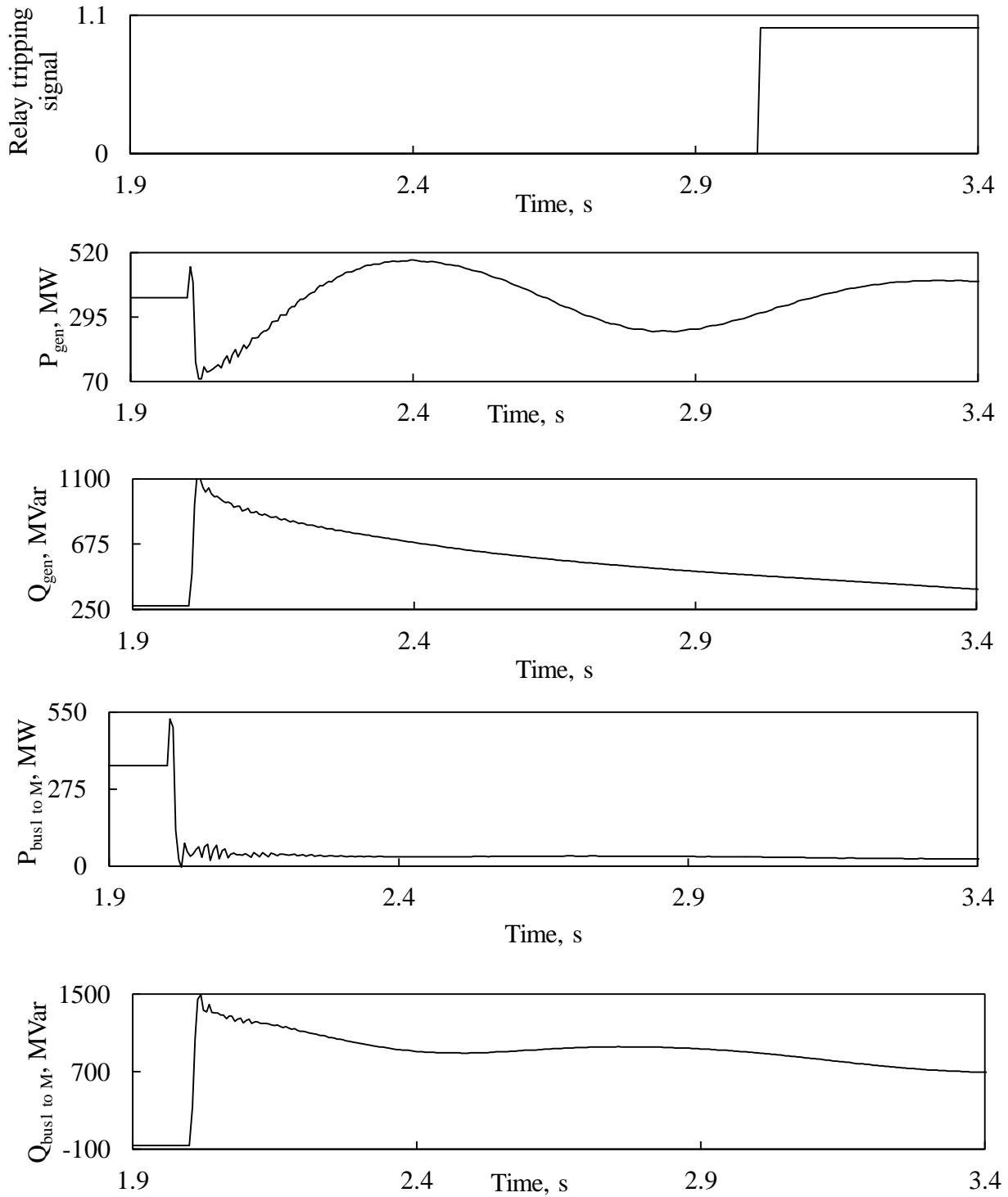


Figure C.51: Relay (21) tripping signal, transient time responses of generator active and reactive powers, active and reactive power flows from Bus 1 to Bus M during a three-phase fault at F_2 (no wind farm in the system).

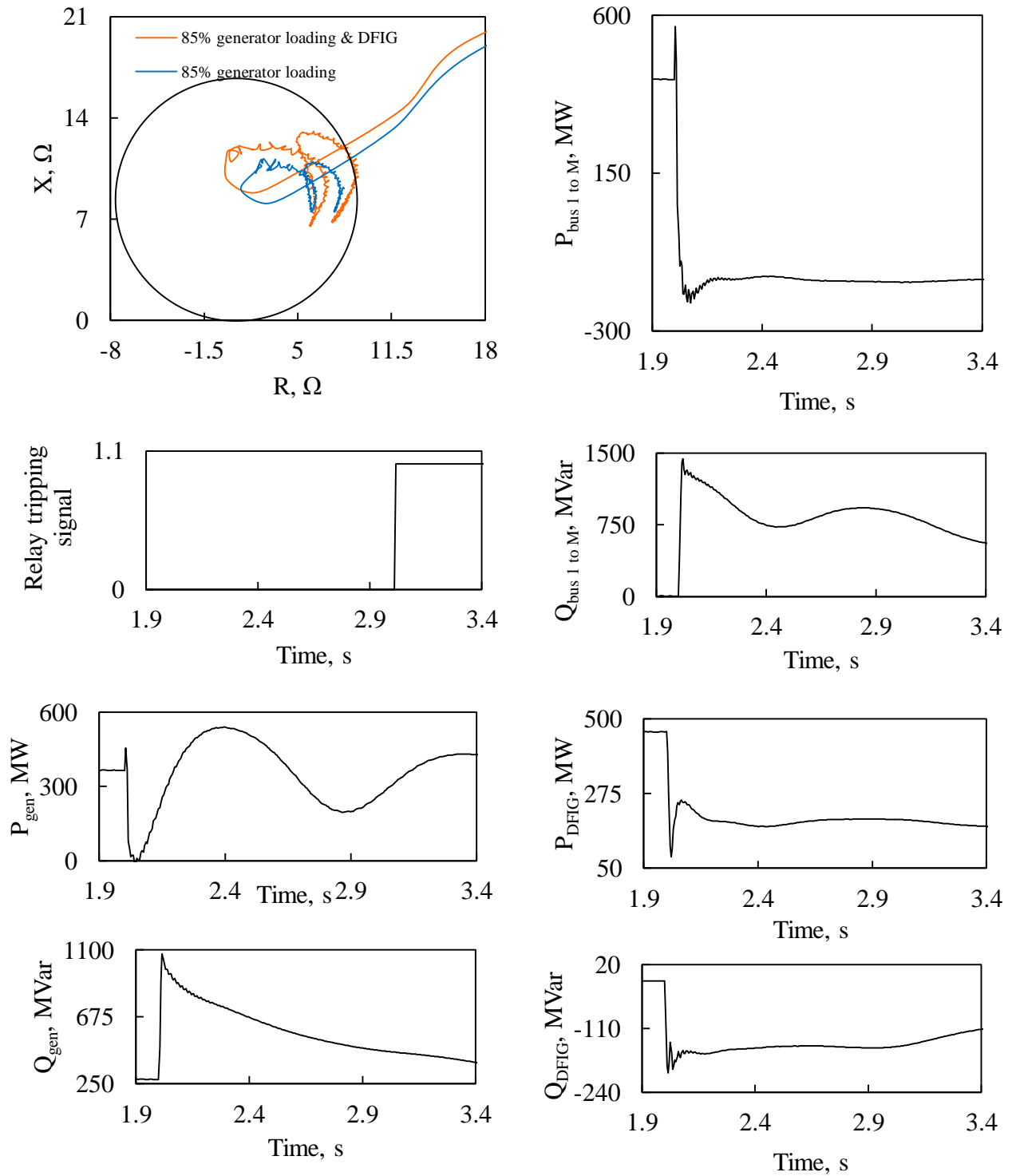


Figure C.52: Relay (21) measured impedance trajectory and its tripping signal, transient time responses of generator active and reactive powers, active and reactive power flows from Bus 1 to Bus M, DFIG-based wind farm active and reactive powers during a three-phase at F₂.

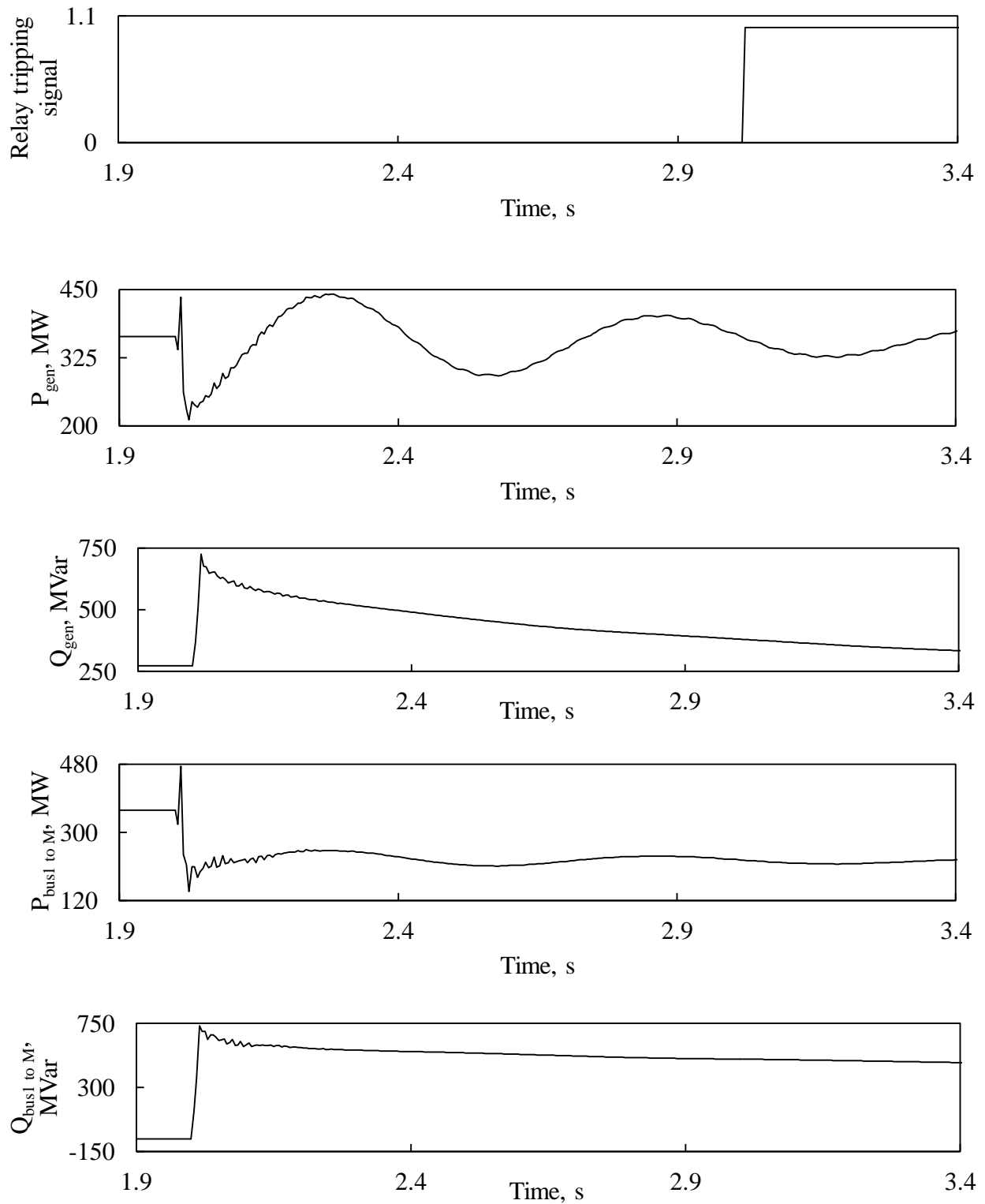


Figure C.53: Relay (21) tripping signal, transient time responses of generator active and reactive powers, active and reactive power flows from Bus 1 to Bus M during a line-to-line fault at F_3 (no wind farm in the system).

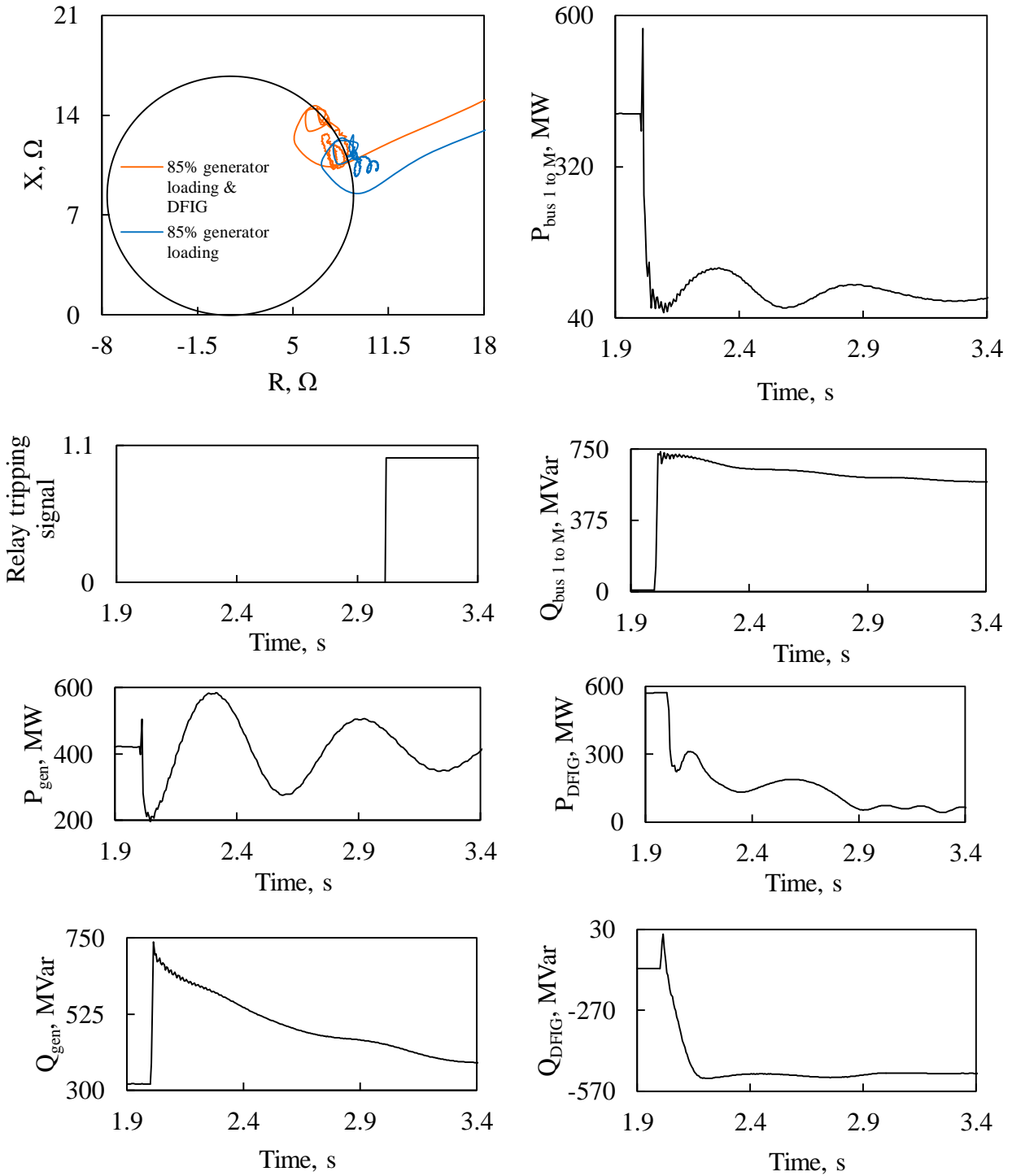


Figure C.54: Relay (21) measured impedance trajectory and its tripping signal, transient time responses of generator active and reactive powers, active and reactive power flows from Bus 1 to Bus M, DFIG-based wind farm active and reactive powers during a line-to-line fault at F₃.

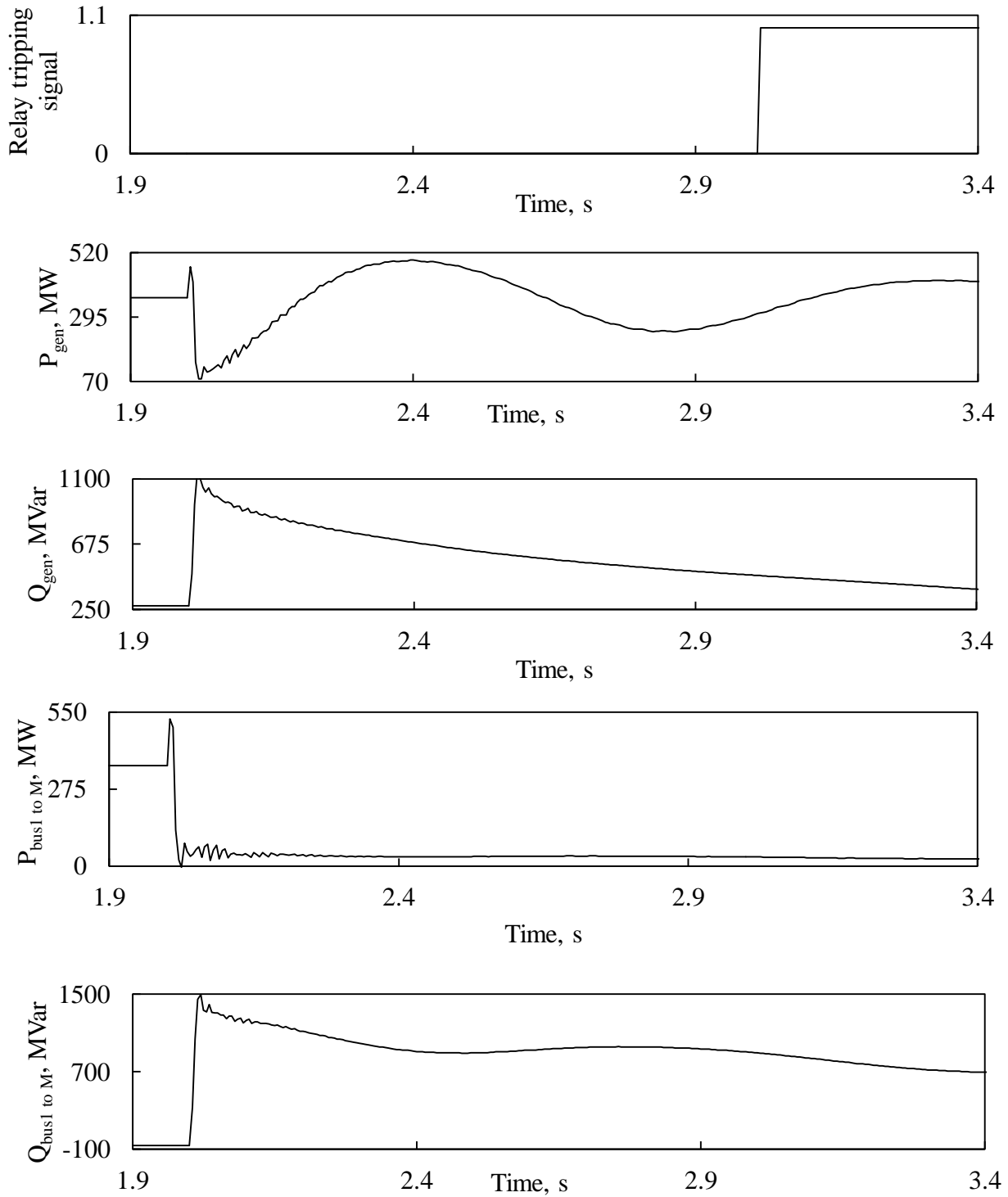


Figure C.55: Relay (21) tripping signal, transient time responses of generator active and reactive powers, active and reactive power flows from Bus 1 to Bus M during a three-phase fault at F_3 (no wind farm in the system).

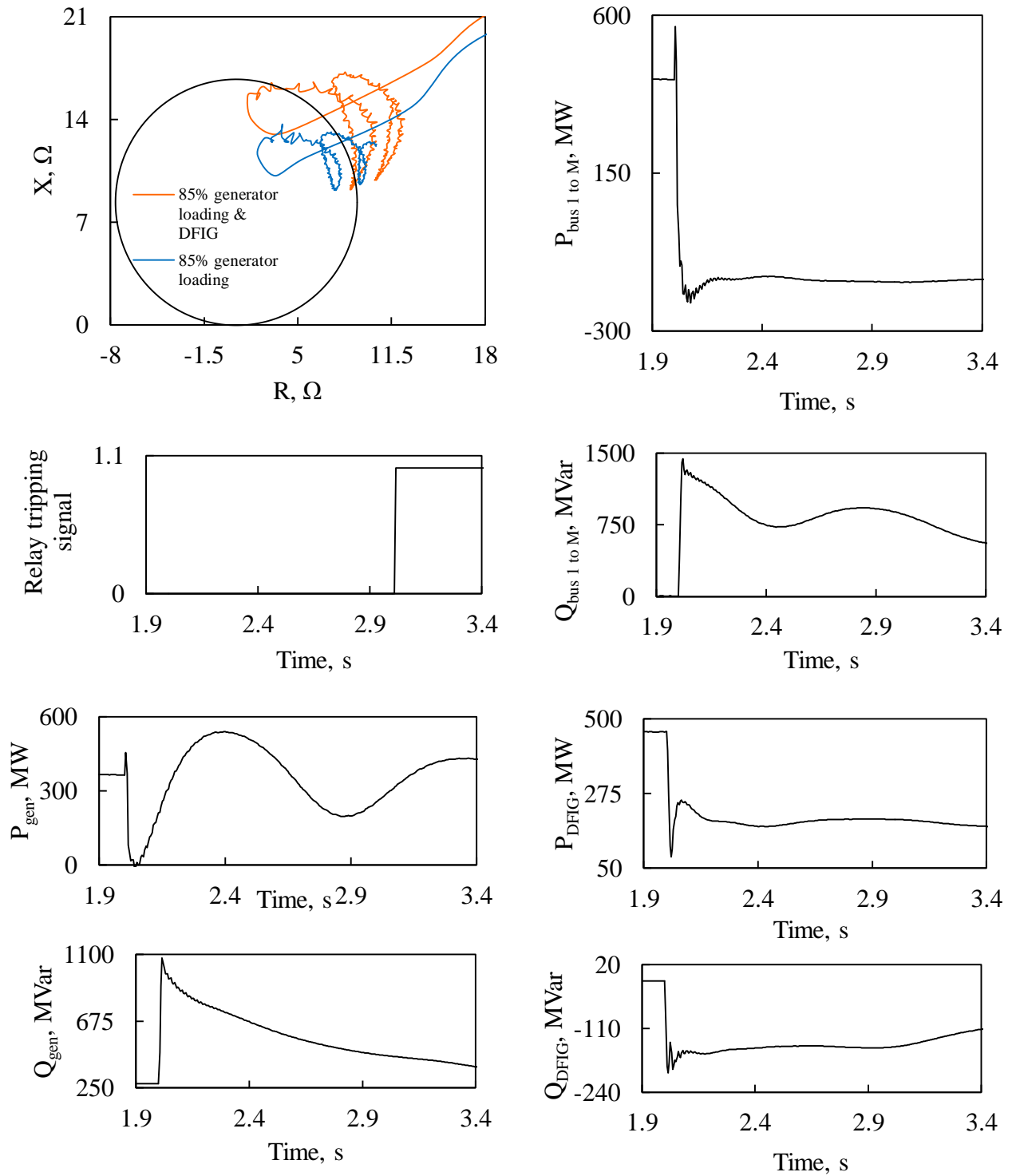


Figure C.56: Relay (21) measured impedance trajectory and its tripping signal, transient time responses of generator active and reactive powers, active and reactive power flows from Bus 1 to Bus M, DFIG-based wind farm active and reactive powers during a three-phase at F_3 .